AZIMUTHAL ANISOTROPIES OF HIGH-p_{T} CHARGED PARTICLES IN PB+PB COLLISIONS AT 5.02 TEV WITH THE ATLAS DETECTOR

BY

XIAONING WANG

DISSERTATION

Submitted in partial fulfillment of the requirements
for the degree of Doctor of Philosophy in Physics
in the Graduate College of the
University of Illinois Urbana-Champaign, 2024

Urbana, Illinois

Doctoral Committee:

Professor Matthias Grosse Perdekamp, Chair
Professor Anne Sickles, Director of Research
Professor Mark Neubauer
Professor Jun Song
Associate Professor Jacquelyn Noronha-Hostler

Abstract

The quark gluon plasma (QGP) is a novel state of matter that forms under extreme temperature and density, in which the normally bounded hadronic states of matter "melt" into constituent quarks and gluons. Understanding the short-distance interactions within the QGP gives us a probe to one of the fundamental forces of nature, strong force. The QGP can be created in ultra-relativistic heavy ion collisions in collider facilities such as the Relativistic Heavy Ion Collider (RHIC) and the Large Hadron Collider (LHC). By colliding accelerated beams of heavy ions and measuring the collision products, bulk properties and short-distance interaction mechanisms of the QGP can be probed. Soft and hard QCD processes both happen in these collisions, the former giving rise to the QGP, and the latter gives high-momentum partons that traverse through and interact with the QGP. It has been observed that the QGP exhibit collective expansion, and significant anisotropies exist in the particle production along the azimuthal direction. In lower momentum particles, studies of this anisotropy lead to the understanding of the transport properties of the QGP, which explain how the initial geometry of the QGP is converted into the final-state particles. In higher momentum particles, this anisotropy reflects the parton energy loss mechanism to the QGP. This is done by colliding accelerated beams of heavy nuclei and measuring the products of the collisions with a particle detector. In particle collisions, partons can scatter off each other with a large momentum transfer, and when they come out of the collisions, they create collimated sprays of particles that are called jets. Therefore, the study of azimuthal anisotropies in the high-momentum sector is powerful probe for the short-distance interactions within the QGP.

This thesis presents a measurement of azimuthal anisotropy coefficients v_2 and v_3 of charged particles produced in Pb+Pb collisions at $\sqrt{s_{\mathrm{NN}}} = 5.02$ TeV using a data set corresponding to an integrated luminosity of 435 μb^{-1} collected with the ATLAS detector at the LHC in 2018. The values of v_2 and v_3 are measured in intervals of centrality covering up to the 60% most central events and a charged-particle transverse momentum (p_{T}) range of 1–400 GeV using the scalar product and multi-particle cumulant methods. These methods are sensitive to event-by-event fluctuations and non-flow effects in the measurements of azimuthal anisotropies. Positive values of v_2 are observed up to 100 GeV from both methods across all centrality intervals. Positive values of v_3 are observed up to approximately 25 GeV using the scalar product method, and the values of v_3 for $p_{\mathrm{T}} > 10$ GeV using the multi-particle cumulant method show a strong centrality dependence. At high p_{T}, charged particles dominantly come from the fragmentation of jets, and the results of this study are sensitive to the path-length dependence of the energy loss of the jets as they traverse the quark-gluon plasma produced in Pb+Pb collisions.

To my dearest grandma, Huanfeng Huang. Your strength and love inspire me always.

Acknowledgments

This work wouldn't have been possible without the support of many individuals: family, my human and feline friends, and colleagues.

I would like to express my gratitude to my advisor, Anne Sickles, for guiding through my research work and gradute school. Her support has been invaluable in helping me advance academically and develop my professional interpersonal skills. The group she has led has been supportive and welcoming, for which I am truly grateful. Graduate school has been a trying experience, especially during the global pandemic, and I sincerely thank her for guiding us through these difficult times.

I extend my heartfelt thanks to everyone in my own and other nuclear physics research groups at UIUC for being wonderful friends and colleagues. I am especially thankful to the postdocs I had the pleasure of working with: Tim Rinn, Sebastian Tapia, and Riccardo Longo. They have all been the most patient mentors and friends. I also want to thank the older graduate students I worked with: Akshat Puri, Mike Phipps, Virginia Bailey, Aric Tate, and Anabel Romero, for sitting through meetings with me and providing insightful suggestions. I have learned so much from each of them, and I genuinely wish everyone a bright future. A special thanks goes to Anabel for being my mentor upon joining the group, a supportive friend during tough times, and one of the kindest souls I've ever met. I would like to thank the younger graduate and undergraduate students in my group: Apurva Narde, Grace Garmire, Justin Bennett, Mina Savic, Abraham Holtermann, Matthew Hoppesch, Mason Housenga, and Saad Altaf. I am confident that each of them will achieve great things in the near future.

I am grateful to my ATLAS collaborators for their invaluable support and quality assurance for my work. In particular, I thank the heavy ion group conveners and correlation and fluctuation subconveners—Martin Rybar, Aaron Angerami, Qipeng Hu, Tomasz Bold, Soumya Mohapatra, Sasha Milov, and Jiangyong Jia—as well as my editorial board members Petr Balek, Jamie Nagle, Klaudia Burka, and Yeonju Go, for reviewing numerous drafts of my paper and providing crucial feedback. I also appreciate the discussions I had with my ATLAS colleagues Dominik Derendarz, Somadutta Bhatta, and Blair Seidlitz, which greatly enriched my learning experience.

Outside of my research, I would like to pay gratitude to the University of Illinois School of Music. Music has been a companion throughout my graduate school journey, giving me the strength during challenging times. I would especially like to thank the University of Illinois Women's Glee Club and my director, Andrea Solya. Her empowerment of us, both as singers and as women, is a priceless treasure I will cherish forever. To my fellow choir friends—Kiran Bond, Sruthi Singar, Aastha Kathuria, Kirin, Kyriaki, and many others—I love each and evey one of you. I also want to thank my voice teachers, Julia Scannell and Berit Johnson, for their guidance and teaching; I hope to carry this musical journey with me into the future.

To my wonderful graduate school friends—Chunyu Lu, Tracy Wu, Jairo Rojas, Akash Vijay, Albur Hassen, Daniel Caballero, Cheng-Hsin Cheng, Anabel Romero, Athira Vijayakumar, Siddarth Mansingh, Shubhang Goswami, Divij Kohli, and many others—thank you for the fun hangouts and emotional support.

I would also like to acknowledge my undergraduate friends: Zixing Wang, Haoxing Pu, Kaiwen Zheng, Jiacong Xu, Mengyuan Jin, and many others. Though we haven't been able to see each other often, their support has been important to me, and I hope our friendships endure.

A special thanks to my beloved feline companions—Blink, Electron, and Atom. Though they won't be reading this dissertation (but we never know), I want them to know how much they have meant to me during my solitary days. I hope to accompany them for as long as possible.

I am immensely grateful to my partner, Edwin David Valenzuela De Leon, for bringing so much joy to my life and for his infinite love.

Lastly, I want to thank my family for their endless love and support. I remember my grandfather, Huilong Wang, who passed away in 2019; the time we shared will forever be cherished. I also honor my great-grandma, Ailian Tang, who sadly passed away in 2020; her memory will always hold a special place in our family. I pay my most heartfelt gratitude to my grandma (my Wai-po), Huanfeng Huang, and my grandpa (my Wai-gong), Guanwu Li, for their unconditional love and guidance. They have been irreplaceable in my life, and it is their love and support that have allowed me to walk this far. Finally, I thank my parents, Qiuling Wang and Linli Li, for their unwavering support throughout my education and beyond. My family members are the reason I am who I am today, and this dissertation is dedicated to them.

Contents

Chapter 1 Introduction **1**
1.1 Quantum Chromodynamics 1
1.1.1 Asymptotic freedom 3
1.1.2 Color confinement 4
1.2 Quark Gluon Plasma 4
1.2.1 Coordinate system 5
1.2.2 Centrality 6
1.2.3 Initial geometry 7
1.2.4 Azimuthal anisotropies 9
1.2.5 Transport properties of the QGP 10
1.3 Hard probes 15
1.3.1 Jets 15
1.3.2 Jets in vacuum 16
1.3.3 Jets in heavy ion collisions 18
1.3.4 R_{AA} 22
1.3.5 High-p_{T} v_n 24

Chapter 2 The LHC and ATLAS **26**
2.1 The Large Hadron Collider at CERN 26
2.2 The ATLAS detector at the LHC 27
2.2.1 Inner detector 28
2.2.2 Calorimeter system 29
2.2.3 Muon spectrometer 31
2.2.4 Trigger system 32

Chapter 3 Measurements of azimuthal anisotropy **33**
3.1 Event plane and scalar product methods 33
3.1.1 Event plane method 33
3.1.2 Scalar-product method 34
3.1.3 Application of the methods 36
3.2 Multi-particle cumulant method 39
3.2.1 Formalism 39
3.2.2 Important Considerations in v_n measurements 40
3.2.3 Method comparison in v_n measurements 41

Chapter 4 Azimuthal anisotropies of high-p_{T} charged particles in Pb+Pb collisions at 5.02 TeV with the ATLAS detector **45**
4.1 Overview of the thesis analysis 45
4.1.1 Motivations 46
4.2 Data and Monte Carlo simulations 47
4.2.1 Pb+Pb data event selection 47
4.2.2 Centrality determination 48

4.2.3 In-time and out-of-time pileup 48
4.2.4 Monte Carlo samples 50
4.3 Track selection 51
4.3.1 Track weight 52
4.4 Analysis method 60
4.4.1 Scalar-product method 60
4.4.2 Multi-particle cumulant method 61
4.5 Systematical uncertainties 69
4.5.1 Systematical uncertainties of scalar product method 69
4.5.2 Systematical uncertainties of multi-particle cumulant method 79
4.6 Results 84
4.6.1 Scalar product method 84
4.6.2 Multi-particle cumulant method 89

Chapter 5 Summary and conclusions 95

Bibliography 97

Appendix A: Additional pile-up rejections 114
A.1 Introduction 114
A.2 Run-by-run difference 115
A.2.1 Run-dependence versus out-of-time pileup Rejections 115
A.2.2 Run-dependence versus in-time pile-up rejections 117
A.2.3 Run-dependence versus detector non-uniformity flattening 119
A.2.4 Run-dependence versus flow vector recentering 123
A.2.5 Run-dependence versus z_{vtx}-dependent weighting map 124
A.3 Additional centralities 125

Appendix B: Result plots in other centrality intervals 130

Chapter 1

Introduction

1.1 Quantum Chromodynamics

The Standard Model [1] of particle physics is a theory that describe how elementary particles of matter are classified and interact through electromagnetic, weak and strong forces. Shown in Figure 1.1 are the known elementary particles, classified into fermionic quarks, leptons, and force carrying bosons. The development of this theory has been fueled the discovery of large species of particles in experimental particle physics. These observed particles, known as the hadrons, were too numerous to be fundamental. Thus theories were proposed to explain the hadrons with hypothetical constituent particles, the fermionic quarks and the force carriers that bound them together, the bosonic gluons. Quarks and gluons are collectively referred to as *partons*, and they interact via the strong interaction. In order to verify the existence of hadron inner structure, leptons such as electrons were shooted toward hadron target, such as protons, to produce deep inelastic scatterings (DIS), during which the target hadrons absorb enough kinetic energy to be "shattered" and emit new particles. A schematic view of DIS is shown in Figure 1.2 With DIS experiments, the Stanford Linear Accelerator Center (SLAC) in the US was the first to reveal that protons have an inner structure in 1968. The scattering patterns were identified as being caused by point-like particles inside the protons [2–4]. Later, the first evidence of gluons were found in 1976 in the e^+e^- collisions at the PETRA collider at DESY, in which gluon bremsstrahlung produced 3-jet events[1] ($e^+e^- \to q\bar{q}g$) [5–7].

The strong interactions of quarks and gluons are described by laws of Quantum Chromodynamics (QCD), a non-abelian gauge theory with symmetry group SU(3) in the standard model [10–12]. In QCD, three kinds of charges can be carried by the strongly interacting partons, and these three charges are referred to as "color charge", by a loose analog of the three primary colors, red, green and blue. Different from the electric charges in Quantum Electrodynamics (QED), color charge is also carried by the force carrier gluons, allowing for self-interactions of gluons. Shown in Figure 1.3 are the possible vertices in a strong interaction. When strongly interacting quarks are moved away from each other in distance, more and more virtual gluons would

[1] Experimentally, a particular collision will trigger the detectors to record a snapshot of particle production corresponding to this collision, known as an *event*.

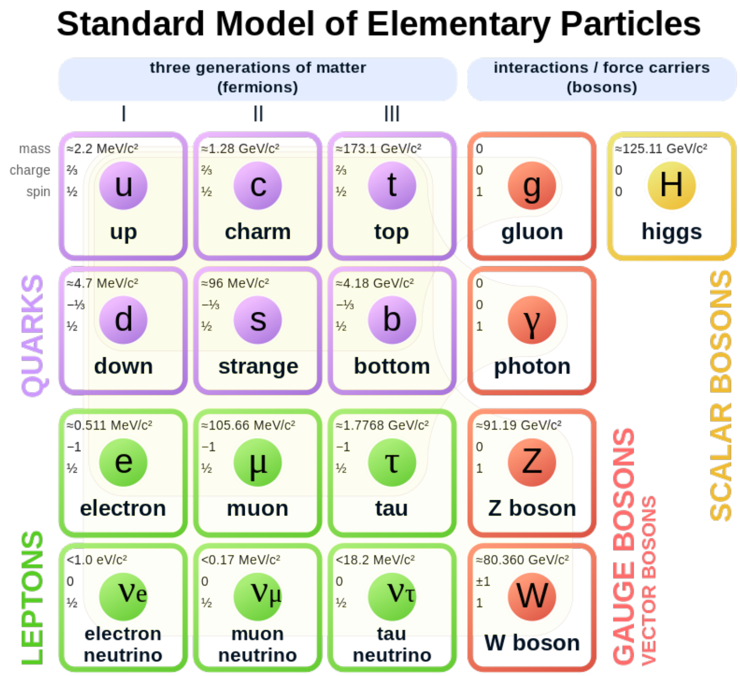

Figure 1.1: The elementary particles of the standard model, taken from Ref. [8]

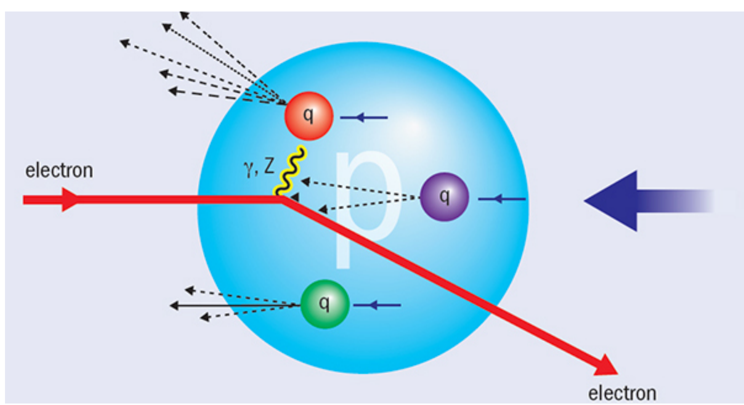

Figure 1.2: Schematic view of deep inelastic scattering of an electron hitting a proton, taken from Ref. [9].

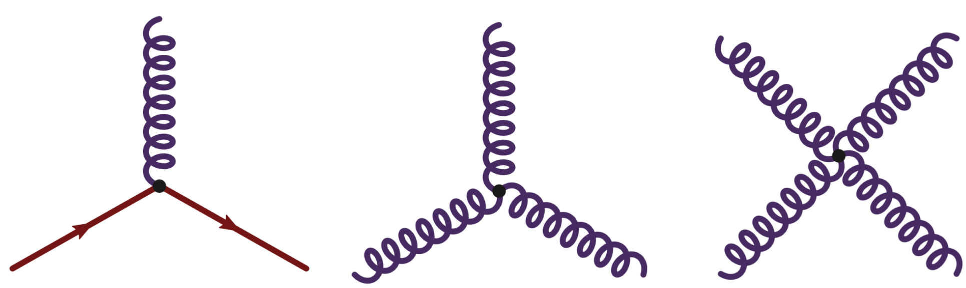

(a) The quark-gluon vertex

(b) The three-gluon vertex

(c) The four-gluon vertex

Figure 1.3: Possible vertices of QCD interactions between quarks and gluons. Figure is taken from Ref. [13].

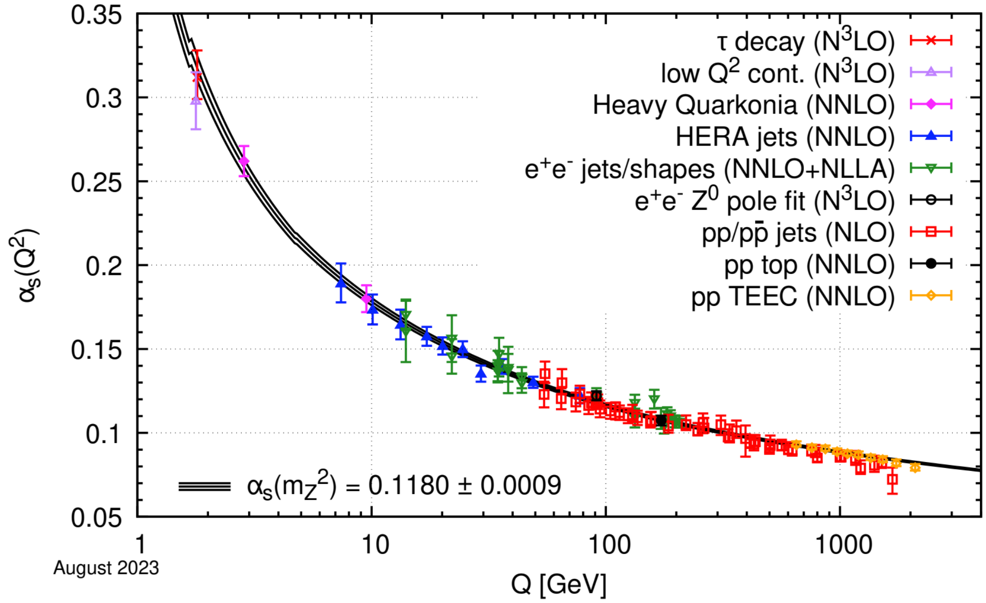

Figure 1.4: The running coupling constant α_s as a function of the momentum transfer Q and experimental measurements. Figure is taken from Ref. [14]

flit in between, increasing the strong force between these quarks, while less gluons are exchanged between quarks when they are closer together, yielding a weaker strong force. This behavior of strong force is opposite to that of QED, giving rise to two properties of QCD: asymptotic freedom and color confinement.

1.1.1 Asymptotic freedom

The DIS experiments at SLAC not only revealed the existence of quarks as point-like constituents of protons, but also that these quarks within the protons transfer momentum and energy like a free particle when the proton was struck by high-momentum electron. This is the QCD phenomena known as "asymptotic freedom" [10–12]. As the strong force between quarks becomes asymptotically weaker at decreasing distance or increasing energy, quarks act almost freely at short distance or large energy scale, for example, within a hadron. At long distance or low energy, the strong force increases. The coupling constant α_s in a QCD scattering process depends on the amount of momentum transferred Q, a feature known as the *running coupling*, as shown in Figure 1.4. QCD processes involving large momentum transfers are referred to as *hard* processes, while those with low Q as *soft* processes. As a result of the changing α_s, different formalism are required to describe hard and soft QCD processes.

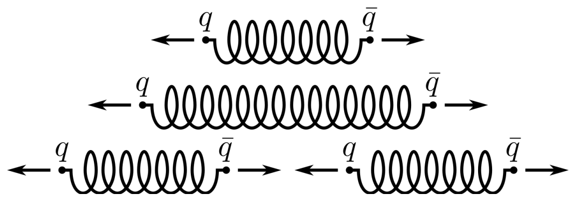

Figure 1.5: Demonstration of a new quark-antiquark pair creation as two quarks are separated from each other, taken from Ref. [16]

1.1.2 Color confinement

The QCD coupling becomes increasingly large at longer distance that at sufficient distance, it is energetically favorable to produce a new quark–antiquark pair instead of maintaining the gluon field between the two original quarks [15] . Therefore under normal conditions, removing a quark from its hadron will creates a new quark-antiquark pair to form hadrons with the remaining quarks and the removed quark. This process is demonstrated in Figure 1.5. This is known as the color confinement, as natural combinations of partons are always maintained in the color neutral bound states of hadrons.

1.2 Quark Gluon Plasma

Under normal conditions, partons in an nucleus are color confined within their hadrons. However, under extreme temperature and particle density the composite states of hardons dissolve into their constituents patrons [17]. This novel state of matter is called the *quark gluon plasma* (QGP) [18]. Figure 1.6 shows a theoretical model of phase diagram for nuclear matters and where the QGP state is located. Studying the QGP is interesting for a number of reasons. Understanding the interactions within the QGP unveils the short-distance mechanism of the strong force between color-charged partons. Furthermore, in the Big Bang theory of universe evolution, the QGP fills the early universe before approximately $10\,\mu$s after the Big Bang [19], and therefore the study of the QGP will facilitate our understanding on how early universe expands, cools and further evolves, especially on how hadronic states of matters form.

The temperature and energy density requirements to form the QGP are met in the ultra-relativistic heavy ion collisions [17] at facilities such as the Relativistic Heavy Ion Collider (RHIC) at Brookehaven National Lab [21–24] and the Large Hadron Collider (LHC) at CERN [25], where evidences of QGP production have been found in the early 2000s.

Figure 1.7 shows a diagram of the space-time evolution of heavy ion collisions [26]. Starting with the nuclear impact, constituent partons those originally move along beam direction scatter off each other and randomize their directions. The initial stage of the collision right after $\tau = 0$ is dominated by hard QCD

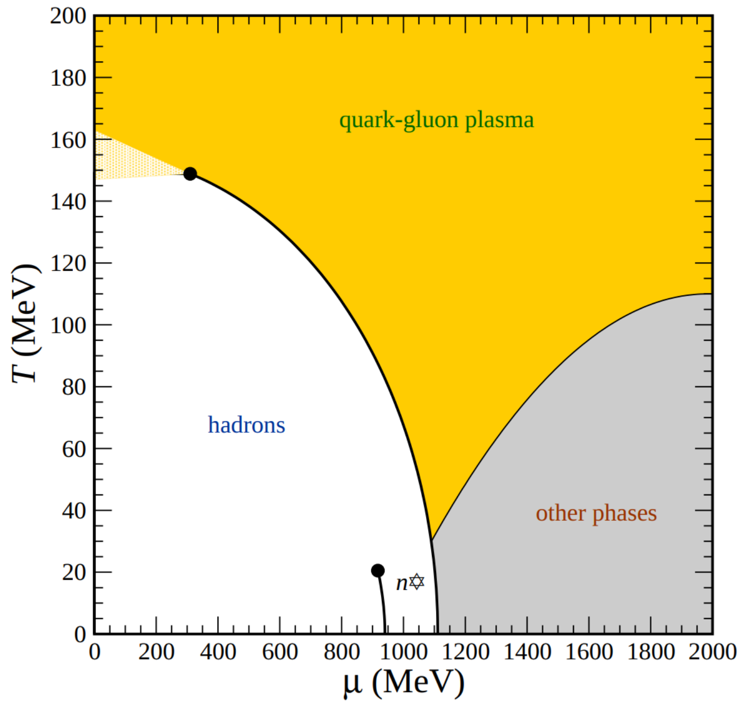

Figure 1.6: The phase diagram of nuclear matter in temperature T and baryon chemical potential μ plane. The n^* indicates the neutron star. Figure is taken from Ref. [20].

processes. With large amount of momentum transferred, these processes are hence the fastest due to the uncertainty principle. Hard processes are rare in comparison to lower energy, soft processes. These scattered partons interact with each other, and eventually thermalize into the QGP within approximately $\sim$1 fm/c [17]. The QGP matter then expands, forming large pressure gradients inside of the matter. As the medium continues to expand and decrease energy density, eventually quarks and gluons begin to hadronize back into bounded states. These hadrons continue to interact with each other, re-scattering and decaying. The final state particles are collected by the particle detectors. The production and evolution of the QGP takes place in an extremely short time-scale and the studying of interactions within the QGP can carried out only through analyzing these final state particles.

1.2.1 Coordinate system

In particle collider experiments, beams travel and collide in circular piles. A right-handed coordinate system is used with its origin at the nominal interaction point (IP) located in the center of the detector, and the z-axis along the beam pipe. The x-axis points from the IP to the center of the accelerator ring, and the y-axis points upward. The transverse direction is defined along the plane transverse to the beam direction, extended by the x-y axes. Quantities measured along direction of this plane are typically denoted subscript T.

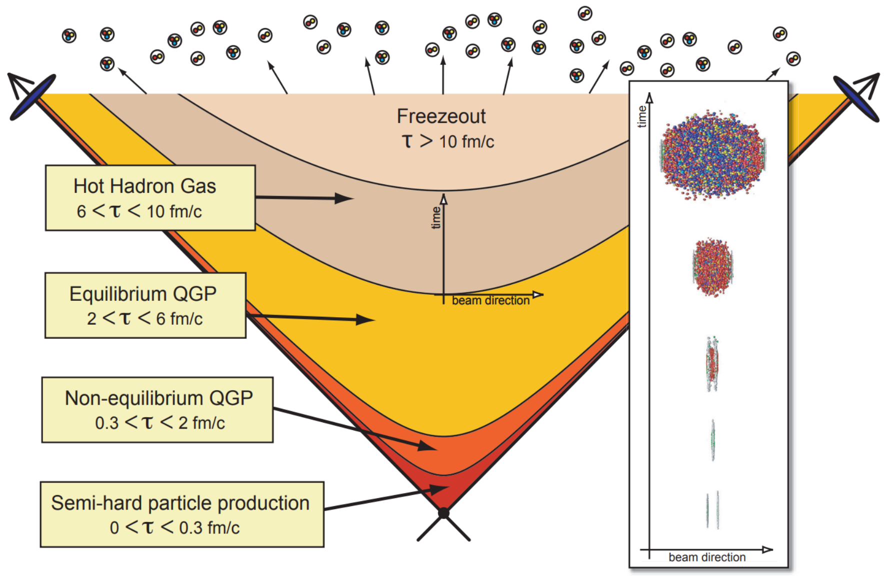

Figure 1.7: (left) Space-time diagram for a heavy ion collision. The color indicates the temperature of the QGP formation. Figure is taken from Ref. [26].

Cylindrical coordinates (r, ϕ) are used in the transverse plane, ϕ being the azimuthal angle around the z-axis. The rapidity is defined as $y = \frac{1}{2}\ln[(E + p_z)/(E - p_z)]$ where E and p_z are the energy and z-component of the momentum along the beam direction respectively. The pseudorapidity is defined in terms of the polar angle θ as $\eta = -\ln\tan(\theta/2)$, and is an approximation of rapidity when particle mass becomes negligible in relativisitic speed. Transverse momentum and transverse energy are defined as $p_{\mathrm{T}} = p\sin\theta$ and $E_{\mathrm{T}} = E\sin\theta$, respectively. The angular distance between two objects with relative differences $\Delta\eta$ in pseudorapidity and $\Delta\phi$ in azimuth is given by $\sqrt{(\Delta\eta)^2 + (\Delta\phi)^2}$.

1.2.2 Centrality

Before the nuclear impact, two nuclei are Lorentz contracted along the beam direction and moving toward each other in the lab frame. The impact parameter, b, of the nuclear impact measures the distance between centers of the colliding nuclei at the point of closest approach. A more central collision expects more nucleon interactions and a larger amount of QGP produced. The overlap, thus geometry of the QGP produced also depends on centrality of a collision.

However, the impact parameter cannot be experimentally measured, and heavy ion collisions are categorized based observables correlated with the impact parameter, such as total transverse energy, charged particle multiplicity, and number of neutrons that did not participate in the collision. These quantities can be related to collision geometry through nuclei collision simulations such as Glauber model simulations [27]. In this simulation, the colliding nuclei are modeled with a nucleon density profile given by a Fermi-Dirac Distribution. An important parameter for this simulation is the nuclear thickness function T_{AB}, which describes the effective overlap area of the incoming nuclei where nucleons can interact, and can be calculated as,

$$T_{AB}(\mathbf{b}) = \int T_A(\mathbf{s}) T_B(\mathbf{s} - \mathbf{b}) d^2 s. \tag{1.1}$$

For each collision, the number of participants, defined as nucleons that participate in at least one inelastic

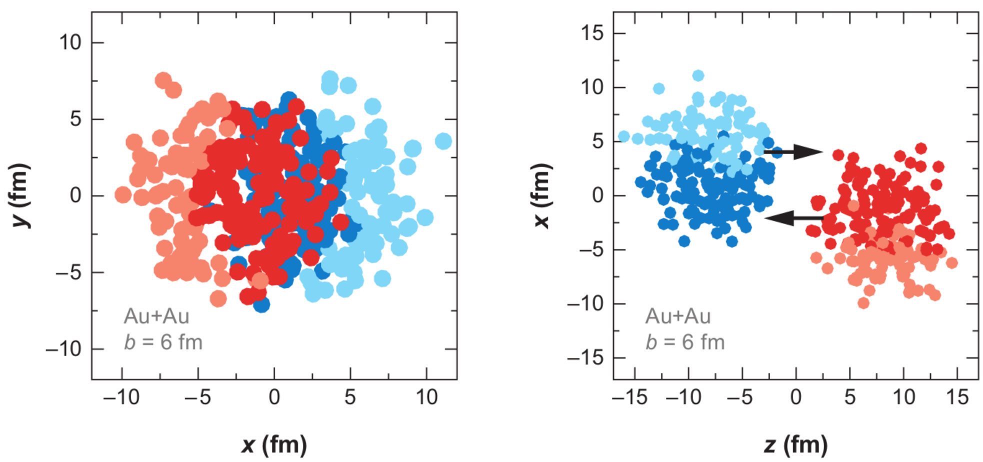

Figure 1.8: A Glauber Monte Carlo event for Au + Au at $\sqrt{s_{\mathrm{NN}}} = 200$ GeV with impact parameter of 6 fm/c, seen from (left) transverse plane and (right) along the beam axis. Darker colored circles represent the participant nucleons while lighter colors spectators. Figure is taken from Ref. [27].

nucleon-nucleon collision, and the number of spectators, defined as nucleons that pass through the collisions unaffected, are counted. The number of participants, N_{part}, helps categorizing the collisions into *central* collisions, in which the two nuclei collide "head-on", or *peripheral*, when the two nuclei almost "pass-by" each other. Figure 1.8 shows a Glauber model simulated Monte Carlo event with nucleon positions shown, in transverse plane and along the beam axis.

Centralities are frequently expressed in percentiles, as shown in the example of Figure 1.9, in which the categorization is based on the total transverse energy measured in each collision. The centrality percentiles start from the most "head-on" collisions. For example, the 0-10% most central collisions are events with the top 10% highest amount of transverse energies measured.

1.2.3 Initial geometry

Figure 1.10 shows a demonstration of the collision geometry in the transverse plane. The initial geometry of the overlapped nuclear matters can be described by a series of harmonic eccentricity coefficients ϵ_n and

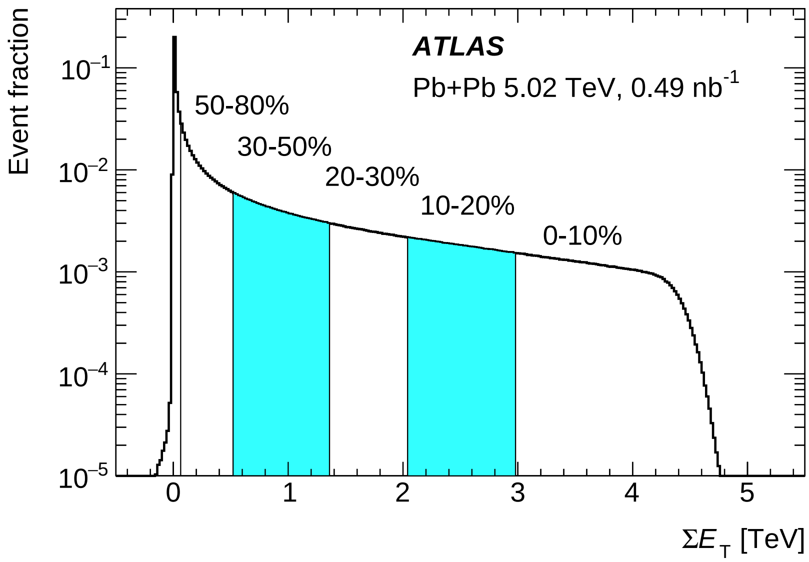

Figure 1.9: The event distribution as a function of the total transverse energy and corresponding centrality percentiles. Figure is taken from Ref. [28].

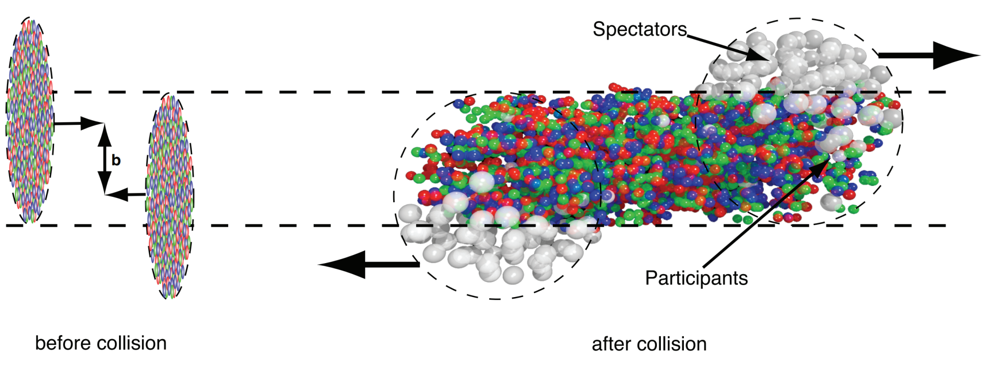

Figure 1.10: Carton of a a heavy ion collision for before and after the collision. Figure is taken from Ref. [29].

associated angles Φ_n in the transverse plane:

$$\epsilon_n e^{in\Phi_n} \equiv -\frac{\int dr\, d\phi\, r^n e^{in\phi} e(r,\phi)}{\int dr\, d\phi\, r^n e(r,\phi)} (n > 1), \tag{1.2}$$

where $e(r, \phi)$ is the initial energy density distribution in the transverse plane, and is bigger where the volume is smaller. Different orders of eccentricities ϵ_n and the associated angle Φ_n are shown in Figure 1.11.

The expected initial geometry of two overlapping heavy ions is, for the most part, elliptical, which gives a non-zero ϵ_2. A key insight in understanding the source of higher-order eccentricities, ϵ_n where $n > 2$, is the role of fluctuations [30]. It can be shown by Monte Carlo simulation that, the participant nucleons are not always within the elliptical overlap of the two colliding nuclei. Instead, their positions fluctuate for each collision. Figure 1.12 shows a simulation of nucleon positions in a heavy ion collision, and the nucleons in the two nuclei are shown in gray and black, respectively. Participant nucleons are indicated as solid circles, while spectators are dotted. This particular collision has created an approximately triangular geometry, giving a non-zero ϵ_3. These fluctuations from collision to collision are referred to as event-by-event fluctuations.

1.2.4 Azimuthal anisotropies

Figure 1.13 shows a demonstration of the QGP expansion. Due to the initial geometry of the QGP, the pressure gradient created during the QGP expansion is expected to be anisotropic. For an approximately elliptical geometry, the minor axis, defined by Φ_2, is shorter and thus more dense in comparison to the major axis. Similarly for higher-order ϵ_n, higher pressure gradients form along the shorter axes of the n-th order eccentricity. These pressure gradients are then converted into momentum anisotropies of the final-state particle productions, causing the particle production preferential in the direction along Φ_n. The angular modulation of final-state particles along azimuthal direction can be characterized by a Fourier decomposition [31],

$$\frac{dN}{d\phi} = \frac{N}{2\pi}\left(1 + 2\sum_{n=1}^{\infty} v_n \cos(n(\phi - \Psi_n))\right), \tag{1.3}$$

where $dN/d\phi$ is the number of particles detected at azimuthal angle ϕ, v_n is the n^{th} order Fourier coefficient and Ψ_n is the so-called n^{th} order event plane angle, which measures orientation of the n^{th} order symmetry in the final state particles. The event plane angle Ψ_n is an experimental estimation of the eccentricity axis Φ_n, and the former are sensitive to additional fluctuations in the expansion process as well as detector defects.

Different features of the initial geometry give rise to different orders of v_n. Magnitudes of v_1 describe the global side-ward shift of all particles. On average, the expected geometry of the nuclei overlap is elliptical, and this gives rise to a significant v_2. Non-zero v_n where $n > 2$ arise from the fluctuations in initial geometry which gives higher-order eccentricities in the QGP.

1.2.5 Transport properties of the QGP

The discovery of significant v_2 [21–24] serve as important evidence that the QGP is a strongly interacting medium which transferred features of the initial geometry to final-state particles. The bulk properties of the QGP can be well described as a relativistic fluid undergoing collective, hydrodynamic flow [32]. Therefore, the measurements of v_n in the soft sector are referred to as *flow harmonics* [29, 33], and this evolution can be well described by hydrodynamic models [31].

In 2001, for the first time, experimental data from the Au+Au collisions at RHIC agreed with predictions using ideal fluid hydrodynamics [34]. However this ideal fluid model diverges from data at larger impact parameters. It was later proposed that the transition to later hadronic stage needs a microscopic modeling, and a small but non-zero viscosity is required for the QGP, motivating for a series of "hybrid models" those combines pre-QGP, post-QGP treatments with viscous hydrodynamics [35].

Important transport properties of the QGP, such as the specific shear and bulk viscosities which are defined as the ratios of shear and bulk viscosities to entropy dentity and denoted by η/s and ζ/s, respectively, can be extracted by matching model calculations with measurements of flow harmonics. In an ideal fluid, η/s and ζ/s are both zero. Recent predictions of v_n with viscous hydrodynamics has been successful in the soft sector [36–39], using a η/s near the theoretical lower bound of $1/4\pi$ [40, 41], making the QGP an nearly ideal fluid with one of the smallest η/s found in nature. The importance of specific bulk viscosity ζ/s and its interplay with η/s in collective expansion was also studied [42–45] and incorporated into current hydrodynamic models. While η/s reduces collectivity in the expansion and attenuates the flow harmonics, ζ/s can decrease this attenuation by η/s and enhance the flow harmonics [37]. Figure 1.14 shows the viscous hydrodynamics model calculations utilized a fixed set of parameters determined in the $\sqrt{s_{\mathrm{NN}}} = 200$ GeV Au+Au collisions, and achieved overall good agreement with both RHIC and LHC measurements of v_n[2].

However, significant uncertainties remain in these estimations of parameters for the following reasons. Hydrodynamic models require an initial condition profile for the QGP, and depending on the choice of this profile, different transport properties will be estimated. Furthermore, by using this model-by-model testing and fitting, constraints from one set of experimental observables might contradict with another set of experimental inputs. Figure 1.15 shows the predictions of event multiplicity, mean p_{T}, denoted as $\langle p_{\mathrm{T}} \rangle$, for identified particles, and v_n compared with experimental measurements. Values of $\langle p_{\mathrm{T}} \rangle$ is very sensitive to the bulk viscosity and provides important constraints on the extraction of the latter [39, 46]. It can be

[2]The specific measurements of v_n shown, denoted the notion $v_n\{2\}$, is known as a two-particle cumulant v_n. Details of different methods for measuring v_n is discussed in Section 3.2.

observed that very different values of shear and bulk viscosities are needed to give good predictions for $\langle p_{\mathrm{T}} \rangle$ versus for v_n. Therefore, in recent years, the more flexible phenomenological model T$_\mathrm{R}$ENTo [47–53] allows for simultaneous estimation of both initial condition parameters and the QGP transport properties, as well as fitting over a variety of experimental variable, which significantly reduced the uncertainties on the bulk property estimations. Figure 1.16 shows a model calculation using the best-fit parameters from the Bayesian analysis in comparison to the experimental measurements [52].

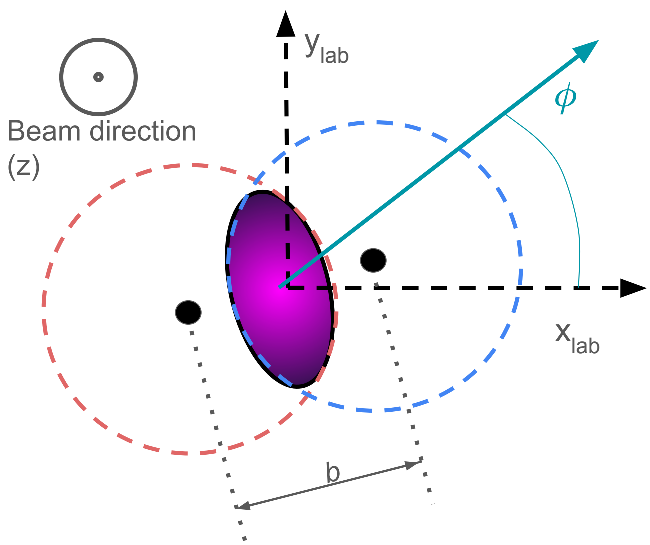

(a)

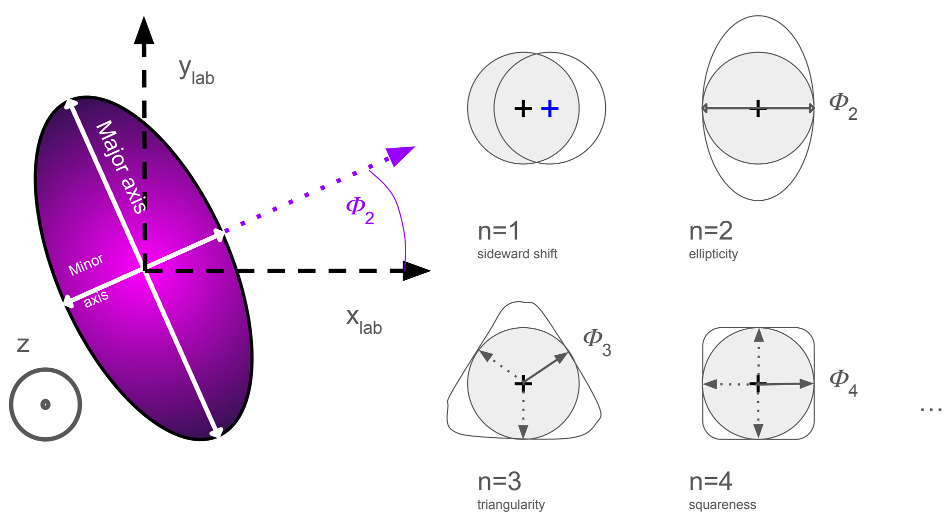

(b)

Figure 1.11: (a) Initial geometry of heavy ion collisions, with impact parameter and direction of azimuthal angle labeled, measured in lab frame as measured in the transverse plane for a heavy ion collision. (b) Initial geometry of the heavy ion collisions, with different orders of eccentricity ϵ_n and associated angle Φ_n.

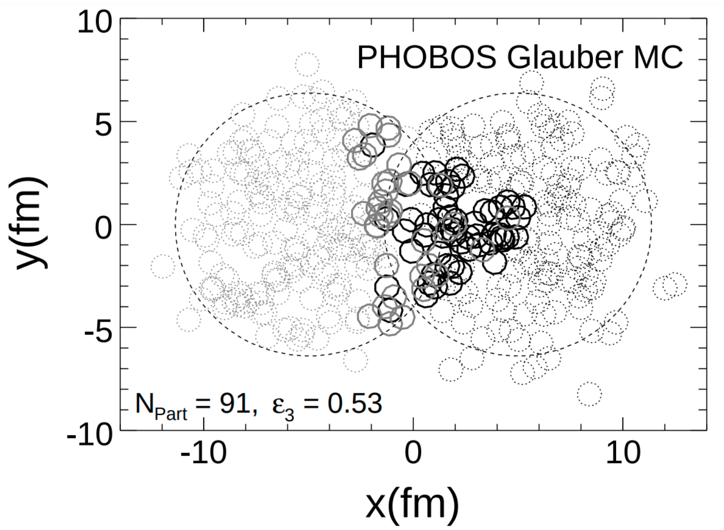

Figure 1.12: (left) Simulated nucleon positions and triangular geometry from a particular collision. Figure is taken from Ref. [30].

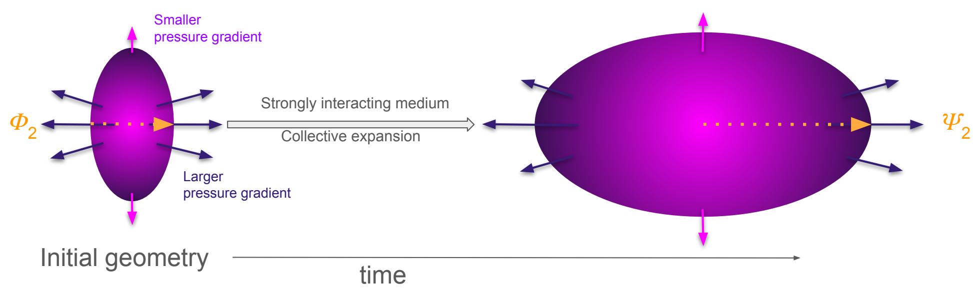

Figure 1.13: Cartoon of the initial geometry of the nuclei overlap (left) and expanded QGP (right).

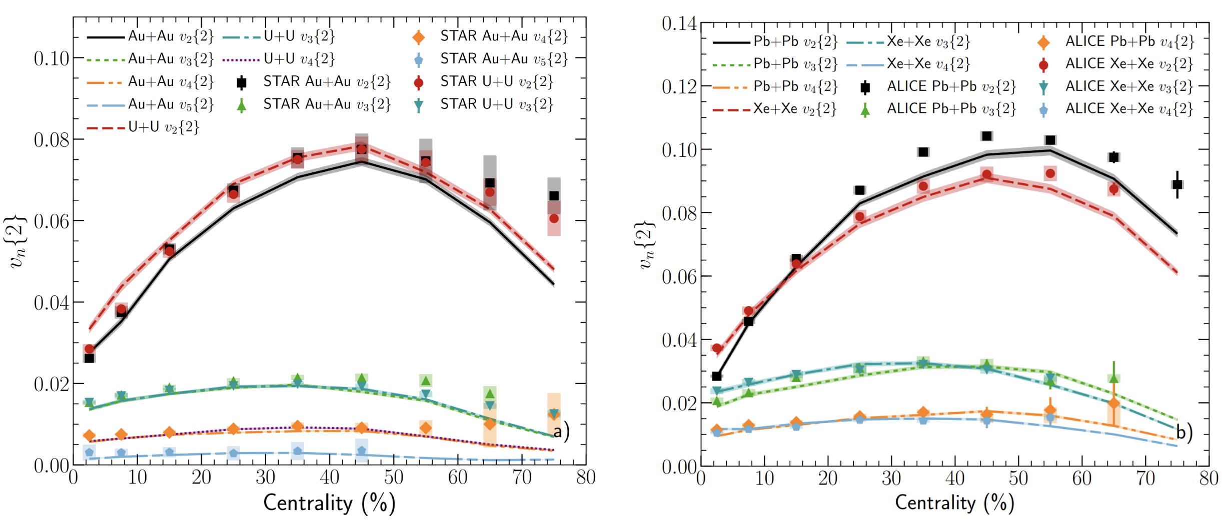

(a) (b)

Figure 1.14: Comparison of predictions of low-p_T v_n with viscous hydrodynamics models and measurements from (a) RHIC and (b) LHC. Figure is taken from Ref. [39].

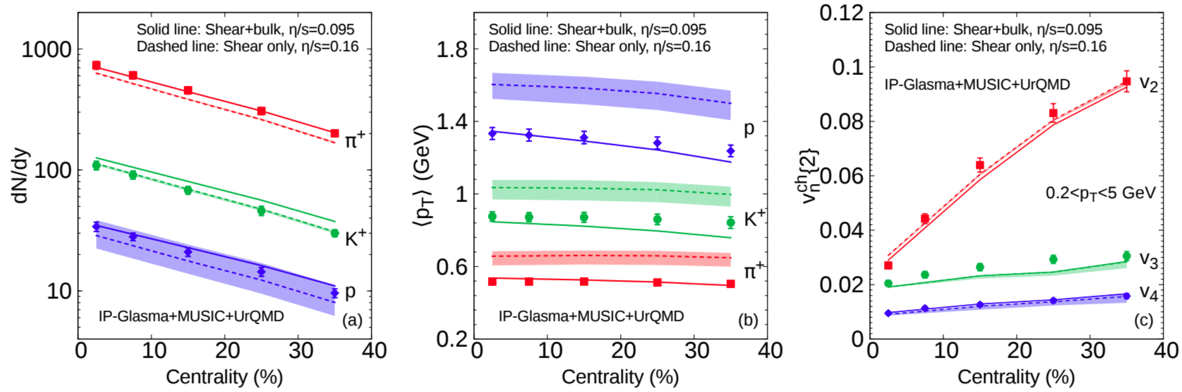

Figure 1.15: Predictions for (a) event multiplicity, (b) average p_{T} for identified particles, and (c) inclusive v_n compared with data. Solid and dashed lines are predictions made using different specific shear viscosity values as shown in legend, and points are from measurements by the ALICE collaboration [54, 55]. Figure is taken from Ref. [46].

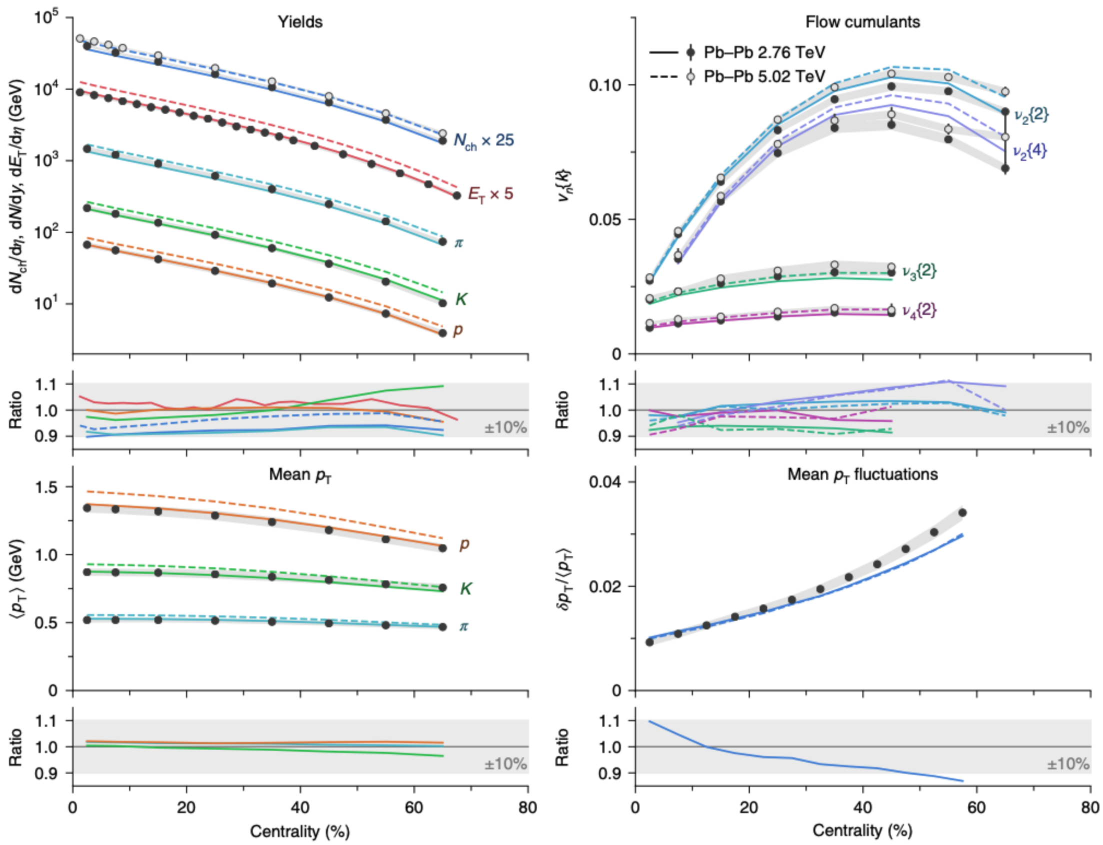

Figure 1.16: Model calculations for multiplicity, v_n, $\langle p_{\mathrm{T}}\rangle$ and $\delta_{\langle p_{\mathrm{T}}\rangle}$ fluctuations based on best-fit parameters from Bayesian analysis. Figure is taken from Ref. [52].

1.3 Hard probes

The momentum of final-state particles measured in the transverse plane, denoted as p_{T}, is dependent on the momentum transfer Q during the initial QCD processes, and categorize the measured particles into soft and hard probes, corresponding to the soft and hard QCD processes, respectively. The *soft* probes represent the majority of measured particles, and come directly from hadronization of the QGP matter. The measurements of soft probes focus on the description of QGP bulk properties, like explained in Section 1.2, using observables such as flow harmonics v_n. On the other hand, the *hard* probes are higher-p_{T} particles generated by the hard processes that precede the formation of the QGP. These highly energetic partons experience the full evolution of the QGP while traversing through and interacting with the latter, before hadronizing into final state hadrons. Therefore, the short-distance interactions within the QGP can be probed by studying the modifications on these high-p_{T} products. A schematic view of soft-hard interactions with the heavy ion collision stages is shown in Figure 1.17.

1.3.1 Jets

In the much rarer hard scattering during nucleon-nucleon collision, pairs of back-to-back travelling partons with large transverse momentum (p_T) are produced. As a result of the running coupling in strong interaction, increasing amount of energy is needed to dissociate partons as they move away from the interaction vertex, until it becomes more favorable to produce new partons (quark-antiquark pair). Therefore, the highly energetic partons from hard scatterings continue to create new partons, which eventually hadronize and form highly collimated cones of particles known as *jets* [56]. A *dijet* is formed when a pair of outward partons are produced from a hard scattering. Figure 1.18 shows an event display of an approximately back-to-back dijet

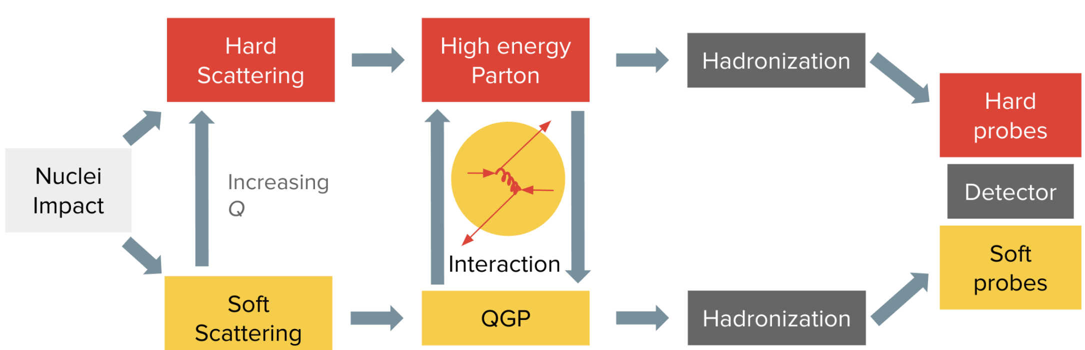

Figure 1.17: Schematic view of soft-hard interactions during different stages of the heavy ion collisions.

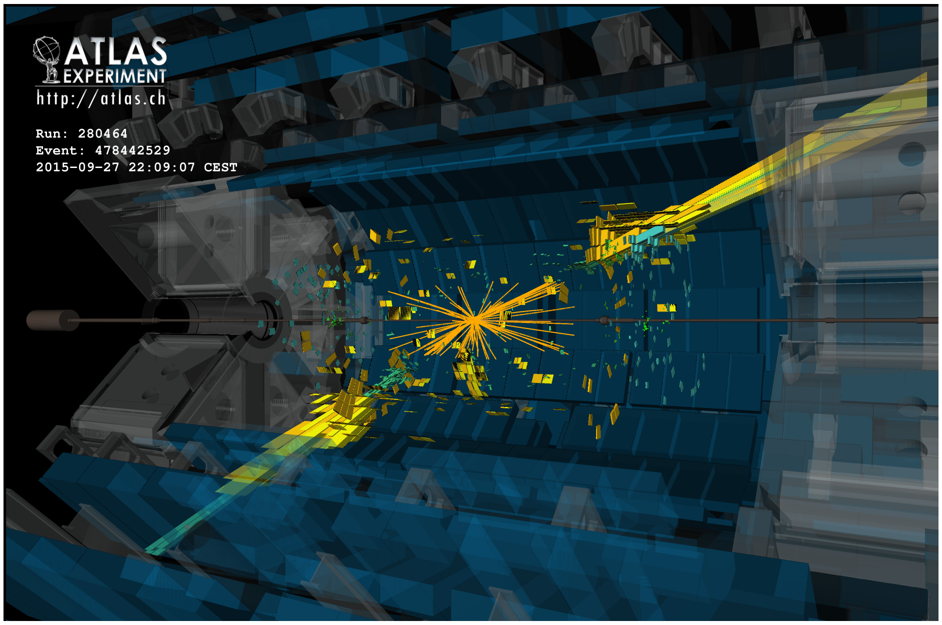

Figure 1.18: A display of the highest-mass dijet event measured in ATLAS in a pp collision at $\sqrt{s_{\mathrm{NN}}}$=13 TeV from 2015. Orange lines indicate reconstructed particle trajectories while the colored blocks show energy deposits in the ATLAS calorimeters. Figure is taken from Ref. [57].

measured in the ATLAS detector.

In experiments, jets are reconstructed with jet algorithms, which cluster measured objects based on their spatial proximity and momentum. The anti-k_t algorithm [58] is currently the most widely used jet algorithm, which sequentially cluster the objects and start from higher-p_{T} objects. Figure 1.19 shows the clustered jets using anti-k_t algorithm. Kinematics of a jet in experiment is measured by summing over particles within the constructed jet cone.

1.3.2 Jets in vacuum

In absence of a medium effect, for example, in pp collisions, the production of high-p_{T} hadrons from hard scattering is well described in the formalism of perturbative QCD (pQCD). From the initial hadronic collision to parton scattering and jet production, these processes can be factorized into the parton distribution

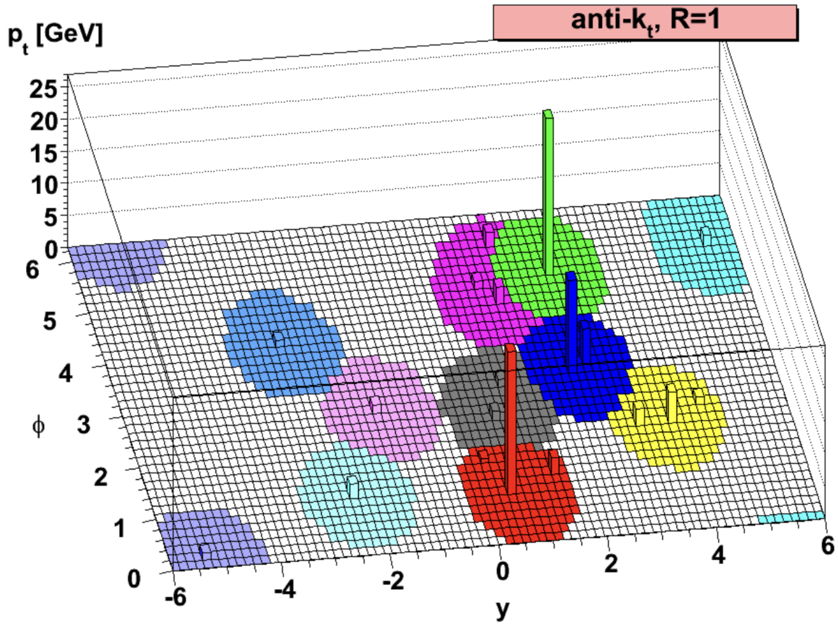

Figure 1.19: Jet cones clustered using anti-k_t algorithm. This simulation samples parton-level events (generated with Herwig [59]), together with many random simulated soft particle production. Figure is taken from Ref. [58].

functions (PDFs), scattering cross sections, and final state fragmentation functions (FFs) as follow [60]:

$$
\begin{aligned}
d\sigma_{pp\to hX} \approx \sum_{abjd} \int dx_a \int dx_b \int dz_j f_{a/p}(x_a, \mu_f) \\
\otimes f_{b/p}(x_b, \mu_f) \\
\otimes d\sigma_{ab\to jd}(\mu_f, \mu_F, \mu_R) \\
\otimes D_{j\to h}(z_j, \mu_F),
\end{aligned}
\tag{1.4}
$$

where x_a and x_b are the initial momentum fractions of momentum carried by interacting partons in their respective incoming protons. Similarly, z_j is the momentum fraction carried by the final state hadron with respect to the total jet momentum. The PDFs of the interacting partons are given by $f_{a/p}(x_a, \mu_f)$ and $f_{b/p}(x_b, \mu_f)$, where μ_f is the factorization scale. The cross section for the parton scattering is given by $d\sigma_{ab\to jd}(\mu_f, \mu_F, \mu_R)$, where μ_F is the fragmentation scale and μ_R is the renormalization scale. The scales are usually given by the scale of the hadron p_{T} or the momentum transfer Q. Finally, $D_{j\to h}(z_j, \mu_F)$ is the fragmentation function (FF) from parton j to hadron h, which describes the probability of a hadron h with given kinematics fragments from the jet. The partonic hard scattering cross section can be calculated perturbatively, while PDFs and FFs are obtained experimentally, and shown to be universal across $e^{\pm}$

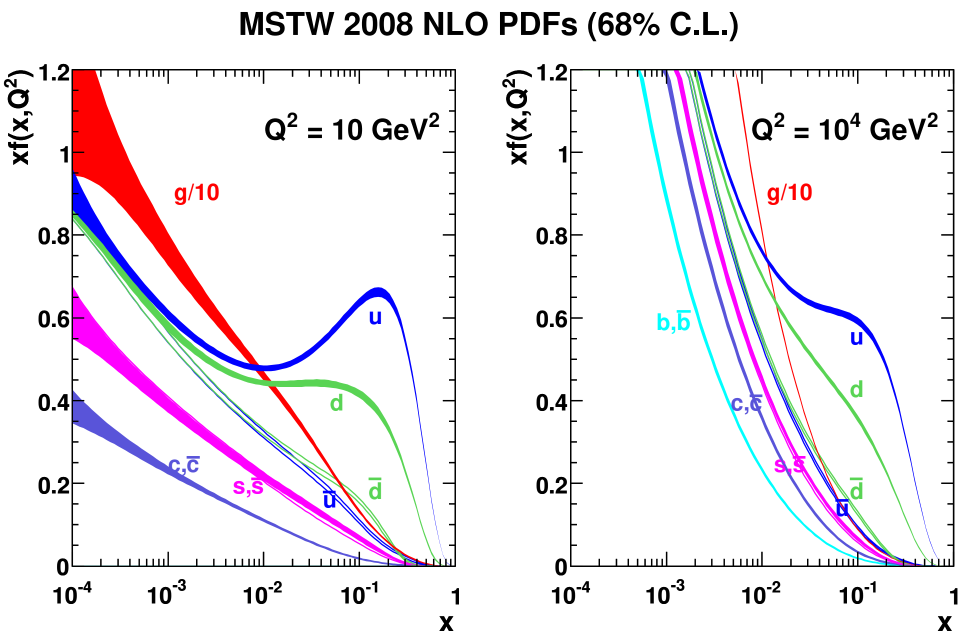

Figure 1.20: The next to leading order (NLO) PDFs of nucleons at (left) $Q^2 = 10\text{GeV}^2$ and (right) $Q^2 = 10^4\text{GeV}^2$. The band shows range of 1σ uncertainty. Figure is taken from Ref. [61].

collisions, deep inelastic scattering, and pp collisions. Figure 1.20 shows the next to leading order PDFs at different momentum transfer (Q^2) determined from DIS experiments, and Figure 1.21 shows a list of of FFs at different collision energies from e^+e^- collisions.

Jet production in pp collisions at the LHC is well predicted by the pQCD calculations. The jet cross-sections at collision center of mass energy $\sqrt{s} = 2.76$, 7, 8 and 13 TeV have been measured [62–65]. Figure 1.22 are the measured jet cross sections compared to NLO calculations from ATLAS [62] and CMS [65] at $\sqrt{s} = 13$ TeV, where measured jet production agrees with theory within uncertainty. Similarly, a comparison of hadron spectra with Monte Carlo simulations is shown in Figure 1.23.

1.3.3 Jets in heavy ion collisions

In heavy ion collisions, jet production and fragmentation differs from those in pp from both different initial state conditions, known as cold nuclear effects, and interactions with the QGP, known as hot nuclear effects.

A free nucleon can differ in structure from those bounded in a nuclei, and a bounded nucleon within a nuclei also experience additional interactions before the hard scattering [69, 70]. Cold nuclear effects can be experimentally measured in p+Pb collisions, where the QGP effects are expected to be small. LHC measurements in such systems have estimated the cold nuclear effects to be small [71–73].

Hot nuclear effects come from the strong interactions of hard scattered partons with constituents of the

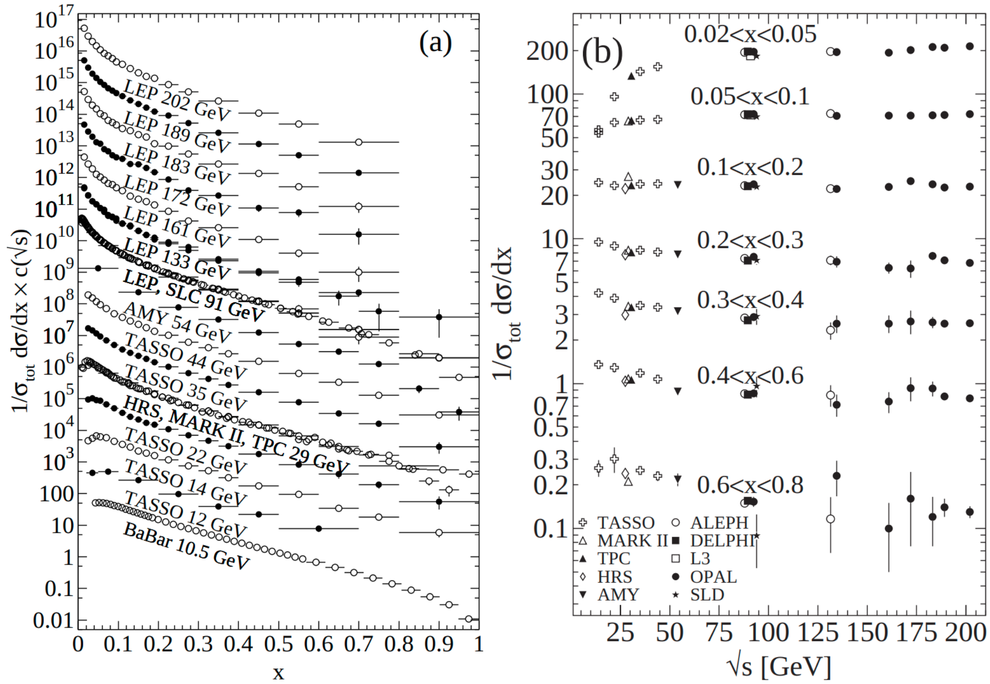

Figure 1.21: Cross section for $e^{\pm}$ collisions for all charged hadrons (a) for different collision energies $\sqrt{s}$ as a function of the fraction x and (b) for various ranges of x as a function of $\sqrt{s}$. Figure is taken from Ref. [14].

QGP. Such interactions cause energy loss in the scattered partons, while the QGP is also modified from this energy dump. This phenomenon is known as *jet quenching* [60]. The hard scattered parton loses energy to the QGP from elastic and inelastic collisions with the constituent partons of the QGP. The energy loss from $2 \rightarrow 2$ elastic collisions is referred to as collisional energy loss. Additional gluon radiations may be induced from multiple scatterings with the constituent partons, and this energy loss from the initial parton is known as radiative energy loss [74]. These two processes are shown in Figure 1.24.

The hard-soft interaction affects both the production and fragmentation of jets [75–77]. Therefore, the hadron production cross section for a heavy ion collision can be described by a modified version of Equation 1.4

$$
\begin{aligned}
d\sigma_{AB\rightarrow hX} \approx \sum_{abjj'd} \int dx_a \int dx_b \int dz_j f'_{a/A}(x_a, \mu_f) \otimes f'_{b/B}(x_b, \mu_f) \otimes d\sigma_{ab\rightarrow jd}(\mu_f, \mu_F, \mu_R) \\
\otimes P_{j\rightarrow j'} \otimes D_{j'\rightarrow h}(z'_j, \mu_F)
\end{aligned}
\tag{1.5}
$$

where the PDFs are now for modified to describe nuclei and an additional interaction term $P_{j\rightarrow j'}$ is included to account for the parton energy loss.

QGP modified hard-scattered parton products serve as "microscopes" for characterizing the QGP from a tomographical point of view [78]. By comparing jets in heavy ion collisions with jets in vacuum, we can understand how jets are modified by the QGP, and therefore gain insights on the collisional and radiative

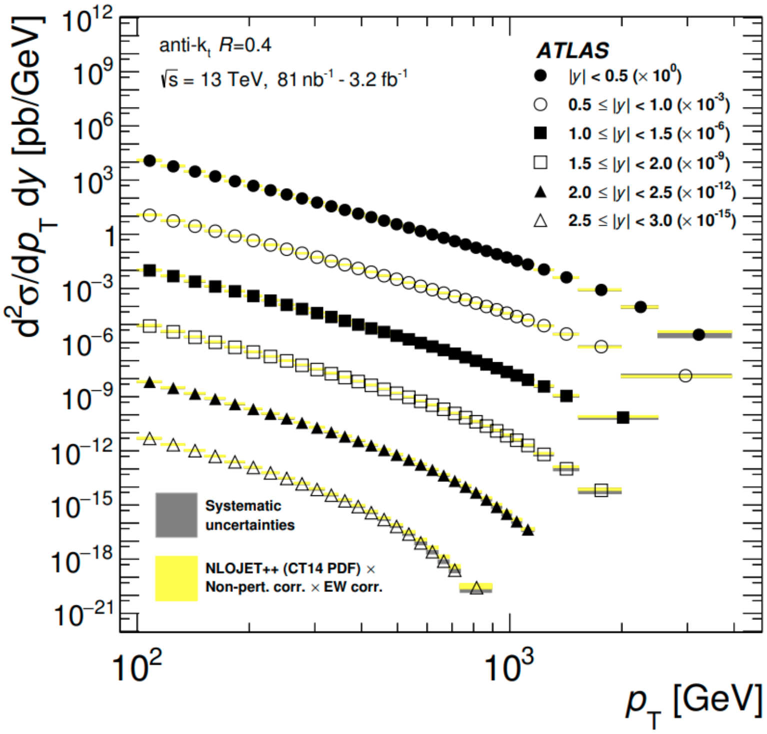

(a)

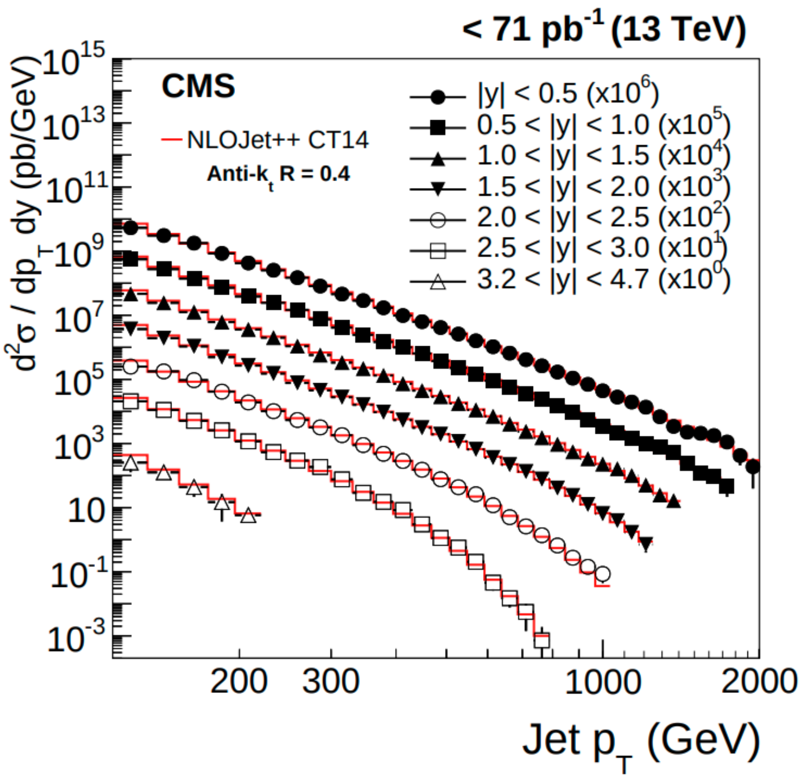

(b)

Figure 1.22: (a) Comparison of NLO pQCD model calculation NLOJET++ [66] to jet production measurements with different rapidity $|y|$ range by ATLAS [64] and CMS [65].

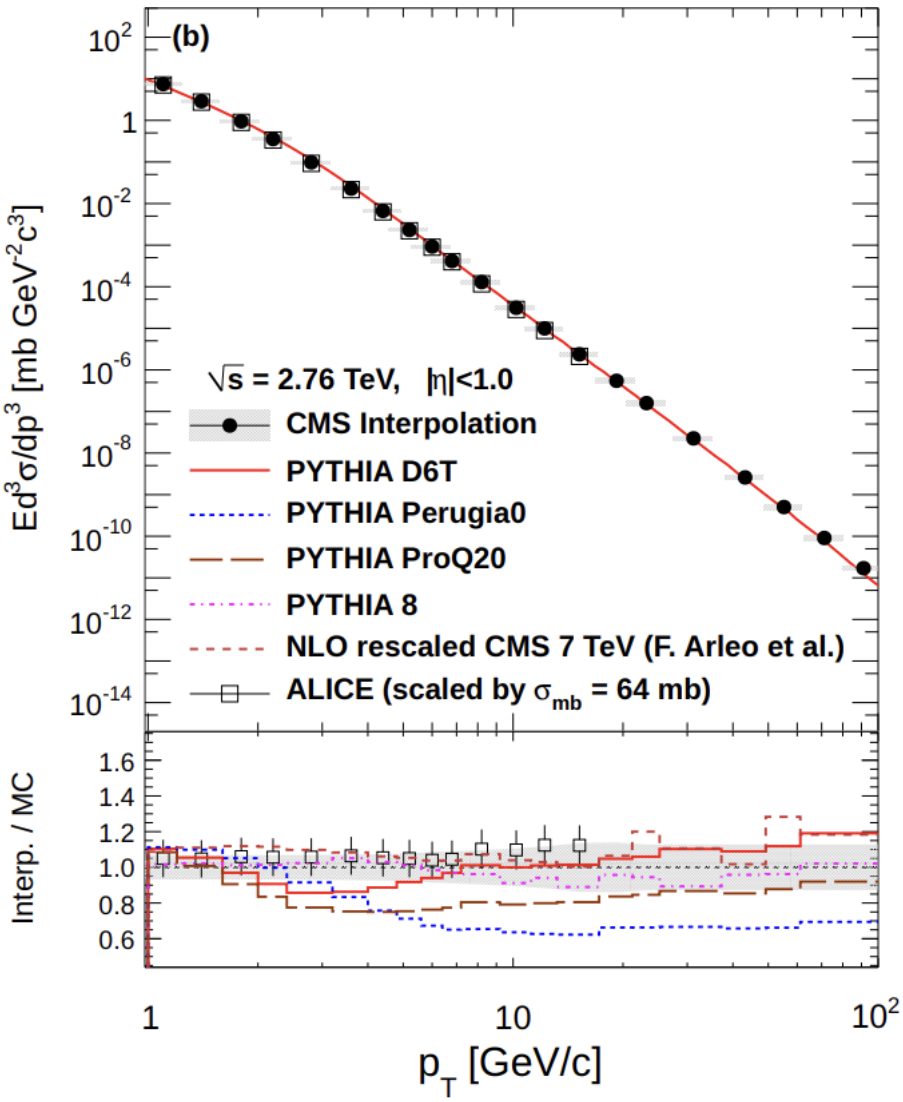

Figure 1.23: Comparison of Monte Carlo simulations to charged hadron spectra measurements by CMS [67] and ALICE [68].

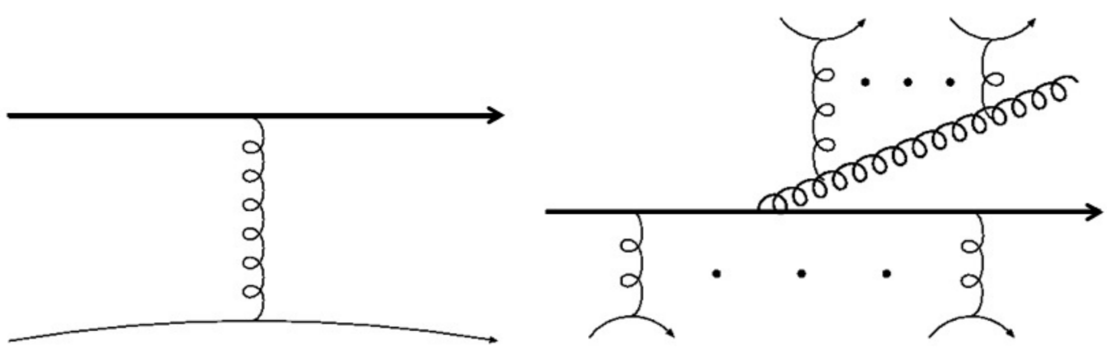

Figure 1.24: Diagrams for (left) collisional and (right) radiative energy losses of a hard scattered parton traversing through the QGP. Figure is taken from Ref. [74].

energy loss processes within the QGP. Therefore, jets serve as an excellent probe for the short-distance strong interactions within the QGP. The parton energy loss affects not only the yields but also fragmentation of jets, which will show up in high-p_{T} charged hadron production. Measurements on jets and high-p_{T} charged hadrons production complement each other in giving a full picture for the parton energy loss and the jet fragmentation [79]. In the following subsection we will give two examples of experimental measurements, $R_{\mathrm{A}A}$ and high-p_{T} v_n, that are sensitive to the parton energy loss.

1.3.4 $R_{\mathrm{A}A}$

The nuclear modification factor $R_{\mathrm{A}A}$ is defined as the ratio of the cross section in a collision in comparison to pp collisions after proper scaling by the expected number of nucleon-nucleon collisions, defined as,

$$R_{\mathrm{AA}} = \frac{\frac{1}{N_{\mathrm{evt}}} \frac{d^2 N_{\mathrm{jet/h^{\pm}}}}{dp_T dy}\big|_{\mathrm{cent}}}{\langle T_{\mathrm{AA}} \rangle \frac{d^2 \sigma_{\mathrm{jet/h^{\pm}}}}{dp_T dy}\big|_{\mathrm{pp}}}, \tag{1.6}$$

where the jet or charged hadron yields are obtained as a function of its respective transverse momentum p_{T} and rapidity y. Total yields are averaged over the number of events N_{evt}. The scaling between proton and nuclei is done by using $\langle T_{\mathrm{AA}} \rangle$, defined as is the average number of nucleon-nucleon collisions divided by the total inelastic nucleon-nucleon cross section, which is obtained using Monte Carlo simulation with the Glauber Model [27].

Figure 1.25 shows the jet $R_{\mathrm{A}A}$ [77] and charged hadron $R_{\mathrm{A}A}$ [79] as a function of its respective transverse momentum for various collision centralities measured by the ATLAS experiment. R_{AA} shown is smaller than 1, indicating jet production is "quenched" in heavy-ion collisions in comparison to *pp*. A clear dependence on the centrality is observed in both measurements, where more central collisions experience greater extent of production suppression, suggesting a correlation between the parton energy loss and the amount of QGP produced. Additionally, the energy loss and jet quenching decreases, shown by the increased $R_{\mathrm{A}A}$, with the transverse momentum. Similar measurements have also been done by other detectors at the LHC, and these measurements are overall in good agreement with each other [65, 80–82].

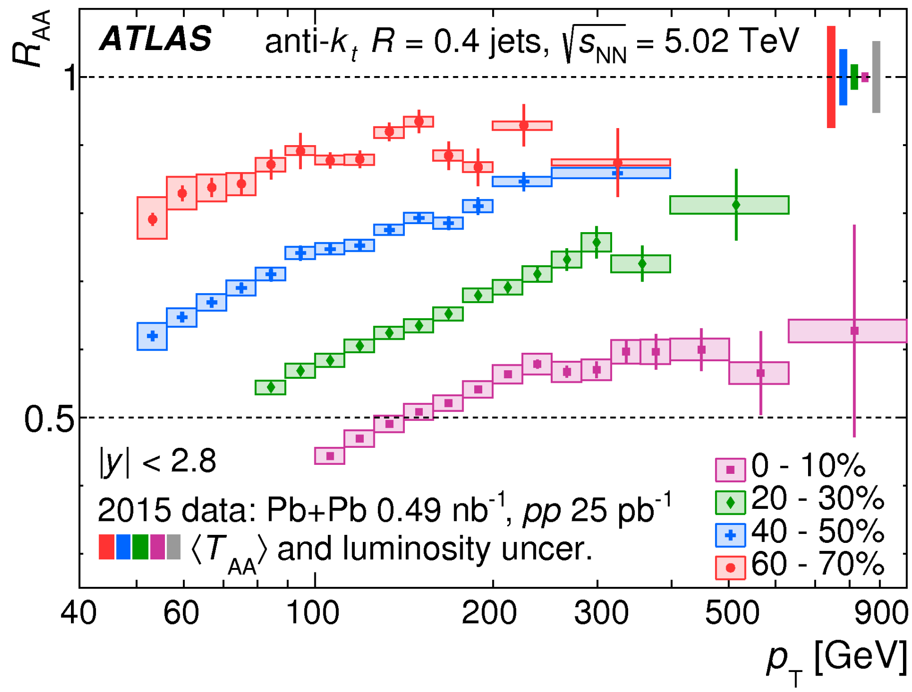

(a)

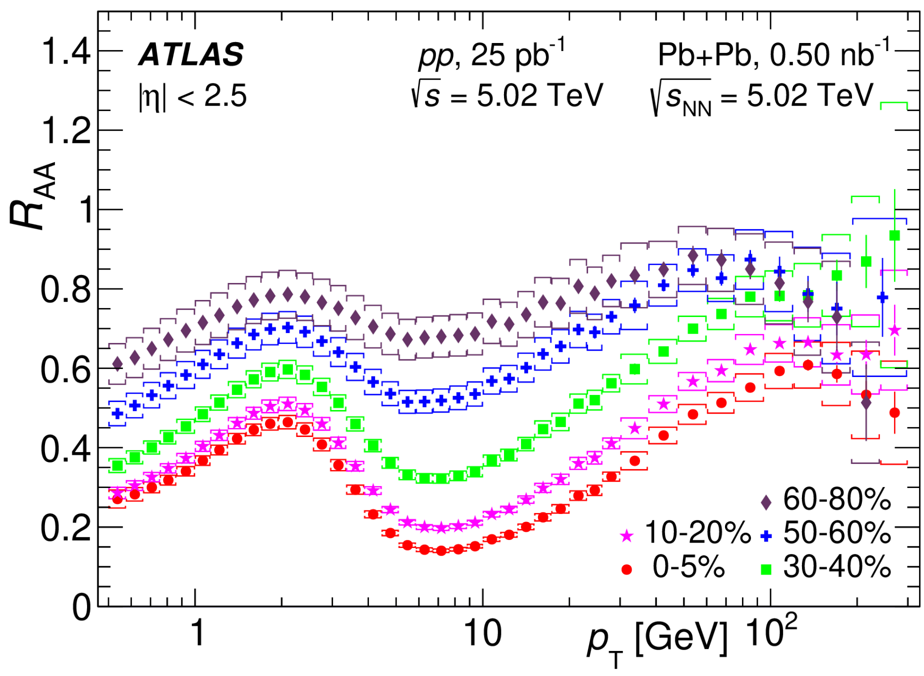

(b)

Figure 1.25: The nuclear modification factor R_{AA} as a function of transverse momentum p_T, for various collision centralities at $\sqrt{s_{NN}} = 5.02$ TeV for (a) jets [77] and (b) charged hadrons [79], measured by ATLAS.

1.3.5 High-$p_{\mathbf{T}}$ v_n

As discussed in Section 1.2.4, the initial geometry of the QGP in a heavy ion collision gives rise to an azimuthal anisotropy in the final state charged hadron production. And this anisotropy can be measured by the fourier coefficient v_n as defined in Equation 1.3. A similar angular modulation in the azimuthal direction can also be found in high-p_{T} sector, due to differential energy loss as a result of the QGP geometry.

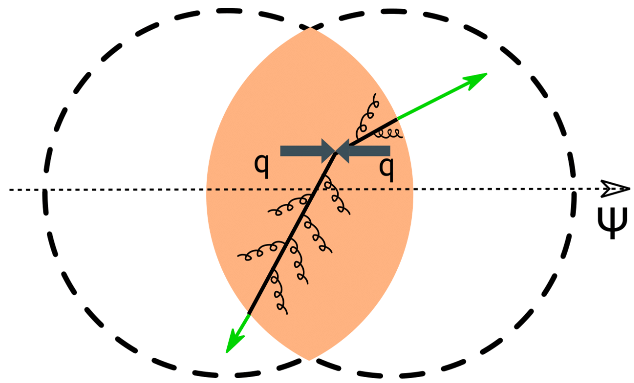

Figure 1.26: Path-length dependence of jet with its angle of ejection with respect to the second order event plane.

The distance in the QGP travelled by a hard-scattered parton is dependent on the angle of ejection relative to event planes of the initial geometry. Therefore, the amount of interaction and energy loss to the QGP is also expected to depend on this angle, as shown in Figure 1.26. This creates anisotropies in high-p_{T} sector corresponding to the initial geometry which gives rise to the soft sector v_n. Besides the initial geometry, azimuthal anisotropies in jets are also sensitive to the parton energy loss mechanism, especially the path-length dependence of energy loss, and jet fragmentation also plays a role in high p_T charged hadrons v_n [83, 84]. The v_n measurements in high-p_{T} and their correlations with the soft sector can provide a great probe to the understanding of soft-hard correlations and path-length dependence of the parton energy loss.

Figure 1.27 shows measurements at the LHC using jets and high-p_{T} charged particles as a function of p_{T}. Both jets and charged hadrons have shown a positive v_2, confirming the path-length dependence of the parton energy loss to the initial state geometry. It can be seen that different p_{T} dependence is observed in jet v_2 and charged particle v_2, due to the additional fluctuations from jet fragmentation. Figure 1.28 shows the measurements of high-p_{T} v_3, which are positive values in mid-central events for charged particle with $20 < p_{\mathrm{T}} < 50$ GeV and for jet with $p_{\mathrm{T}} < 100$ GeV. Positive v_3 in these hard probes suggest that the parton energy loss is sensitive to the event-by-event fluctuations in the initial geometry.

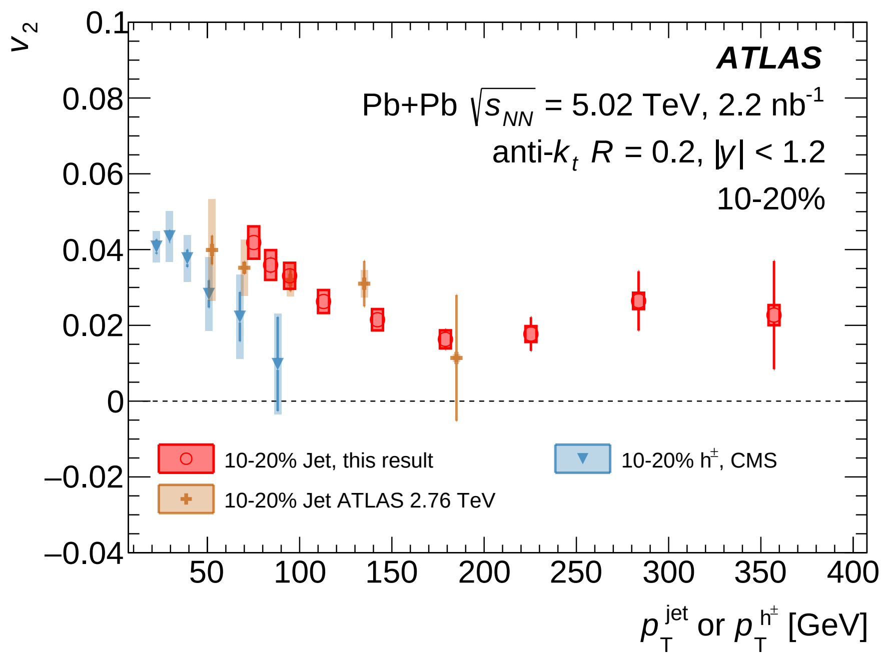

Figure 1.27: Measurements of $v_2(p_T)$ at LHC at $\sqrt{s_{NN}} = 2.76$ TeV with jets by ATLAS [85] and ALICE [86], at $\sqrt{s_{NN}} = 5.02$ TeV with jets by ATLAS [87] and with charged particles (labelled $h^{\pm}$) by CMS [88].

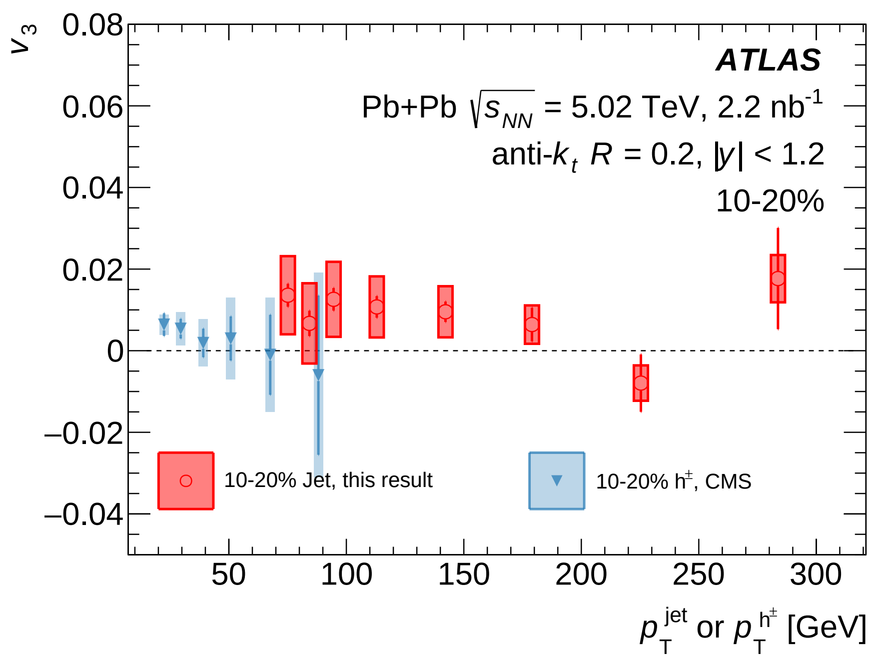

Figure 1.28: Measurements of $v_3(p_T)$ at LHC at $\sqrt{s_{NN}} = 5.02$ TeV with jets by ATLAS [87] and with charged particles (labelled $h^{\pm}$) by CMS [88].

Chapter 2

The LHC and ATLAS

2.1 The Large Hadron Collider at CERN

The Large Hadron Collider (LHC) [89, 90] located at the European Organization for Nuclear Research (CERN) is a the world's largest particle accelerator and collider. The LHC has two parallel beam piles, each has a circumference of ∼27 km, buried between 50 and 175 m underground of France and Switzerland. A schematic view of the CERN accelerator complex and the various facilities associated is shown in Figure 2.1. Particle beams travelling in the the beam piles meet at four interaction points, where the four main LHC detectors are located: A Toroidal LHC Apparatus (ATLAS) [91], Compact Muon Solenoid (CMS) [92], A Large Ion Collider Experiment (ALICE) [93], and Large Hadron Collider - Beauty (LHCb) [94].

The two LHC beam piles encompass particle beams that travel in opposite directions. Studies on elementary particles and search for new physics is enabled by particle collisions at the LHC. The LHC has the capacity to collide a variety of particles, most commonly protons, referred to as *pp* collisions. Fully stripped ions, such as those of lead and xenon, were also collided in the LHC. In the LHC Run 2, heavy ion dataset has been taken for Pb+Pb at a center of mass energy of 5.02 TeV, for $Xe + Xe$ at 5.44 TeV, and for $p + Pb$ at 5.02 and 8 TeV. The LHC Run 3 has also scheduled data taking for oxygen ion collisions [96].

For the ATLAS and CMS interaction points, the proton beams are delivered in bunches with a nominal luminosity of 10^{34} $cm^{-2}s^{-1}$ particles with a distance, referred to as bunch spacing, of 25 ns, with a center of mass energy, denoted by $\sqrt{s}$, of up to 14 TeV. The lead beams are delivered in bunches with a peak luminosity of 10^{27} $cm^{-2}s^{-1}$ particles that collide every 75 or 100 ns with a per-nucleon-pair center of mass energy, denoted by $\sqrt{s_{\mathrm{NN}}}$, of up to 5.5 TeV. Collisions at the interaction point meeting certain requirements will trigger the detector to record a snapshot of particle production, giving the read out of an *event*. A schematic view of relative beam sizes is shown in Figure 2.2

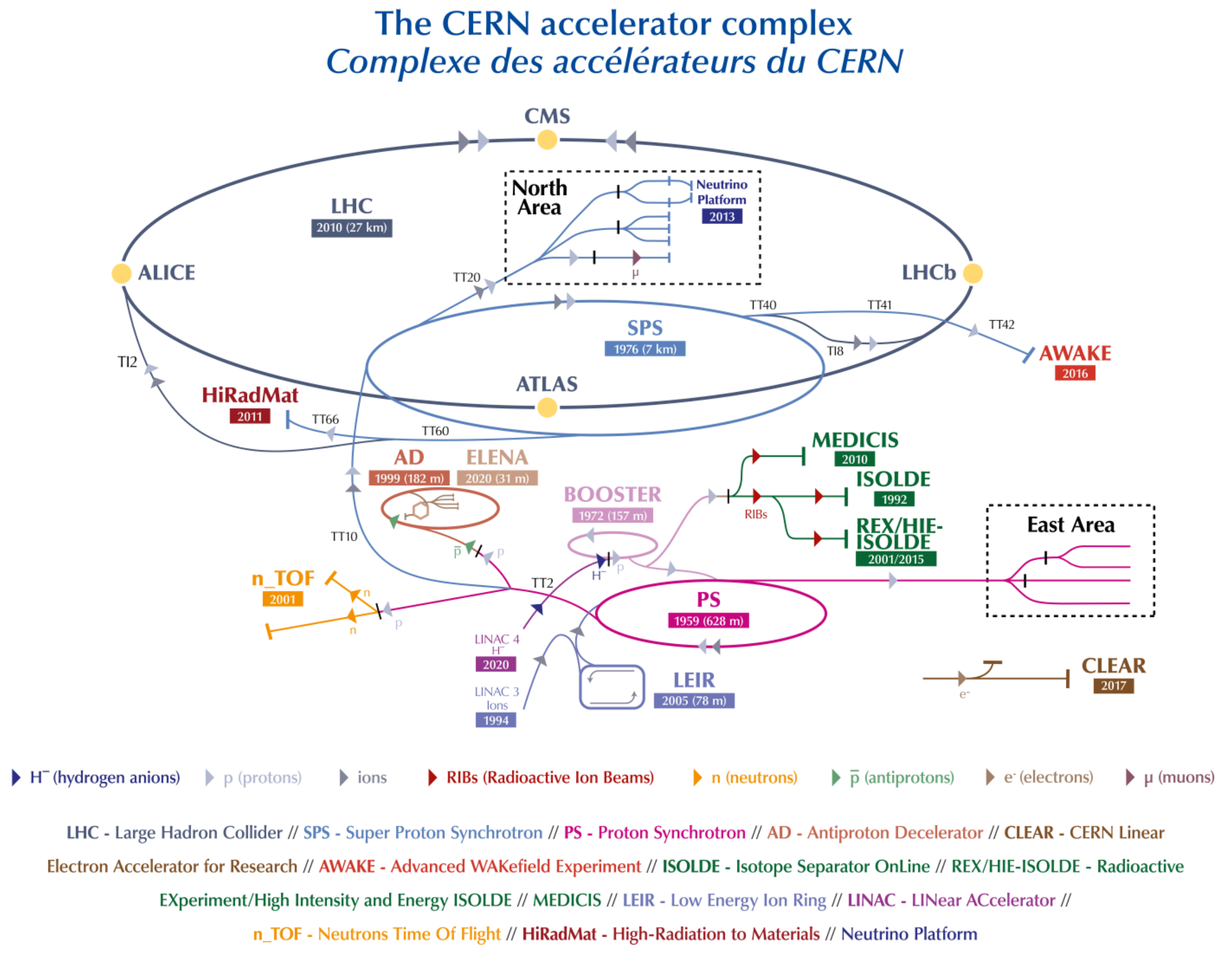

Figure 2.1: Schematic view of the CERN accelerator complex. Figure from [95].

2.2 The ATLAS detector at the LHC

The ATLAS detector [91] is a large general purpose detector located at Interaction Point 1 of the LHC. The ATLAS detector consists of several layers of subdetectors arranged in an overall cylindrical geometry around the beam line with full azimuthal coverage, as shown in Figure 2.3. Starting from the innermost locates an inner detector, calorimeter, and muon spectrometer, surrounded by a superconducting solenoid magnet that produces a 2 T magnetic field for the inner detector and a superconducting toroid magnet for the mnuon spectrometer. The ATLAS calorimeter is subdivided into barrel and end caps, corresponding to the central modules which are concentric along the beam direction and two end calorimeters that are perpendicular to the beam direction. Figure 2.3 shows a diagram of the ATLAS detector [98].

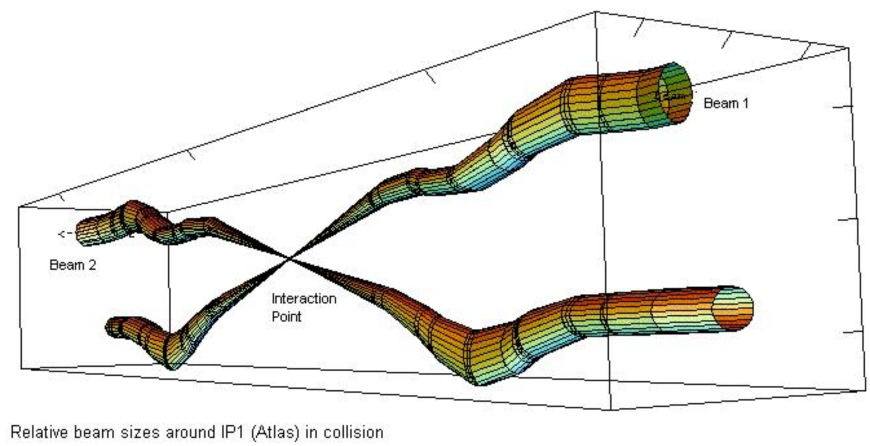

Figure 2.2: Bunch crossing of two incoming beams at the LHC around Interaction Point 1 (ATLAS). Figure is taken from Ref. [97].

2.2.1 Inner detector

The inner detector (ID) [99–101] is designed to accurately reconstruct charged particle trajectories, referred to as *tracks*, from the collisions for particle with a momentum down to 0.5 GeV and covers a wide pseudorapidity range of $|\eta| < 2.5$. It is immersed in a superconducting solenoid that provides a 2 T magnetic field, used to bend the charged particles, and covers a region of 5.3 m long and has a diameter of 2.5 m.

The ID detector is composed of three subsystem, from inner to outer, the pixel detector, the semi-conductor tracker, and the transition radiation tracker. The high-granularity silicon pixel detector covers the vertex region, and consists of the innermost insertable B layer (IBL) made of 14 carbon fiber staves [102] and three silicon pixel detectors. The hit resolution in the barrel region are $8\,\mu\text{m}^2$ (R-ϕ) and $40\,\mu\text{m}^2(z)$ for the IBL, and $10\,\mu\text{m}^2$ (R-ϕ) and $115\,\mu\text{m}^2(z)$ for the silicon pixel layers [103]. It is followed by the silicon microstrip tracker which usually provides four two-dimensional measurement points per track. These silicon detectors are complemented by the transition radiation tracker, which enables radially extended track reconstruction up to $|\eta| = 2.0$. The transition radiation tracker (TRT) also provides electron identification information based on the fraction of hits (typically 30 in total) above a higher energy deposit threshold corresponding to transition radiation.

Charged particle trajectories are used to calculated particle momenta as well as to fit the nuclei interaction

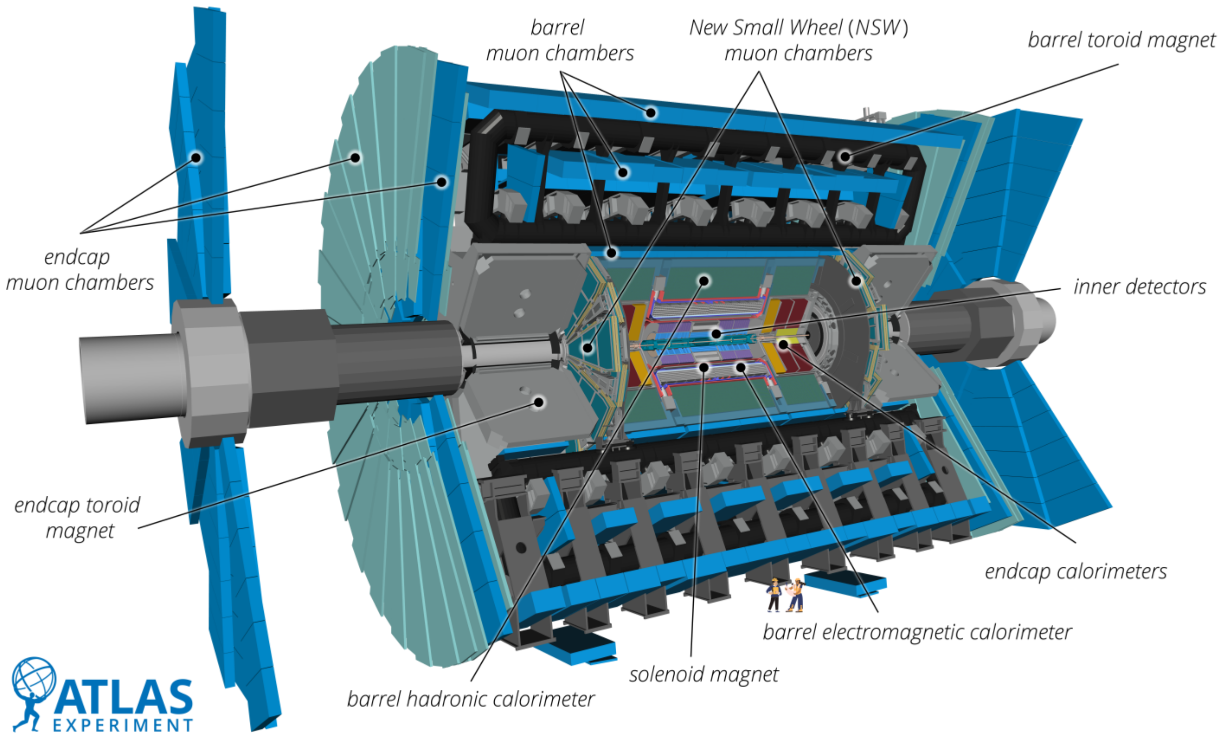

Figure 2.3: The ATLAS detector components. Figure from [98].

point, or primary vertex (PV) [104], in each event. Only one PV is considered in each event. The emitting direction of each track is written in terms of (η, ϕ). Their longitudinal and transverse impact parameters $z_0 \sin\theta$ and d_0 are also calculated with respect to the primary vertex to help determining whether they come from primary interactions or secondary decays.

2.2.2 Calorimeter system

The calorimeter system of the ATLAS detector measures energy deposit made by particles as they meet and lose their energy to the detectors [106]. The calorimeter system covers the pseudorapidity range $|\eta| < 4.9$. Within the region $|\eta| < 3.2$, electromagnetic calorimetry is provided by barrel and endcap high-granularity lead/liquid-argon (LAr) electromagnetic calorimeters, with an additional thin LAr presampler covering $|\eta| < 1.8$ to correct for energy loss in material upstream of the calorimeters. The hadronic calorimeters have three sampling layers longitudinal in shower depth in $|\eta| < 1.7$ and four sampling layers in $1.5 < |\eta| < 3.2$, with a slight overlap in η. The solid angle coverage is completed with forward copper/LAr and tungsten/LAr calorimeter modules (FCal) optimized for electromagnetic and hadronic measurements respectively. The FCals cover a pseudorapidity range of $3.2 < |\eta| < 4.9$.

Used to measure the energy of particles coming from the collisions within a pseudorapidity of $|\eta| < 4.9$ [106].

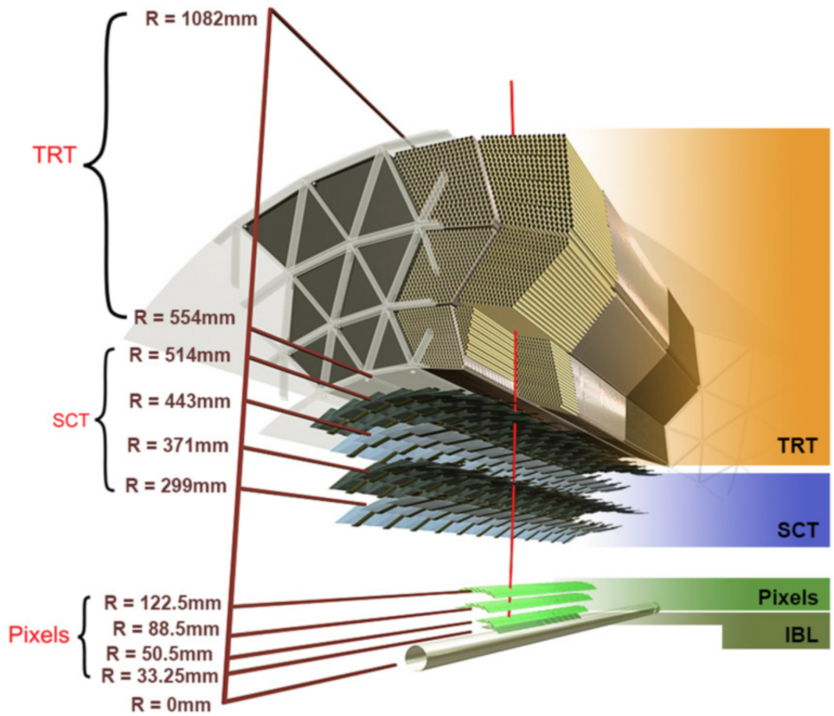

Figure 2.4: Schematic view of the Inner Detector. Figure taken from [105].

The system consists mainly of hadronic, electromagnetic, and forward calorimeters. The ATLAS calorimeter system is a sampling calorimeter composed of an active material, generally a scintillator, that the incoming particles ionize and produce light or charge and a high density absorber medium in which the particles lose most of their energy. Figure 2.5 shows an schematic view of the calorimeter system, and Figure 2.6 shows the pseudorapidity coverages for different components of the ATLAS calorimeter.

Electromagnetic calorimeter The liquid argon Electromagnetic calorimeter (LAr EMCal) consists of alternating layers of liquid argon as the active material and lead plates as the absorber. The barrel EMCal covers $|\eta| < 1.475$ while the end caps covers $1.375 < |\eta| < 3.2$. The LAr EMCal is used to measure the energy of electrons, positron, and photons [108].

Hadronic calorimeter The Hadronic calorimeter consists of the tile, LAr Hadronic end cap, and the LAr forward calorimeter. The tile calorimeter uses steel as the absorber and scintillating tiles for the active material. The tile covers the region $|\eta| < 1.0$, with its two barrels covering the range $0.8 < |\eta| < 1.7$. They are used to measure the energy of hadrons [109]. The LAr hadronic end cap calorimeter (HEC) consist of alternating layers of liquid argon as the active material and copper as the absorber material. It covers a

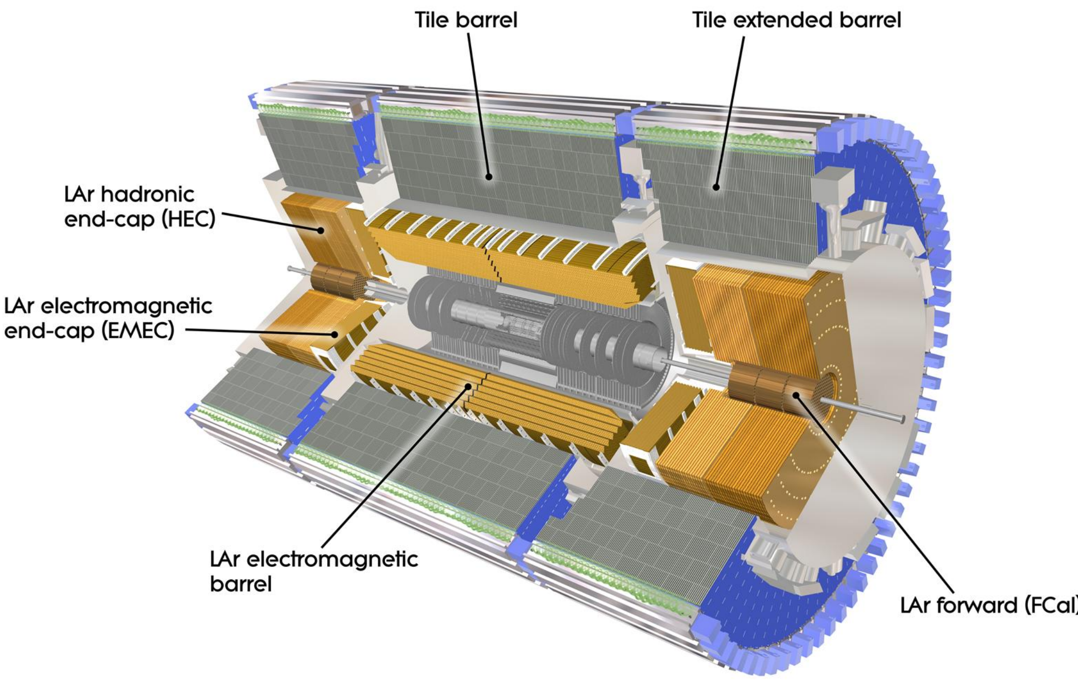

Figure 2.5: Schematic view of the calorimeter system. Figure from [107].

pseudorapidity range of $1.5 < |\eta| < 3.2$. On the other hanb, the LAr Forward calorimeter (FCal) uses liquid argon as the active material, and copper and tunsgsten as the absorber materials. The FCal is covers range $3.2 < |\eta| < 4.9$.

Zero degree calorimeter The zero-degree calorimeters (ZDCs) are located symmetrically at $z = \pm 140$ m and cover $|\eta| > 8.3$ during the Pb+Pb data-taking period. The ZDCs use tungsten plates as absorbers and quartz rods sandwiched between the tungsten plates as the active medium. In Pb+Pb collisions the ZDCs primarily measure spectator neutrons, which are neutrons that do not interact particleically when the incident nuclei collide. A ZDC coincidence trigger is implemented by requiring the pulse height from each ZDC to be above a threshold set to accept the energy of a single neutron.

2.2.3 Muon spectrometer

The muon spectrometer is located outside of the calorimeter system and used to measure the energy and position of muons which do not stop within the calorimeters [110, 111]. It consists of muon chambers of various types and toroid magnets, covering $|\eta| < 2.7$ [112].

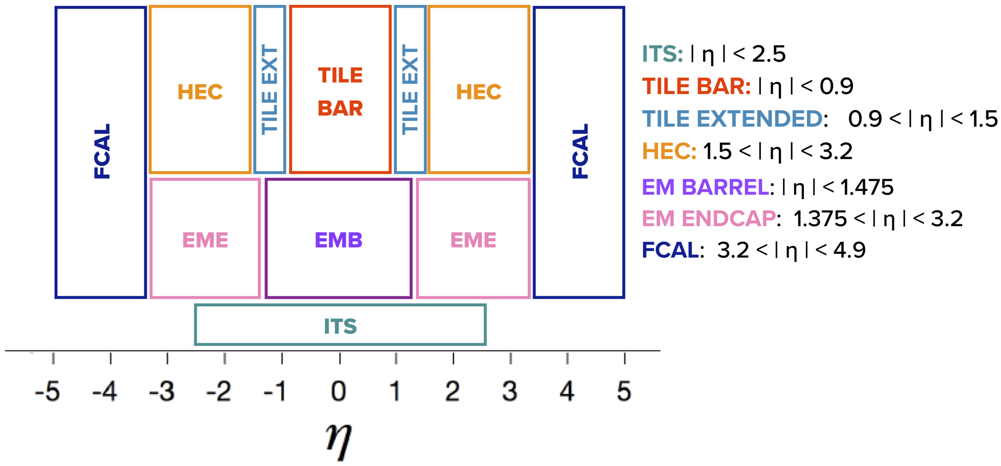

Figure 2.6: Pseudorapidity coverages for components of the ATLAS calorimeter system.

2.2.4 Trigger system

A two-level trigger system is used to select interesting events [113]. The first-level (L1) trigger is implemented in hardware electronics and uses a subset of detector information, including ZDC coincidences in Pb+Pb collisions, to reduce the event rate from 40 MHz bunch crossings to a design value of at most 100 kHz. This is followed by a software-based high-level trigger (HLT) which reduces the event rate to several kHz. An extensive software suite [114] is used in the reconstruction and analysis of real and simulated data, in detector operations, and in the trigger and data acquisition systems of the experiment. Then, the HLT further reduces the rate to approximately 1.2 kHz events, which are recorded.

Chapter 3

Measurements of azimuthal anisotropy

Experimental measurements of v_n are sensitive to a variety of effects, which need to be taken into account when using or interpreting the measured v_n values. This chapter describes three methods of v_n measurements, their sensitivities to some experimental bias and effects, as well as recent measurements using these methods.

3.1 Event plane and scalar product methods

3.1.1 Event plane method

Early v_n measurements in the soft sector directly estimate the event plane angle Ψ_n of each event, and then measure the angular modulation of particle productions with respect to this angle [22, 115–118]. This method is referred to as the *event plane method* [119]. Using orthonogality of trigonometry, it can be easily derived from Equation 1.3 that,

$$v_n = \langle \cos\left[n(\phi_i - \Psi_n)\right]\rangle \tag{3.1}$$

where angular brackets denote an average over all particles, indexed by i with azimuthal angle ϕ_i, in an event, with a particle weight ω_i used to correct for detector non-uniformity. The event plane angle Ψ_n is defined as,

$$\Psi_n = \arctan\left(\frac{\sum_i \omega_i \sin(n\phi_i)}{\sum_i \omega_i \cos(n\phi_i)}\right)/n \tag{3.2}$$

The event plane angle Ψ_n is evaluated over a limited number of particles, and thus has a dispersion from the real underlying eccentricity angle Φ_n. This dispersion is referred to as "resolution" of the event plane angle [120], expressed as,

$$R \equiv \langle e^{in(\Psi_n - \Phi_n)}\rangle \tag{3.3}$$

Therefore the final expression for v_n from event plane method, after the resolution correction, is written as,

$$v_n\{\mathrm{EP}\} = v_n^{obs}/R, \tag{3.4}$$

where v_n^{obs} is evaluated by Equation 3.1. In measurements, event planes and charged particle or jet productions are measured from different subevents to avoid auto-correlations. Typically event planes are estimated in regions of larger rapidities, or *forward* rapidites, and charged particles or jets are measured from more barrel regions of the detectors [117, 121, 122]. The event plane resolution R of an event can be estimated from data by using two subevents, denoted here as A and B, of approximately same statistics. An example of such two subevents are the two ends of the forward calorimeters. The two subevents are assumed to have the same R, and it can be derived that [119],

$$\langle e^{in(\Psi_n^A - \Psi_n^B)} \rangle = \langle e^{in(\Psi_n^A - \Phi_n)} \rangle \langle e^{in(\Psi_n^B - \Phi_n)} \rangle = R^2, \tag{3.5}$$

where Ψ_n^A and Ψ_n^B are event plane angles estimated by subevent A and B, respectively. Therefore, in measurements, R is calculated as $\sqrt{\langle \cos[n(\Psi_n^A - \Phi_n^B)] \rangle}$. For compact notation, we define for a set of N particles from an event a *flow vector* [119], evaluated as,

$$Q_n \equiv \frac{1}{N} \sum_j e^{in\phi_j} = |Q_n| e^{in\Psi_n}. \tag{3.6}$$

The formula of event plane method expressed in this notation can be written as,

$$v_n\{\mathrm{EP}\} = \frac{\langle \cos[n(\phi_j - \Psi_n^{A|B})] \rangle}{\langle \cos[n(\Psi_n^A - \Phi_n^B)] \rangle} = Re \frac{\left\langle e^{in\phi_j} \frac{Q_n^{A|B*}}{|Q_n^{A|B}|} \right\rangle}{\left\langle \frac{Q_n^{A*}}{|Q_n^{A*}|} \frac{Q_n^B}{|Q_n^B|} \right\rangle}, \tag{3.7}$$

in which Q_n^A and Q_n^B are respectively the flow vectors of subevent A and B, the index j goes over all particles measured, and $Q_n^{A|B}$ is obtained using either subevent A or B depending on the position of the particle used for $e^{in\phi_j}$, and typically chosen to maximally suppress experimental biases that are unrelated to flow harmonics.

3.1.2 Scalar-product method

This subsection is based on the discussion presented in Ref. [123] and Ref. [120]. In case the event plane angle resolution R is constant or has a linear dependence on the mean v_n, Equation 3.4 should reproduce the original mean v_n. However, the measurement of event plane angle is on an event-by-event basis. Therefore, R depends on the relative magnitude of v_n to the statistical abundance of soft particles for each event, and thus also have an underlying distribution due to the non-trivial event-by-event fluctuations in v_n itself. Given the underlying v_n value, the measured $v_n\{\mathrm{EP}\}$ with this method has the following expression [123],

$$v_n\{\mathrm{EP}\} = \frac{\langle v_n R(v_{nA})\rangle v_n}{\sqrt{\langle R(v_{nA})^2\rangle v_n}}, \tag{3.8}$$

where A indicates the subevent where the event plane angle is evaluated. This subevent is typically separate from evaluation of v_n to exclude self-correlations. For heavy ion collisions, it is assumed that for v_n/v_{nA} is close to 1 and does not have significant event-by-event fluctuations. However, based on this formulation, the flow-dependent resolution poses a problem for the measurements when v_n has event-by-event fluctuations, meaning the second moment of $R(v_n)$ does not equal to square of mean $R(v_n)$. It was suggested that, measurements of v_n using the event plane method yields an ambiguous measurements between the mean value of v_n, i.e., $\langle v_n\rangle$, and the square of second moment of v_n, $\sqrt{v_n{}^2}$. In the limit where resolution is low and linearly dependent on v_n [118], this measurement becomes,

$$v_n\{\mathrm{EP}\} \xrightarrow{\text{low res.}} \sqrt{\langle v_n^2\rangle}, \tag{3.9}$$

where as when the detector is infinitely fine binned and $R(v_n) \approx 1$,

$$v_n\{\mathrm{EP}\} \xrightarrow{\text{high res.}} \langle v_n\rangle, \tag{3.10}$$

This motivates the development of the scalar product method, which no longer explicitly calculates the event-plane angle on a single-event basis, but rather directly correlates two subevents. The formula for scalar product method v_n, denoted as $v_n\{\mathrm{SP}\}$, can be evaluated by directly computing the scalar product between flow vectors of two subevents without explicitly evaluating for Ψ_n,

$$v_n\{\mathrm{SP}\} = \frac{\langle Q_n Q_{nA}^*\rangle}{\sqrt{\langle Q_{nA} Q_{nB}^*\rangle}}, \tag{3.11}$$

where A and B are indicating two symmetric subevents in which the resolution of detector is estimated. It can be easily derived using Equation 1.3 that,

$$\langle Q_n e^{-in\Phi_i}\rangle_{|v_n} = v_n. \tag{3.12}$$

By utilizing Equation 3.12, and applying the assumption that no significant fluctuations exist for v_n/v_{nA} or

v_n/v_{nB}, we obtain from Equation 3.11,

$$v_n\{\mathrm{SP}\} = \frac{\langle v_n v_{nA}\rangle_{|v_n}}{\sqrt{\langle v_{nA}^2\rangle_{|v_n}}} = \sqrt{\langle v_n^2\rangle}, \tag{3.13}$$

which does not depend on detector resolution, thus constituting a more well defined measurement.

3.1.3 Application of the methods

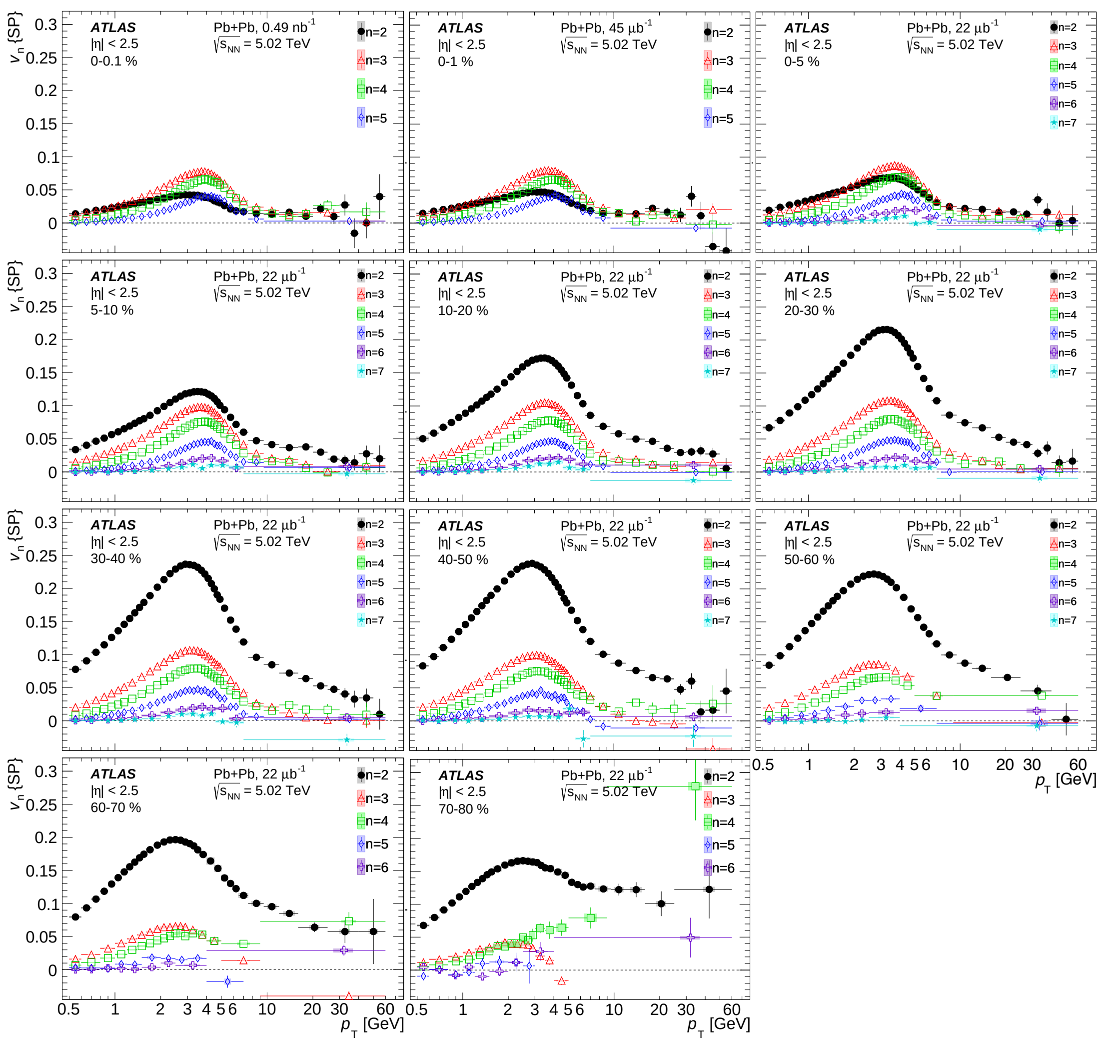

Figure 3.1: Measurements of $v_n\{\mathrm{SP}\}$ for $n = 2-7$ as a function of p_T in panels of centrality intervals. Figure is taken from Ref. [122].

Figure 3.1 shows the scalar product measurements of flow harmonics up to v_7 by ATLAS at $\sqrt{s_\mathrm{NN}} =$ 5.02 TeV. In all mid-central collisions, the values of v_n decreases with n. In these centrality intervals, the average geometry dominates, and higher orders of geometry harmonics are less pronounced. In central collisions, on the other hand, where the average geometry is expected to close to a circle with low ellipticity, the fluctuation-driven v_3 becomes the dominating mode.

Figure 3.2 compares the v_n values measured with the EP and SP methods as a function of p_{T} and N_{part}. The measurements versus N_{part} are integrated over p_{T} ranges of $0.5 < p_{\mathrm{T}} < 60$ GeV. A small difference between the two methods can be observed, which is most pronounced in v_2 for the mid-central collisions. Values of $v_n\{\mathrm{SP}\}$ are slightly larger than values of $v_n\{\mathrm{EP}\}$. If v_n has non-trivial fluctuations, we obtain $\sqrt{\langle {v_n}^2 \rangle} > \langle v_n \rangle$, and this could explain the observed difference in $v_n\{\mathrm{SP}\}$ and $v_n\{\mathrm{EP}\}$ given Eqn. 3.9, Eqn. 3.10 and Eqn. 3.13. Although the average ϵ_n is expected to be the same for events of the same centrality, every order of ϵ_n has non-trival fluctuations in its probability distribution due to the event-by-event fluctuations of the nucleon positions, as explained in Section 1.2.4. This maps into v_n, and thus giving $v_n\{\mathrm{SP}\} >= v_n\{\mathrm{EP}\}$ depending on the resolution of the event plane estimation.

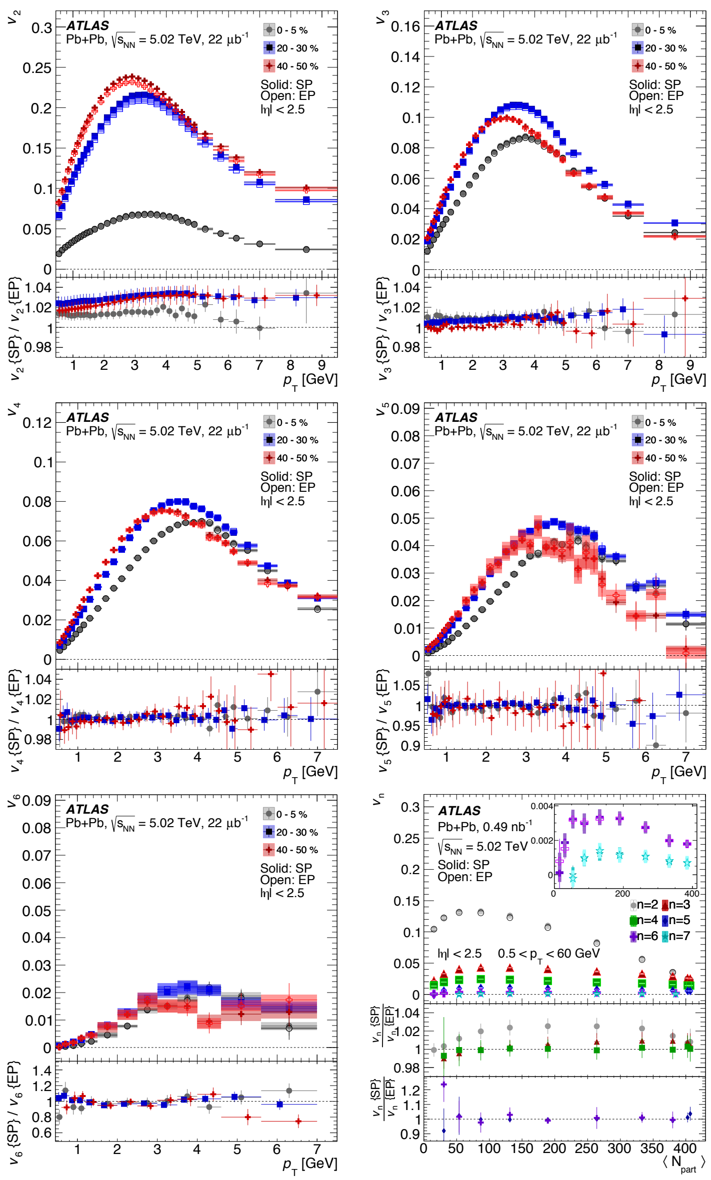

Figure 3.2: Comparison of the v_n obtained with EP and SP methods as a function of $p_{\rm T}$ in three centrality intervals. The right bottom panel shows the v_n as a function of N_{part}, integrated over $0.5 < p_{\rm T} < 60$ GeV. Figure is taken from Ref. [122].

3.2 Multi-particle cumulant method

Both the event plane and scalar product methods are two-particle type correlations, since two subevents, one for event plane estimation and one for particle production distribution, are correlated. These measurements yield a v_n with the mean and variance of the distribution, but do not give further information on the shape of the underlying distributions, such as the skewness. These limitations have motivated the measurements of higher order cumulants v_n [88, 124–130], which are a set of variables built from different orders of moments from the underlying v_n distribution [131–134].

3.2.1 Formalism

Values of v_n measured using $2k$-particle cumulants is denoted as $v_n\{2k\}$. The proposed formalism [131, 132] computes *genuine* higher-order correlations by removing the lower-order groups of correlations. This event-averaged, genuine multi-particle correlations are denoted by $\langle\langle 2k \rangle\rangle$. For example, two-particle correlations are removed from four-particle correlations by using,

$$\begin{aligned} \langle\langle e^{in(\phi_1+\phi_2-\phi_3-\phi_4)} \rangle\rangle &\equiv \langle e^{in(\phi_1+\phi_2-\phi_3-\phi_4)} \rangle - \langle e^{in(\phi_1-\phi_3)} \rangle - \langle e^{in(\phi_2-\phi_4)} \rangle \\ &= -(v_n\{4\})^4. \end{aligned} \tag{3.14}$$

In this formulation, only direct four-particle correlations will contribute to the measurements but not those from pairwise correlations. In Ref. [135], properties of higher-order cumulants are calculated with a Gaussian ansatz for the underlying v_n distribution. Here the Gaussian ansatz is the distribution of the magnitude of v_n when integrating over angles of the vector $v_n = v_n e^{in\Psi_n}$ as a 2D Gaussian distribution. It can be derived that under this ansatz, $v_n\{2k\}$ for $(2k >= 4)$ gives an estimation of $\langle v_n \rangle$ without contributions from fluctuation terms. Combining with what we know about the event plane and scalar product methods, we have,

$$v_n\{2\} > v_n\{4\} \approx v_n\{6\} \approx v_n\{8\}, \tag{3.15}$$

where $v_n\{2\}$ can be replaced by other two-particle type measurements, such as $v_n\{\mathrm{SP}\}$ or $v_n\{\mathrm{EP}\}$. Higher-order cumulants and their comparison with two-particle type measurements serve as an useful tool to study the Gaussianity of underlying v_n distribution [135–138].

3.2.2 Important Considerations in v_n measurements

Important experimental caveats should be explained before interpreting measurements of v_n using different methods. In all previous discussions of v_n, the initial QGP eccentricities are assumed to be the only source of measured azimuthal anisotropies and approximately as a 2D geometry. In practice, not all measured correlations in v_n come from the global collectivity, and the QGP is a 3D volume with small but non-zero thickness along the z-axis. These two effects, known as "nonflow effects" and "longitudinal decorrelation" respectively, will now be explained.

Nonflow effects By observing Equation 1.3, we shall notice that there is no physical meaning attached to this decomposition regarding the origin of the measured correlations [134]. That is, any local or global correlations between particles that give rise to anisotropies in the azimuthal direction contribute to the experimentally measured v_n. Correlations that are unrelated to the initial geometry of the QGP are referred to as *nonflow* effects [131, 132].

Some examples of nonflow correlations are transverse momentum conservations, resonance decay, quantum correlations between identical particles (the Hanbury-Brown and Twiss effect [139, 140]), and for high-p_{T} sector, a back-to-back dijet. There are three categories of methods attempted to properly account for nonflow effects: (a) to measure only in phase space where such effects are expected to be small [141], (b) to explicitly subtract them in the analysis, or (c) to systematically suppress them regardless of the source [132]. The last category of methods is now most extensively used as it has the obvious advantage that no detailed knowledge of nonflow sources is required. Any nonflow sources of a direct, local origin, that is, from particle decay correlations, can be suppressed be explicitly requiring spatial separation along the beam direction between the correlated objects. This is frequently done in the event plane and scalar product methods, in where a significant rapidity gap is applied between where the event planes are estimated and where the particle production is measured. On the other hand, such local correlations are typically of a few-particle nature, and can be effectively suppressed by genuine multi-particle correlations of higher-order, as done in the multi-particle cumulant method. The magnitudes of local particle decay products [131] are estimated to scale with M^{1-2k} for a $2k$-particle correlation, where M is the particle multiplicity in an event.

It should be noted that nonflow effects contribute to v_n on an event-by-event basis. Consequently, nonflow effects also have event-by-event fluctuations, and contribute to the fluctuations of v_n in addition to the fluctuations in ϵ_n. Therefore, non-Gaussianity of v_n in experimental measurements can arise from flow or nonflow contributions. On the other hand, some nonflow sources are highly centrality dependent as a result of their dependence on collision multiplicity and energy. Since correlations from short-distance resonance

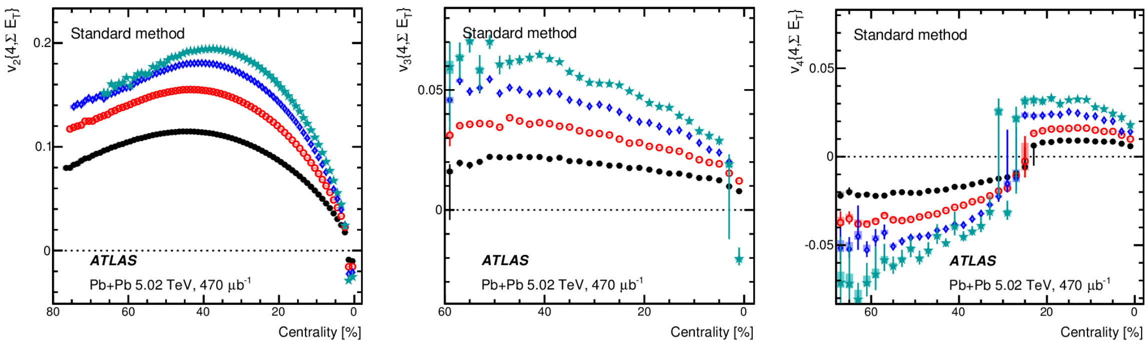

Figure 3.3: Measurements of $v_n\{4\}$ for different harmonics. Negative values are plot presentation of magnitude of the imaginary $v_n\{4\}$. Figure is taken from Ref. [149].

decay scale with $(1-2k)$-th power of event multiplicity for $2k$-particle correlations [131], short-range nonflow effects more pronounced in peripheral, lower multiplicity events. Correlations from initial state parton correlations, such as those from a back-to-back dijet, are also stronger in peripheral events as a result of the low multiplicity in these events. Particles from jet constitute a larger fraction of the overall production where the QGP volume is smaller.

Longitudinal decorrelation In all previous discussions, it is assumed that the energy density profile of the QGP is approximately invariant along the beam direction, thus enabling the discussion to be limited to a 2D approximation in the transverse plane. However, in recent models [142–144] and experimental studies [145–148], it has been shown that the energy profile may not be uniform in the beam direction, thus creating a rapidity-dependent event plane angle Ψ_n and flow coefficient v_n. This is referred to as the *longitudinal flow decorrelation*. As a result of this decorrelation, v_n measured between objects of larger gap along the beam direction are decreased. Longitudinal decorrelations are expected to contribute when significant rapidity gaps are applied between correlated particles, although the magnitudes are expected to be small in comparison to flow signals.

3.2.3 Method comparison in v_n measurements

The multi-particle cumulant methods have been applied in soft [55, 125–127, 129, 130, 149–151] and hard v_n [88, 124]. Figure 3.3 shows an ATLAS measurements at $\sqrt{s_{\mathrm{NN}}}$=5.02 TeV for $v_n\{4\}$ in fine centrality intervals. Strong centrality dependence is observed in v_2, which increases magnitudes from central to mid-central and then decreases toward peripheral events, as expected from the ellipticity of the average geometry. A change of sign is observed for v_2 in ultra-central collisions and for v_4 in peripheral collisions. For presentation purpose, these plots have shown the magnitude of imaginary $v_n\{4\}$ as negative-valued

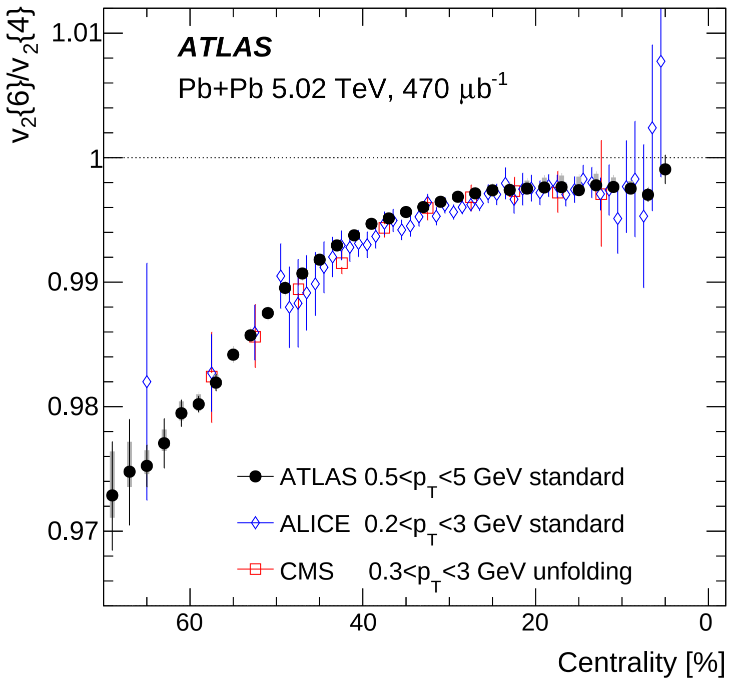

Figure 3.4: Ratio of cumulants $v_2\{6\}/v_2\{4\}$ as a function of centrality from ATLAS [149], CMS [129], and ALICE [150]. Figure is taken from Ref. [149].

$v_n\{4\}$. The sign change suggests that strong fluctuations exist in the underlying v_n distributions in these region in comparison to the mean, and can suggest a non-Gaussianity in the underlying v_n distributions. For v_2, it could arise from initial state fluctuations or non-flow fluctuations, which can be more systematically studied using simulations [152]. Initial state fluctuations such as volume fluctuations of nuclei [153, 154] have been suggested as an explanation for the sign-change in ultra-central collisions. Volume fluctuations create centrality fluctuations in events, and cause experimental measurements of v_n to mix events of different *real* collision centralities, thus creating a non-Gaussianity. For v_4, the sign change also gives insights for the interplay between linear response from ϵ_4 and non-linear contributions of ϵ_2 to the measured v_4. A primarily linear mapping from ϵ_n to v_n can be assumed in the two lowest modes of flow harmonics, v_2 and v_3, whereas higher order flow harmonics are sensitive to both higher and lower order eccentricities [155, 156].

In the soft sector, abundant statistics are available which enables measurements of higher-order cumulants, such as $v_n\{6\}$ and $v_n\{8\}$, and their ratios are calculated. Figure 3.4 shows the $v_2\{6\}/v_2\{4\}$ as a function of centrality for measurements at the LHC [129, 149, 150]. As predicted for Gaussian distributions, this ratio is very close to 1 in the central collisions. However significant centrality dependence is observed, and in the peripheral region, the deviation of less than 3% is observed. The centrality dependence non-Gaussianity suggest non-zero high-order fluctuations in the initial geometry and stronger nonflow effects in the peripheral

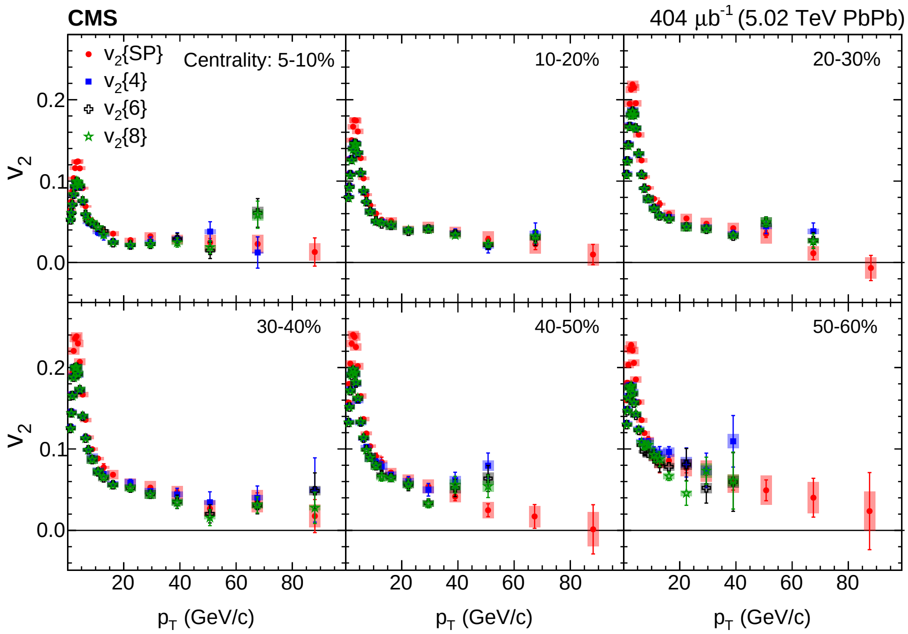

Figure 3.5: Measurements of v_2 and v_3 using scalar product and multi-particle cumulant methods, in seven collision centrality intervals compared with model predictions. CUJET3.0 predictions come from Ref. [158] and SHEE models com from Ref. [157]. Figure is taken from Ref. [88].

regions.

With increased luminosity and collision energies at the LHC, measurements of v_n are able to be pushed toward higher p_T for hard sector studies. Figure 3.5 shows the CMS measurements of flow harmonics for v_2 and v_3, using scalar product and multi-particle cumulant methods, up to 100 GeV [88]. With the scalar product method, a positive v_2 is obtained up to a p_T of approximately 60–80 GeV in all except for the most central collisions measured. Meanwhile, $v_3\{\mathrm{SP}\}$ is positive up to a p_T of 20 GeV for 0–40%. In v_2, the trend of $v_n\{\mathrm{SP}\} > v_n\{4\} \approx v_n\{6\} \approx v_n\{8\}$ is observed, similar to that observed in the soft sector, suggesting a correlation between the parton energy loss and the event-by-event QGP geometry. A comparison with theoretical model is also provided, where the SHEE model [157] shows better agreement. This measurement, however, did not provide with multi-particle cumulant measurements of high-p_T v_3, possibly from the significant statistical fluctuations.

The positive jet $v_3\{\mathrm{EP}\}$ (see Figure 1.28 from Section 1.3.5) and charged particle $v_3\{\mathrm{SP}\}$ for $p_T > 10$ GeV provides evidences for the hard sector responses for the event-by-event fluctuations in the QGP geometry. However, higher-order cumulants of v_3 have been statistically limited, as shown on Figure 3.6, thus making it difficult for a quantitative understanding of the v_3 fluctuations in the hard sector. This motivates the measurements conducted in this thesis. Using a bigger dataset collected using the ATLAS detector, a systematic study on the v_2 and v_3 and their cumulants is conducted in the hard sector.

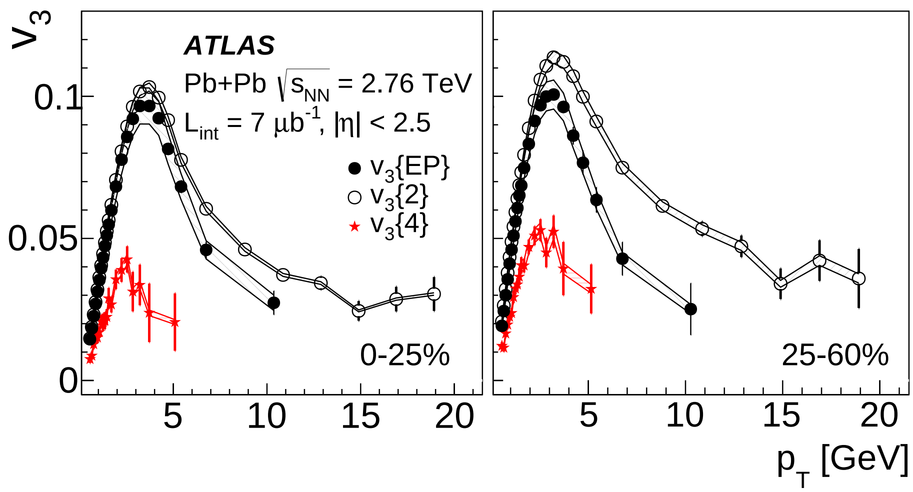

Figure 3.6: Measurements of $v_3\{\mathrm{EP}\}$, $v_3\{2\}$ and $v_3\{4\}$ at centrality interval (left) 0–25% and (right) 25–60% as a function of charged particle p_{T} in Pb+Pb collisions at $\sqrt{s_{\mathrm{NN}}} = 2.76$ TeV. Figure is taken from Ref. [124].

Chapter 4

Azimuthal anisotropies of high-p_{T} charged particles in Pb+Pb collisions at 5.02 TeV with the ATLAS detector

4.1 Overview of the thesis analysis

Like introduced in Chapter 1, measurements of jets originating from hard parton scatterings in the early stages of heavy-ion collisions provide information about the short-distance-scale interactions of high-energy partons with the QGP. This is seen in the suppression of jet and high-p_{T} hadron productions [77, 79, 130, 159, 160]. This suppression can be explained by the energy loss of partons propagating through the QGP, and the magnitude of this jet energy loss depends on the amount of QGP that the jet travels through. The geometry of the overlap of the two nuclei leads to a shorter average path length if the jet is oriented along the direction of the collision impact parameter than if the jet is oriented in the perpendicular direction. This is expected to lead to a dependence of the jet yield on the azimuthal angle [161–163]. Charged particles with p_{T} greater than 10 GeV, hereinafter referred to as high-p_{T} charged particles, are likely come from jet fragmentation. Therefore, the measurements of azimuthal anisotropies of high-p_{T} charged particles are useful for investigating the path-length dependence of jet energy loss. A similar azimuthal modulation is also present in the low-p_{T} charged particles due to the hydrodynamic *flow* of the QGP. The amplitudes of these anisotropies can be used to constrain the bulk properties of the QGP.

The key observable for this analysis is the azimuthal anisotropies quantified via the v_n Fourier coefficient values describing the azimuthal angular distribution of charged particles with respect to the event planes:

$$\frac{dN}{d\phi} \propto 1 + 2\sum_{n=1}^{\infty} v_n \cos(n(\phi - \Psi_n)),$$

where Ψ_n is the n-th order event plane and ϕ is the azimuthal angle of charged particles, as measured experimentally. Measurements of v_n also include contributions from non-flow effects, defined as the correlations unrelated to the initial geometry of the QGP, such as resonance decays, global momentum conservation, jet fragmentation, and dijet production. Chapter 3 reviews some methods have been developed to suppress non-flow effects and applied in v_n measurements at the LHC [85, 87, 88, 122, 164] and Relativistic Heavy Ion

Collider (RHIC) [165, 166]. The *scalar-product* (SP) method [165, 167] provides an estimate of $\sqrt{(v_n)^2}$ that is independent of the detector resolution. In addition, the non-flow contributions are mitigated if a rapidity gap is imposed between the correlated sub-detectors. Alternatively, lower-order short-distance correlations from particle decays can be effectively suppressed by utilizing genuine multi-particle correlations within the *multi-particle cumulant* (MPC) framework [131, 132, 168], which can be efficiently implemented using the so-called Q-cumulants [133, 134]. The formalism of Q-cumulants sum over correlated particle multiplets in a single looping of particles. Following the convention from this framework, correlations, cumulants, and v_n measurements that are integrated in p_{T} are termed *reference*, in contrast to the *differential* quantities that are differential in p_{T}. The three-subevent Q-cumulant method extends the standard method by requiring a rapidity gap between some of the correlated particles. This has been shown to reduce further the short-range non-flow effects in measurements of reference v_n [149, 152, 169]. The measurements of MPCs used to obtain v_n are conducted over events of similar centralities, which define an event ensemble known as an event class. It has been observed that the results obtained with the MPC method are also sensitive to the centrality resolution of the event class chosen. Therefore, different strategies of constructing the v_n values in a centrality interval have been investigated in the low-p_{T} sector [149].

4.1.1 Motivations

Some recent measurements of v_n for the hard probes were also reviewed in Chapter 3, as done with jets [85–87] as well as high-p_{T} charged particles [88, 122, 124]. Some key observations obtained are summarized here. For jets with $p_{\mathrm{T}} > 70$ GeV, positive values of v_2 are measured for all collisions except for the most central collisions, and positive values of v_3 are measured for mid-central collisions [87]. A centrality dependence that is qualitatively similar to the soft-sector has been observed in jet v_n. For charged particles, v_2 values measured with both the SP and the MPC method decrease with p_{T} for a p_{T} greater than 20 GeV while remaining positive up to a p_{T} of approximately 80 GeV for the 60% most central collisions. Meanwhile, the values of v_3 measured with the SP method remain positive up to a p_{T} of approximately 20 GeV for the 40% most central collisions [88]. The positive jet $v_3\{\mathrm{EP}\}$ and charged particle $v_3\{\mathrm{SP}\}$ for $p_{\mathrm{T}} > 10$ GeV provides qualitative evidences for the hard sector responses for the event-by-event fluctuations in the QGP geometry. Multi-particle cumulant v_3 has been very limited in statistics and not available above 10 GeV.

Jets and high-p_{T} charged particles are different probes and they complement each other in the understanding of parton energy loss to the QGP. Although they both aim to probe hard scatteded partons, additional mechanism in jet fragmentation gives them different quantitative values. These two probes are different yet complement each other in the understanding of parton energy loss to the QGP. Therefore, a systematic study on high-p_{T} v_n using charged particles is an important follow up for the jet v_n studies done at the Pb+Pb collisions at $\sqrt{s_{\mathrm{NN}}} = 5.02$ TeV. On the other hand, limited statistics has been a challenge in differential-p_{T} v_n measurements, especially those with multi-particle cumulant methods. An improvement in statistics allows for higher p_{T} ranges probed, as well as for systematic studies of different effects in high-p_{T} region, such as pseudorapidity dependence, the sensitivity to nonflow effects, and how different methods affect the v_n values measured.

This paper extends the measurement of v_n values for charged particles by the SP method in $\sqrt{s_{\mathrm{NN}}} =$ 5.02 TeV Pb+Pb collisions to higher p_{T} and presents measurements of p_{T}-differential four-particle cumulant v_3 up to 100 GeV using a data set corresponding to an integrated luminosity of 435 μb^{-1} collected by the ATLAS detector in 2018. Measurements of v_n were performed in intervals of p_{T} up to 400 GeV and intervals of centrality spanning 0–60% most central collisions. Measurements of v_n with the SP method, denoted by $v_n\{\mathrm{SP}\}$, were carried out for tracks in three pseudorapidity ranges $|\eta| < 1.1$, $1.1 < |\eta| < 2.5$ and $0 < |\eta| < 2.5$. And measurements of v_n using the MPC method were performed for four-particle cumulants, denoted by $v_n\{4\}$, for charged particles over the pseudorapidity range of $|\eta| < 2.5$. Furthermore, the three-subevent Q-cumulant method used for reference v_n measurements is expanded to include p_{T}-differential $v_2\{4\}$ and $v_3\{4\}$. A comparison of these quantites with those obtained using the standard Q-cumulants is included. The results are presented in 5% or 10% wide centrality intervals. For the MPC method, the cumulants are firstly computed within narrower centrality intervals before combining into wider ones. The differences in the MPC measurements by using different centrality intervals before combining are shown. Finally, results from the SP method and the MPC method are compared with each other.

4.2 Data and Monte Carlo simulations

4.2.1 Pb+Pb data event selection

The Pb+Pb dataset used in this analysis corresponds to an integrated luminosity of 435 μb^{-1}. Events were required to satisfy one of the three L1 minimum-bias (MB) triggers. The first MB trigger requires an event to have a total transverse energy (TE) measured in the calorimeter system above 600 GeV. The second MB trigger requires an event to have a TE above 50 GeV and less than 600 GeV. The third MB trigger will fire when an event is veto-ed by both of the previous two triggers and satisfies a ZDC coincidence trigger at L1 and have at least one track in the HLT. The MB triggers above have a small prescale[1] of approximately 3.95. This is enabled by a novel strategy known as the partial event building (PEB) [113, 170], in which data

[1]A prescale is a number that defines what fraction of events are recorded out of all possible events that would have passed the trigger requirements.

from selected ATLAS subdetectors are used to compose an event, thus enabling higher recording rate and optimized event size. For this analysis, events are required to have the z-coordinate of the primary vertex within 100 mm of the nominal interaction point. This dataset is referred to as the PEB dataset.

A smaller dataset with approximately 10% of the PEB stream events is used for testing purpose. This dataset set has its events constructed with all detectors and is useful for testing certain analysis procedure and corrections. It uses the same criteria for minimum bias triggering (excpet for triggering them on HLT instead of L1), and it therefore referred to as the MinBias (MB) dataset.

4.2.2 Centrality determination

The centrality determination in ATLAS is done with the total transverse energy recorded in Forward calorimeters (FCal), denoted by ΣE_{FCal}, an observable related to the impact parameter of nuclei collision. Mininum bias events of Pb+Pb collisions are sorted by ΣE_{FCal} values above a threshold designed to remove photonuclear and diffractive interactions between the nuclei. An MC Glauber simulation fitted to the data is used to describe the distribution of ΣE_{FCal} in hadronic interactions, which finds approximately 85% of events from data follow the simulated trend. The ΣE_{FCal} distributions from these data are then divided into 85 bins of equal number of events, and the point of division in ΣE_{FCal} is used for centerality percentile determination in ATLAS analyses.

4.2.3 In-time and out-of-time pileup

By design, each event recording should contain information from only one collision. A pileup event is an event in which there are multiple Pb+Pb interactions. An in-time pileup is an event with more than one hadronic interaction from the same bunch crossing. An out-of-time pileup is when an event records additional hadronic interactions from just before or right after the collision of interest.

In-time pileup rejection

In-time pileup events record multiple interactions as one, therefore the total transverse energy recorded in Forward calorimeters (FCal), denoted by ΣE_{FCal}, is the summation of multiple interactions, making the event "appear" to be a central collision when it actually consists of multiple peripheral collisions. These events were suppressed by utilizing the observed anti-correlation, expected from the nuclear geometry, between $\Sigma E_{\mathrm{T}}^{\mathrm{FCal}}$, correlated with number of participant nucleons, and the energy in the ZDC, which is proportional to the number of observed spectator neutrons. The distribution of number of neutrons $N_{neutron}$ against $\Sigma E_{\mathrm{T}}^{\mathrm{FCal}}$

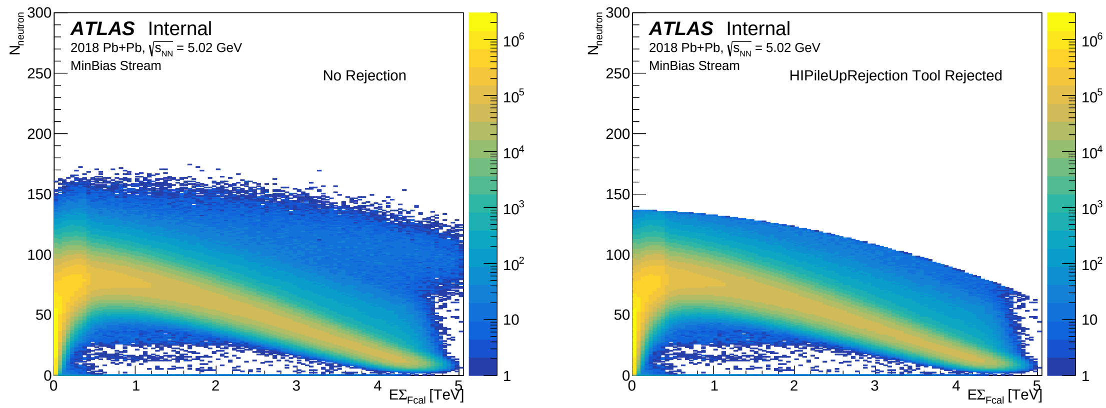

Figure 4.1: Left: Distribution of event counts on $N_{neutron}$ against $\Sigma E_{\mathrm{T}}^{\mathrm{FCal}}$ before in-time pile-up rejection using the tool. Right: Distribution of event counts on $N_{neutron}$ against $\Sigma E_{\mathrm{T}}^{\mathrm{FCal}}$ after in-time pile-up rejection using the tool.

before and after in-time pile-up rejections is shown in Figure 4.1. In-time pileul events are estimated to be less than 0.5% of collisions.

Out-of-time pileup

Additional hadronic interactions from just before or right after the collision of interest could interfere with calorimeter performance and centrality determinations. Criteria for rejecting these events are determined by the expected strong and linear correlation between charged particle multiplicity and measured $\Sigma E_{\mathrm{T}}^{\mathrm{FCal}}$. Events with a charged particle multiplicity that falls out of this correlation are rejected. Figure 4.2 shows the N_{ch} vs $\Sigma E_{\mathrm{T}}^{\mathrm{FCal}}$ correlation froms MB events. Pile-up events have lower than expected $\Sigma E_{\mathrm{T}}^{\mathrm{FCal}}$ when the calorimeter is not properly zeroed for the current event when it's restoring from the previous events, and higher than expected $\Sigma E_{\mathrm{T}}^{\mathrm{FCal}}$ when it records more than current event's energy, such as gas splash. To determine the upper and lower bound of rejections, a Gaussian fitting is applied to the N_{trk} distributions for each $\Sigma E_{\mathrm{T}}^{\mathrm{FCal}}$ slice of 0.05 TeV. Events are rejected when they have a N_{ch} value outside of 5σ from the central value. The red dots on the left plot of Figure 4.2 are upper and lower 5σ boundaries.

A very stringent criteria were chosen to remove such events, excluding approximately 15% of events nearly independent of centrality. This rejection was made necessary due to the focus of this analysis on measuring correlations of small magnitudes and a smaller bunch spacing used in the ATLAS 2018 Pb+Pb dataset. The ATLAS 2015 dataset for Pb+Pb collisions at $\sqrt{s_{\mathrm{NN}}}$=5.02 TeV used a bunch spacing interval of 100 ns, while a bunch spacing interval of 75 ns was used for approximately half of the ATLAS 2018 dataset for higher event rate. See details for the determination of this out-of-time pileup rejection criteria in 5.

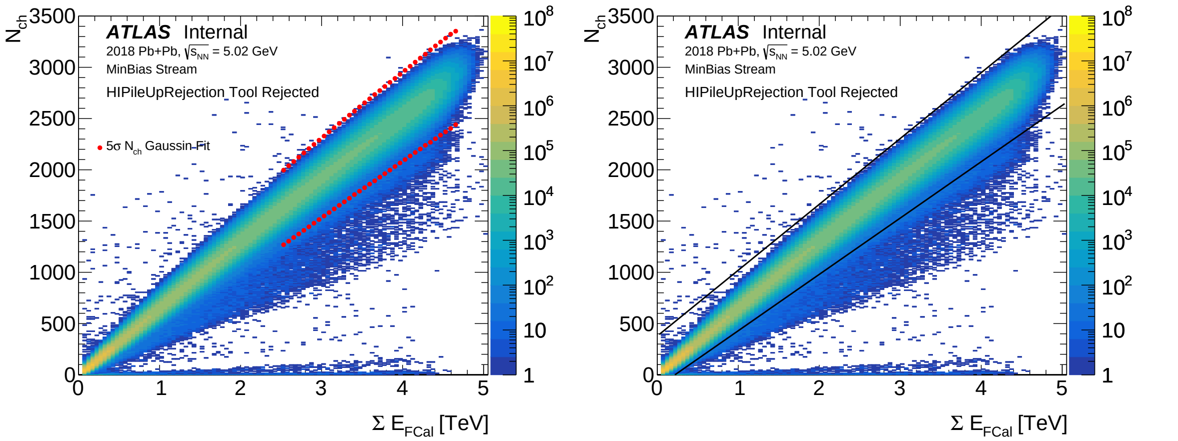

Figure 4.2: Left: Positive and negative 5σ fit of N_{ch} for each $\Sigma E_{\mathrm{T}}^{\mathrm{FCal}}$ bin shown in red dots with $\Sigma E_{\mathrm{T}}^{\mathrm{FCal}}$ ranging from 2.5 TeV to 4.7 TeV. Right: Linear function fitted to the 5σ range.

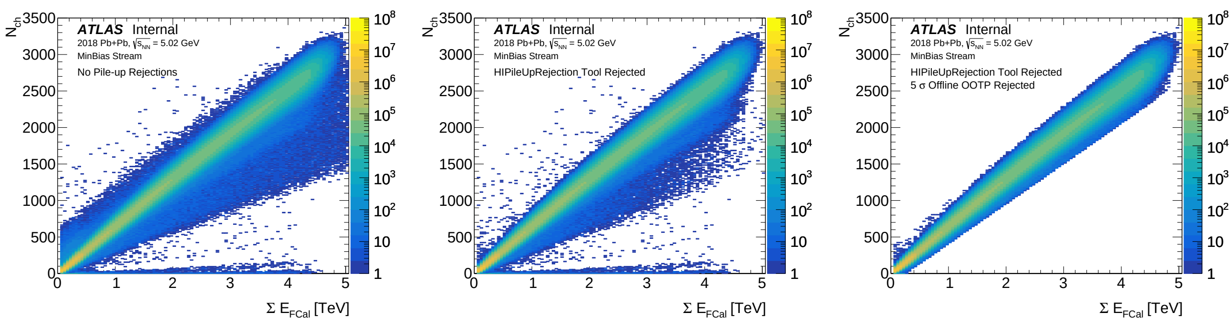

Figure 4.3: Left: All events before pile-up rejections. Middle: After only HIPileUpRejection tool rejections. Right: After HIPileUpRejectionTool and offline OOTP rejections.

Number of events rejected in each process is summarized in Table. 4.1. "Online selected" are number of events after ATLAS selections related to data taking qualities.

4.2.4 Monte Carlo samples

Monte Carlo (MC) simulations are used in this analysis to evaluate the track reconstruction performance. The MC sample used in this analysis consists of 4M events generated with HIJING [171]. After the generation, the flow effect was added to the simulated events using an "afterburner" [119] procedure, which implements the p_{T}, η, and centrality dependence of the v_n, as measured in the $\sqrt{s_{\mathrm{NN}}} = 2.76$ TeV Pb+Pb data [115], by artificially rearranging the ϕ positions of the generated particles. The detector response is simulated with FastSim [172] for calorimeters and GEANT4 [173, 174] for the ID. The simulated events are then reconstructed using the same configuration as data events.

Rejections (ordered)	Events Remaining	Percentage Remaining
Online selected	2566544465	100.00%
Offline pile-up rejection (this Section)	2566144098	99.98%
$\lvert z_{vtx}\rvert < 100$ mm	2484675872	96.81%
Additional pile-up rejection (See 5)	2111356566	82.26%

Table 4.1: Number of events after each additional rejection procedure defined for this analysis for PEB stream data and fraction of events selected as a percentage of the number of online selected events.

4.3 Track selection

Tracks of charged particles are reconstructed from hits in the inner detector using a track reconstruction algorithm that was optimized for the high hit density in heavy-ion collisions. The following requirements are met for tracks used in this analysis,

- $p_{\mathrm{T}} \ > 1\,\mathrm{GeV}$
- $|\eta| \ < 2.5$
- if expected require hit in the innermost layer (either IBL or if not expected in innermost Pixel layer)
- $N_{SCT} \ >= 8$
- $N_{Pixel} \ >= 2$
- $N_{SCTHoles} \ <= 1$
- $|d_0| <= 0.47 \times e^{(-0.15 \times p_{\mathrm{T}})} + 0.19 \times e^{(0.00034 \times p_{\mathrm{T}})}$ mm
- $|d_0/\sigma_{d_0}| < 3$
- $|z_0 \sin\theta/\sigma_{z_0 \sin\theta}| < 3$

This selection follows the ATLAS recommendation, with additional criteria, listed as the last three items in the list above, imposed on the impact parameters to suppress the contribution from secondary particles,[2] The last criteria is extracted from jet fragmentation study by ATLAS from Ref. [175], and the requirements on impact parameter significances were also used in ALTAS charged hadron spectra measurements available in Ref. [79].

[2]Primary particles are defined as particles with a mean lifetime $\tau > 0.3 \times 10^{-10}$ s either directly produced in the collisions or from subsequent decays of particles with a shorter lifetime. All other particles are considered to be secondary.

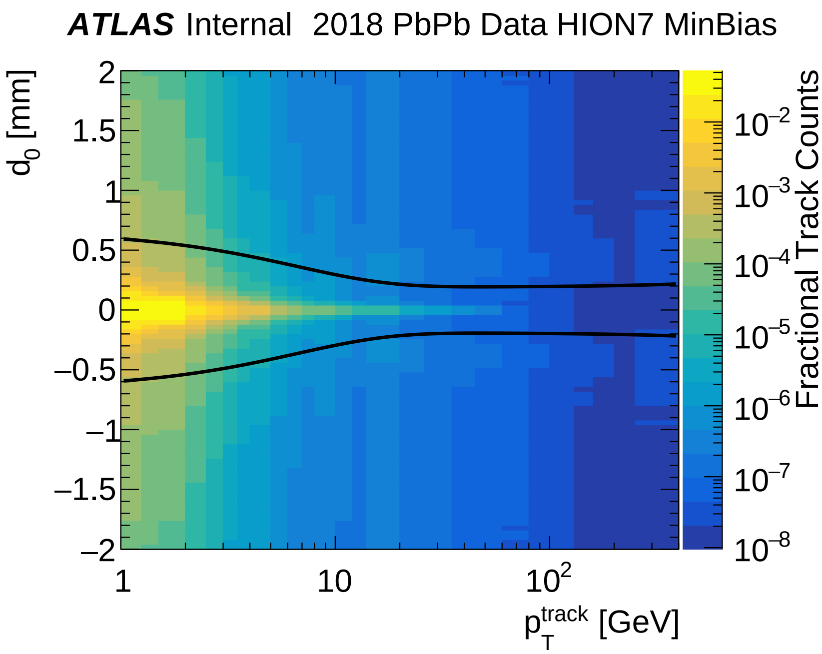

Figure 4.4: The parameterization of the $|d_0|$ cut as a function of charged-particle track p_T, denoted by p_T^{trk}, (black lines) and the d_0 distribution of all tracks before cuts used in this analysis.

4.3.1 Track weight

The detector non-uniformity and reconstruction inefficiency are corrected in this analysis with track weights. This section describes the three corrections done to correct for these detector effects: detector non-uniformity flattening, flow vector recentering, and track reconstruction efficiency.

Detector non-uniformity flattening

Tracks are also weighted for detector acceptance non-uniformity on a run-by-run basis. It is assumed that the tracks should distribute approximately uniformly after averaging over events in ϕ-direction. The detector is binned in each 0.1 binning in both η and ϕ directions, and the ratio is taken to be the weight and used in this analysis on a track-by-track basis, defined by the equation $w_{trk} = \frac{N^{\eta}}{64N^{\eta,\phi}}$. Figure 4.5 shows, from left to right, the unweighted raw track distributions in 2D η-ϕ directions, the weights calculated as described here, and the resultant weighted track distribution after track weighting.

The interaction point of each collision varies with respect to the detector coordinates along the beam direction, and this variation can be quantified as primary vertex z-direction component. Depending on the position of the collision vertex, the detector geometry seen by the particles differs. The η values of particles were reconstructed with respect to the primary vertex of each collision instead of absolute detector coordinate, and therefore the tracker acceptance map made by stacking η distributions of tracks from events of different z_{vtx} is smeared by this primary vertex fluctuations. To reduce this effect, in this analysis, track acceptance weight maps were divided into four z_{vtx} bin of 50 mm and applied separately to each event based on the z_{vtx} value. The maps for the same run is shown in Figure 4.6, where a clear difference in η coordinates is shown. Red dots in the map indicate a 0.1×0.1 η-ϕ grid in which the detector dead area is receiving very little signals and have a track weight $\omega_i > 20.0$. The entire η bin of width 0.1 containing such dead areas are excluded for each z_{vtx} event class.

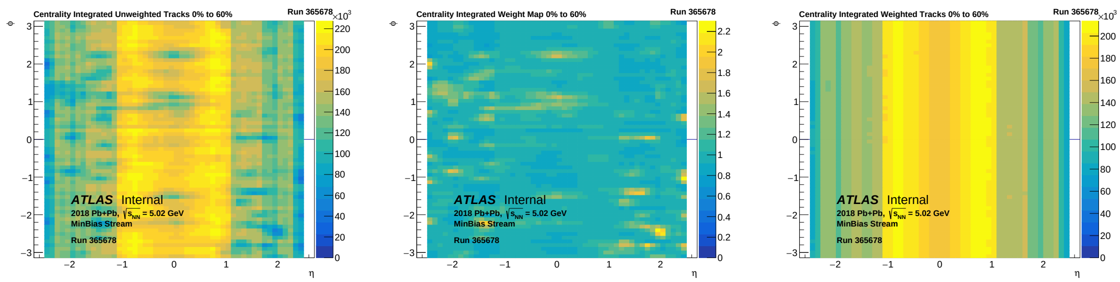

Figure 4.5: The example η-ϕ map before track weighting (left panel) extracted from one run 365678, the η-ϕ map of track weights (middle panel), and the same η-ϕ map after weights are applied.

Flow vector recentering

Following Ref. [176], in addition to the flattening weights from Section 4.3.1, the flow vectors Q_n measured for FCal are corrected for detector non-uniformity by subtracting the mean Q_n in each 1% centrality bin on a run-by-run basis:

$$Q_n = Q_n^{raw} - \langle Q_n^{raw} \rangle. \tag{4.1}$$

This correction centers both the real and imaginary parts of the Q_n vector at zero.

Figure 4.7 shows the mean flow vectors from all runs as a function of event centrality before and after this correction for $n = 2$–3 and for the positive and negative rapidity side of the FCal in the PEB dataset. Left panels correspond to real part of Q_n vectors while right panels show imaginary part of Q_n vectors. The real and imaginary parts of the Q_n vectors after the correction are centered at 0 over the centrality range used in this analysis (0–60% collisions).

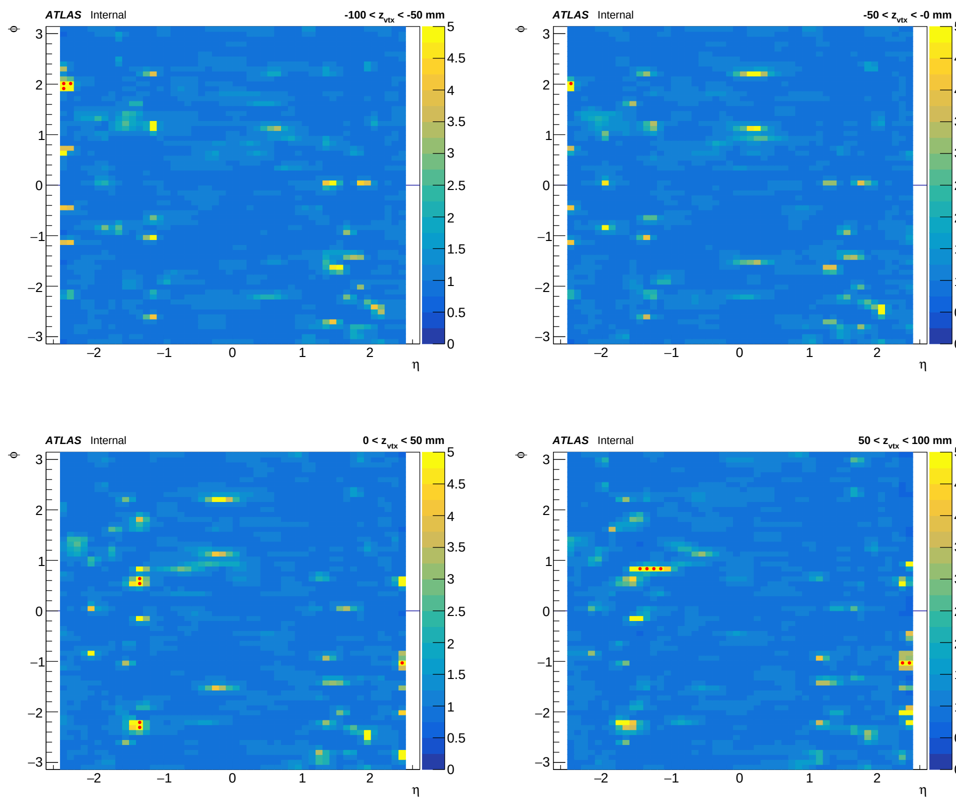

Figure 4.6: Acceptance weight maps of different z_{vtx} ranges. The left and right plot in top row is, respectively, $-100 < z_{vtx} < -50$ mm and $-50 < z_{vtx} < 0$ mm, and the left and right plot in the bottom row is, respectively, $0 < z_{vtx} < 50$ mm, and $50 < z_{vtx} < 100$ mm. Red dots show detector holes where the weight is greater than 20.0.

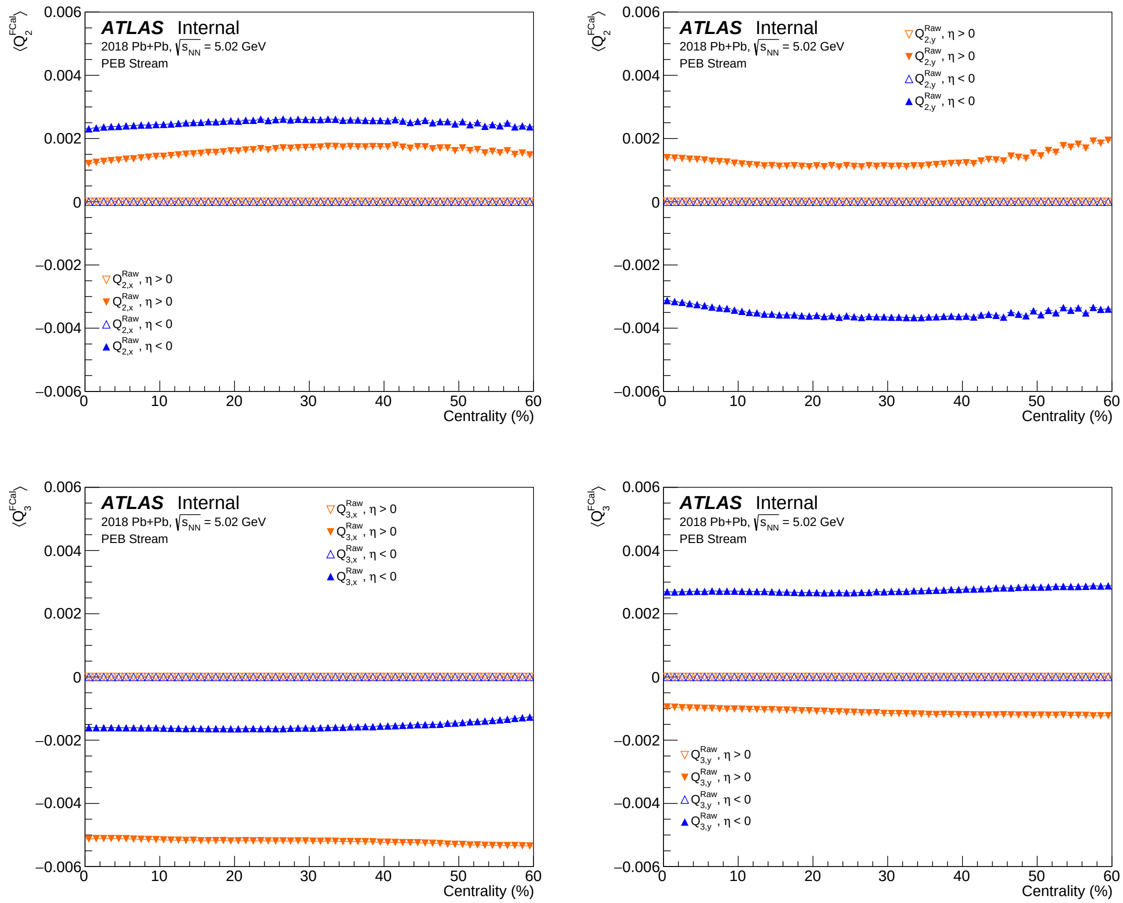

Figure 4.7: Mean Q-vector components as a function of centrality before and after calibration for harmonics n = 2-3 (from top to bottom). Open points show the raw values prior to the calibration and solid points show the calibrated values. The left panels show the real part of the Q_n-vectors and the right panels show the imaginary part of the Q_n-vectors.

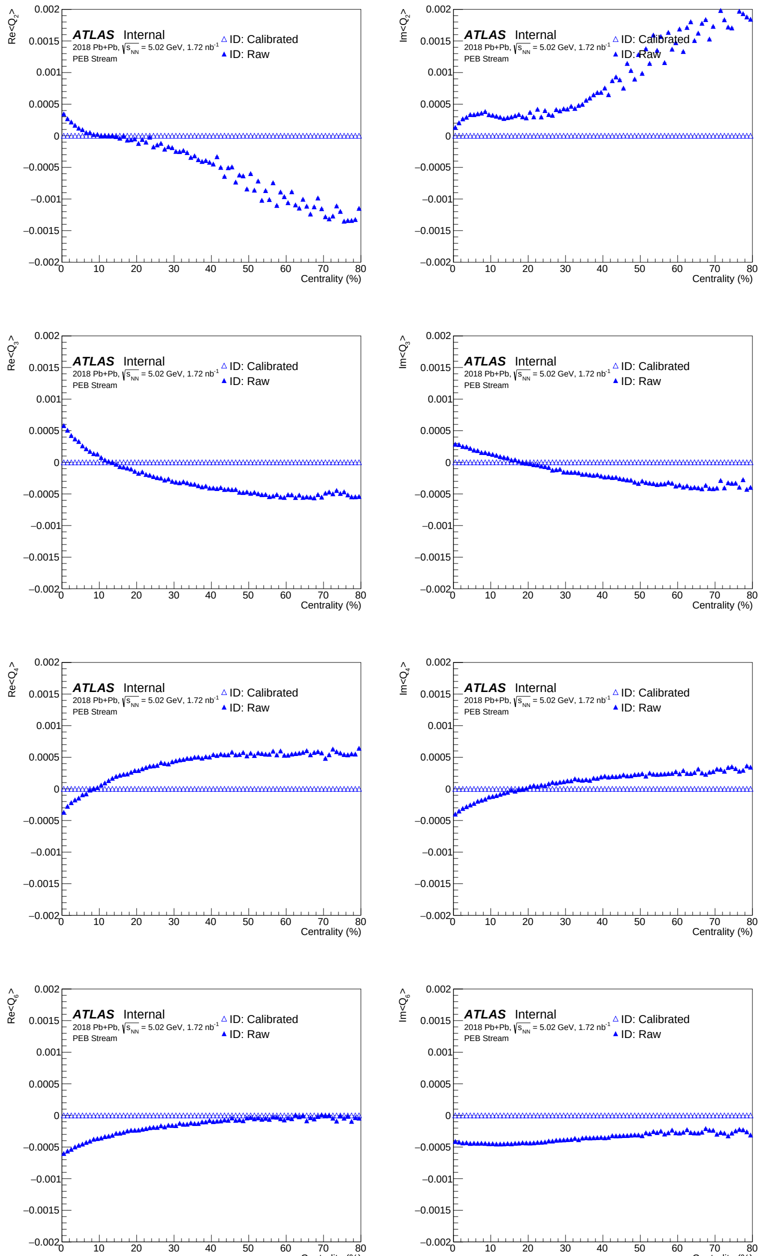

Figure 4.8: Mean Q-vector components of inner detector after run-by-run track weights correction as a function of centrality before and after calibration for harmonics $n = 2, 3, 4, 6$ (from top to bottom). Open points show the raw values prior to the calibration and solid points show the calibrated values. The left panels show the real part of the Q_n-vectors and the right panels show the imaginary part of the Q_n-vectors.

The inner detector acceptance non-uniformity is corrected by the same procedure as FCal recentering, by subtracting the mean ID Q_n vectors from Q_n^{raw}vectors used in calculation. The raw and calibrated Q_n vectors are shown in Figure 4.8, where shows Q_n vectors up to the 6^{th} order that are needed for the calculations of up to four-particle cumulants v_2 to v_3.

Track reconstruction efficiency

The track reconstruction efficiency for charged particles, ϵ, is measured using the MC samples as a function of $p_{\mathrm{T}}^{\mathrm{truth}}$ for two ranges of η as,

$$\epsilon(p_{\mathrm{T}}^{\mathrm{truth}}, \eta) = \frac{N(p_{\mathrm{T}}^{\mathrm{truth}})_{ch,reco|matched\ to\ truth}}{N(p_{\mathrm{T}}^{\mathrm{truth}})_{ch,truth}} \tag{4.2}$$

where the counting of denominators and numerators is done for each $p_{\mathrm{T}}^{\mathrm{truth}}$ and η bin. $N_{ch,truth}$ is the truth stable charged particles, and $N_{ch,reco|matchedtotruth}$ is the number of reconstructed charged particles which have a truth match. The reco-to-truth matching criteria is defined by the shared detector hits between track and truth charged particle trajectory as follow [177],

$$mc_{\mathrm{prob}} = \frac{10N_{\mathrm{pix}}^{\mathrm{common}} + 5N_{\mathrm{SCT}}^{\mathrm{common}} + N_{\mathrm{TRT}}^{\mathrm{common}}}{10N_{\mathrm{pix}}^{\mathrm{track}} + 5N_{\mathrm{SCT}}^{\mathrm{track}} + N_{\mathrm{TRT}}^{\mathrm{track}}} \tag{4.3}$$

where N_X^{common} are the number of hits in detector X in common between the truth and reconstructed track. N_X^{track} is the number of total hits in the reconstructed track. The matching threshold used is $mc_{\mathrm{prob}} > 0.3$.

The track reconstruction efficiencies are shown in Figure 4.9 to Figure 4.11. Track reconstruction shows a strong pseudorapidity dependence, shown in Figure 4.9, most obviously between the two regions divided by $|\eta| = 1.1$. Meanwhile, the centrality dependence of track reconstruction efficiency is on 4% level for track range $|\eta| < 1.1$ and on 8% level for track range $1.1 < |\eta| < 2.5$, as shown in Figure 4.10 To minimize fluctuations from the finite statistics in the MC samples, the efficiencies are fitted before applying to the tracking weights. The fitting are done for each centrality and pseudorapidity range as shown in Figure 4.10. A linear-log function is fitted against the efficiency for each rapidity bin, and the efficiencies are taken to be constant for $p_{\mathrm{T}} > 20$ GeV. This smooth efficiency correction is shown in the example in Figure 4.11 and applied to the data.

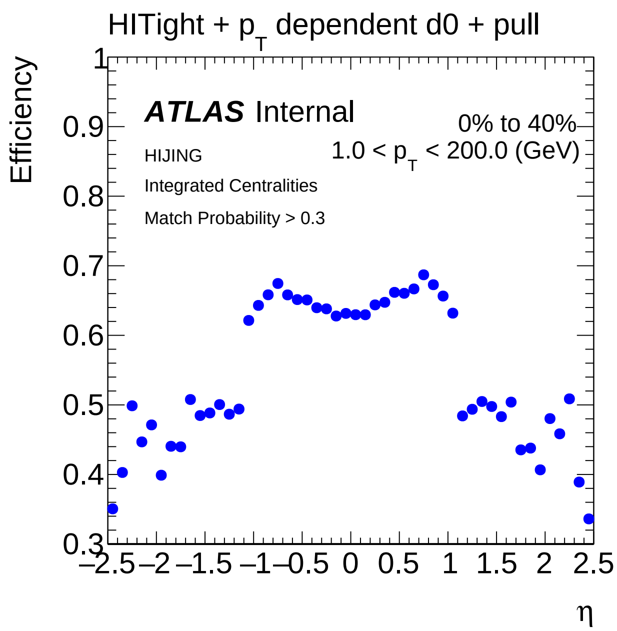

Figure 4.9: Track reconstruction efficiency versus η for HIJING MC

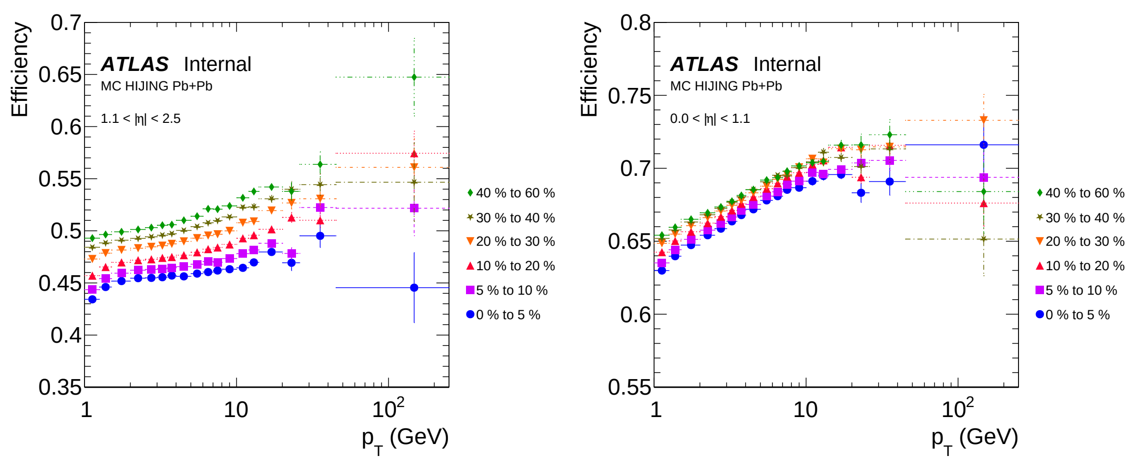

Figure 4.10: Track reconstruction efficiency for HIJING MC in two η ranges and different centralities.

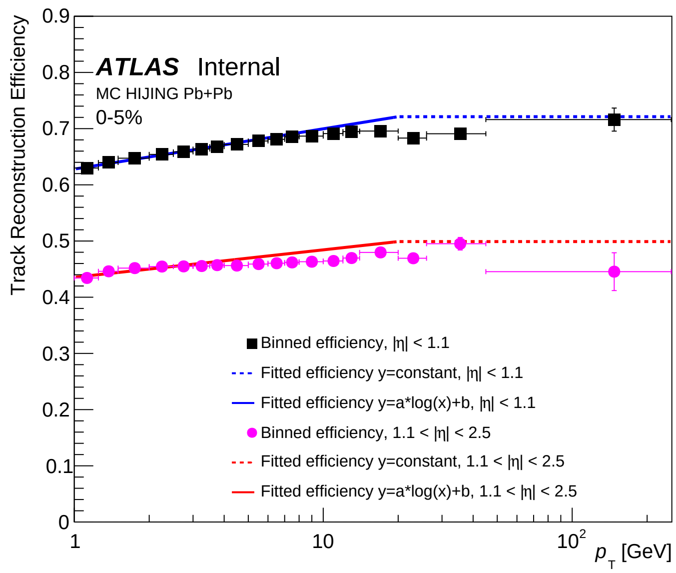

Figure 4.11: Fitted rack reconstruction efficiency for HIJING MC.

In order to obtain averaged quantities tracking inefficiencies have to be taken into account. Each sum over the tracks is weighted by the factor $1/\epsilon(\eta_{trk}, p_{\mathrm{T}}^{\mathrm{trk}})$ on a track-by-track basis.

4.4 Analysis method

4.4.1 Scalar-product method

The SP method is defined in Ref. [165], further discussed in Ref. [167], and results using this method for Pb+Pb and Xe+Xe collisions have been published by ATLAS in Refs. [122, 178]. It uses flow vectors $u_{n,j}$ and Q_n, where the $u_{n,j}$ for each object of interest j, for example, a charged-particle track or energy deposited at a single calorimeter tower, is defined as,

$$u_{n,j} = e^{in\phi_j}, \tag{4.4}$$

and the average flow vector Q_n of a subevent, for example, one side of the FCal, is defined as,

$$Q_n = \frac{1}{\sum_j \omega_j} \sum_j \omega_j u_{n,j}, \tag{4.5}$$

where the summation goes over all objects of interest in the subevent. In this analysis, flow vectors are evaluated separately for the two sides of the FCal and are denoted $Q_n^{N|P}$, where the N and P correspond to a pseudorapidity range of $-4.9 < \eta < -3.2$ and $3.2 < \eta < 4.9$, respectively. In this case, the sum in Equation 4.5 runs over the calorimeter towers with approximate granularity of $\Delta\eta \times \Delta\phi = 0.1 \times 0.1$ and the weights ω_j are the transverse energies E_{T} measured in the towers.

The azimuthal anisotropy coefficients using the this method, $v_n\{\mathrm{SP}\}$, are defined for each p_{T} and centrality interval as,

$$v_n\{\mathrm{SP}\} \equiv Re \frac{\left\langle u_{n,j} Q_n^{N|P^*} \right\rangle}{\sqrt{\left\langle Q_n^N Q_n^{P^*} \right\rangle}} = \frac{\left\langle |u_{n,j}||Q_n^{N|P}| \cos\left[n\left(\phi_j - \Psi_n^{N|P}\right)\right]\right\rangle}{\sqrt{\langle |Q_n^N||Q_n^P| \cos\left[n\left(\Psi_n^N - \Psi_n^P\right)\right]\rangle}}. \tag{4.6}$$

The numerator calculates the scalar product of the flow vector of the reference subevent, $Q_n^{N|P}$, and that of each charged-particle track, $u_{n,j}$, where the $\langle\rangle$ denotes an average over all tracks within the particular p_{T} interval from all events of the given centrality interval. This average is weighted for each track to correct for ID non-uniformity along the azimuthal direction and track reconstruction inefficiency. The denominator calculates the estimated detector resolutions, as determined using two reference subevents, positive and negative ends of the FCal, of the same event, and the $\langle\rangle$ denotes an average over all events in the given centrality interval. The flow vector Q_n^P (Q_n^N) of the calorimeter is correlated with tracks with $\eta < 0$ ($\eta > 0$).

This implementation of the SP method imposes a pseudorapidity gap of at least 3.2 between the reference Q_n and tracks, thus suppressing short-range non-flow correlations, such as those arising from resonance decays and same-jet correlations [123]. The $v_n\{\mathrm{SP}\}$ values are measured for ID pseudorapidity ranges of $|\eta| < 2.5$, $|\eta| < 1.1$, and $1.1 < |\eta| < 2.5$.

4.4.2 Multi-particle cumulant method

The multi-particle cumulant method using standard Q-cumulants, as applied in this analysis, is based on the generic framework described in Ref. [134]. The three-subevent Q-cumulants method extends this framework and was introduced in Ref. [152] for reference $v_n\{4\}$ measurements. This analysis extends the three-subevent Q-cumulant to p_{T}-differential $v_n\{4\}$ measurements. The following subsections will describe in basic definitions of cumulants, reference versus differential flow, followed by the standard Q-cumulants and three-subevent Q-cumulants.

Definitions of cumulants

For a single event, the n-th order two- and four-particle azimuthal correlators are denoted as $\langle 2\rangle_n$ and $\langle 4\rangle_n$, respectively, and defined as [133, 134],

$$\begin{aligned} \langle 2\rangle_n \equiv& \langle e^{in(\phi_1-\phi_2)}\rangle, \\ \langle 4\rangle_n \equiv& \langle e^{in(\phi_1+\phi_2-\phi_3-\phi_4)}\rangle, \end{aligned} \tag{4.7}$$

where ϕ_i represents the azimuthal angles of distinct charged-particle tracks. The different indices mean that two or four different particles are correlated (no self-correlation). The single bracket takes a weighted average over all possible combinations in a single event. The definition can be similarly extended to higher number of particles as long as the defined variable is invariant of coordinate system. The event averaged correlator $\langle\langle 2k\rangle\rangle_n$ is the event-average of $\langle 2k\rangle_n$ weighted by total weights of each event, defined as,

$$\begin{aligned} \langle\langle 2\rangle\rangle_n \equiv& \langle\langle e^{in(\phi_1-\phi_2)}\rangle\rangle = \frac{\sum_i^{events}(W_{(2)})_i\langle 2\rangle_i}{\sum_i^{events}(W_{(2)})_i}, \\ \langle\langle 4\rangle\rangle_n \equiv& \langle\langle e^{in(\phi_1+\phi_2-\phi_3-\phi_4)}\rangle\rangle = \frac{\sum_i^{events}(W_{(4)})_i\langle 4\rangle_i}{\sum_i^{events}(W_{(4)})_i}, \end{aligned} \tag{4.8}$$

where $W_{(2k)}$ is the event weight for the corresponding correlator pair $\langle 2k \rangle_n$. It can be easily shown that $\langle\langle 2k \rangle\rangle_n$ gives to the $2k$ moments of v_n since,

$$\begin{aligned}\langle\langle 2k \rangle\rangle_n \equiv& \langle\langle e^{in(\phi_1+\ldots+\phi_k-\phi_{k+1}-\ldots-\phi_{2k})} \rangle\rangle = \langle\langle e^{in(\phi_1-\Psi_n+\ldots+\phi_k-\Psi_n-\phi_2+\Psi_n-\ldots-\phi_{2k}+\Psi_n)} \rangle\rangle \\ =& \langle \langle e^{in(\phi_1-\Psi_n)} \rangle \ldots \langle e^{-in(\phi_{2k}-\Psi_n)} \rangle \rangle = \langle v_n^{2k} \rangle.\end{aligned} \tag{4.9}$$

Therefore we can now define the $2k$-th order cumulants of v_n, which attempt to extract genuine $2k$-particle correlations without lower-order correlations, and the corresponding $v_n\{2k\}$ using the multi-particle correlators as,

$$\begin{aligned}c_n\{2\} \equiv& \langle\langle e^{in(\phi_1-\phi_2)} \rangle\rangle - \langle\langle e^{in\phi_1} \rangle\rangle \langle\langle e^{-in\phi_2} \rangle\rangle = (v_n\{2\})^2 \\ c_n\{4\} \equiv& \langle\langle 4 \rangle\rangle - 2\langle\langle 2 \rangle\rangle^2 = \langle v_n^4 \rangle - 2\langle v_n^2 \rangle^2 = 2\sigma^2(v_n^2) - \langle v_n^4 \rangle = -(v_n\{4\})^4,\end{aligned} \tag{4.10}$$

where $\sigma^2({v_n}^2)$ is the variance of the second moment of v_n. The cumulants in this definition subtracted lower order correlator contribution to get an unbiased estimation [132]. Note the terms subtracted from $\langle\langle\ \rangle\rangle_2$are zero for a perfectly uniform detector. In this analysis, detector effects are accounted for using particle weights as explained in Section 4.3.1. In this definition, $c_n\{4\}$ must be negative to yield a real-valued $v_n\{4\}$. If the flow variable does not have event-by-event fluctuations, $c_n\{4\}$ is negative and $v_n\{4\}$ measures the true flow variable. Sign-change behavior can arise from different sources including non-Gaussianity in the underlying distribution and centrality fluctuations of events [149, 179]. To represent the case where $c_n\{4\}$ is negative in the plot with real axis, the following sign change convention from Ref. [149] is used,

$$v_n\{2\} = \sqrt{c_n\{2\}}, \quad v_n\{4\} = \begin{cases} \sqrt{-c_n\{4\}} & c_n\{4\} \leq 0 \\ -\sqrt{c_n\{4\}} & c_n\{4\} > 0, \end{cases} \tag{4.11}$$

Reference flow and differential Flow

The experimental measurement of p_{T} dependent differential flow harmonics $v_n(p_{\mathrm{T}})$ in the statistically limited high p_{T} region is measured utilizing a correlator of one charged particle of interest (POI) in given p_{T} range to one or more particles with no p_{T} requirement. Denoting the event-averaged differential $2k$-particle correlation as $\langle\langle 2k' \rangle\rangle_n$, the differential cumulants $d_n\{2\}(p_{\mathrm{T}})$, $d_n\{4\}(p_{\mathrm{T}})$ and different flow $v_n\{2\}(p_{\mathrm{T}})$, $v_n\{4\}(p_{\mathrm{T}})$ are derived by Ref. [132, 133] to be,

$$\begin{aligned}d_n\{2\}(p_{\mathrm{T}}) =& \langle\langle 2' \rangle\rangle_n, \\ d_n\{4\}(p_{\mathrm{T}}) =& \langle\langle 4' \rangle\rangle_n - 2\langle\langle 2' \rangle\rangle_n \langle\langle 2 \rangle\rangle_n,\end{aligned} \tag{4.12}$$

$$
\begin{aligned}
v_n\{2\}(p_{\mathrm{T}}) =& \frac{d_n\{2\}(p_{\mathrm{T}})}{(c_n\{2\})^{1/2}}, \\
v_n\{4\}(p_{\mathrm{T}}) =& \frac{-d_n\{4\}(p_{\mathrm{T}})}{(-c_n\{4\})^{3/4}},
\end{aligned}
\tag{4.13}
$$

where $c_n\{4\}$ and $c_n\{2\}$ are computed over soft reference particles (REF) in p_{T} range 1–5 GeV.

Depending on the shape of the underlying reference $v_n\{4\}$ distributions, $c_n\{4\}$ could change sign across different centrality ranges. Values of $c_2\{4\}$ have been observed to become positive in the 2% most central collisions, giving an imaginary reference $v_n\{4\}$ [149]. Therefore for this analysis, the centrality interval 0–5% is omitted for the differential $v_2\{4\}$ measurements to ensure that the values of reference $v_2\{4\}$, thus values of the denominator in the differential $v_4\{2\}$ formula, are always real-valued.

Standard Q-cumulants

In the standard Q-cumulants, all tracks within the pseudorapidity range of $|\eta| < 2.5$ are used. As it is computationally challenging to calculate four-particle correlations using nested loops, the correlators in this analysis are computed using the Q-cumulants, following the generic framework from Ref. [134], with the k-th power weighted flow vector $Q_{n,k}$[3], defined as,

$$
Q_{n,k} = \sum_{j=1}^{M} \omega_j^k u_{n,j}, \tag{4.14}
$$

where M is the charged-particle multiplicity of the event, $u_{n,j}$ is the n-th order flow vector of a single track with corresponding weight ω_j. The single-event 2- and 4-particle correlations have the following formula [133,

[3]The notation $Q_{n,k}$ defined for the MPC method should be distinguished from the notation Q_n defined for the SP method. $Q_{n,k}$ is a weighted summation of $u_{n,j}$, whereas Q_n is a weighted average of $u_{n,j}$ computed by the weighted summation of $u_{n,j}$ normalized by the total weight of $u_{n,j}$.

134] [4],

$$
\begin{aligned}
\langle 2\rangle_n =& \big[|Q_{n,1}|^2 - Q_{0,2}\big]/W_{(2)}, \\
W_{(2)} =& Q_{0,1}^2 - Q_{0,2}, \\
\langle\langle 2\rangle\rangle_n =& \frac{\sum_{i=1}^{N}\langle 2\rangle_n (W_{(2)})_i}{\sum_{i=1}^{N}(W_{(2)})_i}, \\
\langle 4\rangle_n =& \big[|Q_{n,1}|^4 + |Q_{2n,2}|^2 - 2Re[Q_{2n,2}Q_{-n,1}Q_{-n,1}] + 8Re[Q_{n,3}Q_{-n,1}] \\
& - 4Q_{0,2}|Q_{n,1}|^2 - 6Q_{0,4} + 2Q_{0,2}^2\big]/W_{(4)}, \\
W_{(4)} =& Q_{0,1}^4 - 6Q_{0,2}Q_{0,1}^2 + 8Q_{0,3}Q_{0,1} + 3Q_{0,2}^2 - 6Q_{0,4}, \\
\langle\langle 4\rangle\rangle_n =& \frac{\sum_{i=1}^{N}\langle 4\rangle_n (W_{(4)})_i}{\sum_{i=1}^{N}(W_{(4)})_i}.
\end{aligned}
\tag{4.15}
$$

Equation 4.15 defines multi-particle correlators for reference flow. The particles used for reference flow are soft particles, and are referred to as reference particles (REF). The p_{T} differential particle is referred to as particles of interest (POI). In this analysis, particles of p_{T} range 1 to 5 GeV are used as REF. Since this analysis measures p_{T} dependent v_n from 1.0 GeV, a particle in the REF range can also be a POI when correlated with other REF. For a given p_{T} range, if a particle can be both POI and REF, they are referred to as BOTH. In the standard Q-cumulants, all tracks within the pseudorapidity range of $|\eta| < 2.5$ are used. To compute the differential correlator $\langle 2'\rangle_n$ and $\langle 4'\rangle_n$, the following flow vectors are introduced. The POI flow vector is defined as,

$$
p_{n,k} = \sum_{i=1}^{M_p} \omega_i^k q_{n,i}, \tag{4.16}
$$

where M_p is multiplicity of POI particles of given p_{T} bin in this event. The BOTH flow vector is defined as,

$$
q_{n,k} = \sum_{i=1}^{M_q} \omega_i^k q_{n,i}, \tag{4.17}
$$

where M_q is multiplicity of BOTH particles of given p_{T} bin in this event. The differential correlators are

[4] Ref.[133] has a typo in their original formula for $\langle 4\rangle_n$ (Equation B16 in the paper), where the sign for the last term should have been "+". This has been confirmed by the analysis team's communication with the author.

defined as,

$$
\begin{aligned}
\langle 2' \rangle_n =& \big[p_{n,1}Q_{n,1} - q_{0,2}\big]/W_{(2')}, \\
W_{(2')} =& p_{0,1}Q_{0,1} - q_{0,2}, \\
\langle\langle 2' \rangle\rangle_n =& \frac{\sum_{i=1}^{N} \langle 2' \rangle_n (W_{(2')})_i}{\sum_{i=1}^{N} (W_{(2')})_i}, \\
\langle 4' \rangle_n =& \big[p_{n,1}Q_{n,1}Q_{-n,1}Q_{-n,1} - q_{2n,2}Q_{-n,1}Q_{-n,1} - p_{n,1}Q_{n,1}Q_{-2n,2} \\
& - 2Q_{0,2}p_{n,1}Q_{-n,1} - 2q_{0,2}|Q_{n,1}|^2 + 7q_{n,3}Q_{-n,1} - Q_{n,1}q_{-n,3} \\
& + q_{2n,2}Q_{-2n,2} + 2p_{n,1}Q_{-n,3} + 2q_{0,2}Q_{0,2} - 6q_{0,4}\big]/W_{(4')}, \\
W_{(4')} =& p_{0,1}[Q_{0,1}^3 - 3Q_{0,1}Q_{0,2} + 2Q_{0,3}] - 3[q_{0,2}(Q_{0,1}^2 - Q_{0,2}) + 2(q_{0,4} - q_{0,3}Q_{0,1})], \\
\langle\langle 4' \rangle\rangle_n =& \frac{\sum_{i=1}^{N} \langle 4' \rangle_n (W_{(4')})_i}{\sum_{i=1}^{N} (W_{(4')})_i}.
\end{aligned}
\tag{4.18}
$$

Now all correlator pairs required for Equation 4.10 and Equation 4.12 have been calculated, the cumulants c_n, $d_n(p_\mathrm{T})$ and harmonics v_n and $v_n(p_\mathrm{T})$ can be calculated using formula Equation 4.11 and Equation 4.13. To verify the math used in Q-cumulant method, 2- and 4-particle cumulants were calculated using nested loops in an event with 20 tracks. The results are shown to be identical with Q-cumulant method. The same verification is also done in 3-subevent Q-cumulant method that will be explained in the next section.

Three-subevent Q-cumulants

To suppress further the non-flow correlations, rapidity gaps are applied in the MPC method using the three-subevent Q-cumulant [149, 152, 169] The ID acceptance is divided equally into three subevents of non-overlapping pseudorapidity ranges, indexed as a, b and c. The pseudorapidity ranges of these three subevents are as follows,

$$
-2.5 < \eta_a < -\frac{2.5}{3},\ |\eta_b| < \frac{2.5}{3},\ \frac{2.5}{3} < \eta_c < 2.5. \tag{4.19}
$$

$$
\begin{aligned}
\langle 2 \rangle_n^{a|b} \equiv& \langle e^{in(\phi_a - \phi_b)} \rangle \\
\langle 4 \rangle_n^{a,\,a|b,\,c} \equiv& \langle e^{in(\phi_a + \phi'_a - \phi_b - \phi_c)} \rangle
\end{aligned}
\tag{4.20}
$$

where ϕ_{sub} indicates the azimuthal angle of a particle from the subevent sub. The prime label on azimuthal angle ϕ'_a indicates that this is a second particle taken from subevent a, and it is a different particle from the first particle from subevent a.

By permuting the subevents, there are six configurations available for the 4-particle correlators,

$$\text{Group A}\begin{cases} a,a|b,c \\ b,b|c,a \\ c,c|a,b \end{cases} \quad \text{Group B}\begin{cases} a,b|a,c \\ b,c|b,a \\ c,a|c,b \end{cases} \tag{4.21}$$

Configurations from Group A are composed of two pairs of 2-particle correlations which correlate 2 different subevents. For example, configuration $a,a|b,c$ can be decomposed into $a|b$ and $a|c$. Group B configurations do contain same-subevent correlations and will boost local non-flow contributions by including $a|a$ type of 2-particle correlators. Therefore, configurations from Group B are not included in the analysis.

The k-th power weighted flow vector for subevent a, $Q^a_{n,k}$, is defined as,

$$Q^a_{n,k} = \sum_{j=1}^{M_a} \omega_j^k u_{n,j} \tag{4.22}$$

where M_a is the charged-particle multiplicity within subevent a. The three-subevent single-event reference correlators and their corresponding event weights $W_{(2)}$ and $W_{(4)}$, calculated also using flow vectors where $n=0$, are defined as,

$$\begin{aligned} \langle 2\rangle_n^{a|b} &\equiv \langle e^{in(\phi_a-\phi_b)}\rangle = Re\frac{Q^a_{n,1}Q^b_{-n,1}}{W^{a|b}_{(2)}}, \\ W^{a|b}_{(2)} &= Q^a_{0,1}Q^b_{0,1}, \\ \langle\langle 2\rangle\rangle_n^{a|b} &= \frac{\sum_{i=1}^N \langle 2\rangle_n^{a|b}(W^{a|b}_{(2)})_i}{\sum_{i=1}^N (W^{a|b}_{(2)})_i}. \end{aligned} \tag{4.23}$$

$$\begin{aligned} \langle 4\rangle_n^{a,\,a|b,\,c} &\equiv \langle e^{in(\phi_a+\phi'_a-\phi_b-\phi_c)}\rangle = Re\frac{[(Q^a_{n,1})^2-Q^a_{2n,2}]Q^b_{-n,1}Q^c_{-n,1}}{W^{a,\,a|b,\,c}_{(4)}}, \\ W^{a,\,a|b,\,c}_{(4)} &= [(Q^a_{0,1})^2-Q^a_{0,2}]Q^b_{0,1}Q^c_{0,1}, \\ \langle\langle 4\rangle\rangle_n^{a,\,a|b,\,c} &= \frac{\sum_{i=1}^N \langle 4\rangle_n^{a,\,a|b,\,c}(W^{a,\,a|b,\,c}_{(4)})_i}{\sum_{i=1}^N (W^{a,\,a|b,\,c}_{(4)})_i}. \end{aligned} \tag{4.24}$$

where the superscript in event weights $W_{(2)}$ and $W_{(4)}$ corresponds to the track configuration of correlators. Other configurations in Group A can be written by permutation of the subevent indices a,b and c.

The reference cumulants $c_n^{a,\,a|b,\,c}\{4\}$ are calculated from the event-averaged correlators as,

$$c_n^{a,\,a|b,\,c}\{4\} = \langle\langle 4\rangle\rangle_n^{a,\,a|b,\,c} - 2\langle\langle 2\rangle\rangle_n^{a|b}\langle\langle 2\rangle\rangle_n^{a|c}. \tag{4.25}$$

To boost the statistics and reduce η-dependent detector bias, the subevent index a is interchanged with b and c to create two additional configurations. The weighted average of these three measurements is used to obtain three-subevent reference cumulants $c_n^{\text{3-sub}}\{4\}$, computed as,

$$c_n^{\text{3-sub}}\{4\} \equiv \frac{(\Sigma W_{(4)}^{a,\,a|b,\,c})c_n^{a,\,a|b,\,c}\{4\} + (\Sigma W_{(4)}^{b,\,b|c,\,a})c_n^{b,\,b|c,\,a}\{4\} + (\Sigma W_{(4)}^{c,\,c|a,\,b})c_n^{c,\,c|a,\,b}\{4\}}{\Sigma W_{(4)}^{a,\,a|b,\,c} + \Sigma W_{(4)}^{b,\,b|c,\,a} + \Sigma W_{(4)}^{c,\,c|a,\,b}} \tag{4.26}$$

This is computed for each centrality bin where $W_{(4)}^{a}$re summed over events in that centrality bin. The formulas for these reference correlators, presented with different notations, are detailed in Ref. [152].

Each reference correlator configuration of $\langle 2\rangle_n$ is subdivided into two configurations of the differential flow correlators by choosing each of the two particles as the POI. Similarly, each reference correlator configuration of $\langle 4\rangle_n$ is subdivided into four differential correlator configurations. For subevent a, the n-th order harmonic k-th power weighted flow vector using only POIs is denoted by $p_{n,k}^{a}$, which is defined for a given p_{T} interval. Similarly, the flow vector made from particles that are both REF and POI for a given p_{T} interval is denoted by $q_{n,k}^{a}$ for subevent a. These two flow vectors are calculated similarly to Equation 4.22. For $\langle 4\rangle_n$, two formulas were provided: one for when the POI comes from a subevent within which two particles are selected, as shown in Equation 4.28, and the other for when the POI is the only particle from its subevent, as shown in Equation 4.29. A prime in the subevent index indicates that the subevent from which the POI of this correlator is selected.

$$\begin{aligned}
\langle 2'\rangle_n^{a'|b} &= Re\frac{p_{n,1}^{a}Q_{-n,1}^{b}}{W_{(2')}^{a'|b}},\\
W_{(2')}^{a'|b} &= p_{0,1}^{a}Q_{0,1}^{b},\\
\langle\langle 2'\rangle\rangle_n^{a'|b} &= \frac{\sum_{i=1}^{N}\langle 2'\rangle_n^{a'|b}(W_{(2')}^{a'|b})_i}{\sum_{i=1}^{N}(W_{(2')}^{a'|b})_i}.
\end{aligned} \tag{4.27}$$

$$\begin{aligned}
\langle 4'\rangle_n^{a',\,a|b,\,c} &= \langle 4'\rangle_n^{a,\,a'|b,\,c} = Re\frac{(p_{n,1}^{a}Q_{n,1}^{a} - q_{2n,2}^{a})Q_{-n,1}^{b}Q_{-n,1}^{c}}{W_{(4)}^{a',\,a|b,\,c}},\\
W_{(4)}^{a',\,a|b,\,c} &= (p_{0,1}^{a}Q_{0,1}^{a} - q_{0,2}^{a})Q_{0,1}^{b}Q_{0,1}^{c}.
\end{aligned} \tag{4.28}$$

$$\begin{aligned}
\langle 4'\rangle_n^{a,\,a|b',\,c} &= Re\frac{[(Q_{n,1}^{a})^2 - Q_{2n,2}^{a}]p_{-n,1}^{b}Q_{-n,1}^{c}}{W_{(4)}^{a,\,a|b',\,c}},\\
W_{(4)}^{a,\,a|b',\,c} &= [(Q_{0,1}^{a})^2 - Q_{0,2}^{a}]p_{0,1}^{b}Q_{0,1}^{c}.
\end{aligned} \tag{4.29}$$

$$\langle\langle 4'\rangle\rangle_n^{\text{config}} = \frac{\sum_{i=1}^{N}\langle 4\rangle_n^{\text{config}}(W_{(4)}^{\text{config}})_i}{\sum_{i=1}^{N}(W_{(4)}^{\text{config}})_i}. \tag{4.30}$$

Other configurations can be written similarly by permuting the subevent indices. Similar to Equation 4.25, the differential cumulants are defined as,

$$d_n^{a',\,a|b,\,c}\{4\}(p_{\mathrm{T}}) = \langle\langle 4' \rangle\rangle_n^{a',\,a|b,\,c} - 2\langle\langle 2' \rangle\rangle_n^{a'|b} \langle\langle 2 \rangle\rangle_n^{a|c}. \tag{4.31}$$

Each of the three configurations for the reference cumulant corresponds to four configurations for the differential cumulant. The averaged differential cumulant $d_n^{\text{3-sub}}\{4\}(p_{\mathrm{T}})$ can be written in the same manner as Equation 4.26 as the weighted average of all 12 sub-configurations (from three configurations of reference flow cumulant) of $\langle\langle 4' \rangle\rangle_n$, which will not be written out explicitly here. The three-subevent Q-cumulant $v_n\{4\}$, denoted by $v_n^{\text{3-sub}}\{4\}$, is defined as,

$$v_n^{\text{3-sub}}\{4\}(p_{\mathrm{T}}) = \frac{-d_n^{\text{3-sub}}\{4\}(p_{\mathrm{T}})}{(-c_n^{\text{3-sub}}\{4\})^{3/4}}. \tag{4.32}$$

Event combination procedure

In this analysis, the event-averaged cumulants $c_n\{4\}$ and $d_n\{4\}(p_{\mathrm{T}})$ are firstly computed in narrower centrality intervals, and then averaged toward wider centrality intervals in which the final results of v_n are presented. The choice of initial centrality intervals in which the cumulants are calculated defines an event combination procedure. By default, cumulants are calculated within 1% centrality percentiles before combining. For comparison, cumulants are also calculated within 2% centrality percentiles before combining and directly calculated within the quoted centrality intervals for results. Results obtained following these procedures are referred to later as $\langle 1\% \rangle$, $\langle 2\% \rangle$ and $\langle 10\% \rangle$, respectively. The final results are presented in 5% centrality intervals for the most central 10% of events, and in 10% centrality intervals for all other events.

The choice of event combination procedure can affect the measured v_n in different ways. High-p_{T} particle production is biased toward more central events, and therefore, for quantities measured using high-p_{T} charged particles, an average over a wide centrality interval is biased toward the more central edge of the interval. Also, the event-by-event fluctuations in the underlying azimuthal anisotropy distributions are sensitive to the event combination procedure. Therefore, observables are sensitive to the choice of the initial centrality intervals in the p_{T} range where the fluctuations are significant in comparison to the mean in the underlying distribution. These fluctuations can stem from the initial state geometry or non-flow effects. It has been shown in measurements of reference v_n that the centrality resolution of the initial centrality intervals affects the multi-particle cumulant measurements of v_n due to fluctuations in non-flow effects [149, 152].

4.5 Systematical uncertainties

The systematic uncertainties in this analysis arise form the choice of the rapidity ranges used in reference v definitions, variation of tracks selection criteria, detector material uncertainties affecting reconstruction efficiency and overall imperfections in the detector response. These uncertainties are evaluated by first repeating the analysis with alternative pseudorapidity ranges, the selection criteria on tracks, or particle weights, and then calculating the absolute differences in the measured v_n values from the default results. In addition to $v_n\{\text{SP}\}$ values, the difference between two $v_n\{\text{SP}\}$ measurements using tracks with non-overlapping pseudorapidity ranges is also calculated. Only contributions of systematic uncertainties that are uncorrelated between the two $v_n\{\text{SP}\}$ measurements of non-overlapping ranges are included in this quantity. For this analysis, the charged-particle η-asymmetry and residual sine term uncertainties use non-overlapping parts of sub-detectors and are therefore considered uncorrelated.

4.5.1 Systematical uncertainties of scalar product method

The following variations in analysis methods are done to estimate systematic uncertainties for the scalar product method.

- Residual sine term
- Uncertainty in the tracking efficiency correction fitting procedure
- The effect of η-range of the FCal used to determine the Q_n vectors
- Deviation from η-symmetric results
- Variation in the track selection
- Uncertainty due to centrality determination

The systematic uncertainties are calculated as deviations from the nominal values and propagated as absolute uncertainties. All sources of systematic uncertainties are taken as uncorrelated, and the total systematic uncertainty is calculated as the quadrature sum of the individual components. The upper systematic uncertainty is determined by summing the positive deviations, while the lower is determined by summing over the negative deviations.

p_{T} and centrality rebinning in systematics

Systematic uncertainty terms are affected by limited statistics in high p_{T} and peripheral events. To reduce the effect of statistical fluctuations in systematic uncertainty evaluations, some bins are merged together in

p_{T} and centrality before computing the systematic uncertainties.

A summary of p_{T} rebinning is shown in Table. 4.2 The p_{T} limits only show merged bin edges while other bins stay the same. For example, $8, 14, 35, 100$ means bins within 8 GeV and 100 GeV are merged according to the indicated bin edges 14 and 35 GeV only. Centrality rebinning are indicated in each subsection of systematic uncertainty items.

Systematic Uncertainty	p_{T} [GeV] bins for $v_2\{\mathrm{SP}\}$	p_{T} [GeV] bins for $v_3\{\mathrm{SP}\}$
Residual Sine Term	[8, 14, 35, 400]	[8, 14, 100]
tracking efficiency correction	[8, 14, 35, 400]	[8, 14, 100]
η-range of the FCal	[8, 14, 35, 400]	[8, 14, 100]
η-symmetric	[8, 14, 35, 400]	[8, 14, 35, 100]
track selection	[8, 14, 35, 400]	[8, 14, 100]
centrality variation	[8, 14, 35, 400]	[8, 14, 35, 100]

Table 4.2: Summary of p_{T} and centrality rebinning for $v_2\{\mathrm{SP}\}$ and $v_3\{\mathrm{SP}\}$.

Residual sine term

For a detector with perfect azimuthal symmetry, the imaginary part of the scalar product should be zero. Therefore, the imaginary part of the scalar product, referred to as the residual sine term, is used as a systematic uncertainty,

$$Im\{v_n\} = \frac{Im\langle q_{n,j} Q_n^{N|P^*} \rangle}{R_n} = \frac{\langle |q_{n,j}||Q_n^{N|P}| \sin n(\phi_j - \Psi_n^{N|P}) \rangle}{R_n} \tag{4.33}$$

Figures 4.12 to 4.13 show the relative $Im\{v_n \}$ as a function of p_{T} for v_2, and v_3.

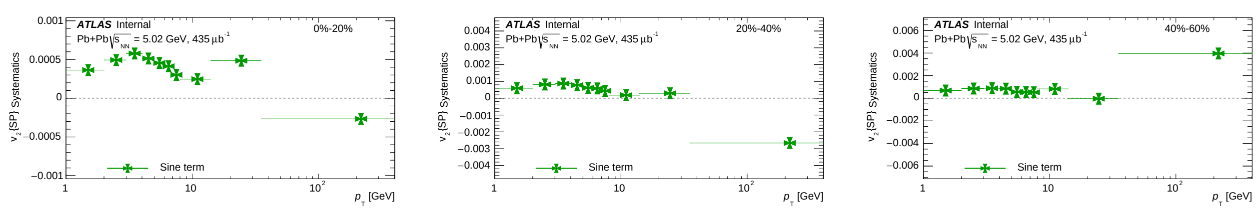

Figure 4.12: The $Im\{v_2\}$ as a function of p_{T} for the combined datasets in respective p_{T} range and centrality binning.

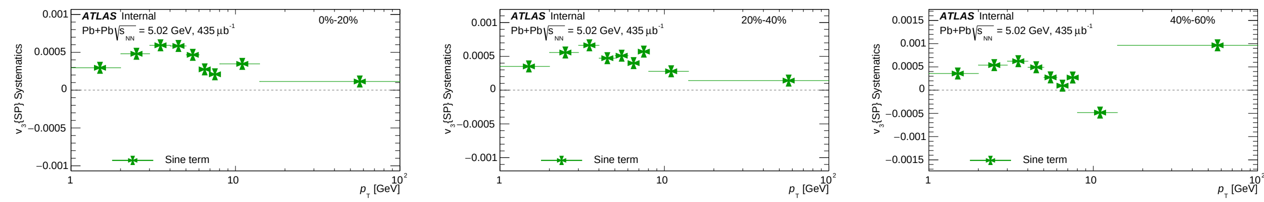

Figure 4.13: The $Im\{v_3\}$ as a function of $p_{\rm T}$ for the combined datasets in respective $p_{\rm T}$ range and centrality binning.

Tracking efficiency correction

Due to the random orientation of the Q_n vectors for each event with respect to the ID and the slow change in the tracking efficiency with respect to the $p_{\rm T}$ bin sizes in this measurement, the analysis is expected to be minimally sensitive to the tracking efficiency correction. Thus, the uncertainty associated with the tracking efficiency correction is estimated by not correcting for the tracking efficiency at all.

Figs. 4.14–4.15 show the effect of this correction for v_2 to v_3.

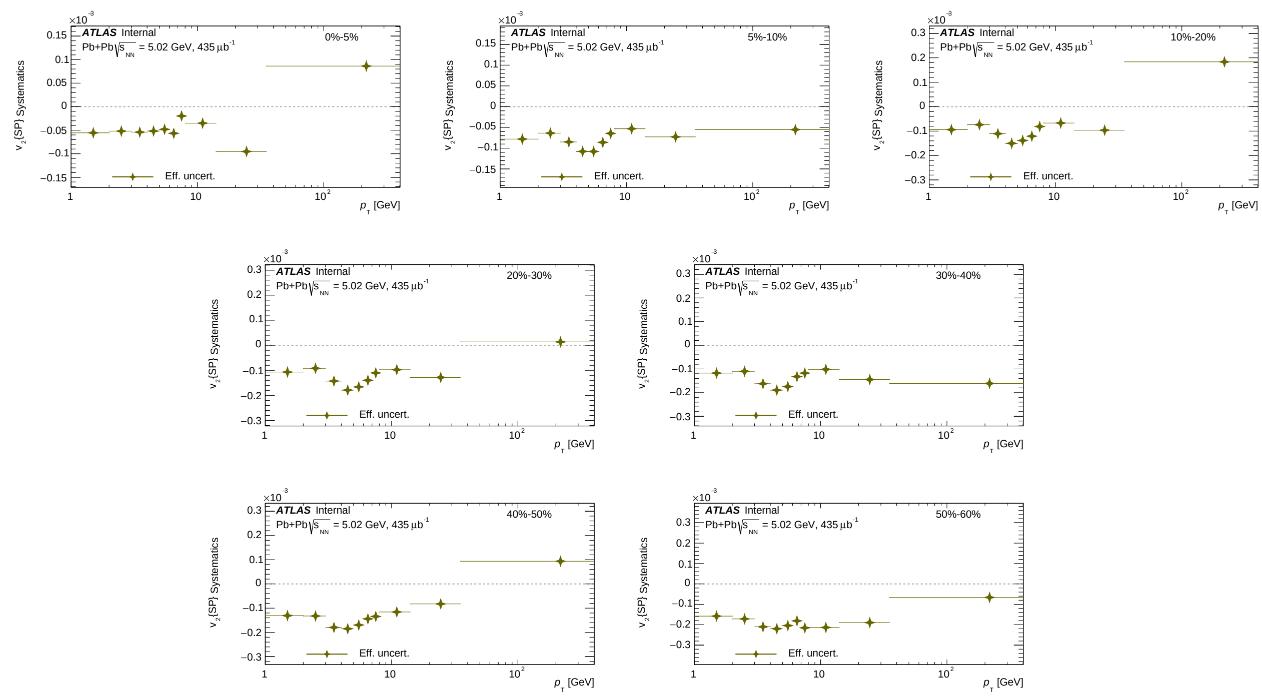

Figure 4.14: The difference of v_2 using a fitted versus bin-wise efficiency correction as a function of $p_{\rm T}$ for combined dataset in respective $p_{\rm T}$ range and centrality binning.

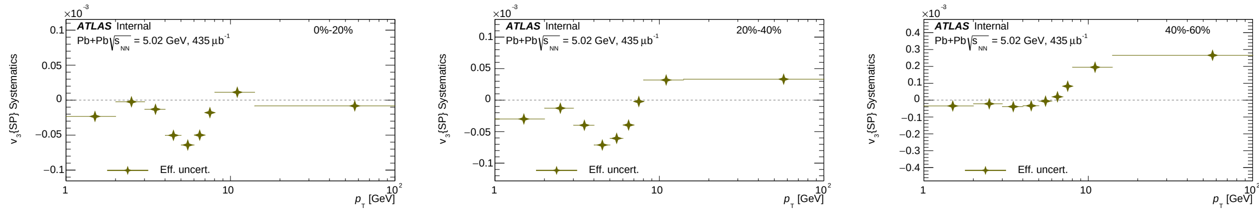

Figure 4.15: The difference of v_3 using a fitted versus bin-wise efficiency correction as a function of p_T for combined dataset in respective p_T range and centrality binning.

η-range of the Q_n vector determination

High-p_T particles dominantly come from jet production. Since jets are largely produced in dijet pairs, the Q_n vector for a given event can be biased if the opposing jet from the dijet pair hits the region of the FCal used to determine the Q_n vector. This effect is minimized by increasing the η separation between the high-p_T particle and the region of the FCal used to determine the Q_n vector.

In this measurement the particles of interest are already separated from the region of the FCal used to determine the Q_n vector by $|\eta| > 3.2$. In order to determine if there is any residual sensitivity to this choice, the Q_n vectors are evaluated with both the inner $(3.2 < |\eta| < 4.0)$ and outer $(4.0 < |\eta| < 4.9)$ regions of the FCal.

The results of this check are shown in Figs. 4.16–4.17.

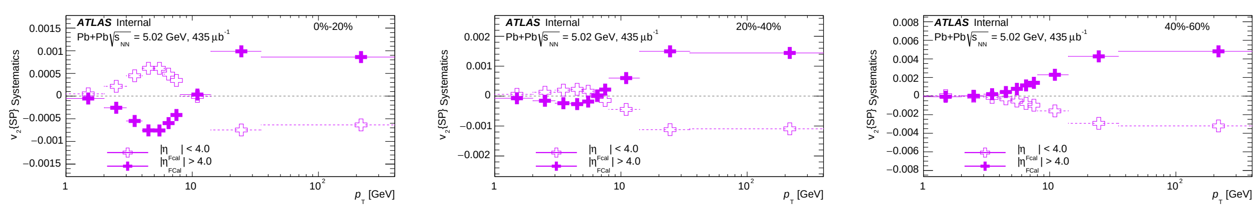

Figure 4.16: The deviation from full range FCal by using only inner or outer half of FCal as a function of p_T in respective p_T range and centrality binning for $v_2\{\mathrm{SP}\}$.

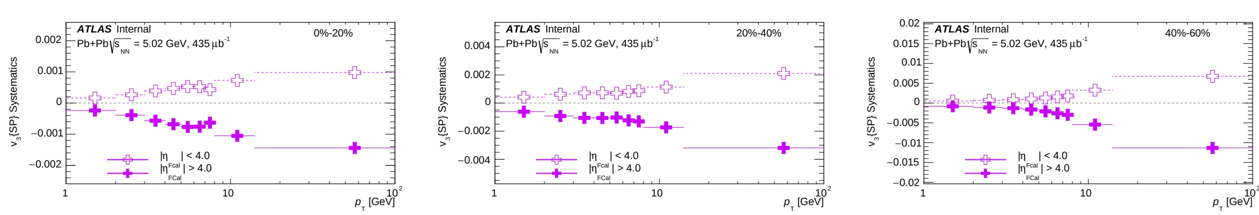

Figure 4.17: The deviation from full range FCal by using only inner or outer half of FCal as a function of p_T in respective p_T range and centrality binning for $v_3\{\mathrm{SP}\}$.

The η symmetry of the v_n results

It is expected that particles produced in a collision are emitted symmetrically with respect to the x-y plane when averaged over many events. However, due to detector limitations and non-ideal efficiency corrections, the measured flow signal, $v_,$ may differ when using only $(\eta < 0)$ or $(\eta > 0)$ range of inner detector to select tracks. The relative difference of the v_n values measured using charged particles with half ID from nominal value, $\Delta_{n,N/P-nominal} = (v_{n,N/P} - v_{n,nominal})/v_{n,nominal}$ is treated as a systematic uncertainty, where N and P refer to the negative and positive η regions of the detector, respectively.

The uncertainty dependence on track p_{T} and centrality is shown in Figures 4.18 to 4.19.

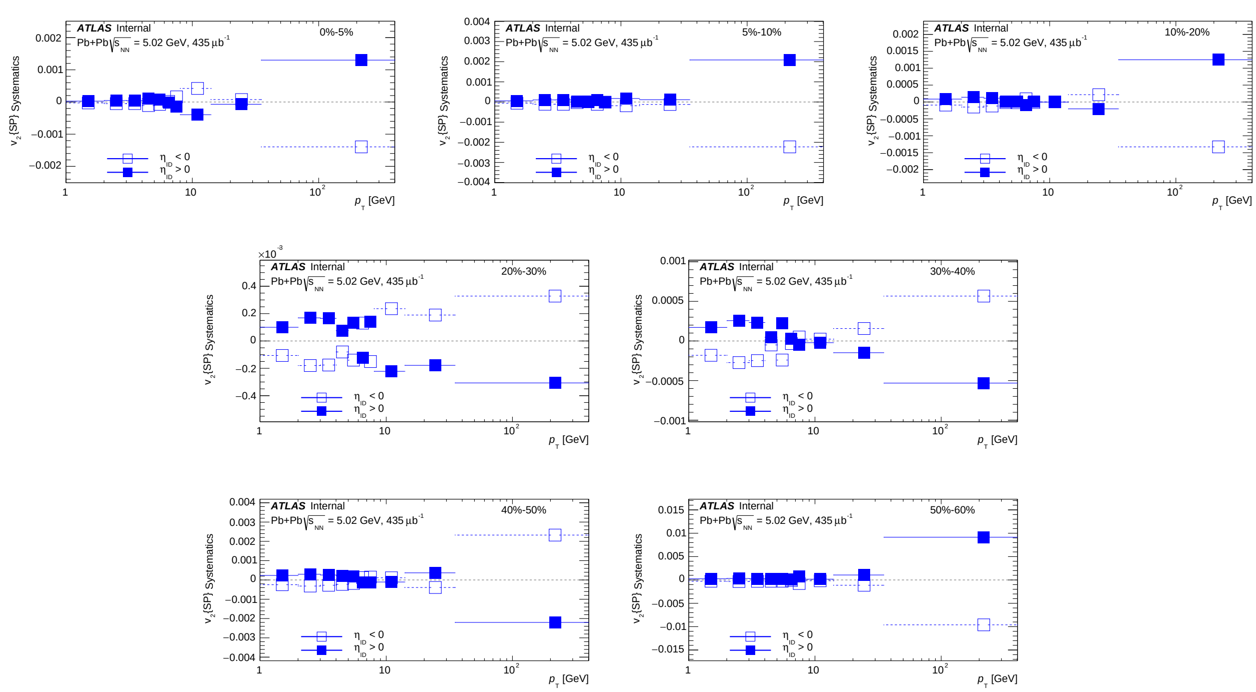

Figure 4.18: The $\Delta_{2,N/P-nominal}$ as a function of p_{T} for the combined dataset in respective p_{T} range and centrality binning.

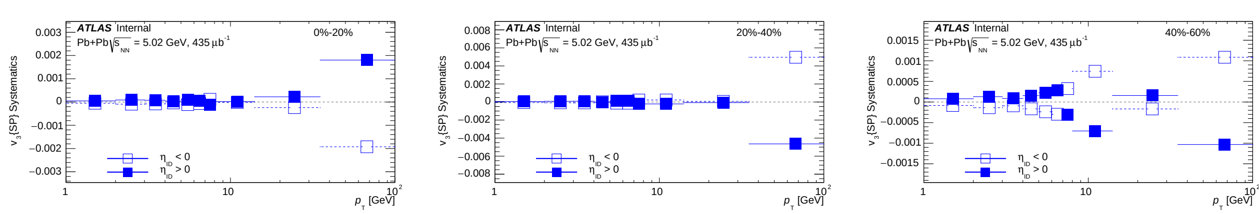

Figure 4.19: The $\Delta_{3,N/P-nominal}$ as a function of p_{T} for the combined dataset in respective p_{T} range and centrality binning.

Variation in the track selection

For the variation in the track selection, we tighten the tracking cuts. The values of these cuts that differ from nominal tracking selection are shown in Table 4.3. The systematic uncertainty is taken as the difference between the v_n value with the nominal tracking selection and the "restrictive" cut.

This uncertainty is shown in Figures 4.20 to 4.21. Both p_{T} and centrality rebinning are done to minimize the effect of large statistical fluctuations.

Parameter	Nominal	Restrictive
N_{hits} IBL+BL (if both expected)	≥ 1	≥ 2
N_{hits} SCT	≥ 8	≥ 9
N_{hits} Pixel	≥ 2	≥ 3

Table 4.3: Restrictive cut in Pb+Pb collisions.

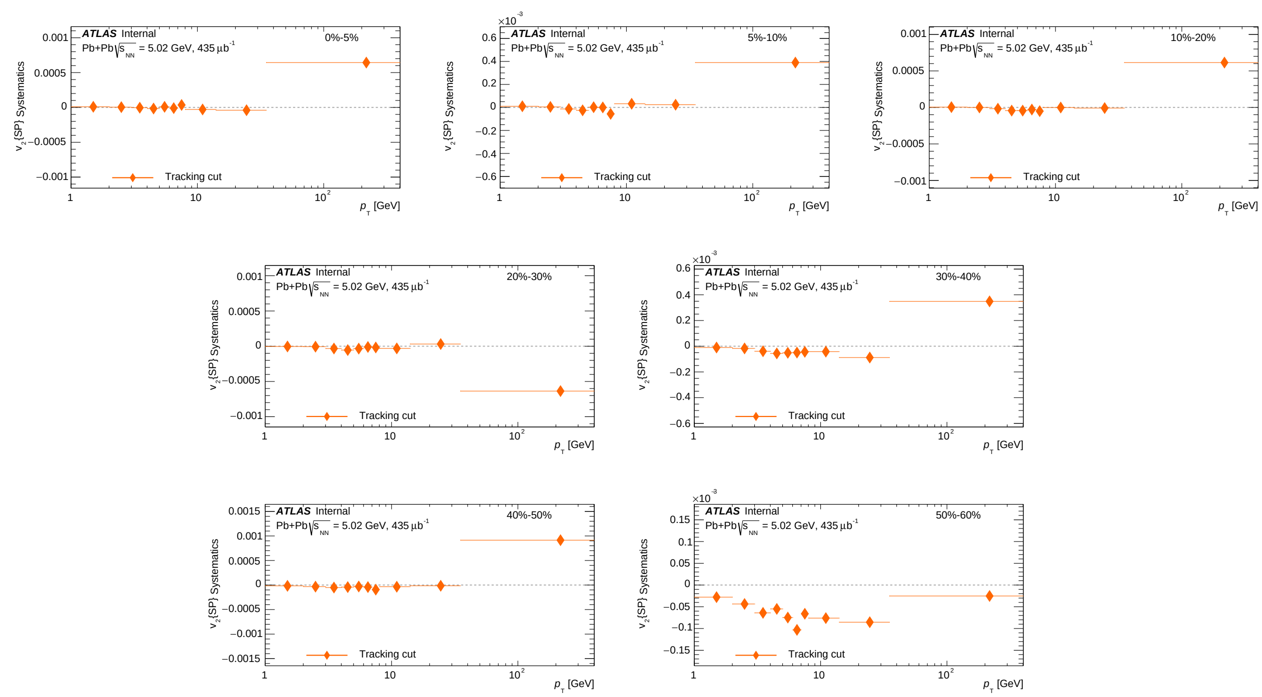

Figure 4.20: The difference in $v_2\{\mathrm{SP}\}$ between using restrictive cut and using nominal cut as a function of p_{T}.

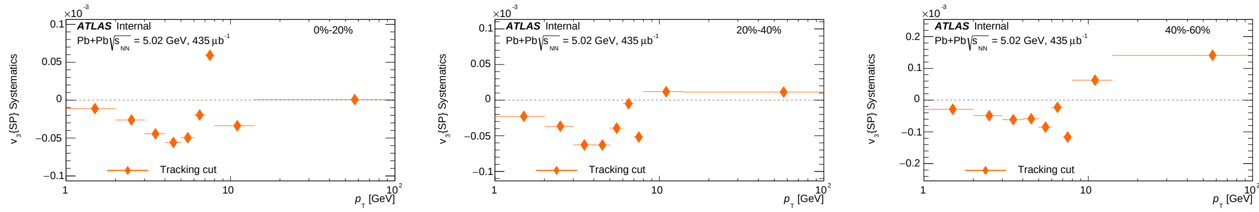

Figure 4.21: The difference in $v_3\{\mathrm{SP}\}$ between using restrictive cut and using nominal cut as a function of p_{T}.

Uncertainty in centrality determination

The centrality bin of this analysis is determined by ΣE_{FCal}. By matching the 85% of Glauber-like data onto the simulation, centrality boundaries are determined based on the corresponded simulated event. The amount of data events matched can be varied by 1%, thus slightly changing the border of ΣE_{FCal} when determining centrality bin. The values of the up- (86%) and down-variation (84%) borders and how they were obtained are documented in [180].

The systematic from centrality determination is made by putting the data into centrality bins according to the up and down variation ΣE_{FCal} borders, and the magnitude of this systematic are shown in Figures 4.22 to 4.23.

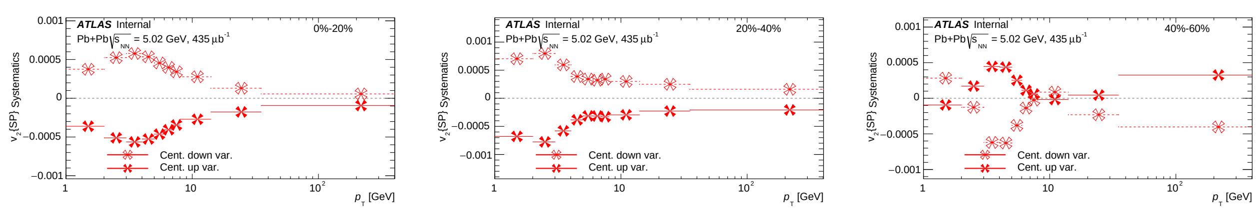

Figure 4.22: The difference in $v_2\{\mathrm{SP}\}$ between using variant version of centrality cuts and using nominal cut as a function of p_{T}.

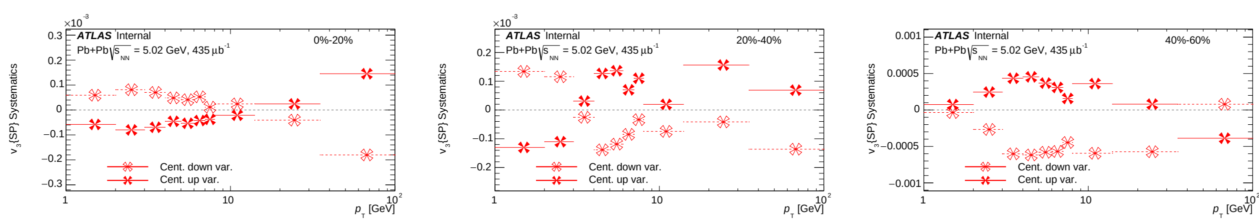

Figure 4.23: The difference in $v_2\{\mathrm{SP}\}$ between using variant version of centrality cuts and using nominal cut as a function of p_{T}.

Summary of systematic uncertainties for the scalar product method

All sources of systematic uncertainty are treated as independent and their absolute values are added together in quadrature. The same systematic uncertainties are evaluated for $v_n\{\mathrm{SP}\}$ results for the three ranges of charged-particle pseudorapidity $|\eta| < 1.1$, $1.1 < |\eta| < 2.5$ and $|\eta| < 2.5$. Shown here are the systematics for results of pseudorapidity $|\eta| < 2.5$.

At high-p_T, we expect that the systematic uncertainties have a large contribution from the sample size in the data. A summary of systematic uncertainties' magnitudes are shown in Figure 4.24 to Figure 4.25. Overall the largest systematic uncertainty is from the η-range of the FCal used to determine the Q_n vectors and separation of positive and negative η-range of the inner detector.

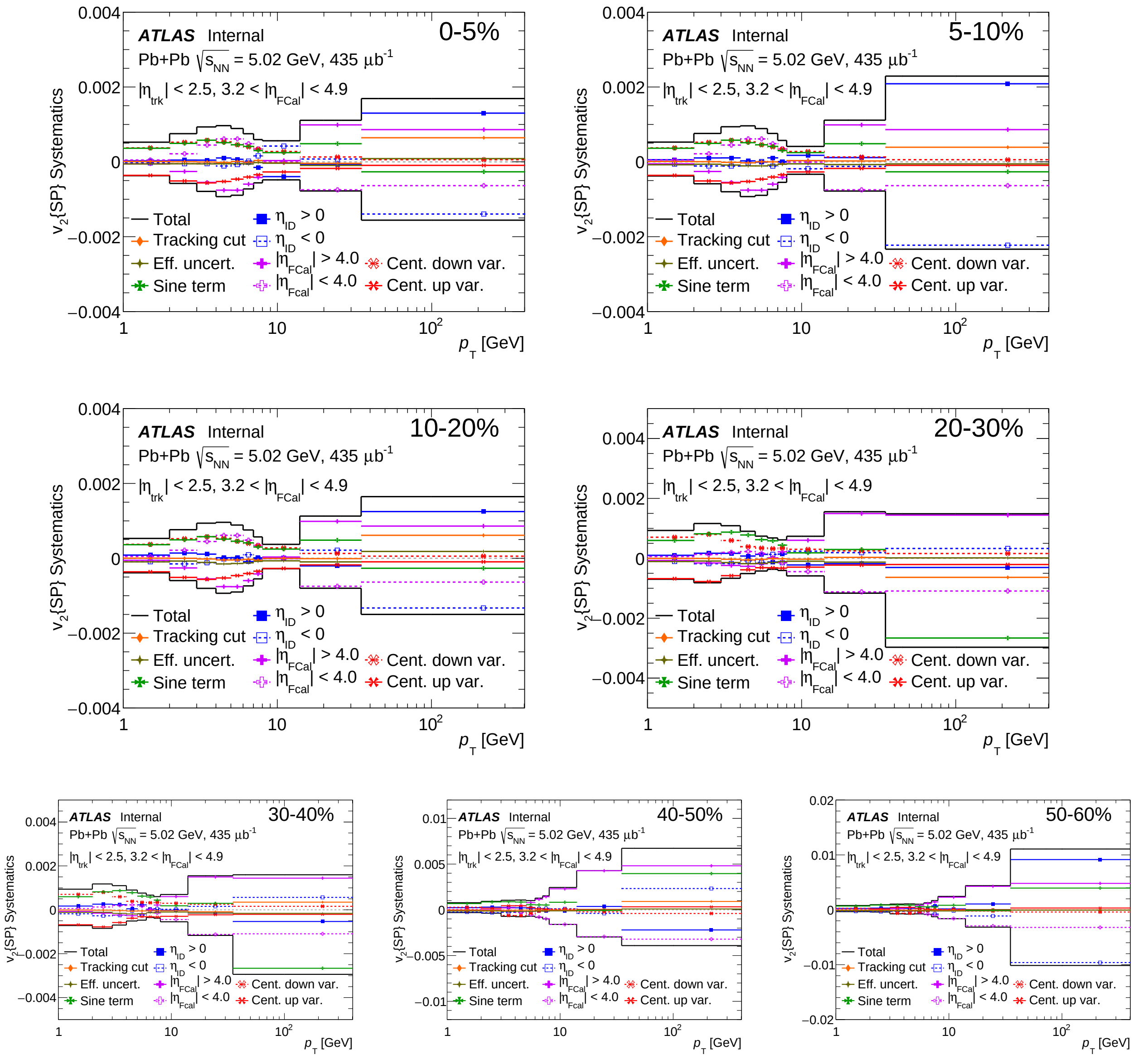

Figure 4.24: Magnitudes of systematics for $v_2\{\text{SP}\}$.

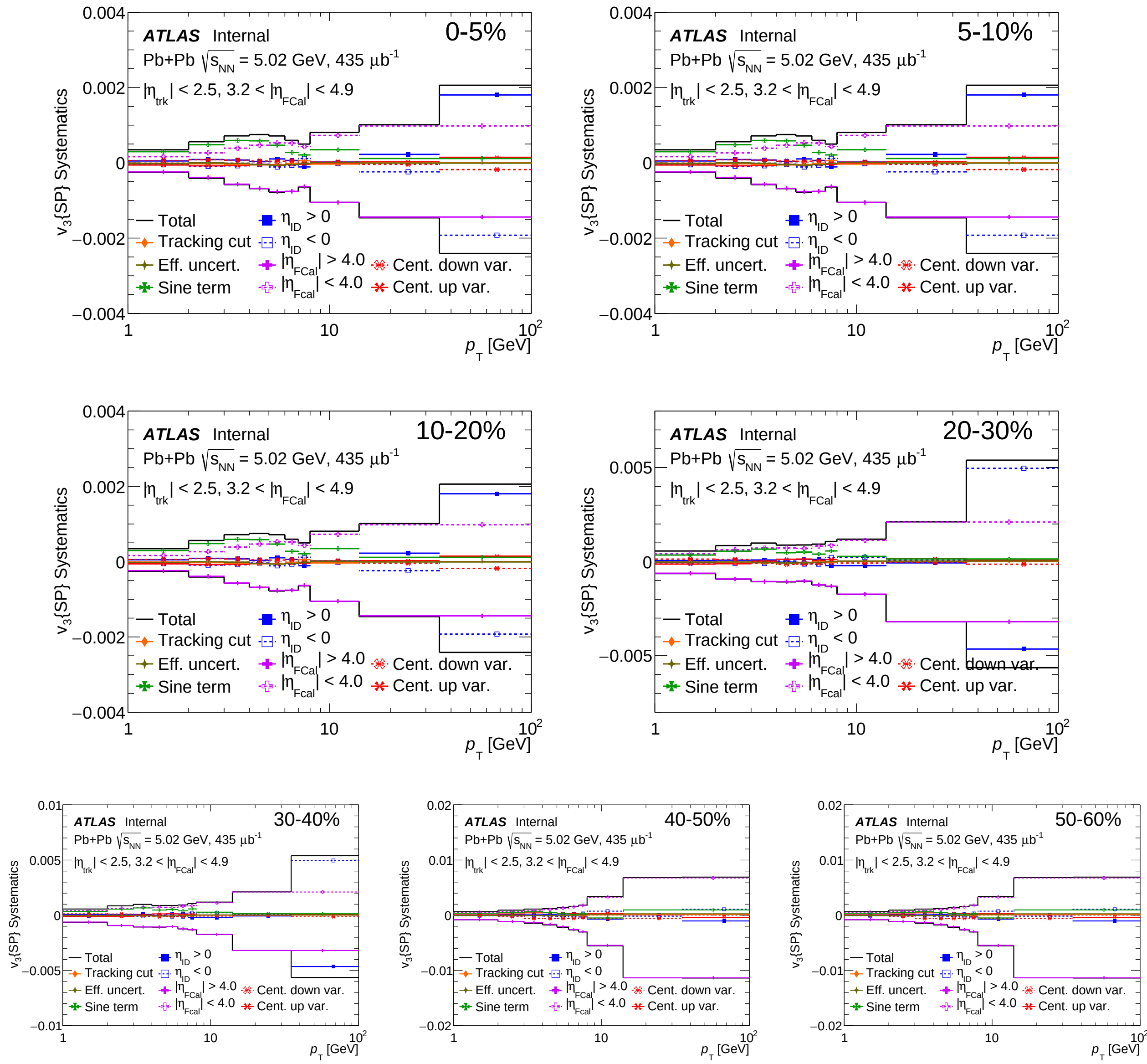

Figure 4.25: Magnitudes of systematics for v_3\{SP\}.

4.5.2 Systematical uncertainties of multi-particle cumulant method

The systematics for multi-particle cumulant method is similar to the integral flow multi-particle cumulant measurements in Run I data [149, 181] as follow,

- Sine residual term in differential correlator (Imaginary part of Equation4.18, see $v_n\{\mathrm{SP}\}$ sine residual term definition in Section4.5.1)
- Variation in track selection (same as Section 4.5.1)
- Tracking efficiency correction (same as Section 4.5.1)
- Uncertainty in centrality determination (same as Section4.5.1)

Figures.4.26 to 4.30 shows the itemized and square summed systematic uncertainty values for $v_2\{4\}$. And Figures.4.31 to 4.35 shows the itemized and square summed systematics for $v_3\{4\}$.

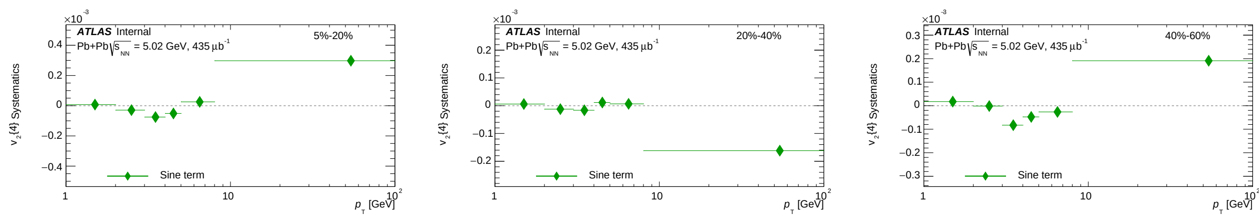

Figure 4.26: The systematic uncertainty from residual detector effects shown as non-zero sine term for $v_2\{4\}$ as a function of p_{T}.

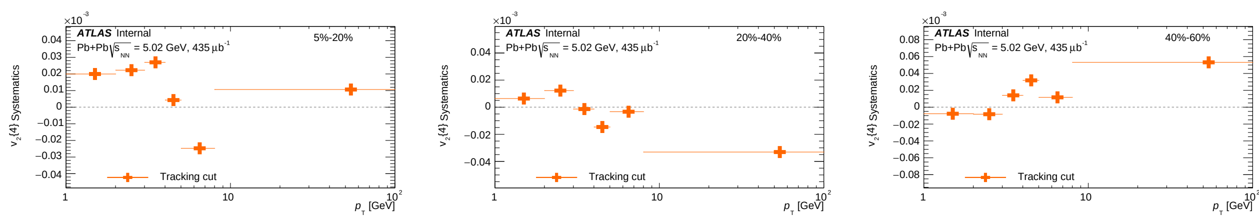

Figure 4.27: The systematic uncertainty from using restrictive versus nominal tracking selections for $v_2\{4\}$ as a function of p_{T}.

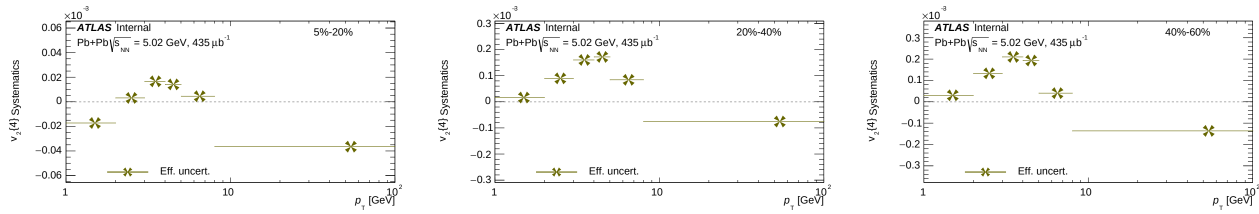

Figure 4.28: The systematic uncertainty from using fitted versus bin-wise tracking reconstruction efficiency for $v_2\{4\}$ as a function of p_{T}.

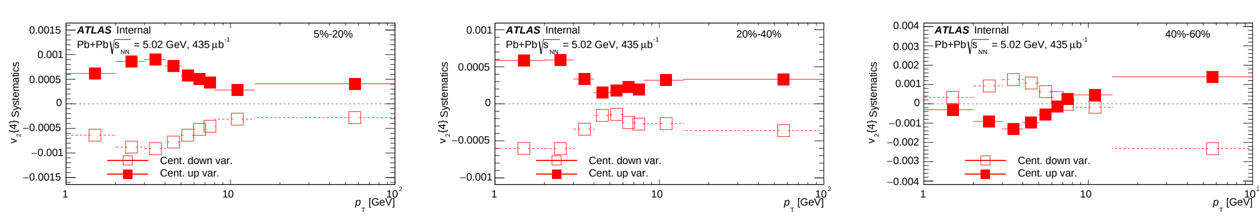

Figure 4.29: The systematic uncertainty from using alternative ΣE_{FCal} centrality cuts for $v_2\{4\}$ as a function of p_{T}.

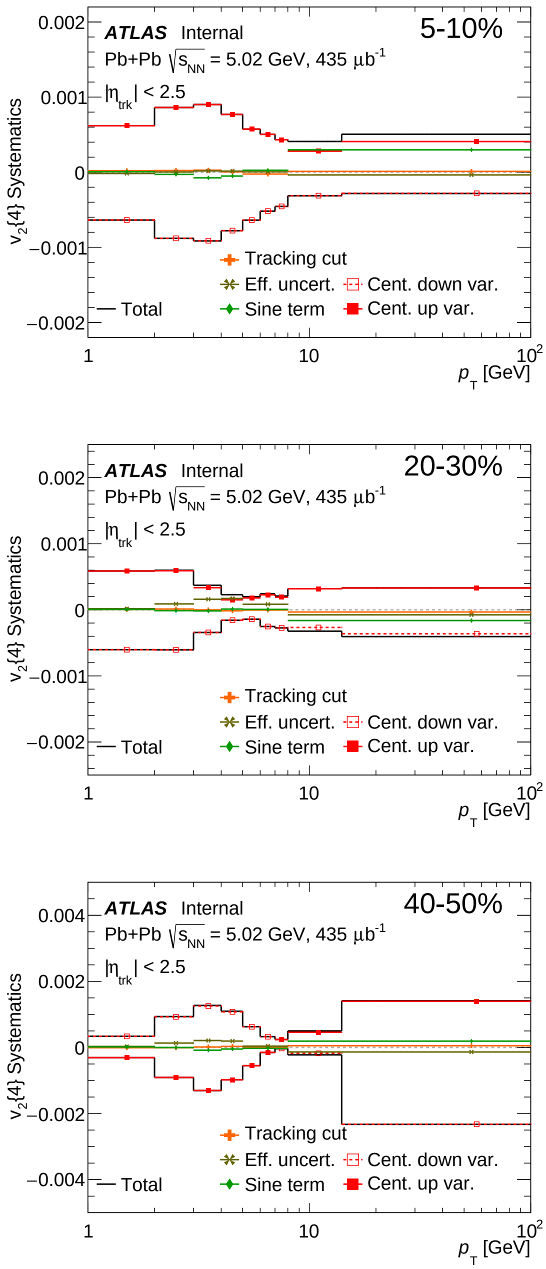

Figure 4.30: Magnitudes of systematics for $v_2\{4\}$.

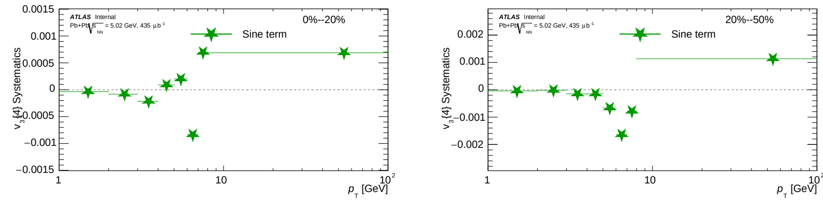

Figure 4.31: The systematic uncertainty from residual detector effects shown as non-zero sine term for $v_3\{4\}$ as a function of p_{T}.

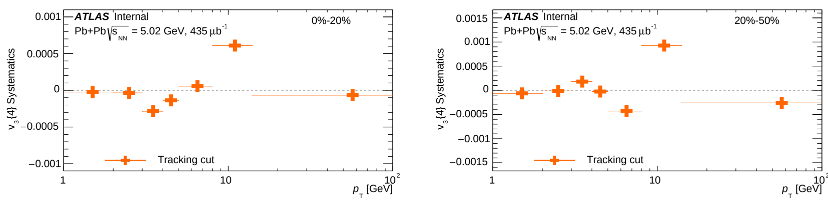

Figure 4.32: The systematic uncertainty from using restrictive versus nominal tracking selections for $v_3\{4\}$ as a function of p_{T}.

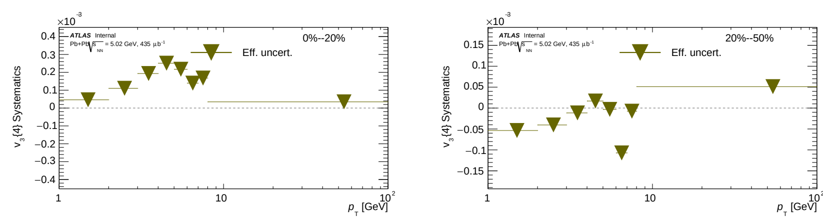

Figure 4.33: The systematic uncertainty from using fitted versus bin-wise tracking reconstruction efficiency for $v_3\{4\}$ as a function of p_{T}.

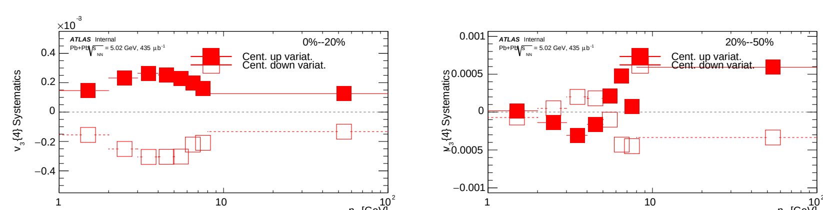

Figure 4.34: The systematic uncertainty from using alternative Fcal energy centrality cuts for $v_3\{4\}$ as a function of p_{T}.

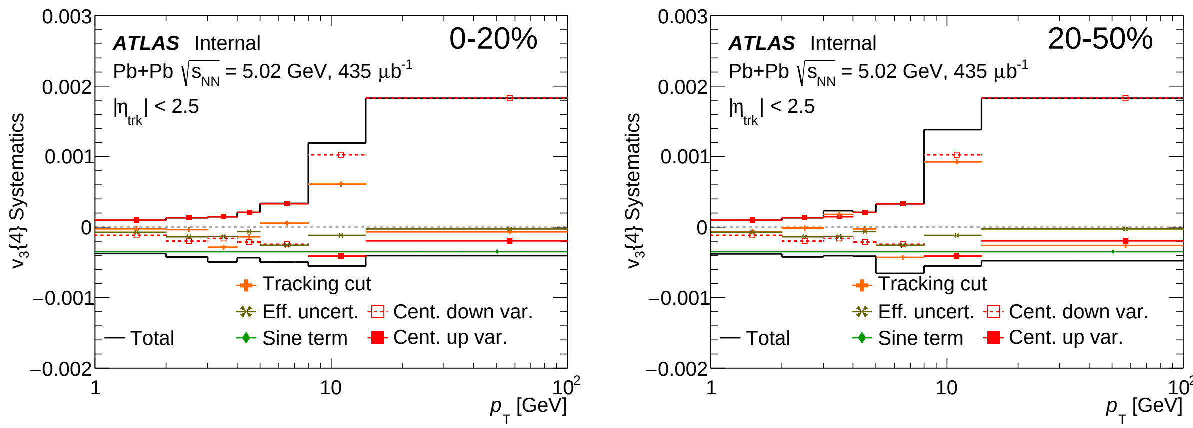

Figure 4.35: Magnitudes of systematics for $v_3\{4\}$.

4.6 Results

This section shows measurements of v_n using the SP method and the MPC method as a function of the charged-particle p_{T} for seven centrality intervals in Pb+Pb collisions: 0–5%, 5–10%, 10–20%, 20–30%, 30–40%, 40–50%, and 50–60%.

4.6.1 Scalar product method

Figure 4.36 shows the $v_2\{\mathrm{SP}\}$ and $v_3\{\mathrm{SP}\}$ values as functions of p_{T} for the selected centrality intervals. The measured $v_2\{\mathrm{SP}\}$ values are positive for the selected centrality intervals up to a p_{T} of 100 GeV, and the measured $v_3\{\mathrm{SP}\}$ values are positive up to approximately 25 GeV for the selected centrality intervals, except for the 50–60% centrality interval. Figure 4.37 and Figure 4.38 show the consistency of the $v_n\{\mathrm{SP}\}$ measured for Pb+Pb collision for $\sqrt{s_{\mathrm{NN}}} = 5.02$ TeV at the LHC for the centrality interval 10–20%. Note that in the two figures, two different pseudorapidity ranges are used for the ATLAS 2018 measurements from this analysis. In Figure 4.37, the ATLAS 2015 measurements [122] quoted use the same pseudorapidity ranges of ID and FCal with the ATLAS 2018 measurements, and the two results show good agreement. In Figure 4.38, the CMS 2015 measurements [88] shown use tracks with pseudorapidity range $|\eta| < 1.0$ and calorimeters in pseudorapidity range $3 < |\eta| < 5$. Overall, good agreement is found between the ATLAS 2018 and the CMS 2015 measurements, except for $v_2\{\mathrm{SP}\}$ in the p_{T} range of 14-50 GeV, where the CMS 2015 measurements yield higher values than the ATLAS 2018 measurements from this analysis.

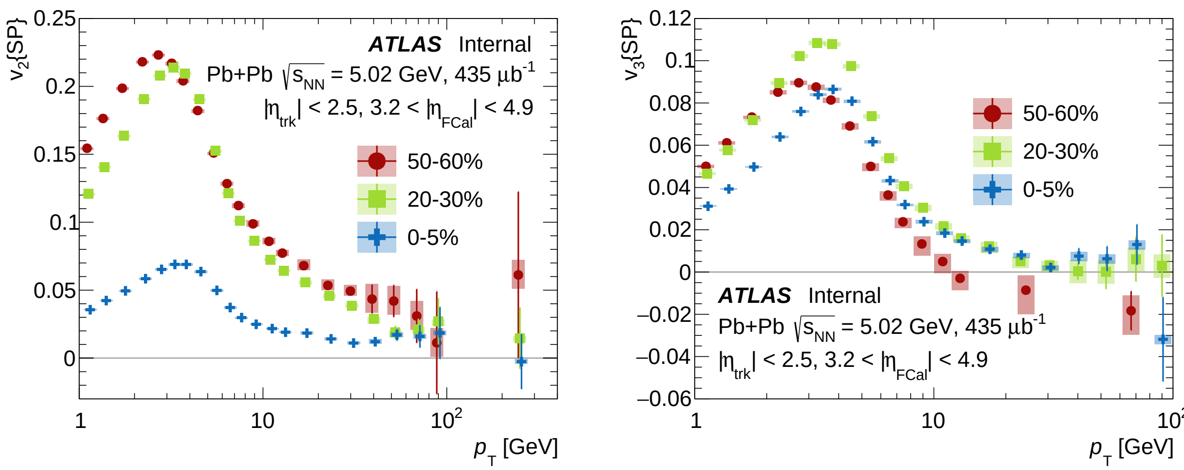

(a) (b)

Figure 4.36: The (a) $v_2\{\mathrm{SP}\}$ and (b) $v_3\{\mathrm{SP}\}$ values as a function of charged-particle p_{T} for centrality intervals 0–5%, 20–30%, and 50–60%. The statistical uncertainties are shown as error bars and the systematic uncertainties are shown as boxes.

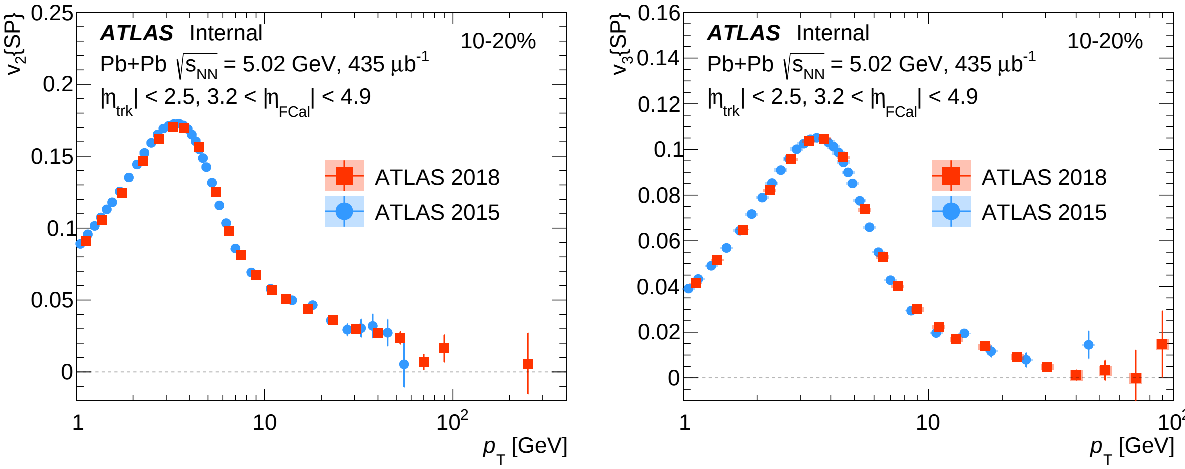

(a) (b)

Figure 4.37: The (a) v_2\{SP\} and (b) v_3\{SP\} values as a function of charged-particle p_{T}, for the 10–20% centrality interval, compared with ATLAS 2015 measurements from Ref. [122] in the same charged particle and calorimeter pseudorapidity ranges. The statistical uncertainties are shown as error bars and the systematic uncertainties are shown as boxes.

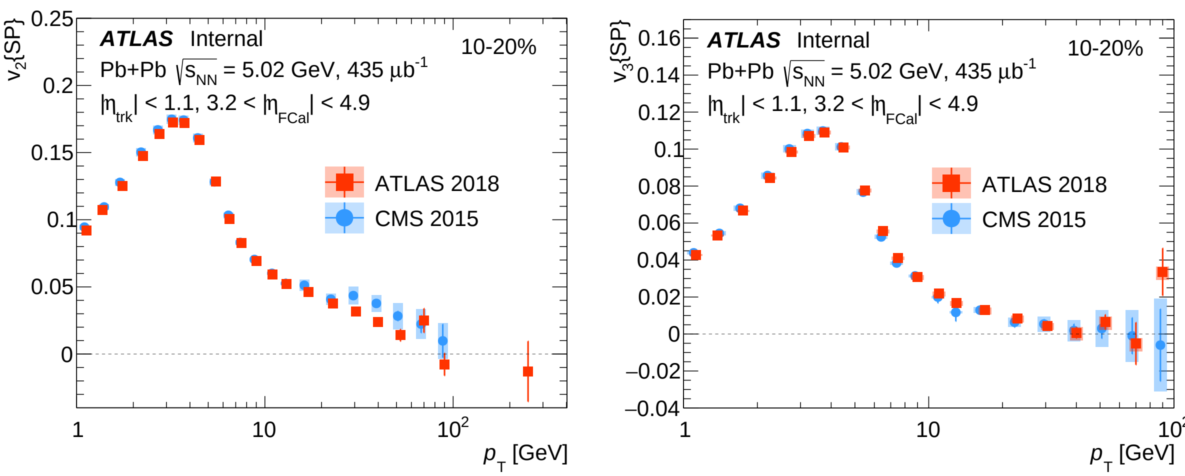

(a) (b)

Figure 4.38: The (a) v_2\{SP\} and (b) v_3\{SP\} values as a function of charged-particle p_{T}, for the 10–20% centrality interval, compared with CMS 2015 measurements from Ref. [88], which uses charged particles with pseudorapidity range $|\eta| < 1.0$ and calorimeter in pseudorapidity range $3 < |\eta| < 5$. The statistical uncertainties are shown as error bars and the systematic uncertainties are shown as boxes.

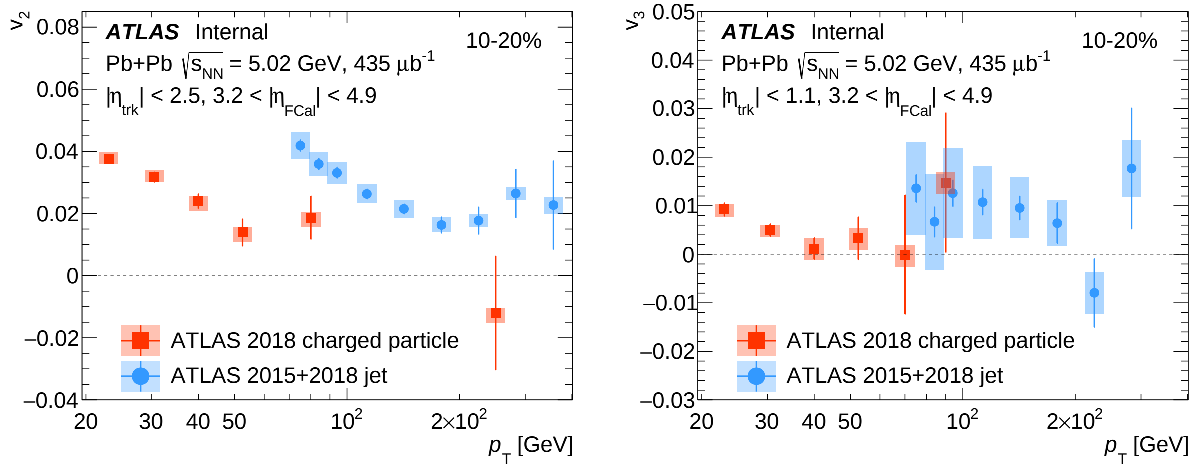

(a) (b)

Figure 4.39: The (a) v_2 and (b) v_3 values as a function of charged particle or jet p_{T}, for the 10–20% centrality interval, compared with ATLAS jet v_n measurements from Ref. [87]. The statistical uncertainties are shown as error bars and the systematic uncertainties are shown as boxes.

In Figure 4.39 and Figure 4.40, a comparison is made between the charged-particle $v_n\{\mathrm{SP}\}$ measurements from this analysis and the jet v_n measurements from ATLAS using the event plane method, denoted as $v_n\{\mathrm{EP}\}$, from Ref. [87]. The measured v_n values are qualitatively similar between the jets and charged particles in this p_{T} range. These high-p_{T} charged particles are from jet fragmentation but carry only a fraction of a given jet's p_{T}.

Measurements of $v_n\{\mathrm{SP}\}$ using two non-overlapping pseudorapidity ranges of tracks are compared in Figure 4.41 for $n = 2$ and Figure 4.42 for $n = 3$. The pseudorapidity range $1.1 < |\eta| < 2.5$ corresponds to a greater average pseudorapidity gap between the tracks and correlated reference Q_n than $|\eta| < 1.1$. At $p_{\mathrm{T}} < 10$ GeV for both centrality intervals shown, tracks with the pseudorapidity range $1.1 < |\eta| < 2.5$ yield smaller values both $v_2\{\mathrm{SP}\}$ and $v_3\{\mathrm{SP}\}$ than tracks with the pseudorapidity range $|\eta| < 1.1$. With a larger pseudorapidity gap imposed, certain non-flow effects are better suppressed, while the longitudinal decorrelation effects in the event plane become stronger [146], both of which reduce the measured values of v_n. At $10 < p_{\mathrm{T}} < 20$ GeV for the 10–20% centrality interval, the $v_2\{\mathrm{SP}\}$ difference is similar to the low-p_{T} region, while $v_3\{\mathrm{SP}\}$ difference becomes consistent with zero, whereas for the 40–50% centrality interval, tracks with the pseudorapidity range $1.1 < |\eta| < 2.5$ yield smaller $v_2\{\mathrm{SP}\}$ values but larger $v_3\{\mathrm{SP}\}$ values than tracks with the pseudorapidity range $|\eta| < 1.1$. In this p_{T} range, particle production is dominated by jets. The observed contrasting behavior of $v_2\{\mathrm{SP}\}$ and $v_3\{\mathrm{SP}\}$ is consistent with a non-flow dijet contamination, which contributes positively to even-order harmonics and negatively to odd-order harmonics.

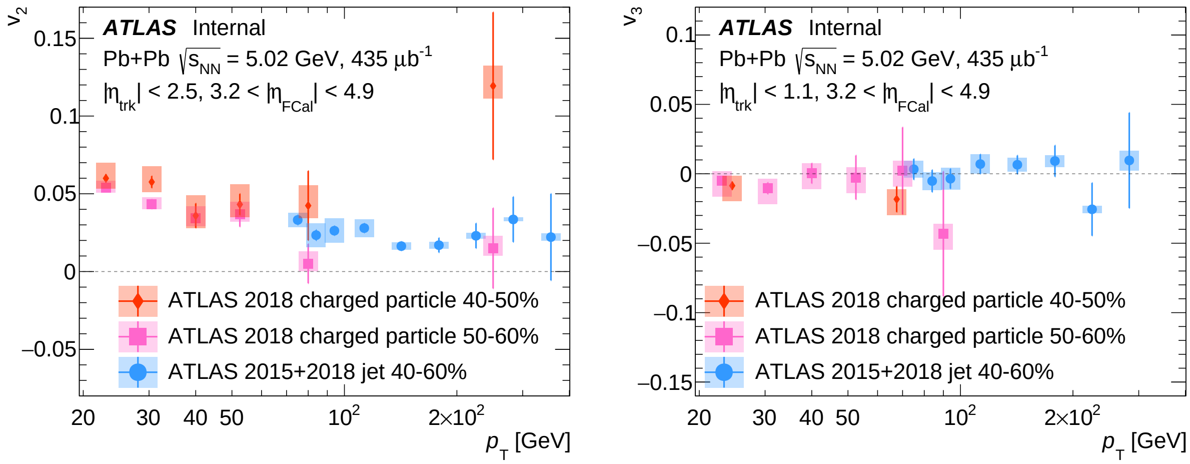

(a) (b)

Figure 4.40: The (a) $v_2\{\mathrm{SP}\}$ and (b) $v_3\{\mathrm{SP}\}$ values as a function of charged particle or jet p_{T}, for the charged particle centrality intervals 40–50% and 50–60%, compared with ATLAS jet v_n measurements from Ref. [87]. The statistical uncertainties are shown as error bars and the systematic uncertainties are shown as boxes.

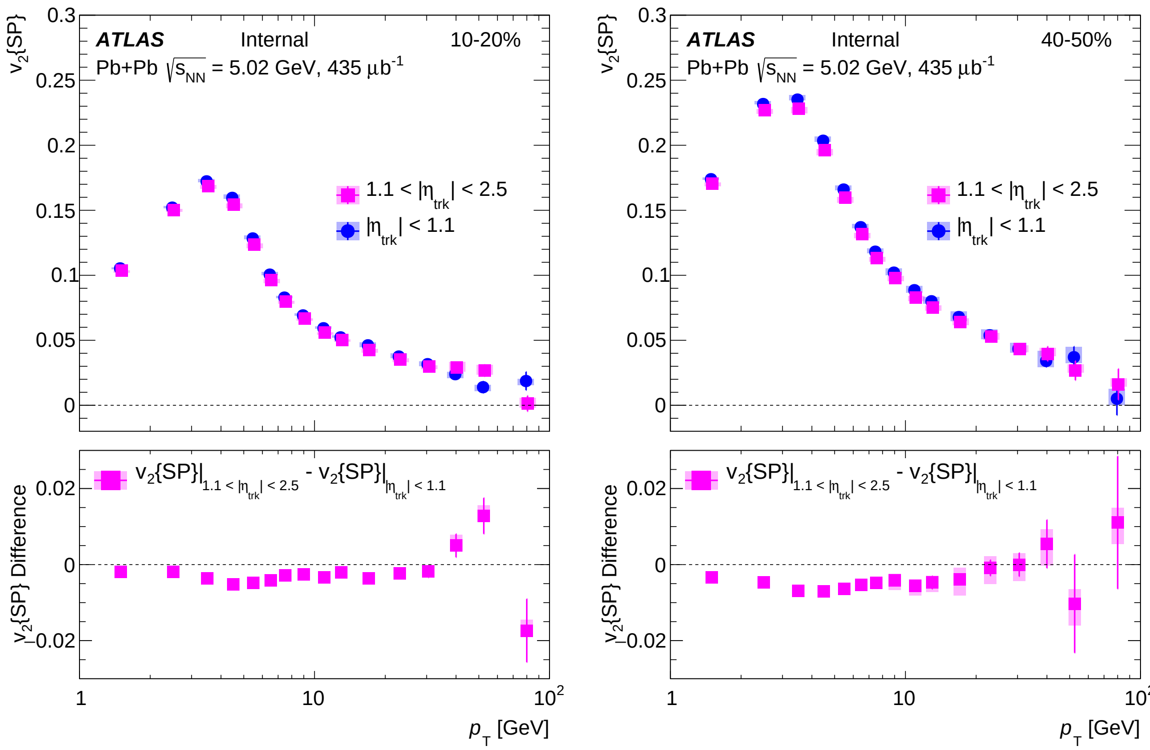

(a) (b)

Figure 4.41: The $v_2\{\mathrm{SP}\}$ values as a function of charged-particle p_{T} for (a) 10–20% and (b) 40–50% for different pseudorapidity ranges. The bottom panel shows the difference in the $v_2\{\mathrm{SP}\}$ measured between the two ranges. The statistical uncertainties are shown as error bars and the systematic uncertainties are shown as boxes.

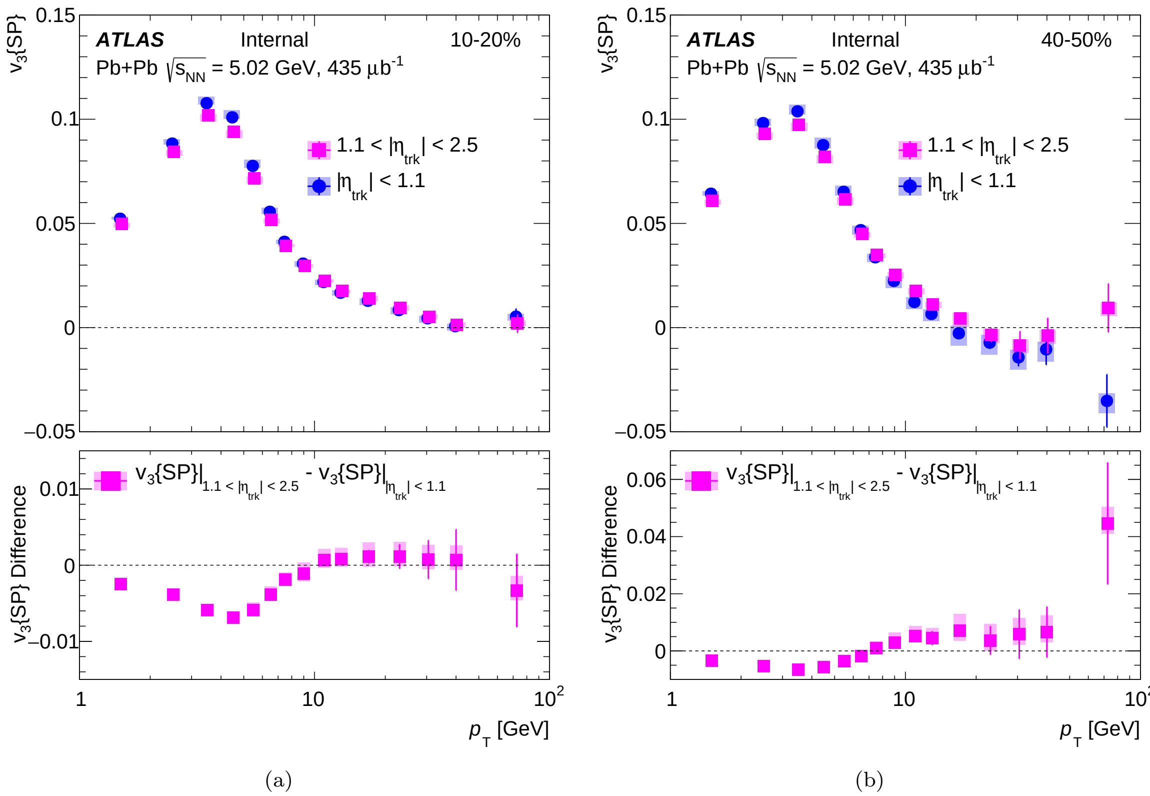

Figure 4.42: The $v_3\{\mathrm{SP}\}$ values as a function of charged-particle p_T for (a) 10–20% and (b) 40–50% for different pseudorapidity ranges. The bottom panel shows the difference in the $v_3\{\mathrm{SP}\}$ measured between the two ranges. The statistical uncertainties are shown as error bars and the systematic uncertainties are shown as boxes.

4.6.2 Multi-particle cumulant method

Measurements of $v_n\{4\}$ with the MPC method with standard Q-cumulants using the $\langle 1\% \rangle$ event combination procedure are shown in Figure 4.43. Due to statistical limitations, $v_3\{4\}$ is measured only up to the 50% most central events. As explained in Section 4.4.2, 0–5% central events are omitted for $v_2\{4\}$ to avoid imaginary-valued reference $v_2\{4\}$. At high p_{T}, above 10 GeV, the $v_2\{4\}$ values for 5–40% decrease with p_{T} across the measured range. In contrast, for the 40–50%, peripheral events, values of $v_2\{4\}$ decrease with p_{T} up to approximately 20 GeV and then increases above p_{T} of 30 GeV. Meanwhile, values of $v_3\{4\}$ become approximately constant above 8 GeV, with an upward an upward fluctuations between approximately 8 and 10 GeV for some centrality intervals.

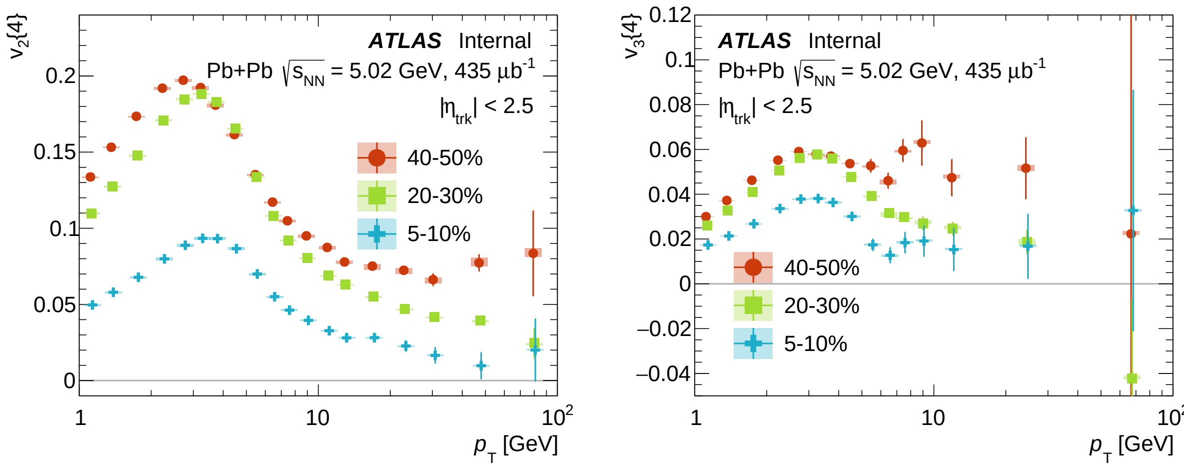

(a) (b)

Figure 4.43: (a) $v_2\{4\}$ and (b) $v_3\{4\}$ using standard Q-cumulants for centrality intervals 5–10%, 10–20%, 30–40%, and 40–50%. The statistical uncertainties are shown as error bars and the systematic uncertainties are shown as boxes.

The flattening and slight increase of v_n with p_{T} in peripheral events could arise from non-flow effects. A comparison is made between the standard Q-cumulant result $v_n\{4\}$ and three-subevent Q-cumulant results $v_n^{\text{3-sub}}\{4\}$ to further understand the role of non-flow effects. Note that $v_3^{\text{3-sub}}\{4\}$ are only measured up to $p_{\mathrm{T}} = 35$ GeV and the most central 50% collisions due to significant statistical fluctuations. As shown in Figure 4.44, values of $v_n^{\text{3-sub}}\{4\}$ agree with $v_n\{4\}$ for central events, and deviate from $v_n\{4\}$ in peripheral events at high-p_{T}. The p_{T} and centrality dependence of this deviation is consistent with a suppression of short-range non-flow correlations by the three-subevent cumulants. As has been shown in Ref. [169], these non-flow correlations have a more significant effect in events of smaller charged-particle multiplicity. Different behaviors are observed for $v_2^{\text{3-sub}}\{4\}$ and $v_3^{\text{3-sub}}\{4\}$ in the 40–50% centrality interval. For $p_{\mathrm{T}} > 20$ GeV, the values of $v_2^{\text{3-sub}}\{4\}$ become nearly constant, whereas the values of $v_3^{\text{3-sub}}\{4\}$ continue to decrease for higher p_{T}. The contrasting behavior between ellipticity and triangularity in the high p_{T} region is consistent with contamination from dijet production, which contributes positively to even-order harmonics and negatively to odd-order harmonics and has a bigger impact in more peripheral events. In these measurements, dijet contributions are more pronounced in the MPC method than the SP method, and can arise from the narrower pseudorapidity range used for the MPC method.

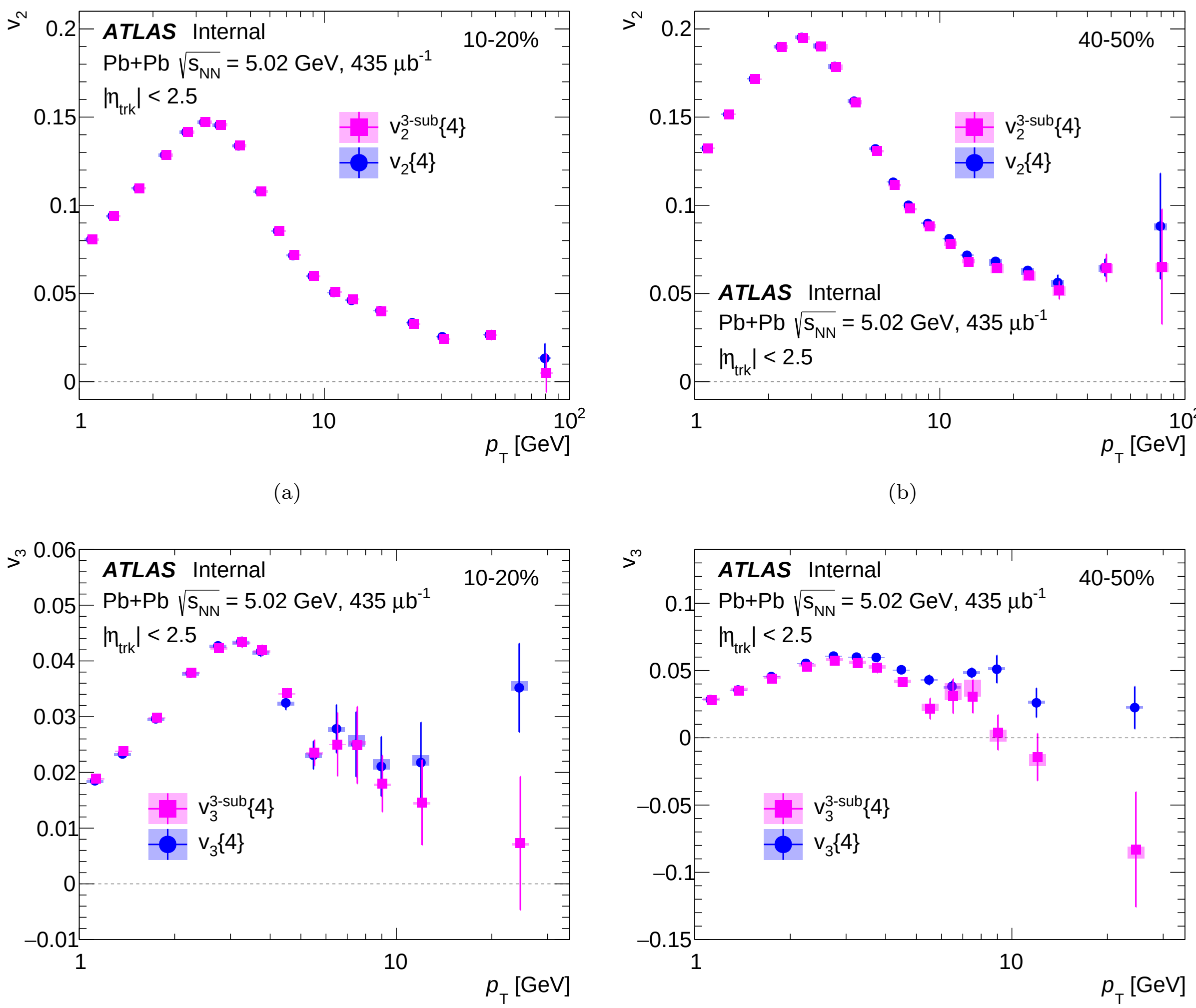

(a) (b) (c) (d)

Figure 4.44: Comparison between standard and three-subevent Q-cumulants for $v_2\{4\}$ in centrality intervals (a) 10–20% and (b) 40–50%, and for $v_3\{4\}$ in centrality intervals (c) 10–20%, and (d) 40–50%. The statistical uncertainties are shown as error bars and the systematic uncertainties are shown as boxes.

The v_n values measured with four-particle cumulants are sensitive to the mean value as well as fluctuations of the underlying distributions, which includes contributions from both non-flow effects and initial state geometry [132]. To better understand how the event-by-event distributions of non-flow effects and the initial state geometry contribute to the measurements of v_n, comparisons of $v_n\{4\}$ using different event combination procedures are shown in Figure 4.45 and Figure 4.46. In all centrality and p_{T} ranges measured, the $\langle 2\% \rangle$ results converge to those obtained with the default $\langle 1\% \rangle$ procedure, indicating that centrality-resolution-related fluctuations are negligible in these measurements when using the $\langle 1\% \rangle$ procedure. In the low-p_{T} region, the event combination procedure affects the fluctuation terms but not the mean value of the underlying distribution, whereas in the high-p_{T} region, computing cumulants directly in a wider centrality interval also biases the mean of measurements toward more central events.

Figure 4.45 shows that for v_2 the impact of the choice of event combination procedure is dependent on centrality, p_{T}, and less pronounced in three-subevent cumulants. In the central 10–20% events, the difference is vanishingly small for both $v_2\{4\}$ and $v_2^{\text{3-sub}}\{4\}$. In peripheral events, a more significant difference between $\langle 10\% \rangle$ and $\langle 1\% \rangle$ is observed for $v_2\{4\}$ than for $v_2^{\text{3-sub}}\{4\}$ toward the high-p_{T} region. The difference between different event combination procedures shows a dependence on centrality, p_{T}, and the three-subevent cumulants similar to that of non-flow effects, suggesting the four-particle cumulant v_2 is primarily sensitive to non-flow fluctuations. Similar observations have been made in studies of low-p_{T} flow [149, 152]. Additionally, high-p_{T} particle production is more biased toward central collisions, further increasing the difference in that region.

Figure 4.46 shows a comparison between different event combination procedures for $v_3\{4\}$ and $v_3^{\text{3-sub}}\{4\}$. It can be seen that the difference between $\langle 10\% \rangle$ and $\langle 1\% \rangle$ is substantial in central and peripheral events for both the standard and the three-subevent cumulants, without a strong dependence on centrality or p_{T}. This shows that v_3 values are more sensitive to fluctuations in initial geometry than those in non-flow effects. It has been found in the measurements of reference flow that the fluctuations of v_3 are more significant relative to the mean in comparison to v_2 [182]. Results from Figure 4.45 and Figure 4.46 suggests that event-by-event initial geometry fluctuations are more pronounced in the triangularity of the initial geometry than the ellipticity.

Figure 4.47 shows a comparison between the SP method and the three-subevent Q-cumulant MPC method using the default $\langle 1\% \rangle$ event combination procedure. The $v_3^{\text{3-sub}}\{4\}$ results are truncated at a p_{T} of 35 GeV due to limited statistics. Values of $v_n\{\mathrm{SP}\}$ are greater than $v_n^{\text{3-sub}}\{4\}$, as predicted in Ref. [135] for Bessel-Gaussian or elliptic power v_n distributions, in the low-p_{T} region across all centrality intervals for both v_2 and v_3. At $p_{\mathrm{T}} > 10$ GeV, the comparison between the two methods contains information about how hard scattered partons respond to the event-by-event distribution of the initial state QGP geometry. Different behaviors are observed for different centrality intervals. In central events, $v_n\{\mathrm{SP}\} > v_n^{\text{3-sub}}\{4\}$ and up to p_{T} of approximately 15 GeV for both v_2 and v_3. The similarity between high-p_{T} and low-p_{T} region suggests

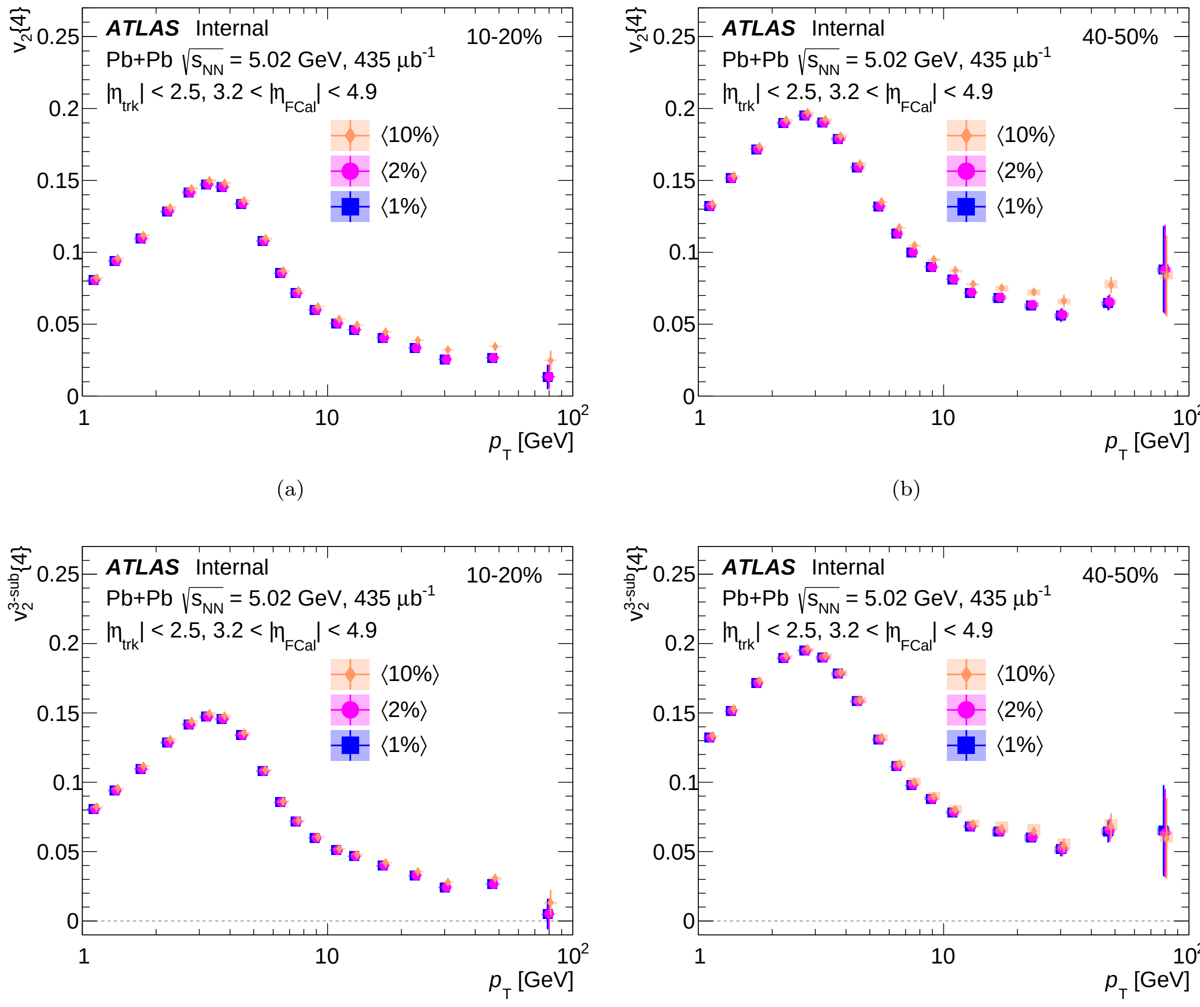

(a) (b) (c) (d)

Figure 4.45: Comparison between ⟨1%⟩, ⟨2%⟩, and ⟨10%⟩ event combination procedures for $v_2\{4\}$ in centrality intervals (a) 10–20% and (b) 40–50%, and for $v_2^{3\text{-sub}}\{4\}$ in centrality intervals (c) 10–20%, and (d) 40–50%. The statistical uncertainties are shown as error bars and the systematic uncertainties are shown as boxes.

that the azimuthal anisotropies in high-p_T region are strongly affected by the initial geometry of the QGP. In peripheral events, the two methods converge with increasing p_T in v_2, whereas in v_3 they diverge from each other for $p_T > 10$ GeV. This difference between v_2 and v_3 suggests residual non-flow dijet contributions, which have greater impact in peripheral events. It should be noted that other non-flow correlations, the effects of the event combination procedure, and event plane longitudinal decorrelation are also more pronounced in peripheral events. The differences observed in peripheral collisions could arise from multiple effects.

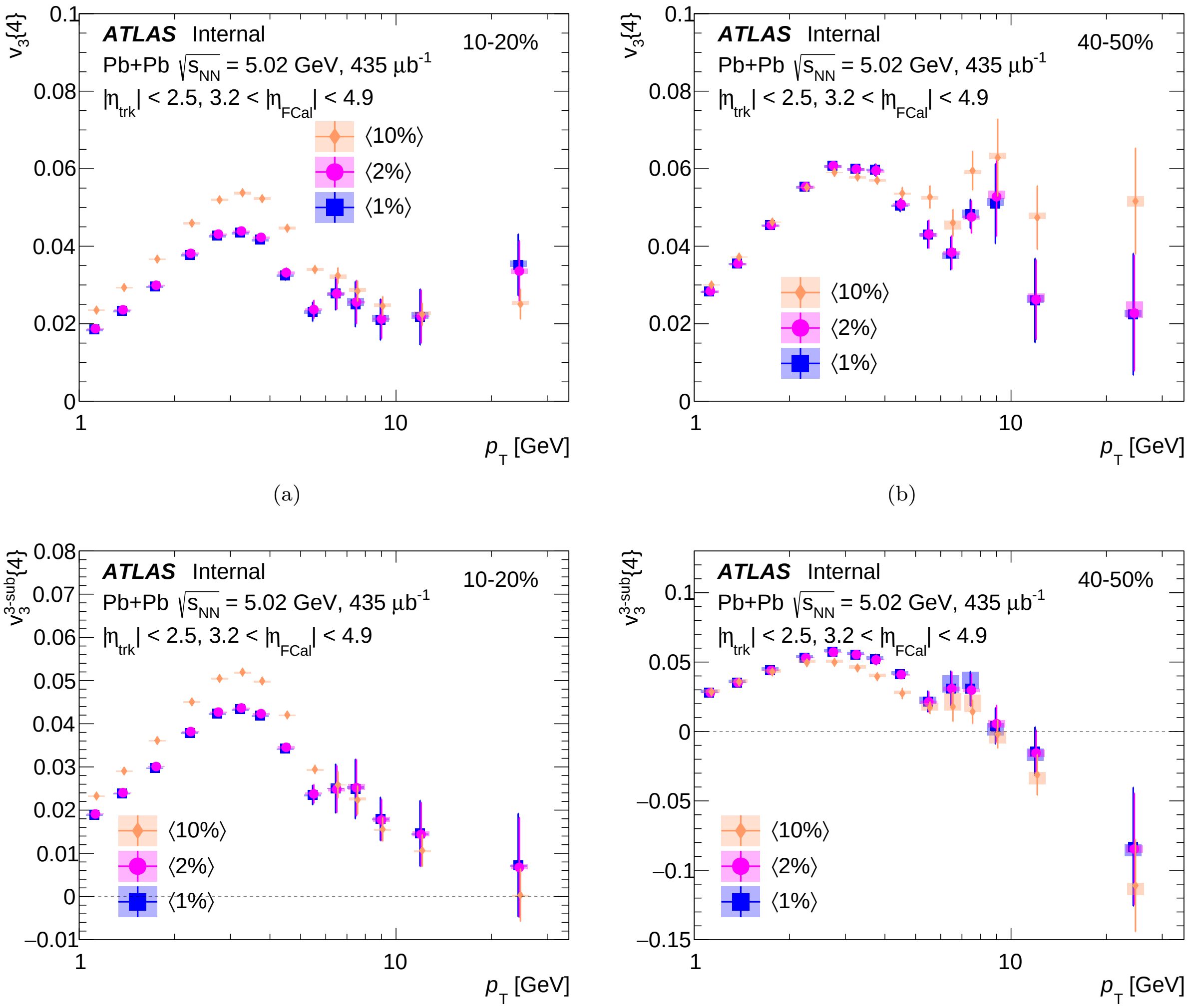

(a) (b) (c) (d)

Figure 4.46: Comparison between ⟨1%⟩, ⟨2%⟩, and ⟨10%⟩ event combination procedures for $v_3\{4\}$ in centrality intervals (a) 10–20% and (b) 40–50%, and for $v_3^{3\text{-sub}}\{4\}$ in centrality intervals (c) 10–20%, and (d) 40–50%. The statistical uncertainties are shown as error bars and the systematic uncertainties are shown as boxes.

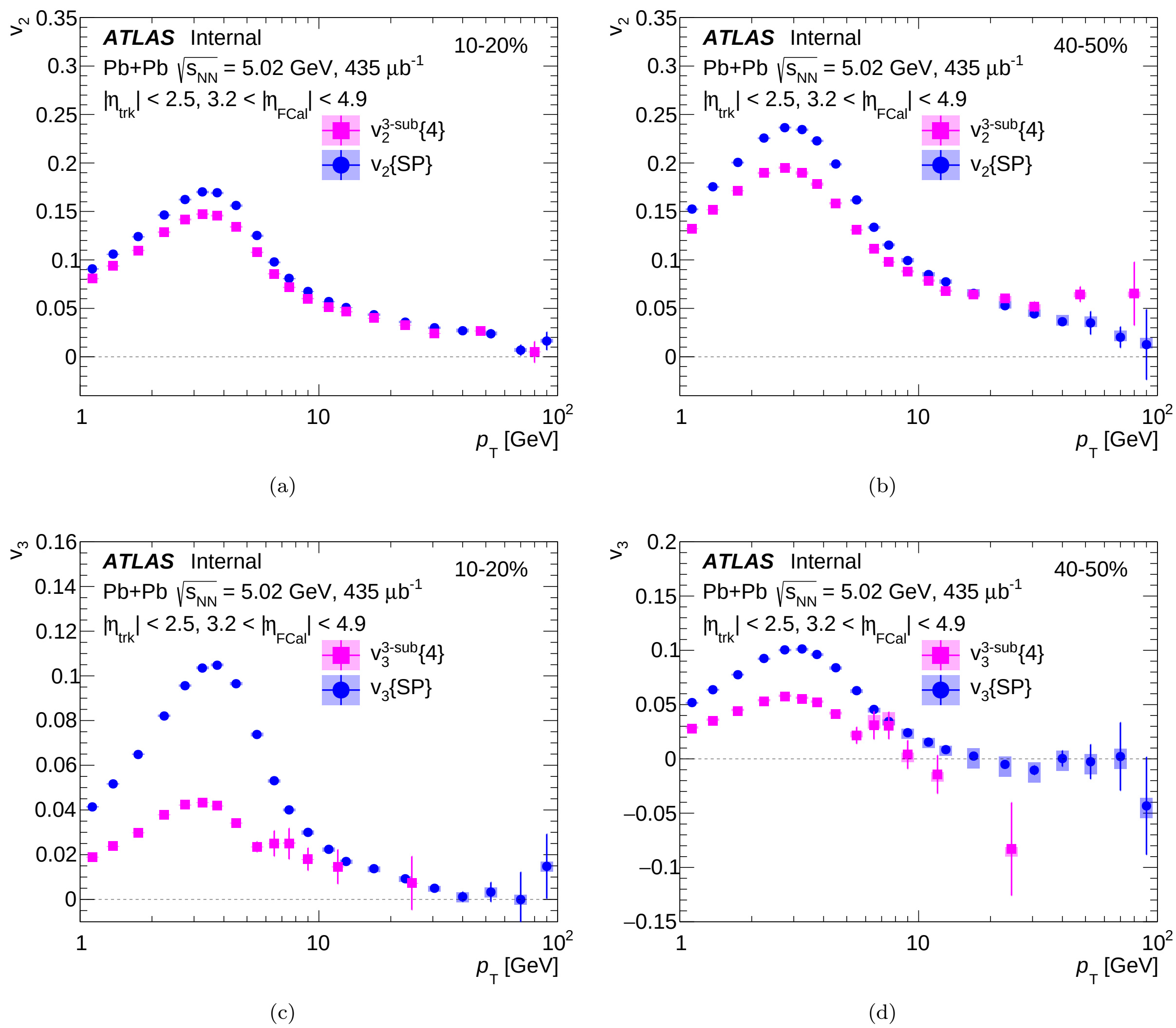

Figure 4.47: Comparison between the $v_n\{\mathrm{SP}\}$ results and $v_n^{\text{3-sub}}\{4\}$ for $n = 2$ in centrality intervals (a) 10–20% and (b) 40–50%, and for $n = 3$ in centrality intervals (c) 10–20%, and (d) 40–50%. The statistical uncertainties are shown as error bars and the systematic uncertainties are shown as boxes.

Chapter 5

Summary and conclusions

The quark gluon plasma (QGP) is a novel state of matter in which partons become deconfined under extreme temperature and density. The QGP are produced in the ultrarelativistic heavy ion collisions at facilities such as the RHIC and the LHC. Partons from hard scatterings in these collisions traverse through the QGP and lose energy to the medium. The study of angular modulation of hard probes, such as high-p_{T} charged particles, provide key insights for the short-distance strong interactions within the QGP.

This thesis describes the measurements of azimuthal anisotropies of charged particles in Pb+Pb collisions at $\sqrt{s_{\mathrm{NN}}} = 5.02$ TeV, using a data set corresponding to an integrated luminosity of 435 μb^{-1} collected with the ATLAS detector at the LHC in 2018. The azimuthal anisotropy coefficients, v_n, are measured using the scalar product and multi-particle cumulant methods for $n = 2$ and $n = 3$. Positive values of v_2 and v_3 are observed in mid-central collisions for charged particles with $p_{\mathrm{T}} > 10$ GeV. In this region, charged particles dominantly come from the fragmentation of jets. These measurements will provide new information to constrain the path-length dependence of jet quenching in Pb+Pb collisions. Meanwhile, the effects of non-flow contributions, longitudinal decorrelation, and different strategies for constructing multi-particle cumulants are evaluated before a comparison between the two methods is presented.

The p_{T}-differential $v_n\{\mathrm{SP}\}$ values are measured over the charged particles with a pseudorapidity range $|\eta| < 2.5$ and a p_{T} up to 400 GeV in several centrality intervals spanning the 0–60% most central collisions. In mid-central collisions, the $v_2\{\mathrm{SP}\}$ values are found to remain positive up to 100 GeV with a value of 1–2%; the $v_3\{\mathrm{SP}\}$ values are found to be positive up to approximately 25 GeV. These results are consistent with previous measurements from the LHC experiments in the overlapping p_{T}, pseudorapidity, and centrality ranges. The increased luminosity and implemented data taking innovations resulted in a larger data set that has allowed for improved precision at high p_{T}.

The p_{T}-differential $v_n\{\mathrm{SP}\}$ values are measured and compared across two additional pseudorapidity ranges: $|\eta| < 1.1$ and $1.1 < |\eta| < 2.5$, with $p_{\mathrm{T}} =$ 1-100 GeV. In the low-p_{T} region, larger pesudorapidity gap decreases both $v_2\{\mathrm{SP}\}$ and $v_3\{\mathrm{SP}\}$. This change can arise from decreased non-flow effects and increased longitudinal decorrelation, both of which decrease $v_2\{\mathrm{SP}\}$ as well as $v_3\{\mathrm{SP}\}$ values. In contrast to that, at high-p_{T} region larger pseudorapidity gap decreases $v_2\{\mathrm{SP}\}$ but increases $v_3\{\mathrm{SP}\}$ values, suggesting non-flow dijet contributions.

Using the multi-particle cumulant method, the values of $v_2\{4\}$ are measured for charged particles with p_{T} = 1–100 GeV, over the pseudorapidity range $|\eta| < 2.5$ and a centrality range of 0–60%. These measurements were carried out using the $\langle 1\% \rangle$ event combination procedure. For $p_{\mathrm{T}} > 10$ GeV, it is observed that the three-subevent Q-cumulants suppress positive, short-range non-flow contributions in comparison to the standard Q-cumulants. Meanwhile, non-flow dijet contributions are still observed with the three-suebvent Q-cumulants. Measurements of $v_2\{4\}$ and $v_3\{4\}$ using two additional event combination procedures, $\langle 2\% \rangle$ and $\langle 10\% \rangle$, were also performed and compared to results using the $\langle 1\% \rangle$ procedure. It is observed that for $v_2\{4\}$, the event combination procedure affects non-flow contributions primarily, whereas, for $v_3\{4\}$, initial geometry contributions are more significantly affected.

The v_n values measured with the SP method are larger than those measured with the MPC method in the low-p_{T} region, as expected from theoretical predictions. A positive v_2 and v_3 in the high-p_{T} charged particles suggest that the energy loss of the hard-scattered partons is influenced by the event-by-event initial geometry of the QGP. In the high-p_{T} region, the difference between the SP and the MPC methods decreases toward zero for $n = 2$ but increases for $n = 3$ for peripheral events, suggesting an increased impact of the remaining non-flow dijet contributions.

Using a bigger dataset collected using the ATLAS detector, a systematic study on the centrality, rapidity, p_{T} and order-of-cumulant dependence of v_2 and v_3 is conducted in the hard sector. At these p_{T} ranges, charged particles dominantly come from the fragmentation of jets. These measurements will provide new information to constrain the path-length dependence of jet quenching in Pb+Pb collisions and facilitate the development of currently missing theoretical calculations on particle flows.

Bibliography

[1] M. K. Gaillard, P. D. Grannis, and F. J. Sciulli, *The Standard model of particle physics*, Rev. Mod. Phys. **71** (1999) S96, arXiv: hep-ph/9812285 (cit. on p. 1).

[2] E. D. Bloom et al., *High-Energy Inelastic $e - p$ Scattering at 6° and 10°*, Phys. Rev. Lett. **23** (16 1969) 930, URL: https://link.aps.org/doi/10.1103/PhysRevLett.23.930 (cit. on p. 1).

[3] M. Breidenbach et al., *Observed Behavior of Highly Inelastic Electron-Proton Scattering*, Phys. Rev. Lett. **23** (16 1969) 935, URL: https://link.aps.org/doi/10.1103/PhysRevLett.23.935 (cit. on p. 1).

[4] E. M. Riordan, *The Discovery of quarks*, Science **256** (1992) 1287 (cit. on p. 1).

[5] J. Ellis, *The Discovery of the Gluon*, Int. J. Mod. Phys. A **29** (2014) 1430072, ed. by H. Fritzsch and M. Gell-Mann, arXiv: 1409.4232 [hep-ph] (cit. on p. 1).

[6] W. B. et al., *Observation of planar three-jet events in e+e annihilation and evidence for gluon bremsstrahlung*, Physics Letters B **91** (1980) 142, ISSN: 0370-2693, URL: https://www.sciencedirect.com/science/article/pii/0370269380906802 (cit. on p. 1).

[7] C. B. et al., *Evidence for gluon bremsstrahlung in e+e annihilations at high energies*, Physics Letters B **86** (1979) 418, ISSN: 0370-2693, URL: https://www.sciencedirect.com/science/article/pii/0370269379908694 (cit. on p. 1).

[8] W. Commons, *Standard Model of Elementary Particles*, 17 September 2019, URL: https://commons.wikimedia.org/wiki/File:Standard_Model_of_Elementary_Particles.svg (cit. on p. 2).

[9] S. Schmitt and M. Wing, *The most precise picture of the proton*, https://cerncourier.com/a/the-most-precise-picture-of-the-proton/, [Accessed 01-03-2024], 2015 (cit. on p. 2).

[10] D. J. Gross and F. Wilczek, *Ultraviolet Behavior of Nonabelian Gauge Theories*, Phys. Rev. Lett. **30** (1973) 1343, ed. by J. C. Taylor (cit. on pp. 1, 3).

[11] H. D. Politzer, *Reliable Perturbative Results for Strong Interactions?*, Phys. Rev. Lett. **30** (1973) 1346, ed. by J. C. Taylor (cit. on pp. 1, 3).

[12] D. J. Gross and F. Wilczek, *Asymptotically Free Gauge Theories - I*, Phys. Rev. D **8** (1973) 3633 (cit. on pp. 1, 3).

[13] F. M. Stokes, *Structure of Nucleon Excited States from Lattice QCD*, PhD thesis: Adelaide U., Sch. Chem. Phys., 2019 (cit. on p. 2).

[14] S. Navas et al., *Review of particle physics*, Phys. Rev. D **110** (2024) 030001 (cit. on pp. 3, 19).

[15] K. G. Wilson, *Confinement of Quarks*, Phys. Rev. D **10** (1974) 2445, ed. by J. C. Taylor (cit. on p. 4).

[16] W. Commons, *Plaques of Lambda Phages on E. coli XL1-Blue MRF*, 2009, URL: https://commons.wikimedia.org/wiki/File:Quark_confinement.svg (cit. on p. 4).

[17] W. Busza, K. Rajagopal, and W. van der Schee, *Heavy Ion Collisions: The Big Picture, and the Big Questions*, Ann. Rev. Nucl. Part. Sci. **68** (2018) 339, arXiv: 1802.04801 [hep-ph] (cit. on pp. 4, 5).

[18] M. Thomson, *Modern particle physics*, New York: Cambridge University Press, 2013, ISBN: 978-1-107-03426-6 (cit. on p. 4).

[19] K. Yagi, T. Hatsuda, and Y. Miake, *Quark-gluon plasma: From big bang to little bang*, vol. 23, 2005 (cit. on p. 4).

[20] A. S. Kronfeld, *Twenty-first Century Lattice Gauge Theory: Results from the QCD Lagrangian*, Ann. Rev. Nucl. Part. Sci. **62** (2012) 265, arXiv: 1203.1204 [hep-lat] (cit. on p. 5).

[21] BRAHMS Collaboration, *Quark gluon plasma and color glass condensate at RHIC? The Perspective from the BRAHMS experiment*, Nucl. Phys. A **757** (2005) 1, arXiv: nucl-ex/0410020 (cit. on pp. 4, 10).

[22] PHENIX Collaboration, *Formation of dense partonic matter in relativistic nucleus-nucleus collisions at RHIC: Experimental evaluation by the PHENIX collaboration*, Nucl. Phys. A **757** (2005) 184, arXiv: nucl-ex/0410003 (cit. on pp. 4, 10, 33).

[23] PHOBOS Collaboration, *The PHOBOS perspective on discoveries at RHIC*, Nucl. Phys. A **757** (2005) 28, arXiv: nucl-ex/0410022 (cit. on pp. 4, 10).

[24] STAR Collaboration, *Experimental and theoretical challenges in the search for the quark gluon plasma: The STAR Collaboration's critical assessment of the evidence from RHIC collisions*, Nucl. Phys. A **757** (2005) 102, arXiv: nucl-ex/0501009 (cit. on pp. 4, 10).

[25] G. Roland, K. Safarik, and P. Steinberg, *Heavy-ion collisions at the LHC*, Prog. Part. Nucl. Phys. **77** (2014) 70 (cit. on p. 4).

[26] M. Strickland, *Anisotropic Hydrodynamics: Three lectures*, Acta Phys. Polon. B **45** (2014) 2355, ed. by M. Praszalowicz, arXiv: 1410.5786 [nucl-th] (cit. on pp. 4, 6).

[27] M. L. Miller, K. Reygers, S. J. Sanders, and P. Steinberg, *Glauber modeling in high energy nuclear collisions*, Ann. Rev. Nucl. Part. Sci. **57** (2007) 205, arXiv: nucl-ex/0701025 (cit. on pp. 6, 7, 22).

[28] ATLAS Collaboration, *Measurement of photon–jet transverse momentum correlations in 5.02 TeV Pb + Pb and pp collisions with ATLAS*, Phys. Lett. B **789** (2019) 167, arXiv: 1809.07280 [nucl-ex] (cit. on p. 8).

[29] R. Snellings, *Collective Expansion at the LHC: selected ALICE anisotropic flow measurements*, J. Phys. G **41** (2014) 124007, arXiv: 1408.2532 [nucl-ex] (cit. on pp. 8, 10).

[30] B. Alver and G. Roland, *Collision geometry fluctuations and triangular flow in heavy-ion collisions*, Phys. Rev. C **81** (2010) 054905, [Erratum: Phys.Rev.C 82, 039903 (2010)], arXiv: 1003.0194 [nucl-th] (cit. on pp. 9, 13).

[31] S. Voloshin and Y. Zhang, *Flow study in relativistic nuclear collisions by Fourier expansion of azimuthal particle distributions*, Zeitschrift fur Physik C Particles and Fields **70** (1996) 665, ISSN: 1431-5858, URL: http://dx.doi.org/10.1007/s002880050141 (cit. on pp. 9, 10).

[32] P. F. Kolb and U. W. Heinz, *Hydrodynamic description of ultrarelativistic heavy ion collisions*, (2003) 634, ed. by R. C. Hwa and X.-N. Wang, arXiv: nucl-th/0305084 (cit. on p. 10).

[33] U. Heinz and R. Snellings, *Collective flow and viscosity in relativistic heavy-ion collisions*, Ann. Rev. Nucl. Part. Sci. **63** (2013) 123, arXiv: 1301.2826 [nucl-th] (cit. on p. 10).

[34] P. Huovinen, P. F. Kolb, U. W. Heinz, P. V. Ruuskanen, and S. A. Voloshin, *Radial and elliptic flow at RHIC: Further predictions*, Phys. Lett. B **503** (2001) 58, arXiv: hep-ph/0101136 (cit. on p. 10).

[35] H. Petersen, *Anisotropic flow in transport + hydrodynamics hybrid approaches*, J. Phys. G **41** (2014) 124005, arXiv: 1404.1763 [nucl-th] (cit. on p. 10).

[36] C. Gale, S. Jeon, B. Schenke, P. Tribedy, and R. Venugopalan, *Event-by-event anisotropic flow in heavy-ion collisions from combined Yang-Mills and viscous fluid dynamics*, Phys. Rev. Lett. **110** (2013) 012302, arXiv: 1209.6330 [nucl-th] (cit. on p. 10).

[37] J. Noronha-Hostler, M. Luzum, and J.-Y. Ollitrault, *Hydrodynamic predictions for 5.02 TeV Pb-Pb collisions*, Phys. Rev. C **93** (2016) 034912, arXiv: 1511.06289 [nucl-th] (cit. on p. 10).

[38] S. Rao, M. Sievert, and J. Noronha-Hostler, *Baseline predictions of elliptic flow and fluctuations for the RHIC Beam Energy Scan using response coefficients*, Phys. Rev. C **103** (2021) 034910, arXiv: 1910.03677 [nucl-th] (cit. on p. 10).

[39] B. Schenke, C. Shen, and P. Tribedy, *Running the gamut of high energy nuclear collisions*, Phys. Rev. C **102** (2020) 044905, arXiv: 2005.14682 [nucl-th] (cit. on pp. 10, 13).

[40] P. Kovtun, D. T. Son, and A. O. Starinets, *Viscosity in strongly interacting quantum field theories from black hole physics*, Phys. Rev. Lett. **94** (2005) 111601, arXiv: hep-th/0405231 (cit. on p. 10).

[41] G. Policastro, D. T. Son, and A. O. Starinets, *The Shear viscosity of strongly coupled N=4 supersymmetric Yang-Mills plasma*, Phys. Rev. Lett. **87** (2001) 081601, arXiv: hep-th/0104066 (cit. on p. 10).

[42] G. S. Denicol, T. Kodama, T. Koide, and P. Mota, *Effect of bulk viscosity on Elliptic Flow near QCD phase transition*, Phys. Rev. C **80** (2009) 064901, arXiv: 0903.3595 [hep-ph] (cit. on p. 10).

[43] A. Monnai and T. Hirano, *Effects of Bulk Viscosity at Freezeout*, Phys. Rev. C **80** (2009) 054906, arXiv: 0903.4436 [nucl-th] (cit. on p. 10).

[44] J. Noronha-Hostler, G. S. Denicol, J. Noronha, R. P. G. Andrade, and F. Grassi, *Bulk Viscosity Effects in Event-by-Event Relativistic Hydrodynamics*, Phys. Rev. C **88** (2013) 044916, arXiv: `1305.1981 [nucl-th]` (cit. on p. 10).

[45] J. Noronha-Hostler, J. Noronha, and F. Grassi, *Bulk viscosity-driven suppression of shear viscosity effects on the flow harmonics at energies available at the BNL Relativistic Heavy Ion Collider*, Phys. Rev. C **90** (2014) 034907, arXiv: `1406.3333 [nucl-th]` (cit. on p. 10).

[46] S. Ryu et al., *Importance of the Bulk Viscosity of QCD in Ultrarelativistic Heavy-Ion Collisions*, Phys. Rev. Lett. **115** (2015) 132301, arXiv: `1502.01675 [nucl-th]` (cit. on pp. 10, 14).

[47] J. Novak et al., *Determining Fundamental Properties of Matter Created in Ultrarelativistic Heavy-Ion Collisions*, Phys. Rev. C **89** (2014) 034917, arXiv: `1303.5769 [nucl-th]` (cit. on p. 11).

[48] S. Pratt, E. Sangaline, P. Sorensen, and H. Wang, *Constraining the Eq. of State of Super-Hadronic Matter from Heavy-Ion Collisions*, Phys. Rev. Lett. **114** (2015) 202301, arXiv: `1501.04042 [nucl-th]` (cit. on p. 11).

[49] E. Sangaline and S. Pratt, *Toward a deeper understanding of how experiments constrain the underlying physics of heavy-ion collisions*, Phys. Rev. C **93** (2016) 024908, arXiv: `1508.07017 [nucl-th]` (cit. on p. 11).

[50] J. E. Bernhard, J. S. Moreland, S. A. Bass, J. Liu, and U. Heinz, *Applying Bayesian parameter estimation to relativistic heavy-ion collisions: simultaneous characterization of the initial state and quark-gluon plasma medium*, Phys. Rev. C **94** (2016) 024907, arXiv: `1605.03954 [nucl-th]` (cit. on p. 11).

[51] D. Devetak et al., *Global fluid fits to identified particle transverse momentum spectra from heavy-ion collisions at the Large Hadron Collider*, JHEP **06** (2020) 044, arXiv: `1909.10485 [hep-ph]` (cit. on p. 11).

[52] J. E. Bernhard, J. S. Moreland, and S. A. Bass, *Bayesian estimation of the specific shear and bulk viscosity of quark–gluon plasma*, Nature Phys. **15** (2019) 1113 (cit. on pp. 11, 14).

[53] G. Giacalone, F. G. Gardim, J. Noronha-Hostler, and J.-Y. Ollitrault, *Correlation between mean transverse momentum and anisotropic flow in heavy-ion collisions*, Phys. Rev. C **103** (2021) 024909, arXiv: `2004.01765 [nucl-th]` (cit. on p. 11).

[54] ALICE Collaboration,
Centrality dependence of π, K, p production in Pb-Pb collisions at $\sqrt{s_{NN}}$ = 2.76 TeV,
Phys. Rev. C **88** (2013) 044910, arXiv: 1303.0737 [hep-ex] (cit. on p. 14).

[55] ALICE Collaboration, *Higher harmonic anisotropic flow measurements of charged particles in Pb-Pb collisions at $\sqrt{s_{NN}}$=2.76 TeV*, Phys. Rev. Lett. **107** (2011) 032301, arXiv: 1105.3865 [nucl-ex] (cit. on pp. 14, 41).

[56] G. F. Sterman and S. Weinberg, *Jets from Quantum Chromodynamics*,
Phys. Rev. Lett. **39** (1977) 1436 (cit. on p. 15).

[57] ATLAS Collaboration, "ATLAS event at 13 TeV - Highest mass dijets angular event in 2015 data", General Photo, 2015, URL: https://cds.cern.ch/record/2113240 (cit. on p. 16).

[58] M. Cacciari, G. P. Salam, and G. Soyez, *The anti-k_t jet clustering algorithm*, JHEP **04** (2008) 063, arXiv: 0802.1189 [hep-ph] (cit. on pp. 16, 17).

[59] G. Corcella et al., *HERWIG 6.5 release note*, (2002), arXiv: hep-ph/0210213 (cit. on p. 17).

[60] G.-Y. Qin and X.-N. Wang, *Jet quenching in high-energy heavy-ion collisions*,
Int. J. Mod. Phys. E **24** (2015) 1530014, ed. by X.-N. Wang, arXiv: 1511.00790 [hep-ph] (cit. on pp. 17, 19).

[61] A. D. Martin, W. J. Stirling, R. S. Thorne, and G. Watt, *Parton distributions for the LHC*,
Eur. Phys. J. C **63** (2009) 189, arXiv: 0901.0002 [hep-ph] (cit. on p. 18).

[62] ATLAS Collaboration, *Measurement of the inclusive jet cross section in pp collisions at sqrt(s)=2.76 TeV and comparison to the inclusive jet cross section at sqrt(s)=7 TeV using the ATLAS detector*, Eur. Phys. J. C **73** (2013) 2509, arXiv: 1304.4739 [hep-ex] (cit. on p. 18).

[63] ATLAS Collaboration, *Measurement of Inclusive Jet and Dijet Cross Sections in Proton-Proton Collisions at 7 TeV Centre-of-Mass Energy with the ATLAS Detector*, Eur. Phys. J. C **71** (2011) 1512, arXiv: 1009.5908 [hep-ex] (cit. on p. 18).

[64] ATLAS Collaboration, *Measurement of the inclusive jet cross-sections in proton-proton collisions at $\sqrt{s} = 8$ TeV with the ATLAS detector*, JHEP **09** (2017) 020, arXiv: 1706.03192 [hep-ex] (cit. on pp. 18, 20).

[65] CMS Collaboration, *Measurement of the double-differential inclusive jet cross section in proton–proton collisions at $\sqrt{s} = 13$ TeV*, Eur. Phys. J. C **76** (2016) 451,
arXiv: 1605.04436 [hep-ex] (cit. on pp. 18, 20, 22).

[66] Z. Nagy, *Three jet cross-sections in hadron hadron collisions at next-to-leading order*, Phys. Rev. Lett. **88** (2002) 122003, arXiv: hep-ph/0110315 (cit. on p. 20).

[67] A. S. Yoon, "Centrality and p_T dependence of charged particle RAA in PbPb collisions at $\sqrt{s_{NN}} = 2.76$ TeV", *22nd International Conference on Ultra-Relativistic Nucleus-Nucleus*, 2011, arXiv: 1107.1862 [nucl-ex] (cit. on p. 21).

[68] ALICE Collaboration, *Suppression of Charged Particle Production at Large Transverse Momentum in Central Pb-Pb Collisions at $\sqrt{s_{NN}} = 2.76$ TeV*, Phys. Lett. B **696** (2011) 30, arXiv: 1012.1004 [nucl-ex] (cit. on p. 21).

[69] Z.-B. Kang, I. Vitev, and H. Xing, *Effects of cold nuclear matter energy loss on inclusive jet production in p+A collisions at energies available at the BNL Relativistic Heavy Ion Collider and the CERN Large Hadron Collider*, Phys. Rev. C **92** (2015) 054911, arXiv: 1507.05987 [hep-ph] (cit. on p. 18).

[70] CMS Collaboration, *Proton-Nucleus Collisions at the LHC: Scientific Opportunities and Requirements*, J. Phys. G **39** (2012) 015010, arXiv: 1105.3919 [hep-ph] (cit. on p. 18).

[71] ATLAS Collaboration, *Centrality and rapidity dependence of inclusive jet production in $\sqrt{s_{\mathrm{NN}}} = 5.02$ TeV proton-lead collisions with the ATLAS detector*, Phys. Lett. B **748** (2015) 392, arXiv: 1412.4092 [hep-ex] (cit. on p. 18).

[72] ALICE Collaboration, *Centrality dependence of charged jet production in p-Pb collisions at $\sqrt{s_{\mathrm{NN}}} = 5.02$ TeV*, (2016), arXiv: 1603.03402 [nucl-ex] (cit. on p. 18).

[73] CMS Collaboration, *Measurement of inclusive jet production and nuclear modifications in pPb collisions at $\sqrt{s_{\mathrm{NN}}} = 5.02$ TeV*, Eur. Phys. J. C **76** (2016) 372, arXiv: 1601.02001 [nucl-ex] (cit. on p. 18).

[74] G.-Y. Qin and B. Müller, *Explanation of Dijet Asymmetry in Pb+Pb Collisions at the Large Hadron Collider*, Phys. Rev. Lett. **106** (2011) 162302, arXiv: 1012.5280 [hep-ph] (cit. on pp. 19, 21), Erratum: Phys. Rev. Lett. **106** (2011) 162302.

[75] CMS Collaboration,
Jet Momentum Dependence of Jet Quenching in PbPb Collisions at $\sqrt{s_{NN}} = 2.76$ TeV,
Phys. Lett. B **712** (2012) 176, arXiv: 1202.5022 [nucl-ex] (cit. on p. 19).

[76] CMS Collaboration, *Measurement of transverse momentum relative to dijet systems in PbPb and pp collisions at $\sqrt{s_{\mathrm{NN}}} = 2.76$ TeV*, JHEP **01** (2016) 006, arXiv: 1509.09029 [nucl-ex] (cit. on p. 19).

[77] ATLAS Collaboration, *Measurement of the nuclear modification factor for inclusive jets in Pb+Pb collisions at $\sqrt{s_{\mathrm{NN}}} = 5.02$ TeV with the ATLAS detector*, Phys. Lett. B **790** (2019) 108, arXiv: 1805.05635 [nucl-ex] (cit. on pp. 19, 22, 23, 45).

[78] B. Betz and M. Gyulassy, *Constraints on the Path-Length Dependence of Jet Quenching in Nuclear Collisions at RHIC and LHC*, JHEP **08** (2014) 090, [Erratum: JHEP 10, 043 (2014)], arXiv: 1404.6378 [hep-ph] (cit. on p. 19).

[79] ATLAS Collaboration, *Charged-hadron production in pp, p+Pb, Pb+Pb, and Xe+Xe collisions at $\sqrt{s_{_{NN}}} = 5$ TeV with the ATLAS detector at the LHC*, JHEP **07** (2023) 074, arXiv: 2211.15257 [hep-ex] (cit. on pp. 22, 23, 45, 51).

[80] CMS Collaboration, *Observation and studies of jet quenching in PbPb collisions at nucleon-nucleon center-of-mass energy = 2.76 TeV*, Phys. Rev. C **84** (2011) 024906, arXiv: 1102.1957 [nucl-ex] (cit. on p. 22).

[81] CMS Collaboration,
Charged-particle nuclear modification factors in PbPb and pPb collisions at $\sqrt{s_{\mathrm{N\,N}}} = 5.02$ TeV,
JHEP **04** (2017) 039, arXiv: 1611.01664 [nucl-ex] (cit. on p. 22).

[82] ALICE Collaboration, *Transverse momentum spectra and nuclear modification factors of charged particles in pp, p-Pb and Pb-Pb collisions at the LHC*, JHEP **11** (2018) 013, arXiv: 1802.09145 [nucl-ex] (cit. on p. 22).

[83] B. Betz et al., *Cumulants and nonlinear response of high p_T harmonic flow at $\sqrt{s_{NN}} = 5.02$ TeV*, Phys. Rev. C **95** (2017) 044901, arXiv: 1609.05171 [nucl-th] (cit. on p. 24).

[84] W. Zhao, W. Ke, W. Chen, T. Luo, and X.-N. Wang, *From Hydrodynamics to Jet Quenching, Coalescence, and Hadron Cascade: A Coupled Approach to Solving the RAA⊗v2 Puzzle*, Phys. Rev. Lett. **128** (2022) 022302, arXiv: 2103.14657 [hep-ph] (cit. on p. 24).

[85] ATLAS Collaboration, *Measurement of the Azimuthal Angle Dependence of Inclusive Jet Yields in Pb+Pb Collisions at $\sqrt{s_{NN}} = 2.76$ TeV with the ATLAS detector*, Phys. Rev. Lett. **111** (2013) 152301, arXiv: 1306.6469 [hep-ex] (cit. on pp. 25, 45, 46).

[86] ALICE Collaboration,
Azimuthal anisotropy of charged jet production in $\sqrt{s_{\mathrm{NN}}} = 2.76$ TeV Pb-Pb collisions,
Phys. Lett. B **753** (2016) 511, arXiv: 1509.07334 [nucl-ex] (cit. on pp. 25, 46).

[87] ATLAS Collaboration, *Measurements of azimuthal anisotropies of jet production in Pb+Pb collisions at $\sqrt{s_{NN}} = 5.02$ TeV with the ATLAS detector*, (2021), arXiv: 2111.06606 [nucl-ex]
(cit. on pp. 25, 45, 46, 86, 87, 130, 141, 142).

[88] CMS Collaboration, *Azimuthal anisotropy of charged particles with transverse momentum up to 100 GeV/ c in PbPb collisions at $\sqrt{s}_{NN}$=5.02 TeV*, Phys. Lett. B **776** (2018) 195,
arXiv: 1702.00630 [hep-ex] (cit. on pp. 25, 39, 41, 43, 45, 46, 84, 85, 130, 134, 135).

[89] L. Evans and P. Bryant, *LHC Machine*, JINST **3** (2008) S08001 (cit. on p. 26).

[90] O. S. Brüning et al., *LHC Design Report*, CERN Yellow Reports: Monographs, Geneva: CERN, 2004,
URL: https://cds.cern.ch/record/782076 (cit. on p. 26).

[91] ATLAS Collaboration, *The ATLAS Experiment at the CERN Large Hadron Collider*,
JINST **3** (2008) S08003 (cit. on pp. 26, 27).

[92] CMS Collaboration, *The CMS Experiment at the CERN LHC*, JINST **3** (2008) S08004 (cit. on p. 26).

[93] ALICE Collaboration, *The ALICE experiment at the CERN LHC*, JINST **3** (2008) S08002
(cit. on p. 26).

[94] LHCb Collaboration, *The LHCb Detector at the LHC*, JINST **3** (2008) S08005 (cit. on p. 26).

[95] CERN, *The CERN accelerator complex, layout in 2022*,
https://cds.cern.ch/images/CERN-GRAPHICS-2022-001-1,
URL: https://cds.cern.ch/images/CERN-GRAPHICS-2022-001-1 (cit. on p. 27).

[96] *LHC Run 3: physics at record energy starts tomorrow — home.cern*, https://home.cern/news/news/physics/lhc-run-3-physics-record-energy-starts-tomorrow,
[Accessed 20-10-2024], 2022 (cit. on p. 26).

[97] C. Collaboration, https://lhc-machine-outreach.web.cern.ch/images/2-beams-IP.gif,
[Accessed 20-10-2024] (cit. on p. 28).

[98] Bianchi, Riccardo Maria and ATLAS Collaboration,
"ATLAS experiment schematic or layout illustration", General Photo, 2022,
URL: https://cds.cern.ch/record/2837191 (cit. on pp. 27, 29).

[99] ATLAS Collaboration, *ATLAS Inner Detector: Technical Design Report, Volume 1*, ATLAS-TDR-4; CERN-LHCC-97-016, 1997, URL: https://cds.cern.ch/record/331063 (cit. on p. 28).

[100] ATLAS Collaboration, *ATLAS Inner Detector: Technical Design Report, Volume 2*, ATLAS-TDR-5, CERN-LHCC-97-017, 1997, URL: https://cds.cern.ch/record/331064 (cit. on p. 28).

[101] K. Potamianos, *The upgraded Pixel detector and the commissioning of the Inner Detector tracking of the ATLAS experiment for Run-2 at the Large Hadron Collider*, 2016, arXiv: 1608.07850 [physics.ins-det] (cit. on p. 28).

[102] ATLAS Collaboration, *ATLAS Insertable B-Layer: Technical Design Report*, ATLAS-TDR-19; CERN-LHCC-2010-013, 2010, URL: https://cds.cern.ch/record/1291633 (cit. on p. 28), Addendum: ATLAS-TDR-19-ADD-1; CERN-LHCC-2012-009, 2012, URL: https://cds.cern.ch/record/1451888.

[103] A. Collaboration, *The ATLAS Experiment at the CERN Large Hadron Collider*, Journal of Instrumentation **3** (2008) S08003, URL: https://doi.org/10.1088/1748-0221/3/08/s08003 (cit. on p. 28).

[104] ATLAS Collaboration, *Reconstruction of primary vertices at the ATLAS experiment in Run 1 proton–proton collisions at the LHC*, Eur. Phys. J. C **77** (2017) 332, arXiv: 1611.10235 [physics.ins-det] (cit. on p. 29).

[105] CERN, *Experiment Briefing: Keeping the ATLAS Inner Detector in perfect alignment*, https://cds.cern.ch/images/ATLAS-PHOTO-2020-018-1, URL: https://cds.cern.ch/images/ATLAS-PHOTO-2020-018-1 (cit. on p. 30).

[106] ATLAS Collaboration, *ATLAS Calorimeter Performance: Technical Design Report*, ATLAS-TDR-1; CERN-LHCC-96-040, 1996, URL: https://cds.cern.ch/record/331059 (cit. on p. 29).

[107] CERN, *Computer Generated image of the ATLAS calorimeter*, https://cds.cern.ch/images/CERN-GE-0803015-01, URL: https://cds.cern.ch/images/CERN-GE-0803015-01 (cit. on p. 31).

[108] ATLAS Collaboration, *ATLAS Liquid Argon Calorimeter: Technical Design Report*, ATLAS-TDR-2; CERN-LHCC-96-041, 1996, URL: https://cds.cern.ch/record/331061 (cit. on p. 30).

[109] ATLAS Collaboration, *ATLAS Tile Calorimeter: Technical Design Report*, ATLAS-TDR-3; CERN-LHCC-96-042, 1996, URL: https://cds.cern.ch/record/331062 (cit. on p. 30).

[110] ATLAS Collaboration, *ATLAS Muon Spectrometer: Technical Design Report*, ATLAS-TDR-10; CERN-LHCC-97-022, CERN, 1997, URL: https://cds.cern.ch/record/331068 (cit. on p. 31).

[111] ATLAS Collaboration, *ATLAS Muon Spectrometer Phase-II Upgrade: Technical Design Report*, ATLAS-TDR-026; CERN-LHCC-2017-017, 2017, URL: https://cds.cern.ch/record/2285580 (cit. on p. 31).

[112] *ATLAS muon spectrometer: Technical Design Report*, Technical design report. ATLAS, Geneva: CERN, 1997, URL: https://cds.cern.ch/record/331068 (cit. on p. 31).

[113] ATLAS Collaboration, *Operation of the ATLAS trigger system in Run 2*, JINST **15** (2020) P10004, arXiv: 2007.12539 [physics.ins-det] (cit. on pp. 32, 47).

[114] ATLAS Collaboration, *The ATLAS Collaboration Software and Firmware*, ATL-SOFT-PUB-2021-001, 2021, URL: https://cds.cern.ch/record/2767187 (cit. on p. 32).

[115] ATLAS Collaboration, *Measurement of the azimuthal anisotropy for charged particle production in* $\sqrt{s_{NN}} = 2.76$ *TeV lead-lead collisions with the ATLAS detector*, Phys. Rev. C **86** (2012) 014907, arXiv: 1203.3087 [hep-ex] (cit. on pp. 33, 50).

[116] CERES, *Elliptic flow of charged pions, protons and strange particles emitted in Pb+Au collisions at top SPS energy*, Nucl. Phys. A **894** (2012) 41, arXiv: 1205.3692 [nucl-ex] (cit. on p. 33).

[117] CMS Collaboration, *Measurement of the Elliptic Anisotropy of Charged Particles Produced in PbPb Collisions at* $\sqrt{s}_{NN}$*=2.76 TeV*, Phys. Rev. C **87** (2013) 014902, arXiv: 1204.1409 [nucl-ex] (cit. on pp. 33, 34).

[118] PHOBOS Collaboration, *Importance of correlations and fluctuations on the initial source eccentricity in high-energy nucleus-nucleus collisions*, Phys. Rev. C **77** (2008) 014906, arXiv: 0711.3724 [nucl-ex] (cit. on pp. 33, 35).

[119] A. M. Poskanzer and S. A. Voloshin, *Methods for analyzing anisotropic flow in relativistic nuclear collisions*, Phys. Rev. C **58** (1998) 1671, arXiv: nucl-ex/9805001 (cit. on pp. 33, 34, 50).

[120] J.-Y. Ollitrault, A. M. Poskanzer, and S. A. Voloshin, *Effect of flow fluctuations and nonflow on elliptic flow methods*, Phys. Rev. C **80** (2009) 014904, arXiv: 0904.2315 [nucl-ex] (cit. on pp. 33, 34).

[121] B. Abelev et al., *Anisotropic flow of charged hadrons, pions and (anti-)protons measured at high transverse momentum in Pb-Pb collisions at* $\sqrt{s_{NN}}$*=2.76 TeV*, Phys. Lett. B **719** (2013) 18, arXiv: 1205.5761 [nucl-ex] (cit. on p. 34).

[122] ATLAS Collaboration, *Measurement of the azimuthal anisotropy of charged particles produced in* $\sqrt{s_{_{NN}}}$ *= 5.02 TeV Pb+Pb collisions with the ATLAS detector*, Eur. Phys. J. C **78** (2018) 997, arXiv: 1808.03951 [nucl-ex] (cit. on pp. 34, 36, 38, 45, 46, 60, 84, 85, 130, 132, 133).

[123] M. Luzum and J.-Y. Ollitrault, *Eliminating experimental bias in anisotropic-flow measurements of high-energy nuclear collisions*, Phys. Rev. C **87** (2013) 044907, arXiv: 1209.2323 [nucl-ex] (cit. on pp. 34, 35, 61).

[124] ATLAS Collaboration, *Measurement of flow harmonics with multi-particle cumulants in Pb+Pb collisions at* $\sqrt{s_{\mathrm{NN}}} = 2.76$ *TeV with the ATLAS detector*, Eur. Phys. J. C **74** (2014) 3157, arXiv: 1408.4342 [hep-ex] (cit. on pp. 39, 41, 44, 46).

[125] ALICE Collaboration, *Multiparticle azimuthal correlations in p -Pb and Pb-Pb collisions at the CERN Large Hadron Collider*, Phys. Rev. C **90** (2014) 054901, arXiv: 1406.2474 [nucl-ex] (cit. on pp. 39, 41).

[126] CMS Collaboration, *Multiplicity and Transverse Momentum Dependence of Two- and Four-Particle Correlations in pPb and PbPb Collisions*, Phys. Lett. B **724** (2013) 213, arXiv: 1305.0609 [nucl-ex] (cit. on pp. 39, 41).

[127] STAR Collaboration, *Azimuthal anisotropy in U+U and Au+Au collisions at RHIC*, Phys. Rev. Lett. **115** (2015) 222301, arXiv: 1505.07812 [nucl-ex] (cit. on pp. 39, 41).

[128] ATLAS Collaboration, *Measurement of long-range multiparticle azimuthal correlations with the subevent cumulant method in pp and* $p + Pb$ *collisions with the ATLAS detector at the CERN Large Hadron Collider*, Phys. Rev. C **97** (2018) 024904, arXiv: 1708.03559 [hep-ex] (cit. on p. 39).

[129] CMS Collaboration, *Non-Gaussian elliptic-flow fluctuations in PbPb collisions at* $\sqrt{s_{_{NN}}} = 5.02$ *TeV*, Phys. Lett. B **789** (2019) 643, arXiv: 1711.05594 [nucl-ex] (cit. on pp. 39, 41, 42).

[130] ALICE Collaboration,
Measurements of inclusive jet spectra in pp and central Pb-Pb collisions at $\sqrt{s_{\mathrm{NN}}} = 5.02$ TeV,
Phys. Rev. C **101** (2020) 034911, arXiv: 1909.09718 [nucl-ex] (cit. on pp. 39, 41, 45).

[131] N. Borghini, P. M. Dinh, and J.-Y. Ollitrault,
A New method for measuring azimuthal distributions in nucleus-nucleus collisions,
Phys. Rev. C **63** (2001) 054906, arXiv: nucl-th/0007063 (cit. on pp. 39–41, 46).

[132] N. Borghini, P. M. Dinh, and J.-Y. Ollitrault, *Flow analysis from multiparticle azimuthal correlations*,
Phys. Rev. C **64** (2001) 054901, arXiv: nucl-th/0105040 (cit. on pp. 39, 40, 46, 62, 90).

[133] A. Bilandzic, R. Snellings, and S. Voloshin, *Flow analysis with cumulants: Direct calculations*,
Phys. Rev. C **83** (2011) 044913, arXiv: 1010.0233 [nucl-ex] (cit. on pp. 39, 46, 61–64).

[134] A. Bilandzic, C. H. Christensen, K. Gulbrandsen, A. Hansen, and Y. Zhou,
Generic framework for anisotropic flow analyses with multiparticle azimuthal correlations,
Phys. Rev. C **89** (2014) 064904, arXiv: 1312.3572 [nucl-ex] (cit. on pp. 39, 40, 46, 61, 63).

[135] S. A. Voloshin, A. M. Poskanzer, A. Tang, and G. Wang,
Elliptic flow in the Gaussian model of eccentricity fluctuations, Phys. Lett. B **659** (2008) 537,
arXiv: 0708.0800 [nucl-th] (cit. on pp. 39, 91).

[136] L. Yan, J.-Y. Ollitrault, and A. M. Poskanzer,
Azimuthal Anisotropy Distributions in High-Energy Collisions, Phys. Lett. B **742** (2015) 290,
arXiv: 1408.0921 [nucl-th] (cit. on p. 39).

[137] H. Grönqvist, J.-P. Blaizot, and J.-Y. Ollitrault, *Non-Gaussian eccentricity fluctuations*,
Phys. Rev. C **94** (2016) 034905, arXiv: 1604.07230 [nucl-th] (cit. on p. 39).

[138] G. Giacalone, L. Yan, J. Noronha-Hostler, and J.-Y. Ollitrault, *Skewness of elliptic flow fluctuations*,
Phys. Rev. C **95** (2017) 014913, arXiv: 1608.01823 [nucl-th] (cit. on p. 39).

[139] P. M. Dinh, N. Borghini, and J.-Y. Ollitrault, *Effects of HBT correlations on flow measurements*,
Phys. Lett. B **477** (2000) 51, arXiv: nucl-th/9912013 (cit. on p. 40).

[140] R. Hanbury Brown and R. Q. Twiss, *A Test of a new type of stellar interferometer on Sirius*,
Nature **178** (1956) 1046 (cit. on p. 40).

[141] STAR Collaboration, *Elliptic flow in Au + Au collisions at (S(NN))**(1/2) = 130 GeV*,
Phys. Rev. Lett. **86** (2001) 402, arXiv: nucl-ex/0009011 (cit. on p. 40).

[142] Z.-W. Lin, C. M. Ko, B.-A. Li, B. Zhang, and S. Pal, *A Multi-phase transport model for relativistic heavy ion collisions*, Phys. Rev. C **72** (2005) 064901, arXiv: nucl-th/0411110 (cit. on p. 41).

[143] T. Sjöstrand, S. Mrenna, and P. Skands, *A brief introduction to PYTHIA 8.1*, Comput. Phys. Commun. **178** (2008) 852, arXiv: 0710.3820 [hep-ph] (cit. on p. 41).

[144] L.-G. Pang, H. Petersen, G.-Y. Qin, V. Roy, and X.-N. Wang, *Decorrelation of anisotropic flow along the longitudinal direction*, Eur. Phys. J. A **52** (2016) 97, arXiv: 1511.04131 [nucl-th] (cit. on p. 41).

[145] CMS Collaboration, *Evidence for transverse momentum and pseudorapidity dependent event plane fluctuations in PbPb and pPb collisions*, Phys. Rev. C **92** (2015) 034911, arXiv: 1503.01692 [nucl-ex] (cit. on p. 41).

[146] ATLAS Collaboration, *Measurement of longitudinal flow decorrelations in Pb+Pb collisions at* $\sqrt{s_{NN}} = 2.76$ *and 5.02 TeV with the ATLAS detector*, Eur. Phys. J. C **78** (2018) 142, arXiv: 1709.02301 [nucl-ex] (cit. on pp. 41, 86).

[147] ATLAS Collaboration, *Longitudinal Flow Decorrelations in Xe+Xe Collisions at* $\sqrt{s_{\mathrm{NN}}} = 5.44$ *TeV with the ATLAS Detector*, Phys. Rev. Lett. **126** (2021) 122301, arXiv: 2001.04201 [nucl-ex] (cit. on p. 41).

[148] ATLAS Collaboration, *Measurements of longitudinal flow decorrelations in pp and Xe+Xe collisions with the ATLAS detector*, (2023), arXiv: 2308.16745 [nucl-ex] (cit. on p. 41).

[149] ATLAS Collaboration, *Fluctuations of anisotropic flow in Pb+Pb collisions at* $\sqrt{s_{\mathrm{NN}}} = 5.02$ *TeV with the ATLAS detector*, JHEP **01** (2020) 051, arXiv: 1904.04808 [nucl-ex] (cit. on pp. 41, 42, 46, 62, 63, 65, 68, 79, 91).

[150] S. Acharya et al., *Energy dependence and fluctuations of anisotropic flow in Pb-Pb collisions at* $\sqrt{s_{\mathrm{NN}}} = 5.02$ *and 2.76 TeV*, JHEP **07** (2018) 103, arXiv: 1804.02944 [nucl-ex] (cit. on pp. 41, 42).

[151] CMS Collaboration, *Measurement of Higher-Order Harmonic Azimuthal Anisotropy in PbPb Collisions at* $\sqrt{s_{NN}} = 2.76$ *TeV*, Phys. Rev. C **89** (2014) 044906, arXiv: 1310.8651 [nucl-ex] (cit. on p. 41).

[152] J. Jia, M. Zhou, and A. Trzupek, *Revealing long-range multiparticle collectivity in small collision systems via subevent cumulants*, Phys. Rev. C **96** (2017) 034906, arXiv: 1701.03830 [nucl-th] (cit. on pp. 42, 46, 61, 65, 67, 68, 91).

[153] V. Skokov, B. Friman, and K. Redlich,
Volume Fluctuations and Higher Order Cumulants of the Net Baryon Number,
Phys. Rev. C **88** (2013) 034911, arXiv: 1205.4756 [hep-ph] (cit. on p. 42).

[154] X. Luo, J. Xu, B. Mohanty, and N. Xu, *Volume fluctuation and auto-correlation effects in the moment analysis of net-proton multiplicity distributions in heavy-ion collisions*,
J. Phys. G **40** (2013) 105104, arXiv: 1302.2332 [nucl-ex] (cit. on p. 42).

[155] F. G. Gardim, F. Grassi, M. Luzum, and J.-Y. Ollitrault,
Mapping the hydrodynamic response to the initial geometry in heavy-ion collisions,
Phys. Rev. C **85** (2012) 024908, arXiv: 1111.6538 [nucl-th] (cit. on p. 42).

[156] D. Teaney and L. Yan,
Non linearities in the harmonic spectrum of heavy ion collisions with ideal and viscous hydrodynamics,
Phys. Rev. C **86** (2012) 044908, arXiv: 1206.1905 [nucl-th] (cit. on p. 42).

[157] J. Noronha-Hostler, B. Betz, J. Noronha, and M. Gyulassy,
Event-by-event hydrodynamics + jet energy loss: A solution to the $R_{AA} \otimes v_2$ puzzle,
Phys. Rev. Lett. **116** (2016) 252301, arXiv: 1602.03788 [nucl-th] (cit. on p. 43).

[158] J. Xu, J. Liao, and M. Gyulassy,
Bridging Soft-Hard Transport Properties of Quark-Gluon Plasmas with CUJET3.0,
JHEP **02** (2016) 169, arXiv: 1508.00552 [hep-ph] (cit. on p. 43).

[159] CMS Collaboration,
First measurement of large area jet transverse momentum spectra in heavy-ion collisions,
JHEP **05** (2021) 284, arXiv: 2102.13080 [hep-ex] (cit. on p. 45).

[160] ATLAS Collaboration, *Measurement of suppression of large-radius jets and its dependence on substructure in Pb+Pb collisions at $\sqrt{s_{\mathrm{NN}}} = 5.02$ TeV with the ATLAS detector*, (2023),
arXiv: 2301.05606 [nucl-ex] (cit. on p. 45).

[161] X.-N. Wang, *Jet quenching and azimuthal anisotropy of large p(T) spectra in noncentral high-energy heavy ion collisions*, Phys. Rev. C **63** (2001) 054902, arXiv: nucl-th/0009019 (cit. on p. 45).

[162] M. Gyulassy, I. Vitev, and X. N. Wang, *High p(T) azimuthal asymmetry in noncentral A+A at RHIC*,
Phys. Rev. Lett. **86** (2001) 2537, arXiv: nucl-th/0012092 (cit. on p. 45).

[163] E. V. Shuryak, *The Azimuthal asymmetry at large p(t) seem to be too large for a 'jet quenching'*,
Phys. Rev. C **66** (2002) 027902, arXiv: nucl-th/0112042 (cit. on p. 45).

[164] ALICE Collaboration, *Investigations of Anisotropic Flow Using Multiparticle Azimuthal Correlations in pp, p-Pb, Xe-Xe, and Pb-Pb Collisions at the LHC*, Phys. Rev. Lett. **123** (2019) 142301, arXiv: 1903.01790 [nucl-ex] (cit. on p. 45).

[165] STAR Collaboration, *Elliptic flow from two and four particle correlations in Au+Au collisions at* $\sqrt{s_{NN}} = 130\ GeV$, Phys. Rev. C **66** (2002) 034904, arXiv: nucl-ex/0206001 (cit. on pp. 46, 60).

[166] PHENIX Collaboration, *Multiparticle azimuthal correlations for extracting event-by-event elliptic and triangular flow in Au+Au collisions at* $\sqrt{s_{NN}} = 200\ GeV$, Phys. Rev. C **99** (2019) 024903, arXiv: 1804.10024 [nucl-ex] (cit. on p. 46).

[167] S. A. Voloshin, A. M. Poskanzer, and R. Snellings, *Collective phenomena in non-central nuclear collisions*, Landolt-Bornstein **23** (2010) 293, ed. by R. Stock, arXiv: 0809.2949 [nucl-ex] (cit. on pp. 46, 60).

[168] N. Borghini, P. M. Dinh, and J.-Y. Ollitrault, "Flow analysis from cumulants: A Practical guide", *International Workshop on the Physics of the Quark Gluon Plasma*, 2001, arXiv: nucl-ex/0110016 (cit. on p. 46).

[169] P. Huo, K. Gajdošová, J. Jia, and Y. Zhou, *Importance of non-flow in mixed-harmonic multi-particle correlations in small collision systems*, Phys. Lett. B **777** (2018) 201, arXiv: 1710.07567 [nucl-ex] (cit. on pp. 46, 65, 89).

[170] ATLAS Collaboration, *Performance of the ATLAS Trigger System in 2015*, Eur. Phys. J. C **77** (2017) 317, arXiv: 1611.09661 [hep-ex] (cit. on p. 47).

[171] M. Gyulassy and X.-N. Wang, *HIJING 1.0: A Monte Carlo program for parton and particle production in high-energy hadronic and nuclear collisions*, Comput. Phys. Commun. **83** (1994) 307, arXiv: nucl-th/9502021 (cit. on p. 50).

[172] ATLAS Collaboration, *AtlFast3: The Next Generation Of Fast Simulation in ATLAS*, Comput. Softw. Big Sci. **6** (2021) 7, arXiv: 2109.02551 [hep-ex] (cit. on p. 50).

[173] GEANT4 Collaboration, *GEANT4–a simulation toolkit*, Nucl. Instrum. Meth. A **506** (2003) 250 (cit. on p. 50).

[174] ATLAS Collaboration, *The ATLAS Simulation Infrastructure*, Eur. Phys. J. C **70** (2010) 823, arXiv: 1005.4568 [physics.ins-det] (cit. on p. 50).

[175] ATLAS Collaboration, *Measurement of jet fragmentation in Pb+Pb and pp collisions at $\sqrt{s_{NN}} = 5.02$ TeV with the ATLAS detector*, Phys. Rev. C **98** (2018) 024908, arXiv: 1805.05424 [nucl-ex] (cit. on p. 51).

[176] K. Burka, A. Trzupek, and T. Bold, *Measurement of centrality, pseudorapidity and pT dependence of higer flow harmonics in lead-lead collisions at 5.02 TeV with the ATLAS detector.*, URL: https://cds.cern.ch/record/2151932/ (cit. on p. 53).

[177] A. M. Sickles, M. Rybar, and M. Spousta, *Measurement of jet fragmentation in 5.02 TeV proton-lead and proton-proton collisions with the ATLAS detector*, tech. rep., CERN, 2016, URL: https://cds.cern.ch/record/2235254 (cit. on p. 57).

[178] ATLAS Collaboration, *Measurement of the azimuthal anisotropy of charged-particle production in $Xe+Xe$ collisions at $\sqrt{s_{\mathrm{NN}}} = 5.44$ TeV with the ATLAS detector*, Phys. Rev. C **101** (2020) 024906, arXiv: 1911.04812 [nucl-ex] (cit. on p. 60).

[179] J. Jia and S. Radhakrishnan, *Limitation of multiparticle correlations for studying the event-by-event distribution of harmonic flow in heavy-ion collisions*, Phys. Rev. C **92** (2015) 024911, arXiv: 1412.4759 [nucl-ex] (cit. on p. 62).

[180] D. Perepelitsa, *Centrality determination in 5.02 TeV Pb+Pb collision data in 2015, using the Glauber v3.2 model*, URL: https://cds.cern.ch/record/2672348 (cit. on p. 75).

[181] M. Zhou and J. Jia, *Measurement of flow harmonics with multi-particle cumulants in Pb+Pb collisions at $\sqrt{s_{NN}} = 2.76$ and $\sqrt{s_{NN}} = 5.02$ TeV with the ATLAS detector*, tech. rep., CERN, 2017, URL: https://cds.cern.ch/record/2272101 (cit. on p. 79).

[182] ATLAS Collaboration, *Measurement of the distributions of event-by-event flow harmonics in lead-lead collisions at $\sqrt{s_{_{NN}}}$= 2.76 TeV with the ATLAS detector at the LHC*, JHEP **11** (2013) 183, arXiv: 1305.2942 [hep-ex] (cit. on p. 91).

Appendix A: Additional pile-up rejections

A.1 Introduction

The 2018 PbPb dataset used in this analysis is composed of 44 runs[1], and the first 20 runs have bunch spacing of 100 ns while the later 24 runs have bunch spacing of 75 ns for faster event rate. Due to this change in run condition, a time-dependence is found in some measured quantities, the multi-particle correlators $\langle\langle 4\rangle\rangle_n$ and $\langle\langle 2\rangle\rangle_n$ as well as the cumulant $c_n\{4\}$. The detailed definition of correlators $\langle\langle 4\rangle\rangle_n$ and $\langle\langle 2\rangle\rangle_n$ as well as its related variable $c_n\{4\}$ can be found in Section 4.4.2. This section explains the run-dependence behavior of correlators and a systematic study on additional event rejections required for this analysis to reduce this dependence.

For testing purpose, a smaller minimum bias dataset using high level trigger (HLT) minbias triggers are used in this study, labeled as MB in this section. The triggers used for MB have same requirements as the larger partial event building (PEB) dataset used in this analysis (See Section 4.2.1 for details). Different from the PEB dataset, the MB triggers are determined at HLT instead of level-1 (L1) (for details of HLT and L1, see Section 2.2.4). The PEB dataset has approximately 10 times number of events in comparison to MB.

Unless labelled otherwise, the tracks used in this section pass the same tracking selections required in this analysis except for the minimum p_{T} requirement of 1 GeV. To understand the reasons of the run-dependence observed, the tracks used in this Appendix goes down to 0.5 GeV, which is the lower limit of ATLAS track reconstruction. Events going into this section go through the standard ATLAS online selections as the PEB dataset.

All error bars are statistical only in this section.

[1]A "run" in a dataset refers to a successive period of data production and acquisition.

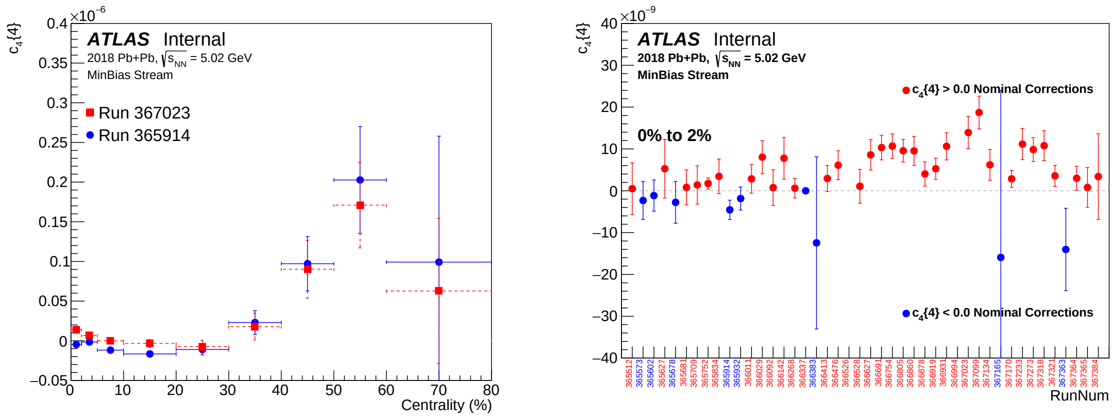

Figure A.1: Left: A centrality dependent comparison of $c_n\{4\}$ values between an earlier run and a later run. Right: Values of $c_n\{4\}$ versus run number for centrality 0–2%.

A.2 Run-by-run difference

As shown in Figure A.1 and Fig A.2, when analyzed using default track selections and corrections explained in Section 4.3 (labeleded in figures as "Nominal corrections"), an obvious run-dependence is seen. This effect is the most obvious in central events. In the following sections, study results are shown for the 0–2% centrality where the most tracks are available for improved statistics. A comparison between before and after the additional cuts for $c_2\{4\}$ and $c_3\{4\}$ in full centrality ranges are available in the Section A.3.

A set of tests were done to understand what corrections to which this dependence is sensitive to.

A.2.1 Run-dependence versus out-of-time pileup Rejections

Out-of-time pile-up rejections are done using the $\Sigma E_{\mathrm{T}}^{\mathrm{FCal}}$ versus N_{ch} distribution as described in Section 4.2.3. It is observed that in later runs, there are more events with $\langle 4\rangle_n$ significantly higher than the rest of events, neighboring the out-of-time pile-up events with higher than expected $\Sigma E_{\mathrm{T}}^{\mathrm{FCal}}$, as shown in Figure A.3. It can also be seen that there are more out-of-time pile-up events in the later runs. Events with distorted FCal measurements could lead to mixing of centrality. As correlators have strong dependence on the centrality, this could lead to a bias in the measurement.

Different levels of OOTP rejections from the positive ΣE_{FCal} side are experimented and tested against values of $c_4\{4\}$, as seen in Figure A.4. For this analysis, a rejection level of 1σ from central was selected, which rejects $\approx 15\%$ of events nearly independent of centrality. In this section, the tests to understand run-dependence is done with lowest reconstructed p_{T} for the tracks to identify biggest difference and boost statistics. The run-by-run results are consistent with each other when using tracks with $p_{\mathrm{T}} > 1$ GeV, as

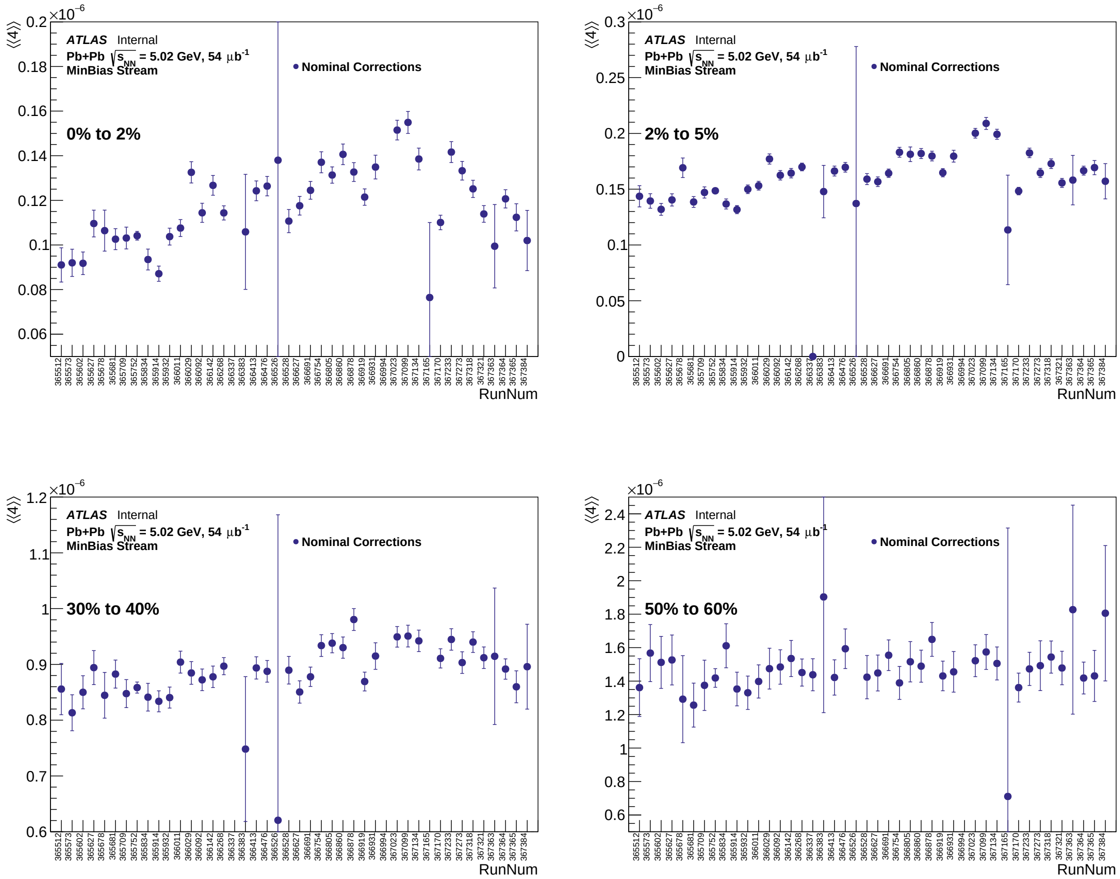

Figure A.2: Top left: Values of $\langle\langle 4\rangle\rangle_n$ versus run number for centrality 0–2%. Top right: Values of $\langle\langle 4\rangle\rangle_n$ versus run number for centrality 2–5%. Bottom left: Values of $\langle\langle 4\rangle\rangle_n$ versus run number for centrality 30–40%. Bottom right: Values of $\langle\langle 4\rangle\rangle_n$ versus run number for centrality 50–60%.

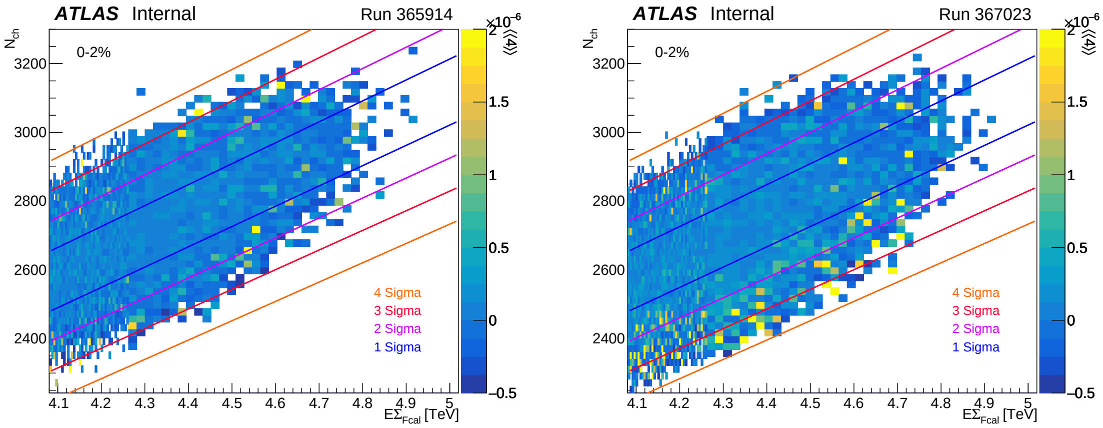

Figure A.3: Left: Mean 4-particle correlators $\langle\langle 4 \rangle\rangle_n$ on a N_{ch} versus $\Sigma E_{\mathrm{T}}^{\mathrm{FCal}}$ map from an earlier run with 100 ns bunch spacing. Right: Mean 4-particle correlators $\langle\langle 4 \rangle\rangle_n$ on a N_{ch} versus $\Sigma E_{\mathrm{T}}^{\mathrm{FCal}}$ map from an later run with 75 ns bunch spacing.

shown in Figure A.5.

A.2.2 Run-dependence versus in-time pile-up rejections

In-time pile-up rejections are done using the anti-correlation between ZDC measurements of spectator neutrons and ΣE_{FCal} in the nominal results, as explained in Section 4.2.3. Tighter selections are done on MB dataset to experiment whether the run-dependence is sensitive to this rejection. As shown in Figure A.6, rejecting events outside of 1σ or 3σ on $N_{neutron}$ distribution does not affect run-dependence of $\langle\langle 4 \rangle\rangle_n$ in centrality 0–2%.

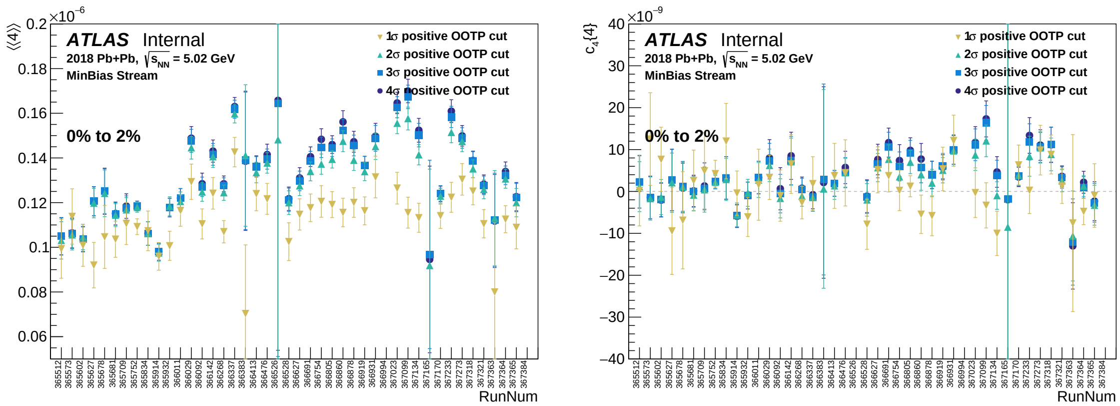

Figure A.4: Run-by-run differences in centrality 0–2% with different σ of OOTP rejections. Left plot shown is for $\langle\langle 4\rangle\rangle_n$ and right hand side plot shown is for $c_4\{4\}$.

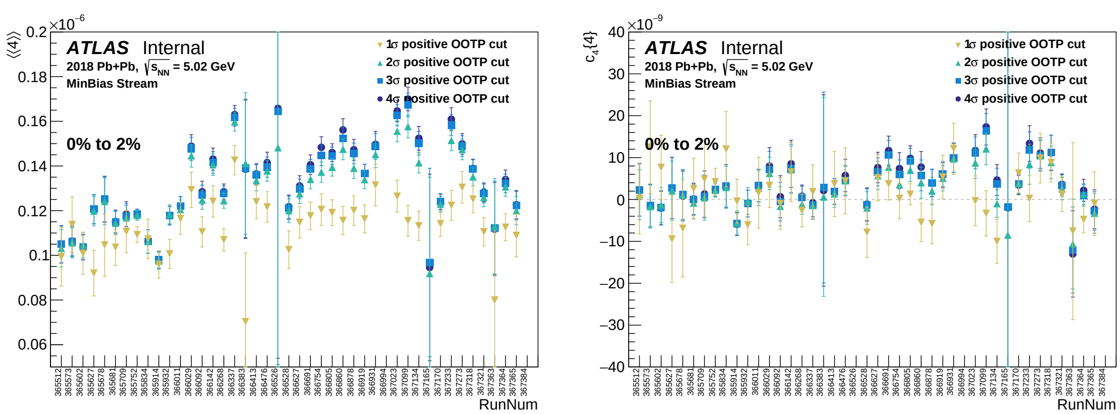

Figure A.5: Run-by-run differences in centrality 0–2% with different σ of OOTP rejections. Left plot shown is for $\langle\langle 4\rangle\rangle_n$ and right hand side plot shown is for $c_4\{4\}$.

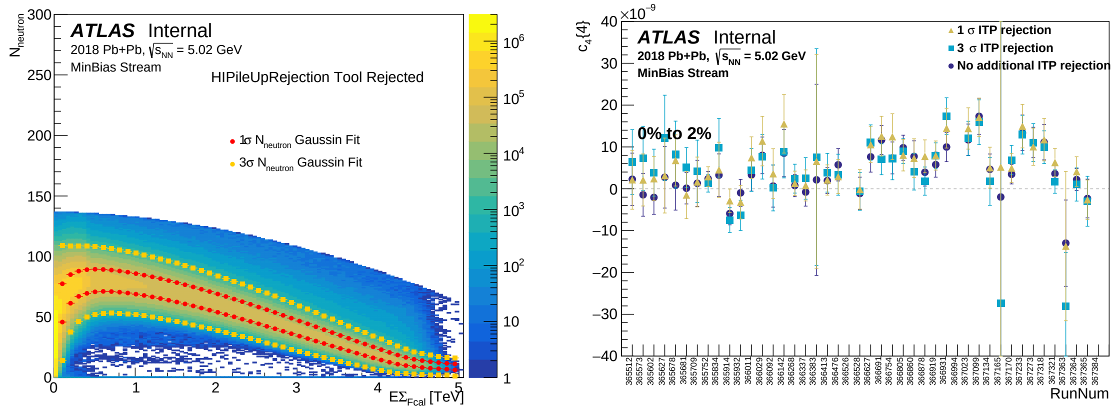

Figure A.6: Left: 1σ and 3σ points used to reject events based on $N_{neutron}$. Right: Comparison of $c_4\{4\}$ results using additional ITP rejections at different σ and not using this rejection.

A.2.3 Run-dependence versus detector non-uniformity flattening

Detector non-uniformity flattening procedures are explained in Section 4.3.1. The flattening can be done on a run-by-run basis or through all runs. See Figure A.7 for the ratio of track weighting maps for individual runs and Figure A.8 for the ratio of the flattened track distributions. Shown in red label are runs with $c_n\{4\}$ being positive for 0–2%, and blue colored run labels have negative $c_n\{4\}$ in this centrality. Both the weighting map and the flattened distribution do not show obvious trend with respect to the sign of $c_n\{4\}$ value. Using a run-by-run or run-averaged map does not significantly change the overall values or run-dependence, as shown in Figure A.9. Using track weighting does globally shifts the measured cumulants, but does not change the extent of run-dependence.

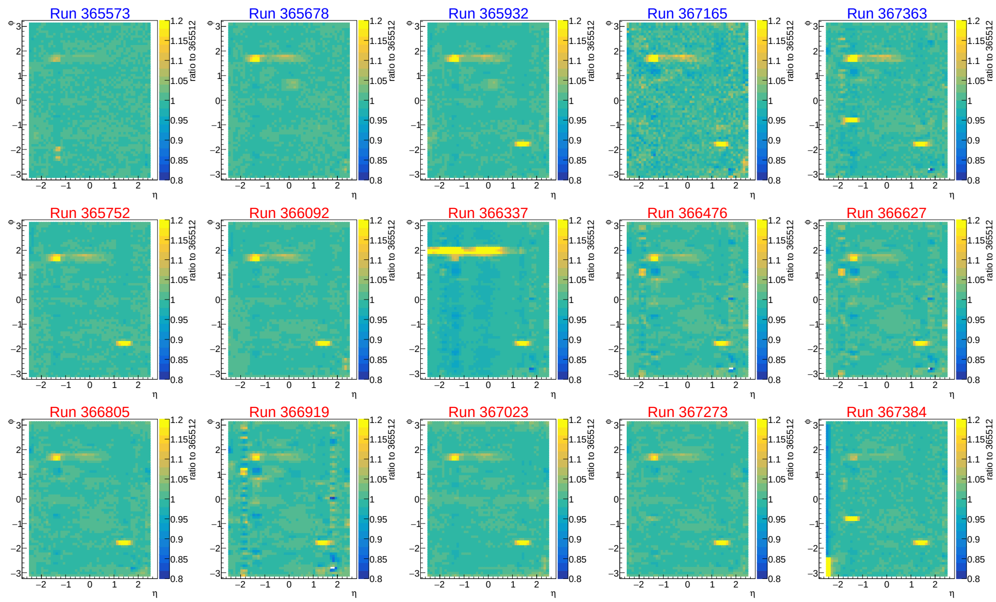

Figure A.7: Ratio of phi-flattening track weights of each run to first run. Dataset used is MinBias stream.

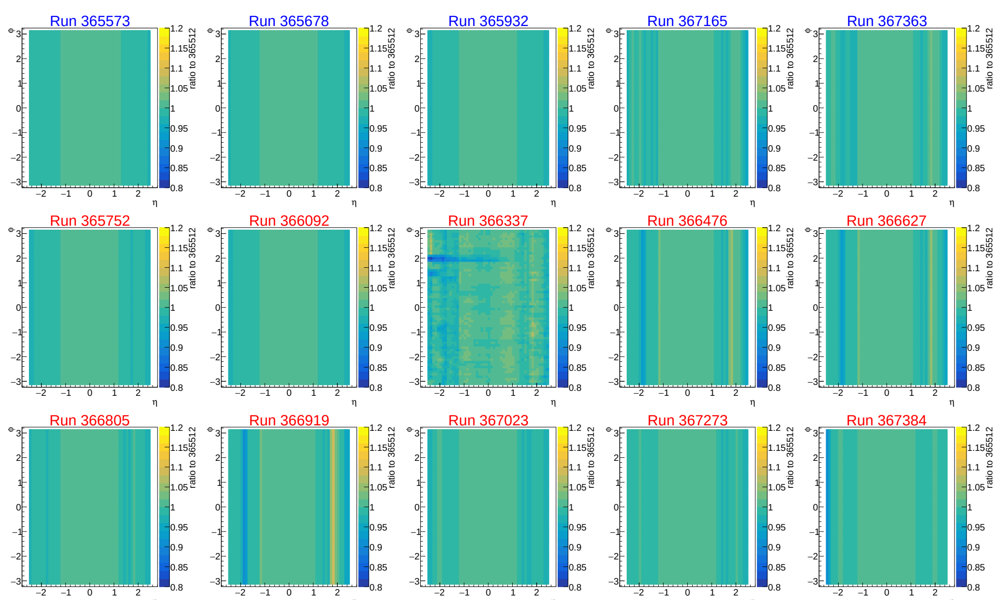

Figure A.8: Ratio of phi-flattening weighted track distributions of each run to first run. Dataset used is MinBias stream.

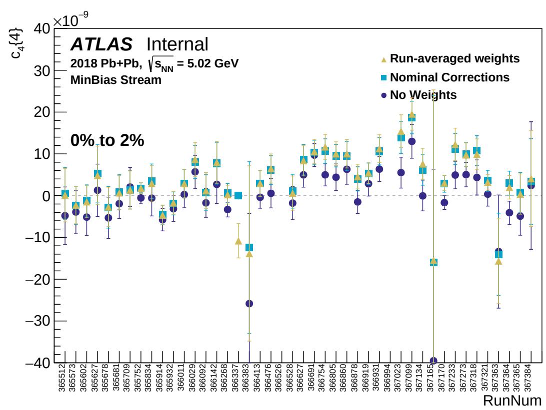

Figure A.9: Comparison of the effect of different weighting maps on $c_n\{4\}$ run-dependence.

To verify whether the remaining fluctuations in phi-flattened track distributions is related with run-fluctuations in any other ways, a weighting scheme based on MC is used for testing purpose only. This is referred to as the "Truth-based weight" in the following tests. This weight is extracted by replacing the real η distribution of reconstructed tracks in each run with the η distribution of tracks from HIJING MC, and weight the run-by-run map by N_{ch} of the run, thus eliminating any η difference in the weighted distributions. The phi-flattening weight now becomes,

$$\omega(\phi, \eta) = \frac{N^{\eta}_{truth}}{64 N^{\phi,\eta}_{reco}} \frac{N_{reco}}{N_{truth}} \tag{1}$$

The truth η distribution, truth-based weighting map and weighted track distributions are shown in Figure A.10. After this procedure all runs are identical in their weighted track distribution. As shown in Figure A.11, the truth weighting does not affect run-dependence of $\langle\langle 4 \rangle\rangle_n$.

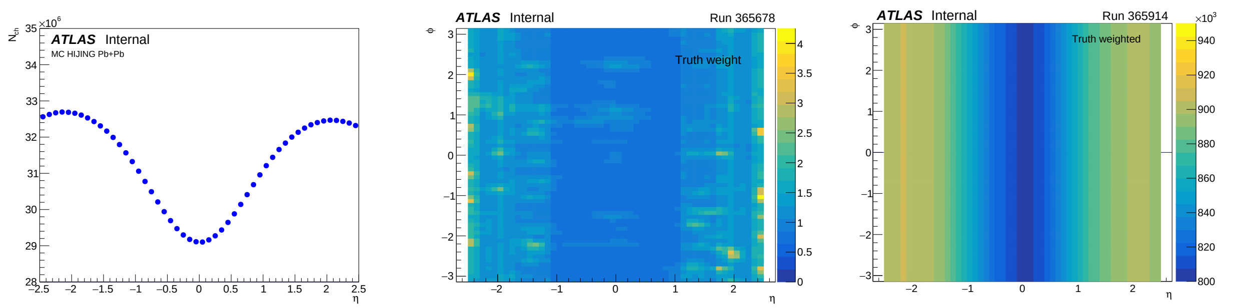

Figure A.10: Left: Truth track distribution as a function of η using MC HIJING. Middle: Track weights made based on truth track η distribution. Right: Truth weighted track distribution.

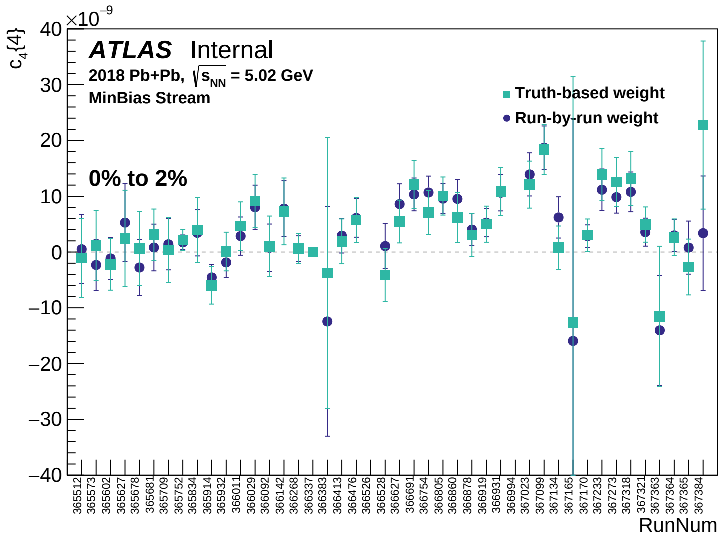

Figure A.11: Comparison of run-by-run truth weighted and run-by-run reconstructed track weighted $c_4\{4\}$ using MinBias stream data in centrality 0–2%.

A.2.4 Run-dependence versus flow vector recentering

The flow vector recentering shifts mean flow vectors of inner detectors and FCals to zero, as explained in Section 4.3.1. It corrects for the residual detector effects that are centrality dependent and finer scale than grid of the ϕ-direction non-uniformity flattening. After run-by-run ϕ-direction non-uniformity flattening, the mean flow vector $\langle Q_n \rangle$ has very small run-dependence, as shown in Figure A.13. It can be seen from Figure A.13 that the recentering correction does not change run-dependence of $c_4\{4\}$.

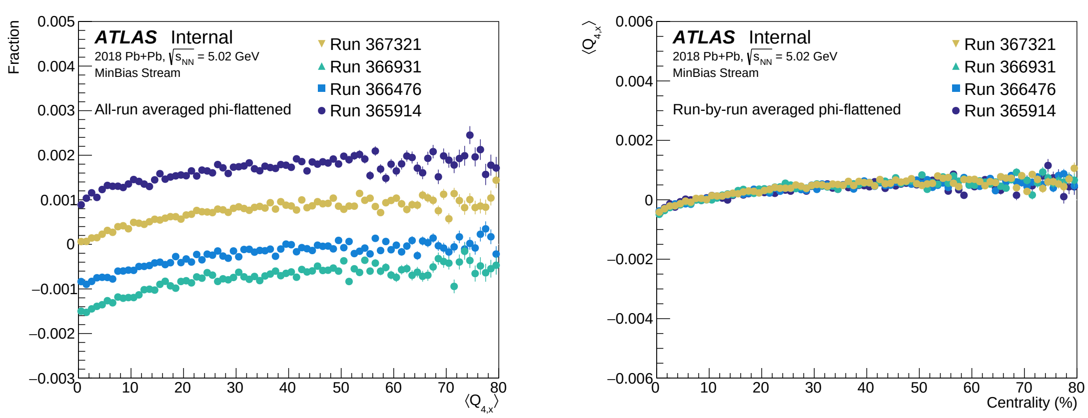

Figure A.12: Left: Mean $Q_(4, x)$ as a function of centrality, when tracks are weighted by all-run averaged phi-flattening. Right: Mean $Q_(4, x)$ as a function of centrality, when tracks are weighted by a run-by-run based phi-flattening.

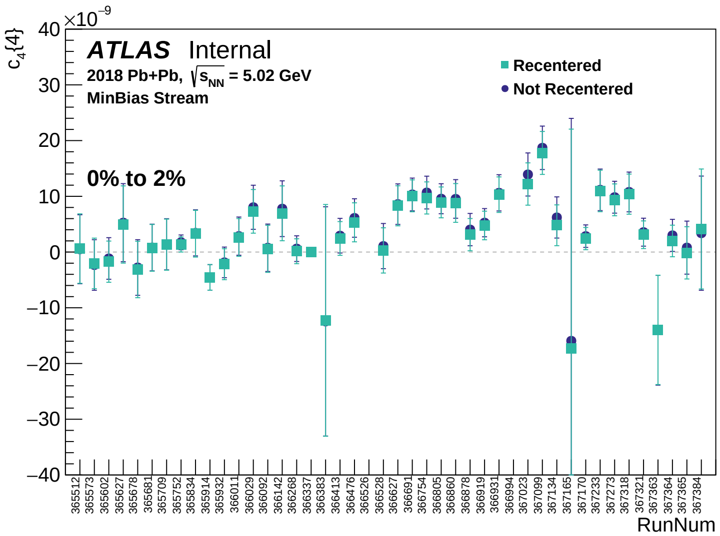

Figure A.13: Comparison of $c_4\{4\}$ run-dependence in 0–2% using run-by-run phi-flattening before and after inner detector recentering.

A.2.5 Run-dependence versus z_{vtx}-dependent weighting map

The weighting map used in this analysis uses a z_{vtx}-dependent weighting map, as explained in Section 4.3.1. It is important to verify whether the exclusion of η bins and utility of z_{vtx}-dependent map systematically shift the observables. It can be seen from Figure A.14 that using either a single, z_{vtx} inclusive weighting map or using z_{vtx}-dependent map and η-bin exclusion does not change run-dependence or value of $c_4\{4\}$.

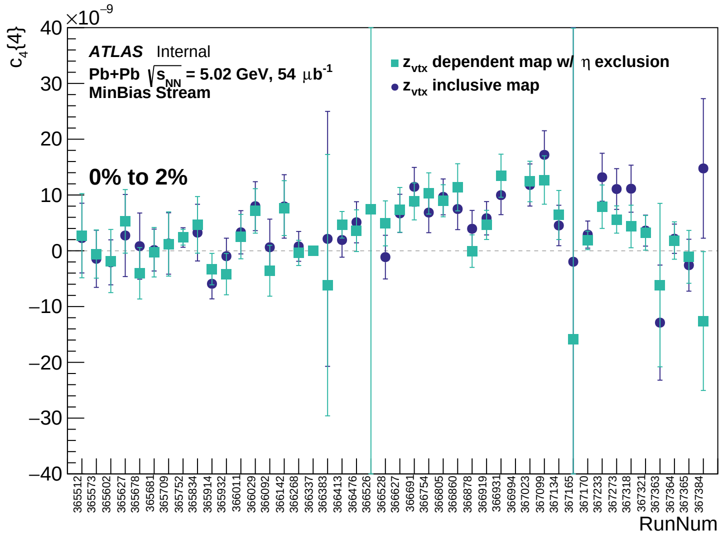

Figure A.14: Comparison of $c_4\{4\}$ run-dependence in 0–2% using z_{vtx} dependent with η exclusion versus with z_{vtx} inclusive map.

A.3 Additional centralities

A comparison between before and after the additional cuts for $c_2\{4\}$ and $c_3\{4\}$ in full centrality ranges for tracks with $p_{\rm T} > 1$ GeV to verify that this additional OOTP rejections do not add any systematic shifts to the observables. Included in the auxiliary materials are the following plots. Run-by-run cumulants of v_2 and v_3 for particles of $p_{\rm T}$ 1–5 GeV by using 4σ versus 1σ OOTP rejections on the positive $\Sigma E_{\rm T}^{\rm FCal}$ side, in Figure A.15 to Figure A.18.

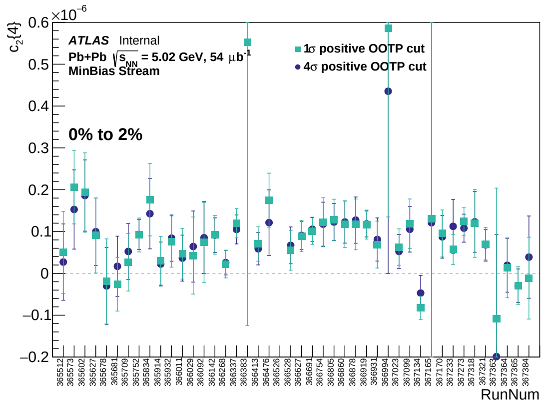

(a)

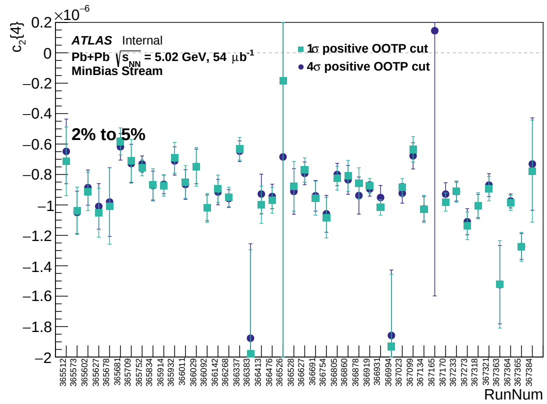

(b)

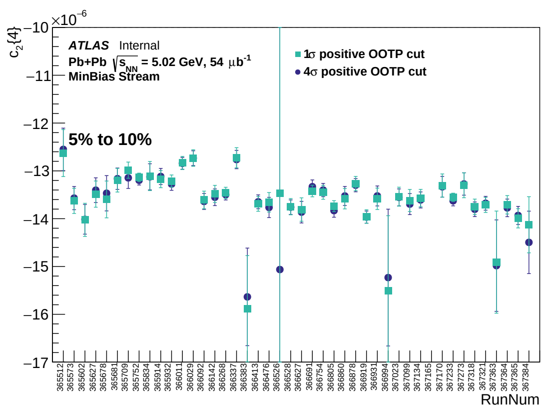

(c)

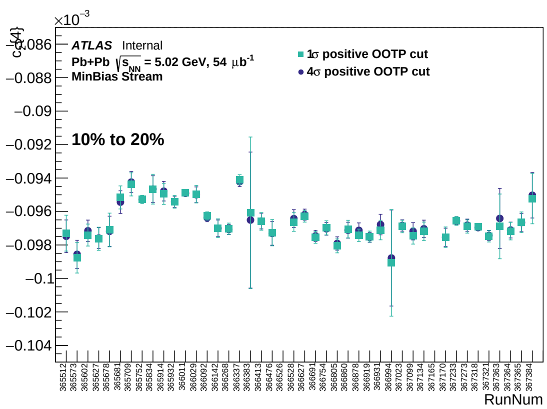

(d)

Figure A.15: Values of $c_2\{4\}$ versus run number for centrality (a) 0–2%, (b) 2–5%, (c) 5–10%, and (d) 10–20%

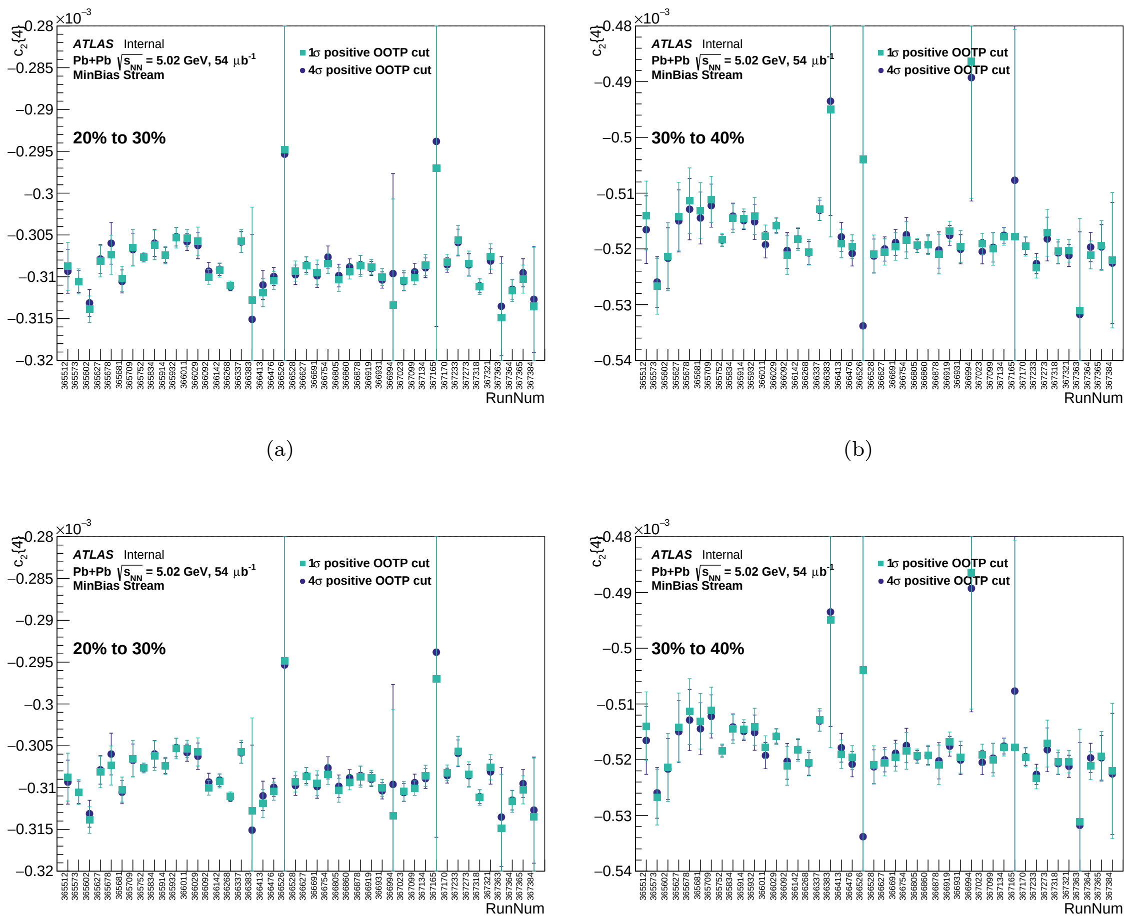

(a) (b)

(c) (d)

Figure A.16: Values of $c_2\{4\}$ versus run number for centrality (a) 20–30%, (b) 30–40%, (c) 40–50%, and (d) 50–60%.

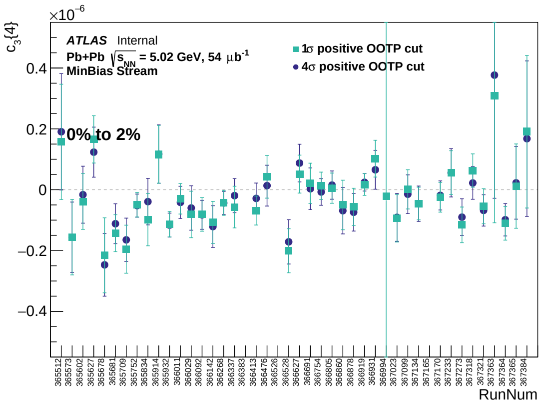

(a)

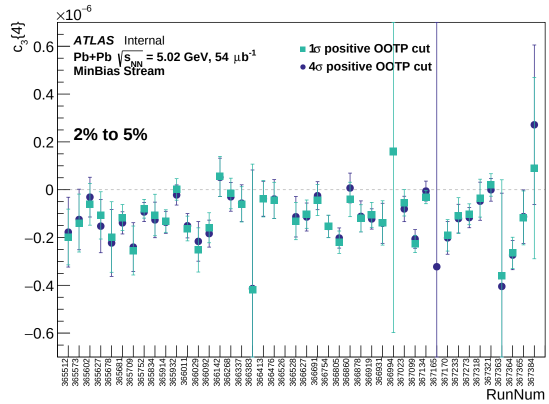

(b)

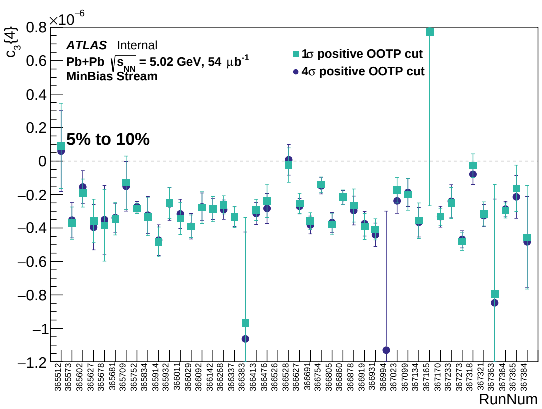

(c)

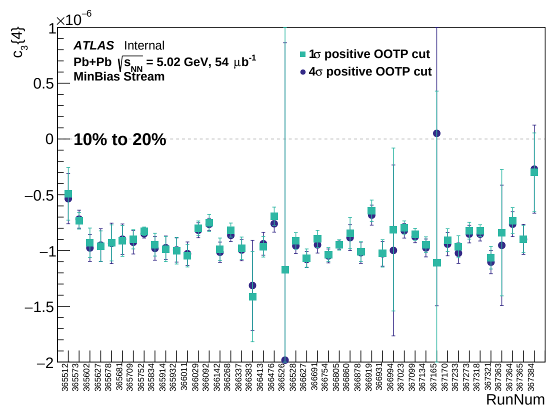

(d)

Figure A.17: Values of $c_3\{4\}$ versus run number for centrality (a) 0–2%, (b) 2–5%, (c) 5–10%, and (d) 10–20%

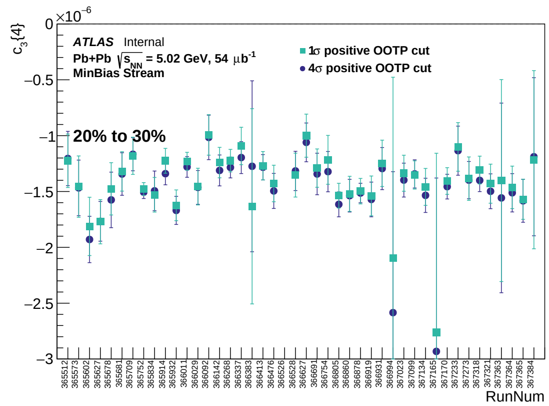

(a)

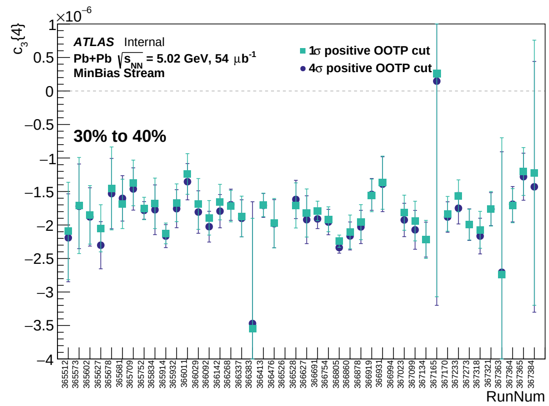

(b)

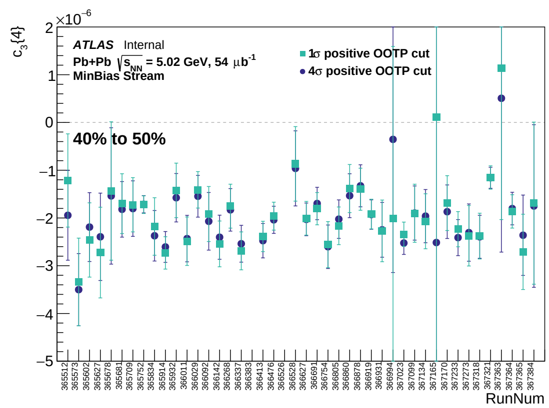

(c)

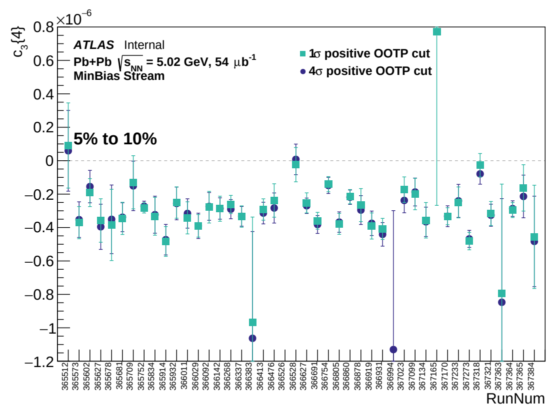

(d)

Figure A.18: Values of $c_3\{4\}$ versus run number for centrality (a) 20–30%, (b) 30–40%, (c) 40–50%, and (d) 50–60%.

Appendix B: Result plots in other centrality intervals

A list of data points not shown in the main body of Section 4.6: Results is included here.

Measurements of $v_2\{\mathrm{SP}\}$ and $v_3\{\mathrm{SP}\}$ as a function of p_T in various centralities are shown in Figure B.1.

Comparison of $v_2\{\mathrm{SP}\}$ with ATLAS SP method measurements from Ref. [122] as a function of p_T in various centralities, charged particles pseudorapidity $|\eta| < 2.5$ are shown in Figure B.2.

Comparison of $v_3\{\mathrm{SP}\}$ with ATLAS SP method measurements from Ref. [122] as a function of p_T in various centralities, charged particles pseudorapidity $|\eta| < 2.5$ are shown in Figure B.3.

Comparison of $v_2\{\mathrm{SP}\}$ with CMS SP method measurements from Ref. [88] as a function of p_T in various centralities are shown in Figure B.4.

Comparison of $v_3\{\mathrm{SP}\}$ with CMS SP method measurements from Ref. [88] as a function of p_T in various centralities are shown in Figure B.5.

Comparison of $v_2\{\mathrm{SP}\}$ with CMS SP method measurements from Ref. [88] and ATLAS jet Event Plane method measurements from Ref. [87] as a function of p_T in varioud centralities, zooming in high-p_T region, are shown in Figure B.11.

Comparison of $v_3\{\mathrm{SP}\}$ with CMS SP method measurements from Ref. [88] and ATLAS jet Event Plane method measurements from Ref. [87] as a function of p_T in varioud centralities, zooming in high-p_T region, are shown in Figure B.12.

Comparisons of $v_2\{\mathrm{SP}\}$ in two different pseudorapidity ranges for different centralities are shown in Figure B.6 to Figure B.8.

Comparisons of $v_3\{\mathrm{SP}\}$ in two different pseudorapidity ranges for different centralities are shown in Figure B.9 to Figure B.10.

Measurements of $v_2\{4\}$ and $v_3\{4\}$ as a function of p_T in various centralities are shown in Figure B.13.

Comparion of MPC method measurements $v_2\{4\}$ using standard and three-subevent Q-cumulants as a function of p_T in various centralities are shown in Figure B.14.

Comparion of MPC method measurements $v_3\{4\}$ using standard and three-subevent Q-cumulants as a function of p_T in various centralities are shown in Figure B.15.

Comparison of MPC method measurements $v_2\{4\}$ using standard Q-cumulants between different event classes as a function of p_T in various centralities are shown in Figure B.16.

Comparison of MPC method measurements $v_2^{\text{3-sub}}\{4\}$ using three-subevent Q-cumulants between different event classes as a function of p_T in various centralities are shown in Figure B.17.

Comparison of MPC method measurements $v_3\{4\}$ using standard Q-cumulants between different event classes as a function of p_T in various centralities are shown in Figure B.18.

Comparison of MPC method measurements $v_3^{\text{3-sub}}\{4\}$ using three-subevent Q-cumulants between different event classes as a function of p_T in various centralities are shown in Figure B.19.

Comparison of v_2 measurements using MPC method with three-subevent Q-cumulants in 1% event class and using SP method as a function of p_T in various centralities are shown in Figure B.20.

Comparison of v_3 measurements using MPC method with three-subevent Q-cumulants in 1% event class and using SP method as a function of p_T in various centralities are shown in Figure B.21.

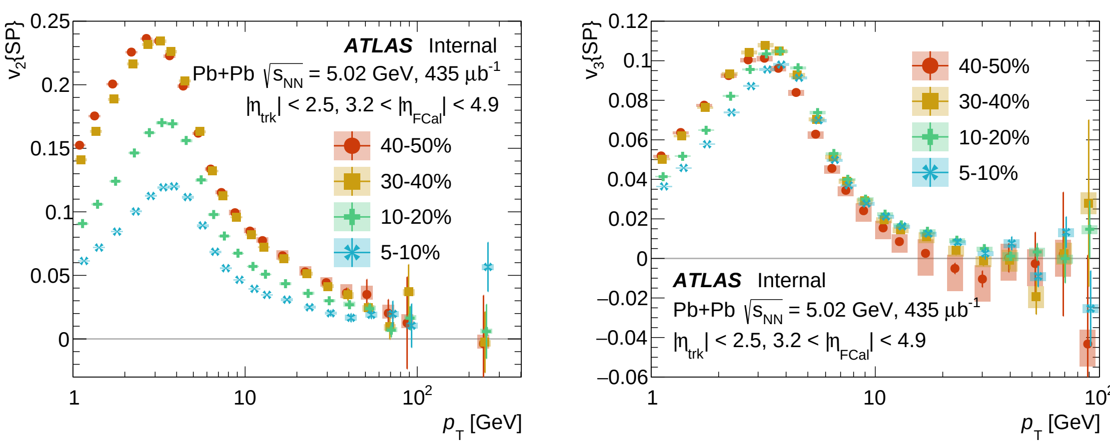

(a)

(b)

Figure B.1: The (a) $v_2\{\mathrm{SP}\}$ and (b) $v_3\{\mathrm{SP}\}$ values as a function of charged-particle p_T for different centrality intervals. The statistical uncertainties are shown as error bars and the systematic uncertainties are shown as boxes.

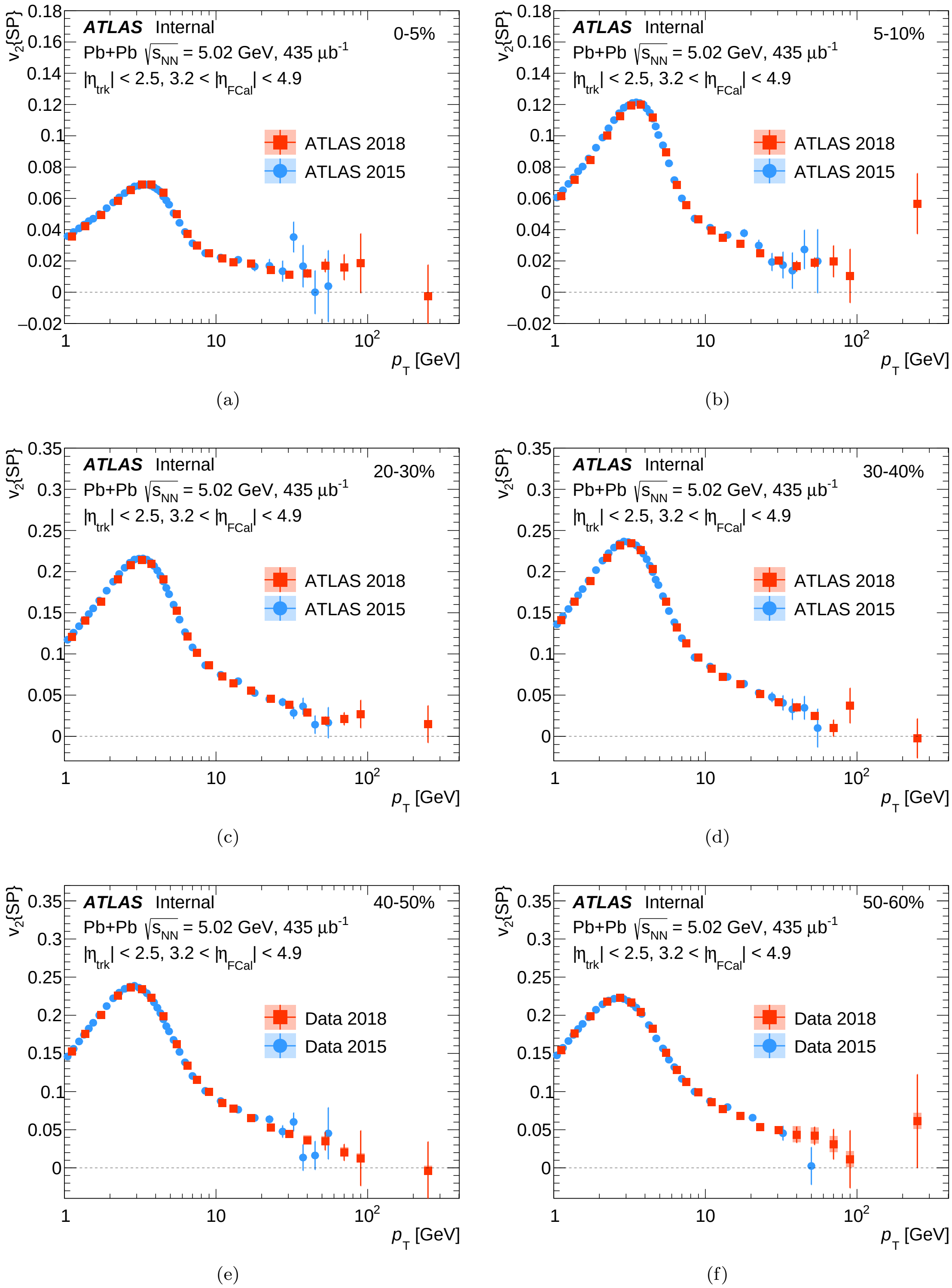

Figure B.2: The $v_2\{\mathrm{SP}\}$ values as a function of particle p_T, for the (a) 5–10%, (b) 5–10%, (c) 20–30%, (d) 30–40%, (e) 40–50%, and (f) 50–60% centrality interval, compared with ATLAS 2015 measurements [122] in the same charged particle and calorimeter pseudorapidity ranges. The statistical uncertainties are shown as error bars and the systematic uncertainties are shown as boxes.

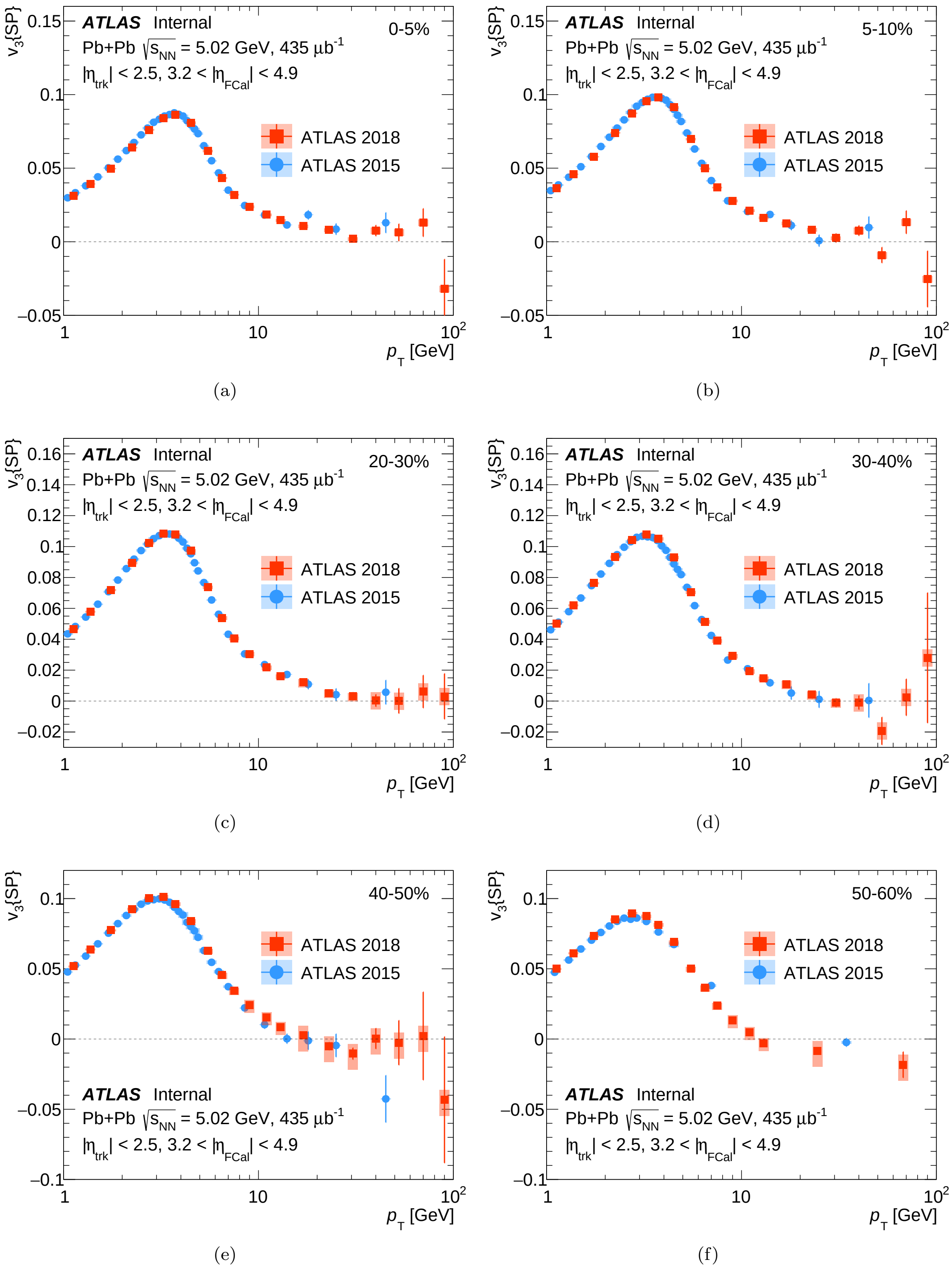

Figure B.3: The $v_3\{\mathrm{SP}\}$ values as a function of particle p_T, for the (a) 0–5%, (b) 5–10%, (c) 20–30%, (d) 30–40%, (e) 40–50%, and (f) 50–60% centrality interval, compared with ATLAS 2015 measurements [122] in the same charged particle and calorimeter pseudorapidity ranges. The statistical uncertainties are shown as error bars and the systematic uncertainties are shown as boxes.

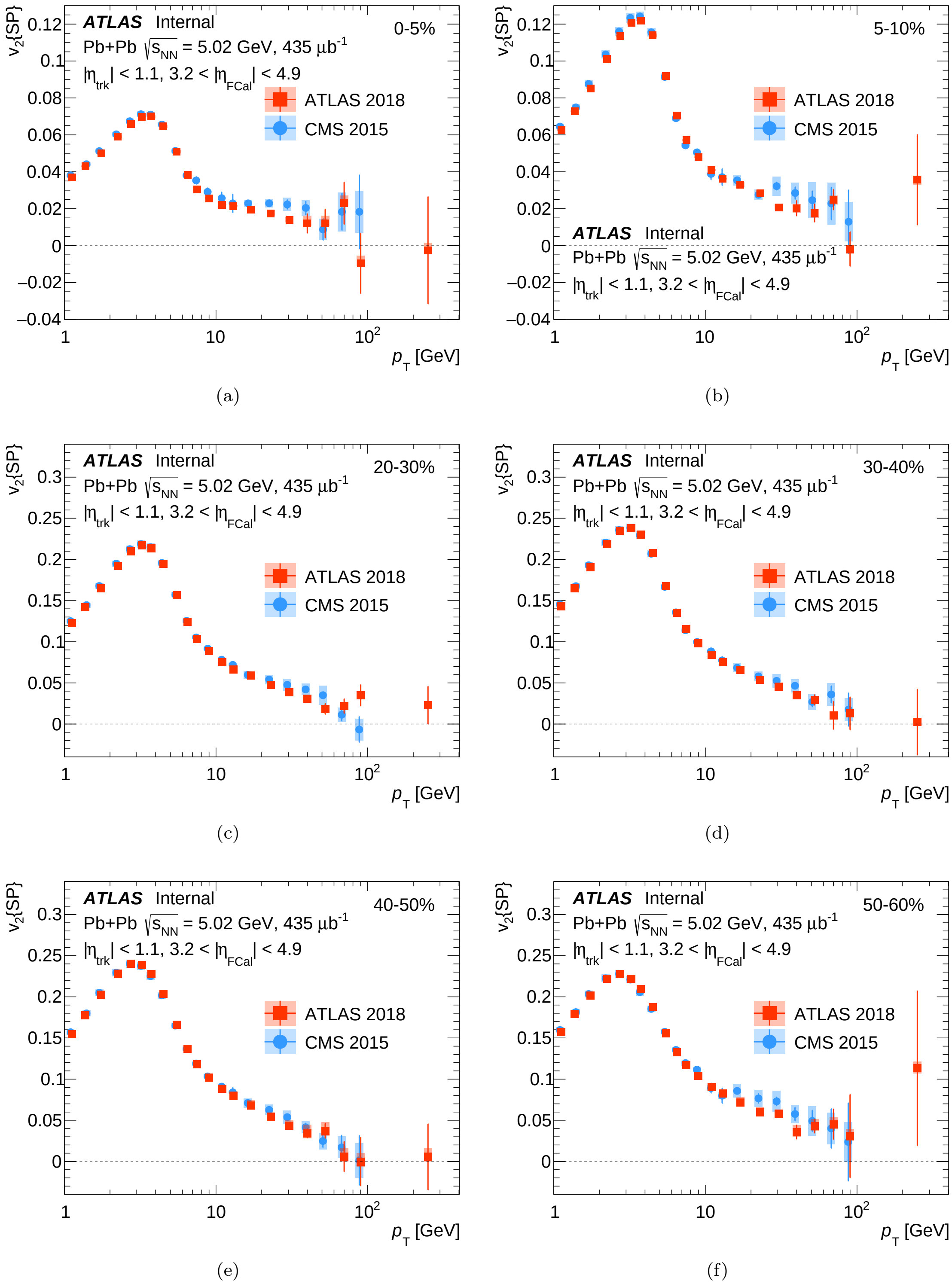

(a) (b) (c) (d) (e) (f)

Figure B.4: The $v_2\{\text{SP}\}$ values as a function of particle p_{T}, for the (a) 0–5%, (b) 5–10%, (c) 20–30%, (d) 30–40%, (e) 40–50% and (f) 50–60% centrality interval, compared with CMS 2015 measurements from Ref. [88], which uses charged particles with pseudorapidity range $|\eta| < 1.0$ and calorimeter in pseudorapidity range $3 < |\eta| < 5$. The statistical uncertainties are shown as error bars and the systematic uncertainties are shown as boxes.

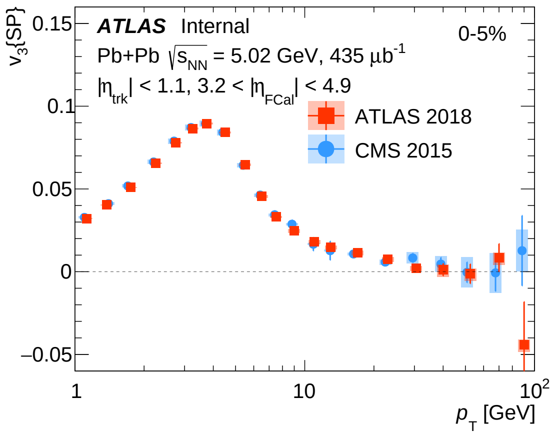

(a)

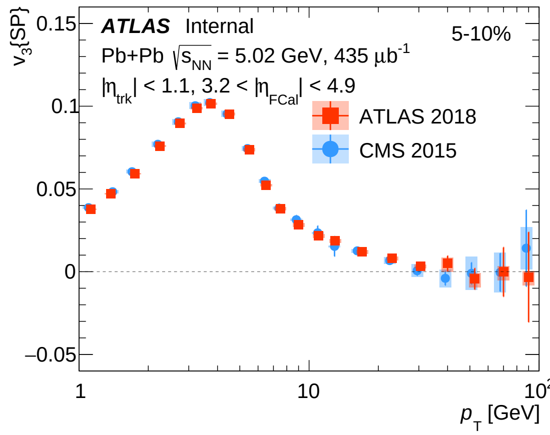

(b)

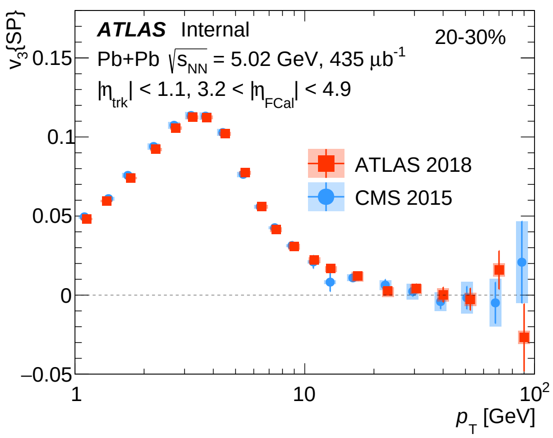

(c)

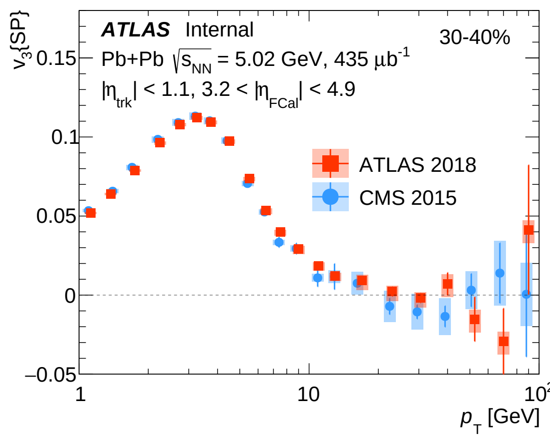

(d)

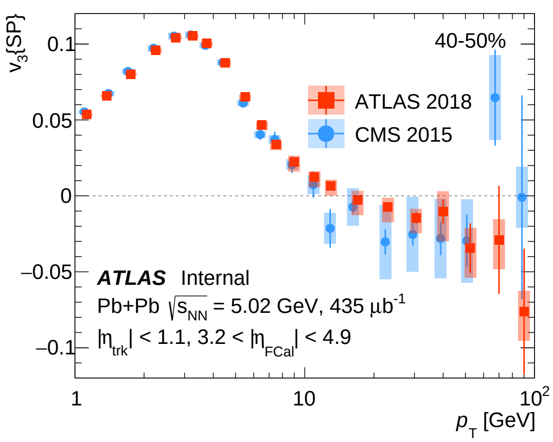

(e)

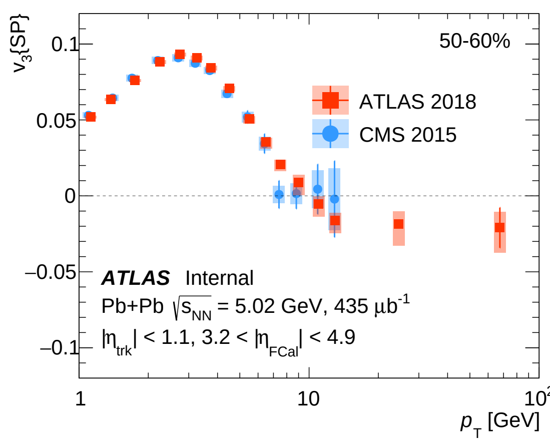

(f)

Figure B.5: The $v_3\{\mathrm{SP}\}$ values as a function of particle p_T, for the (a) 0–5%, (b) 5–10%, (c) 20–30%, (d) 30–40%, (e) 40–50% and (f) 50–60% centrality interval, compared with CMS 2015 measurements from Ref. [88], which uses charged particles with pseudorapidity range $|\eta| < 1.0$ and calorimeter in pseudorapidity range $3 < |\eta| < 5$. The statistical uncertainties are shown as error bars and the systematic uncertainties are shown as boxes.

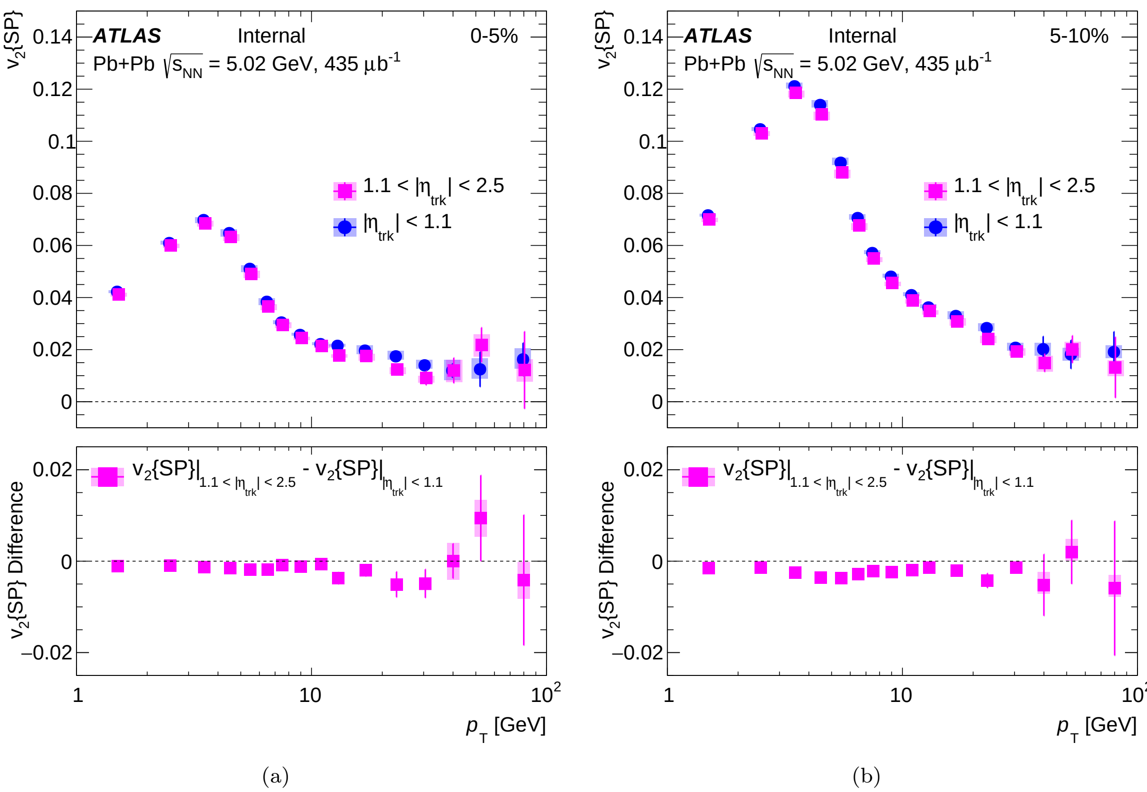

Figure B.6: The $v_2\{\mathrm{SP}\}$ values as a function of charged-particle p_T for (a) 0–5% and (b) 5–10% for different pseudorapidity ranges. The bottom panel shows the difference in the $v_2\{\mathrm{SP}\}$ measured between the two ranges. The statistical uncertainties are shown as error bars and the systematic uncertainties are shown as boxes.

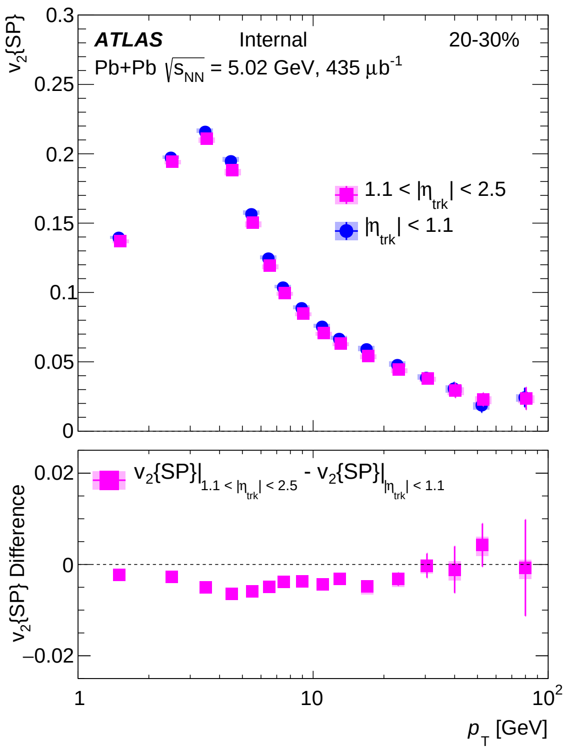

(a)

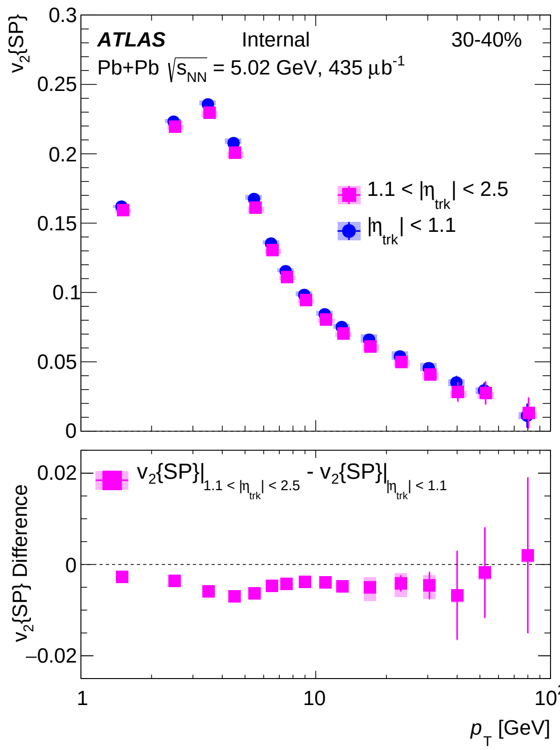

(b)

Figure B.7: The $v_2\{\mathrm{SP}\}$ values as a function of charged-particle p_{T} for (a) 20–30% and (b) 30–40% for different pseudorapidity ranges. The bottom panel shows the difference in the $v_2\{\mathrm{SP}\}$ measured between the two ranges. The statistical uncertainties are shown as error bars and the systematic uncertainties are shown as boxes.

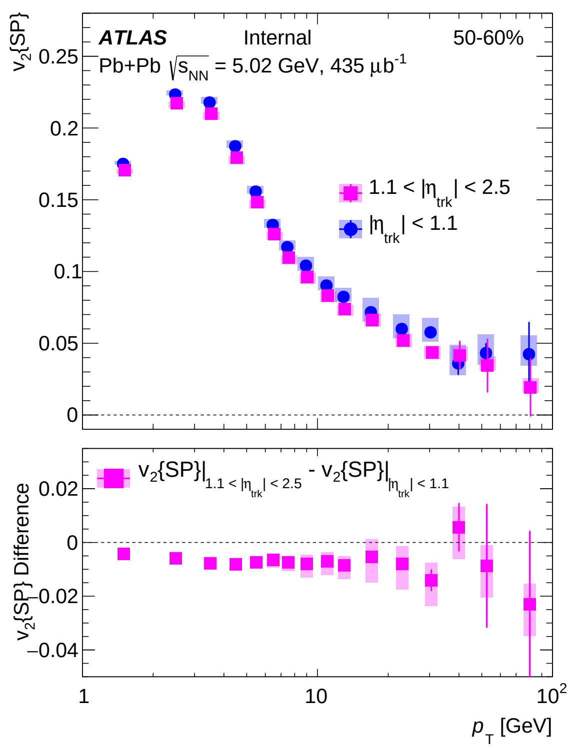

(a)

Figure B.8: The $v_2\{\mathrm{SP}\}$ values as a function of charged-particle p_{T} for 50–60% for for different pseudorapidity ranges. The bottom panel shows the difference in the $v_2\{\mathrm{SP}\}$ measured between the two ranges. The statistical uncertainties are shown as error bars and the systematic uncertainties are shown as boxes.

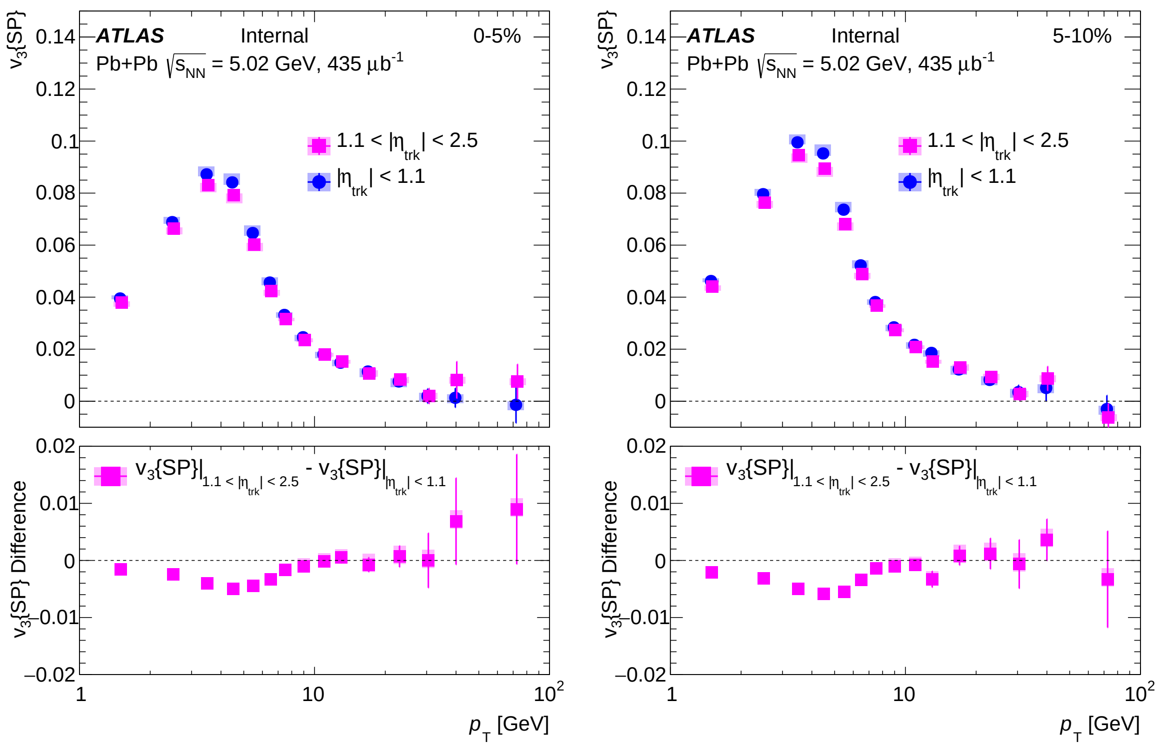

(a)

(b)

Figure B.9: The $v_3\{\mathrm{SP}\}$ values as a function of charged-particle p_{T} for (a) 0–5% and (b) 5–10% for different pseudorapidity ranges. The bottom panel shows the difference in the $v_3\{\mathrm{SP}\}$ measured between the two ranges. The statistical uncertainties are shown as error bars and the systematic uncertainties are shown as boxes.

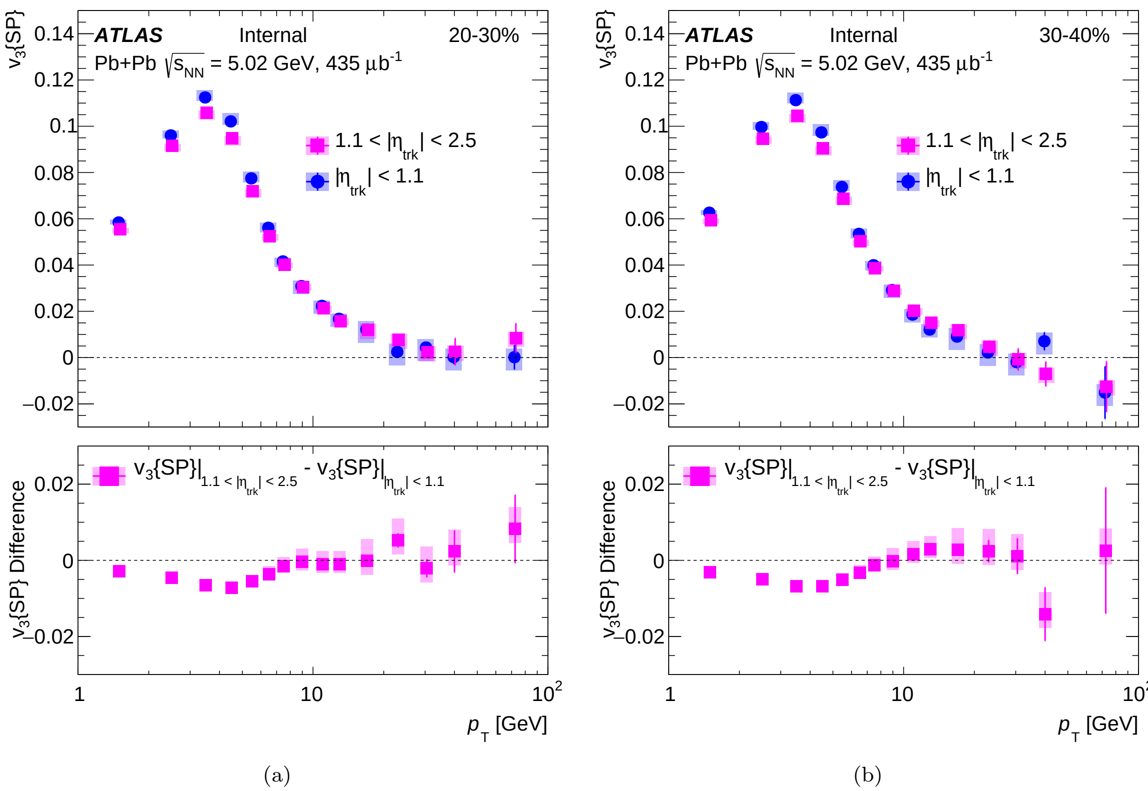

Figure B.10: The $v_3\{\mathrm{SP}\}$ values as a function of charged-particle p_{T} for (a) 20–30% and (b) 30–40% for different pseudorapidity ranges. The bottom panel shows the difference in the $v_3\{\mathrm{SP}\}$ measured between the two ranges. The statistical uncertainties are shown as error bars and the systematic uncertainties are shown as boxes.

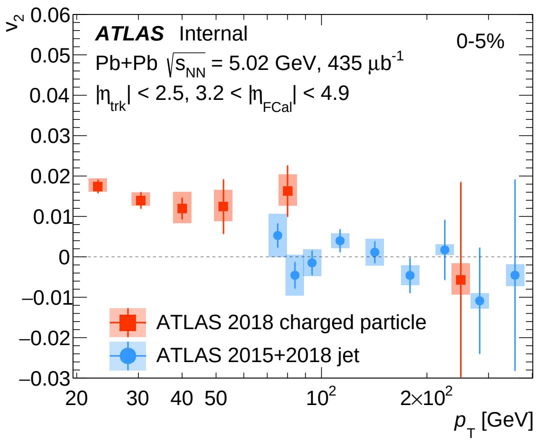

(a)

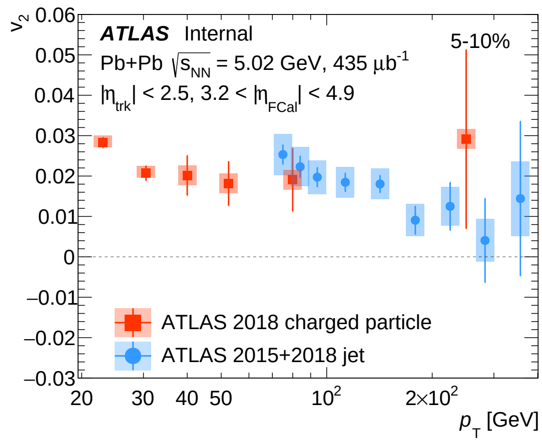

(b)

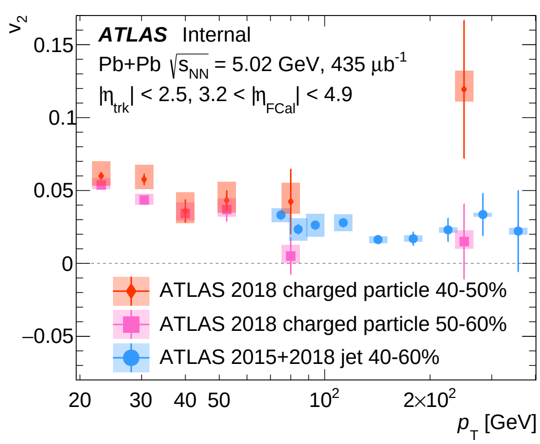

(c)

Figure B.11: The $v_2\{\mathrm{SP}\}$ values as a function of particle p_{T}, for the (a) 0–5%, (b) 5–10%, (c) 40–50% and 50–60% centrality intervals (in centrality intervals of the charged particle results), compared with ATLAS jet v_n measurements from Ref. [87].

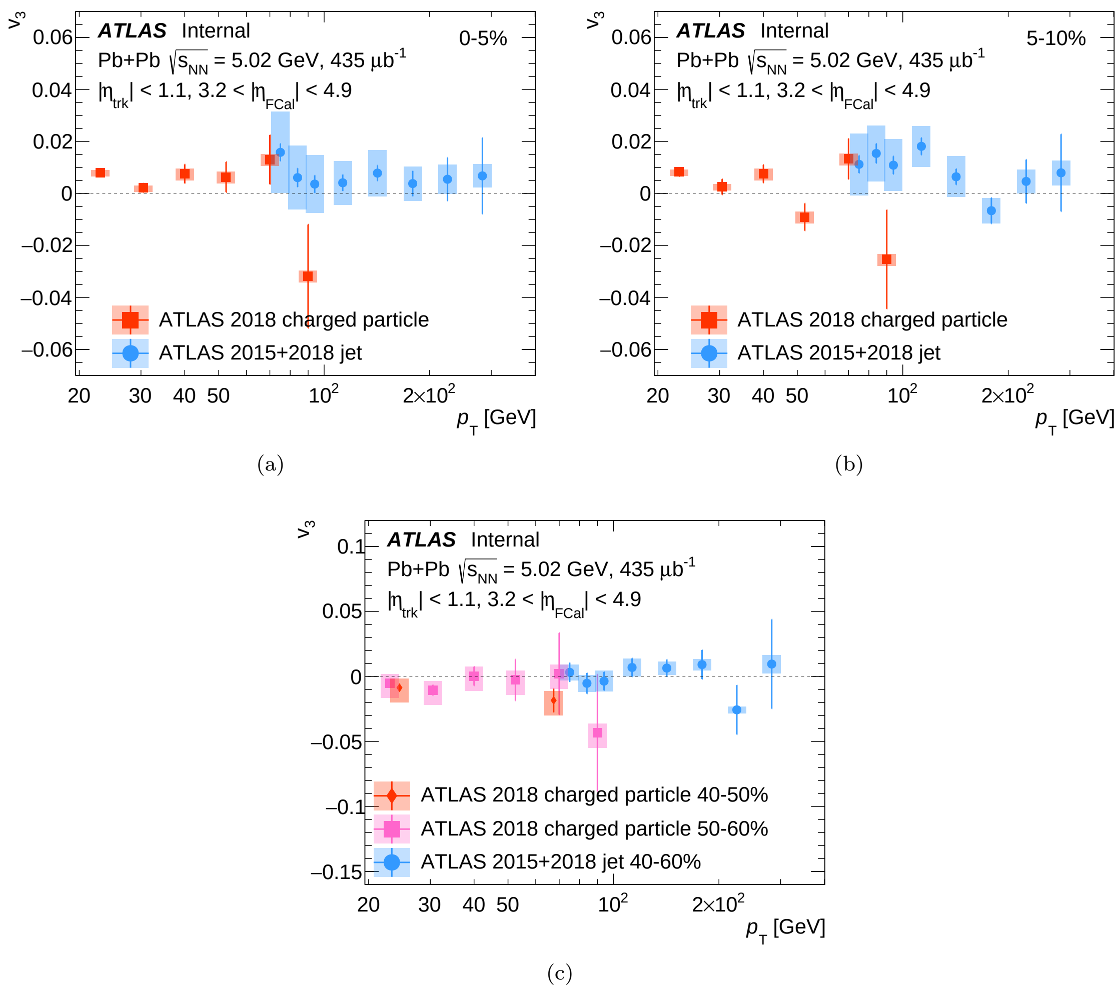

Figure B.12: The v_3\{SP\} values as a function of particle p_T, for the (a) 0–5%, (b) 5–10%, (c) 40–50% and 50–60% centrality intervals (in centrality intervals of the charged particle results), compared with ATLAS jet v_n measurements from Ref. [87].

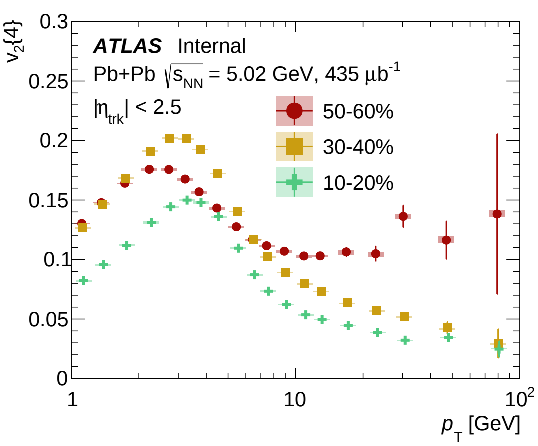

(a)

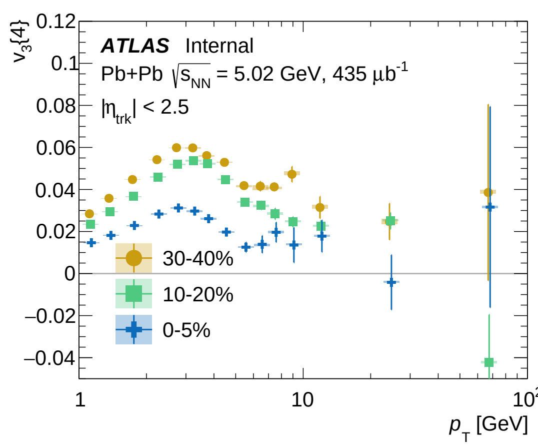

(b)

Figure B.13: The (a) $v_2\{4\}$ and (b) $v_3\{4\}$ values as a function of charged-particle p_{T} for different centrality intervals. For $v_2\{4\}$, 10–20%, 30–40% and 50–60% are shown, and for $v_3\{4\}$, 0–5%, 10–20%, and 30–40% are shown. The statistical uncertainties are shown as error bars and the systematic uncertainties are shown as boxes.

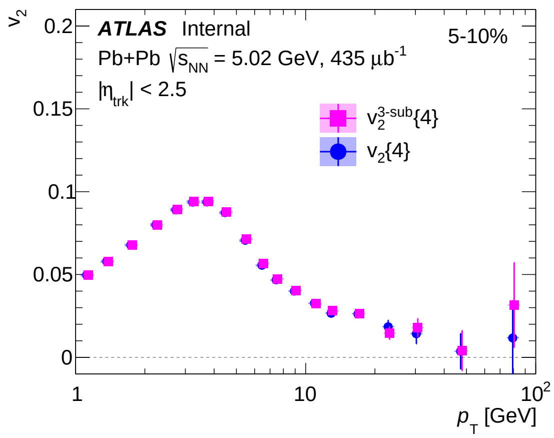

(a)

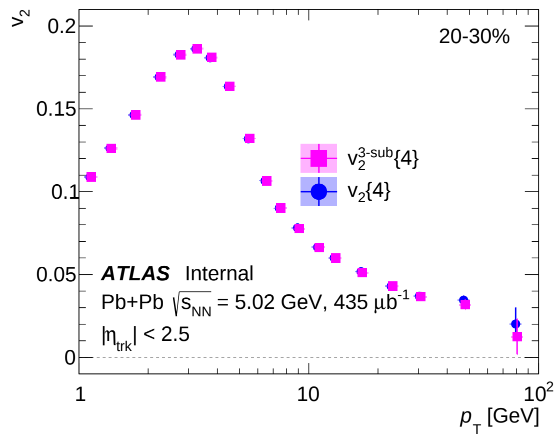

(b)

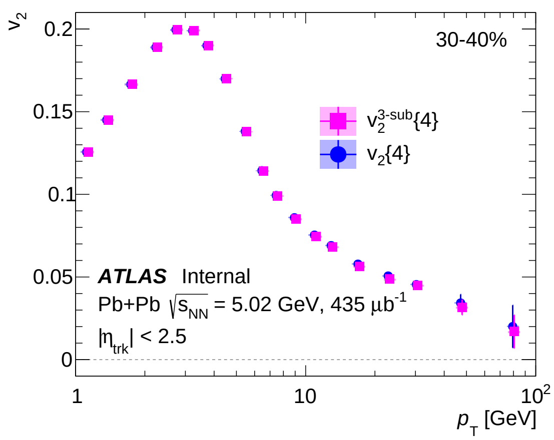

(c)

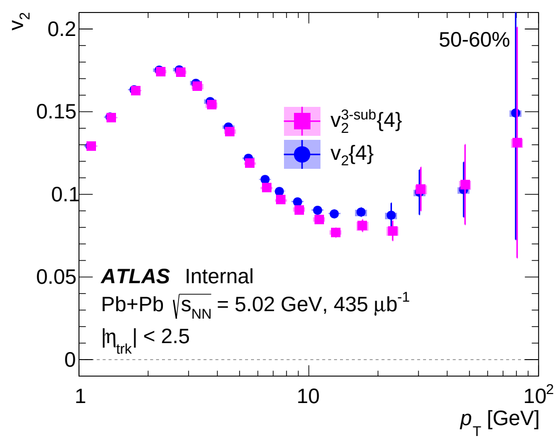

(d)

Figure B.14: $v_2\{4\}$ comparison between standard and three-subevent Q-cumulants in centrality intervals (a) 5–10%, (b) 20–30$, (c) 30–40%, and (d) 50–60%. Error bars shown are from statistical uncertainty and box shows systematics uncertainty.

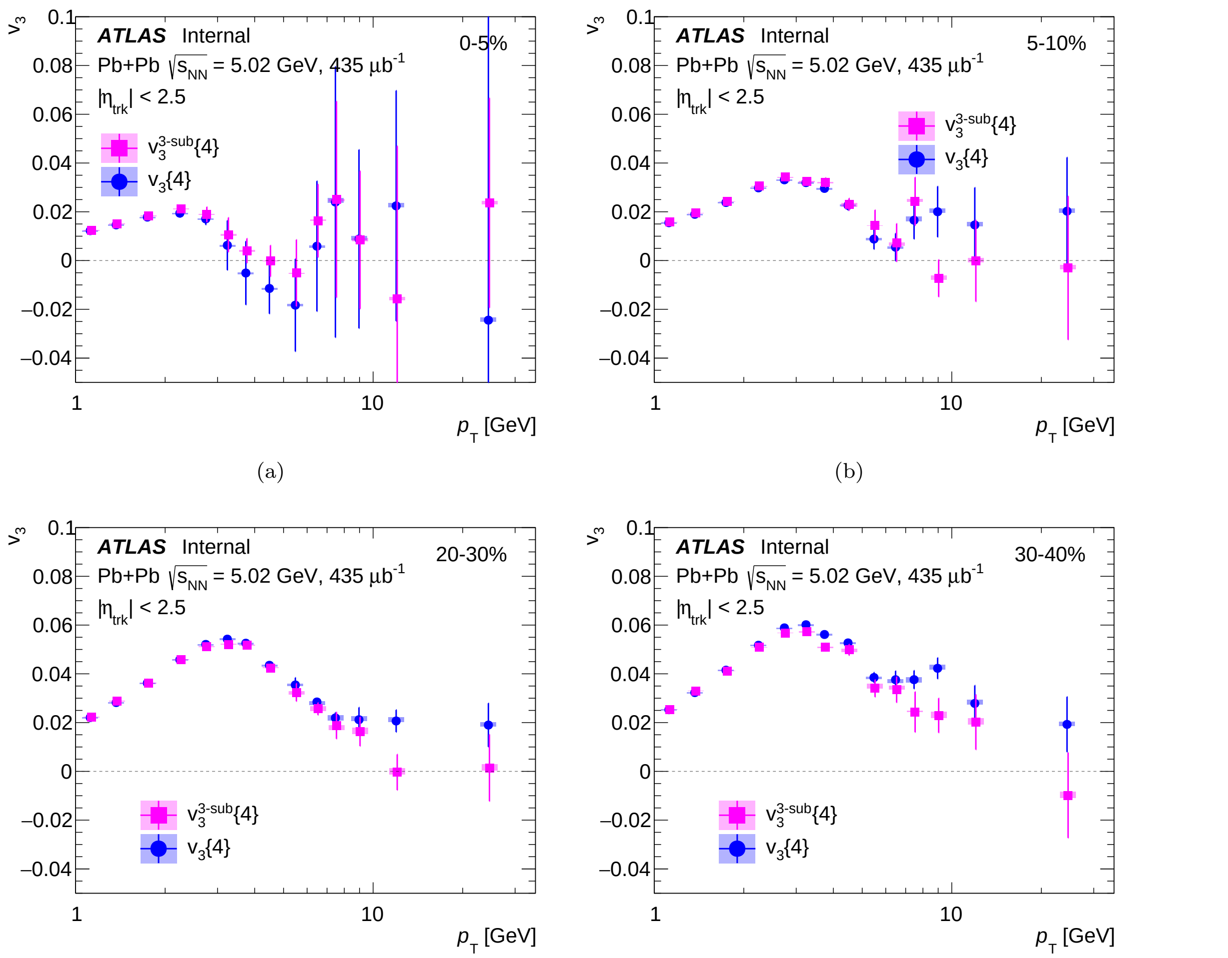

Figure B.15: $v_3\{4\}$ comparison between standard and three-subevent Q-cumulants in centrality intervals (a) 0–5%, (b) 5–10$, (c) 20–30%, and (d) 30–40%. Error bars shown are from statistical uncertainty and box shows systematics uncertainty.

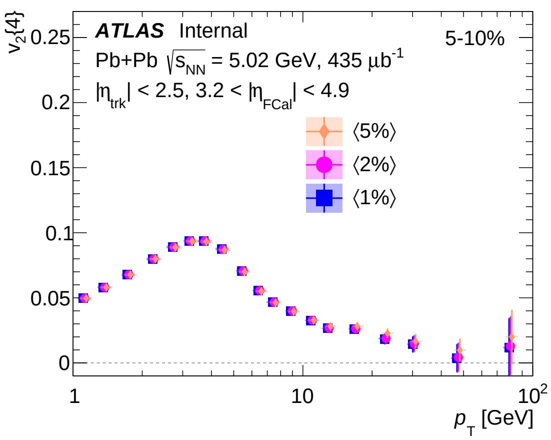

(a)

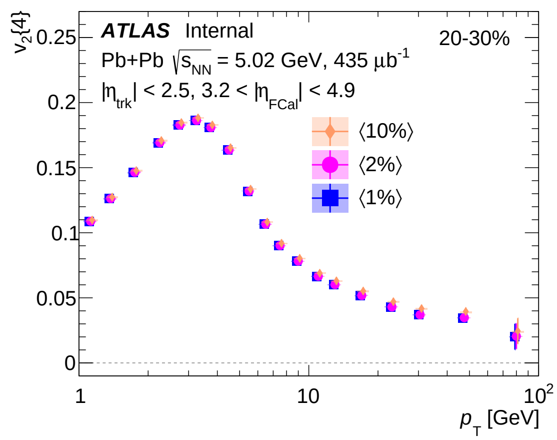

(b)

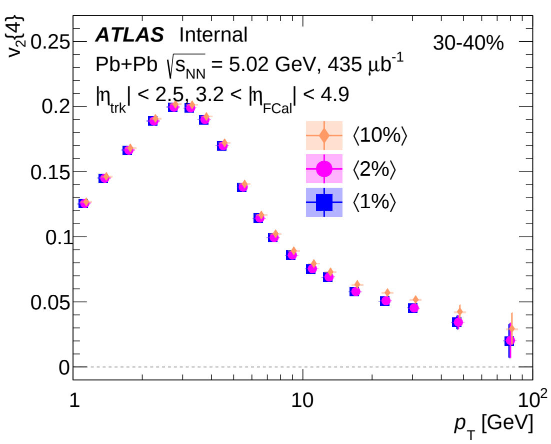

(c)

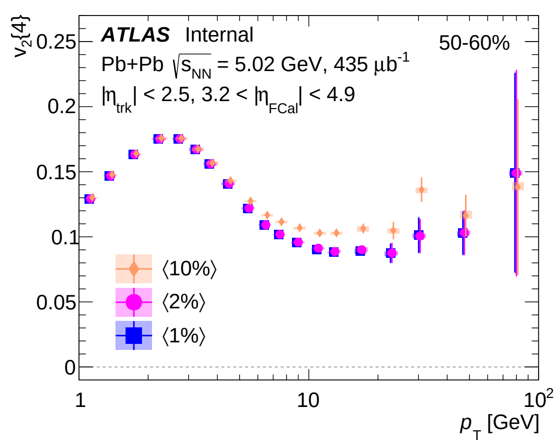

(d)

Figure B.16: Comparison between ⟨1%⟩, ⟨2%⟩ and ⟨10%⟩ (⟨5%⟩ for the centrality interval 5–10%) combination procedures for $v_2\{4\}$ in centrality range (a) 5–10%, (b) 20–30%, (c) 30–40% and (d) 50–60%. The statistical uncertainties are shown as error bars and the systematic uncertainties are shown as boxes.

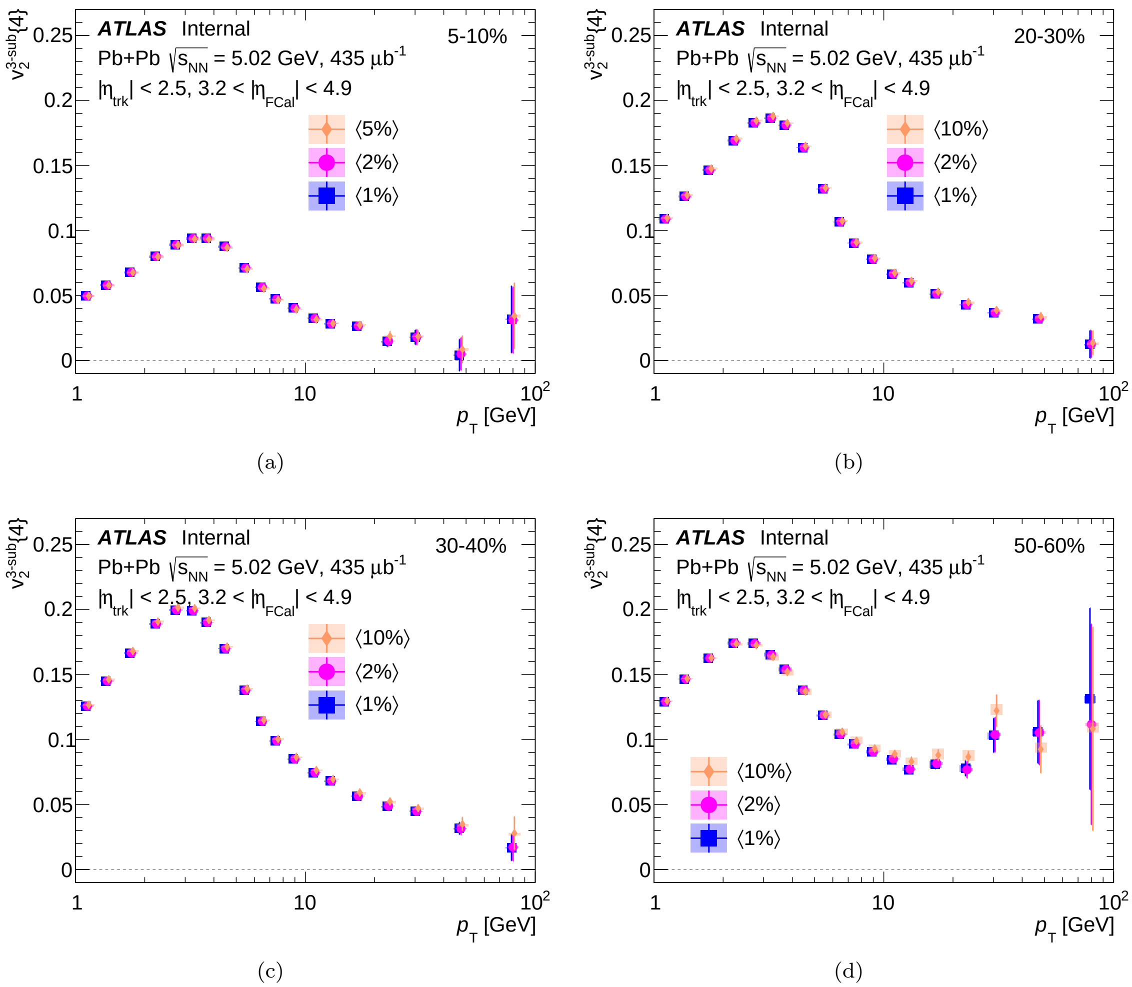

Figure B.17: Comparison between ⟨1%⟩, ⟨2%⟩ and ⟨10%⟩ (⟨5%⟩ for the centrality interval 5–10%) combination procedures for $v_2^{\text{3-sub}}\{4\}$ in centrality range (a) 5–10%, (b) 20–30%, (c) 30–40% and (d) 50–60%. The statistical uncertainties are shown as error bars and the systematic uncertainties are shown as boxes.

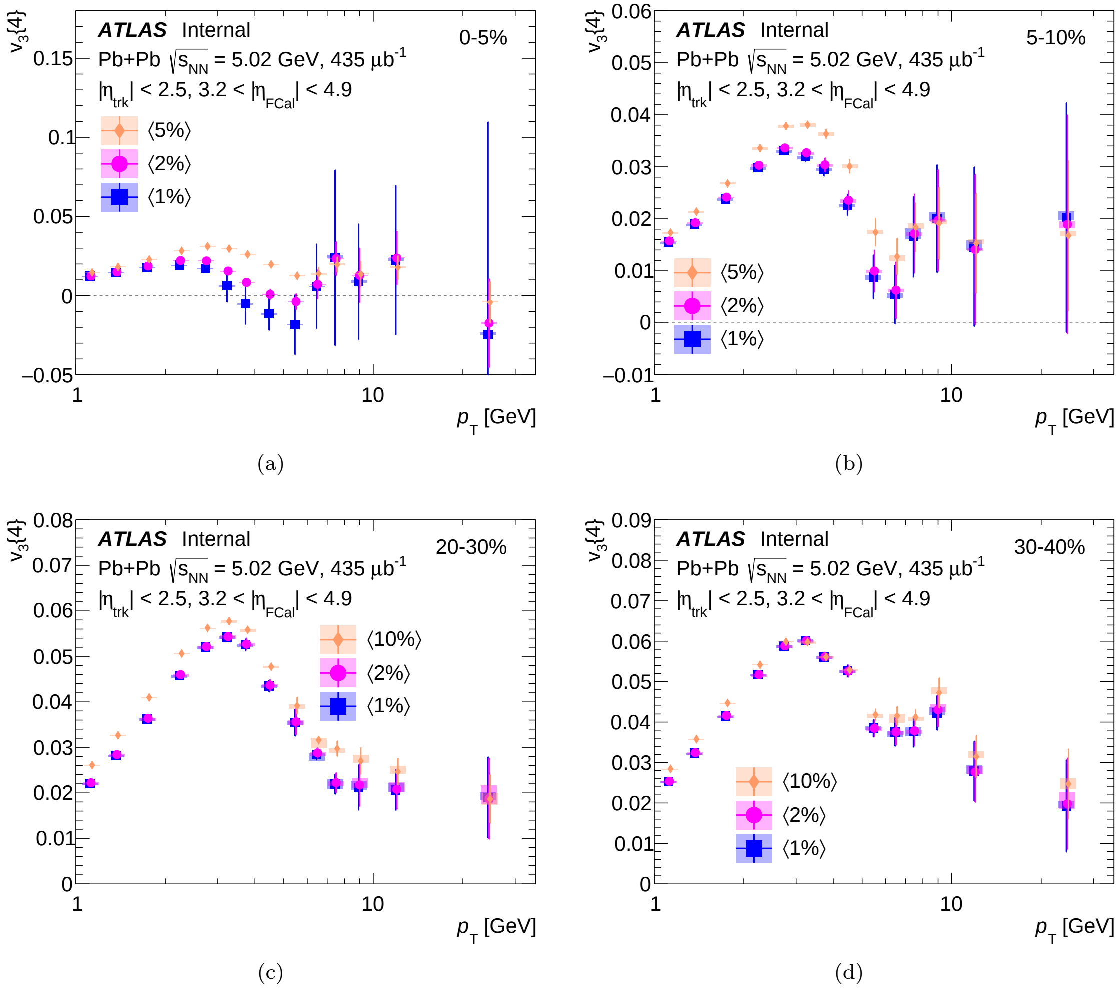

Figure B.18: Comparison between ⟨1%⟩, ⟨2%⟩ and ⟨10%⟩ (⟨5%⟩ for the centrality interval 0–10%) combination procedures for $v_3\{4\}$ in centrality range (a) 0–5%, (b) 5–10%, (c) 20–30% and (d) 30–40%. The statistical uncertainties are shown as error bars and the systematic uncertainties are shown as boxes.

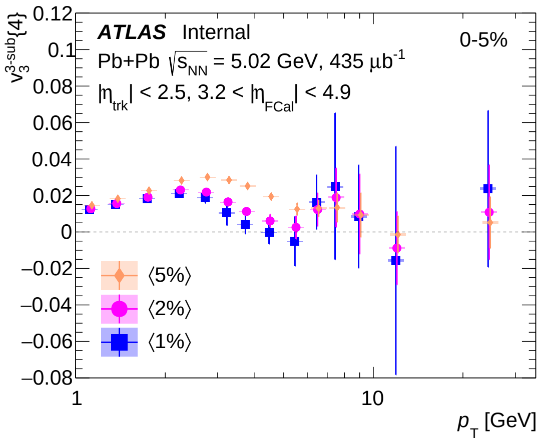

(a)

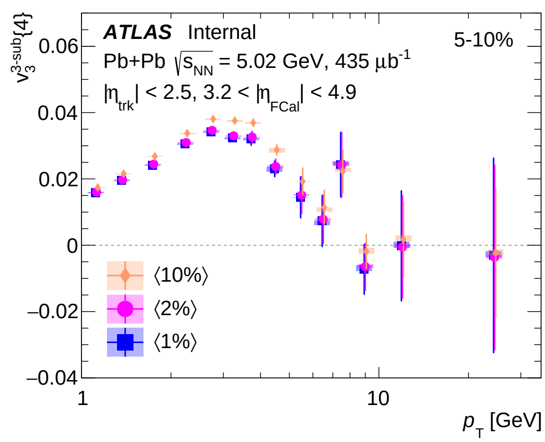

(b)

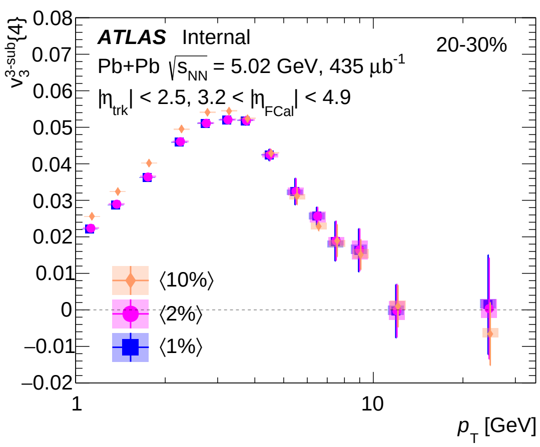

(c)

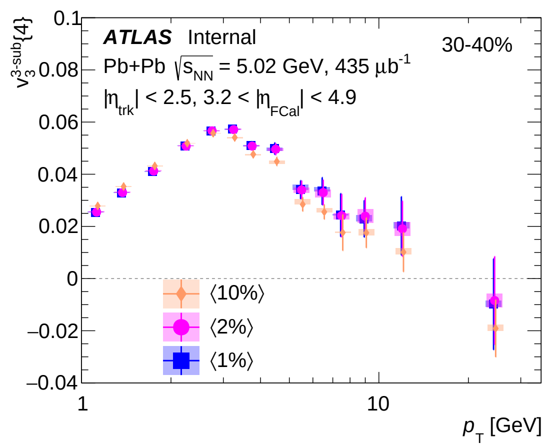

(d)

Figure B.19: Comparison between ⟨1%⟩, ⟨2%⟩ and ⟨10%⟩ (⟨5%⟩ for the centrality interval 0–10%) combination procedures for $v_3^{3\text{-sub}}\{4\}$ in centrality range (a) 0–5%, (b) 5–10%, (c) 20–30% and (d) 30–40%. The statistical uncertainties are shown as error bars and the systematic uncertainties are shown as boxes.

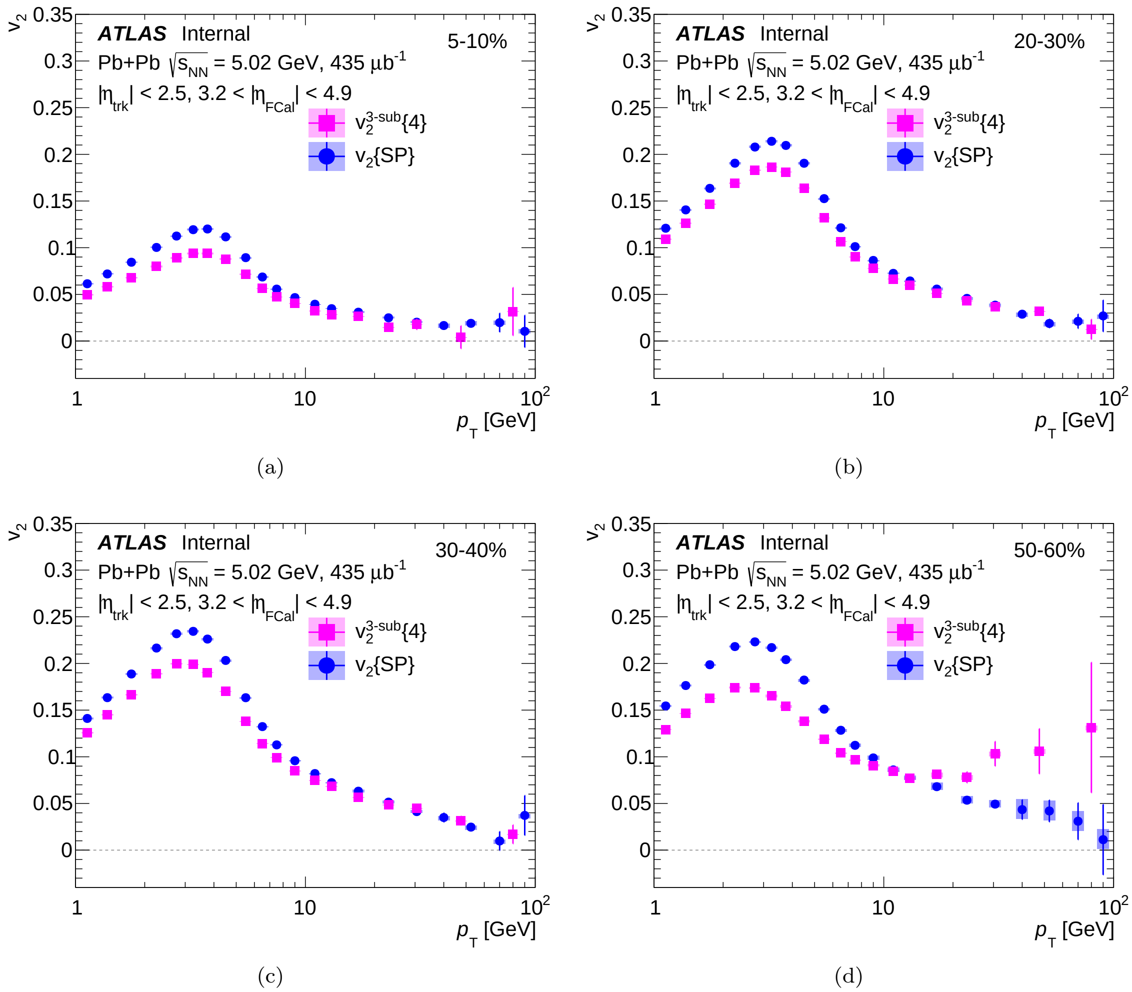

Figure B.20: Comparison between the $v_2\{\mathrm{SP}\}$ results and $v_2^{3\text{-sub}}\{4\}$ in centrality intervals (a) 5–10%, (b) 20–30%, (c) 30–40% and (d) 50–60%. The statistical uncertainties are shown as error bars and the systematic uncertainties are shown as boxes.

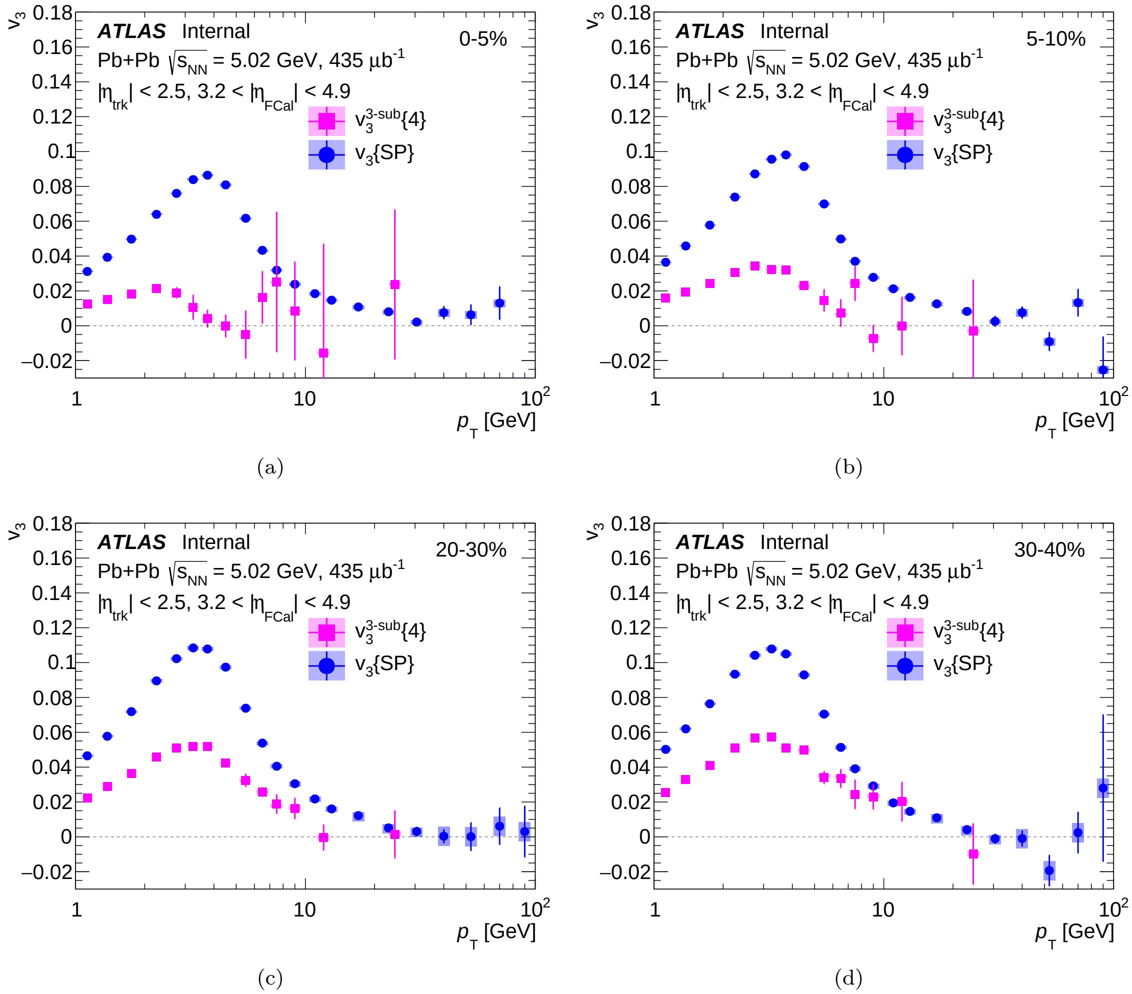

Figure B.21: Comparison between the $v_3\{\mathrm{SP}\}$ results and $v_3^{\text{3-sub}}\{4\}$ in centrality intervals (a) 0–5%, (b) 5–10%, (c) 20–30% and (d) 30–40%. The statistical uncertainties are shown as error bars and the systematic uncertainties are shown as boxes.